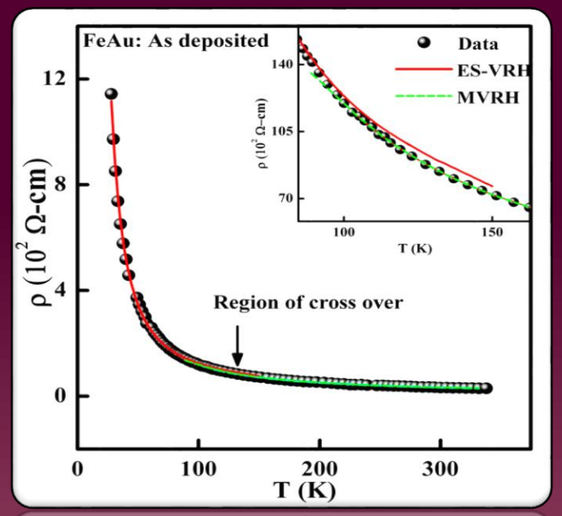

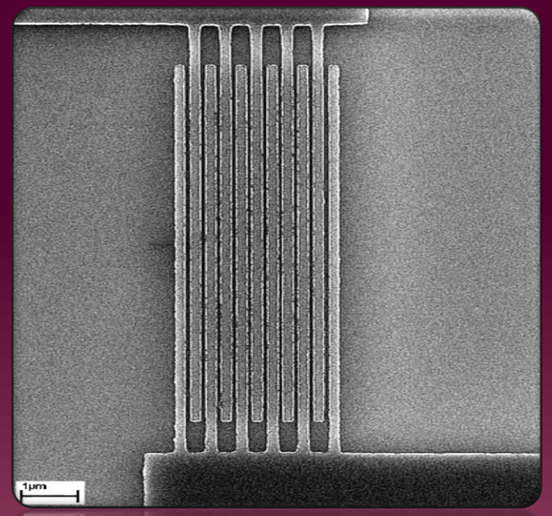

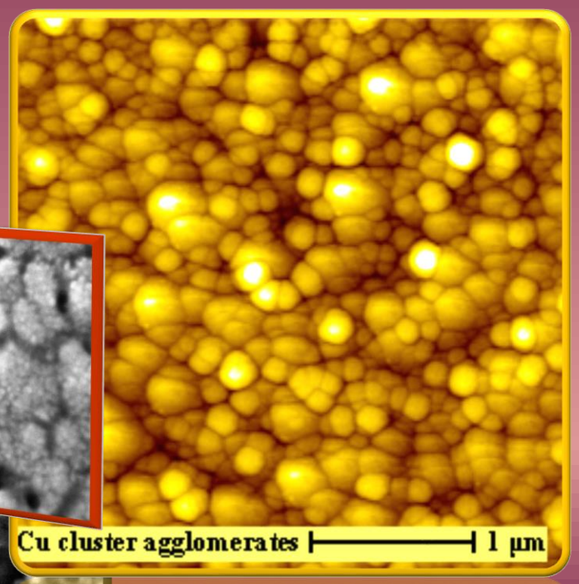

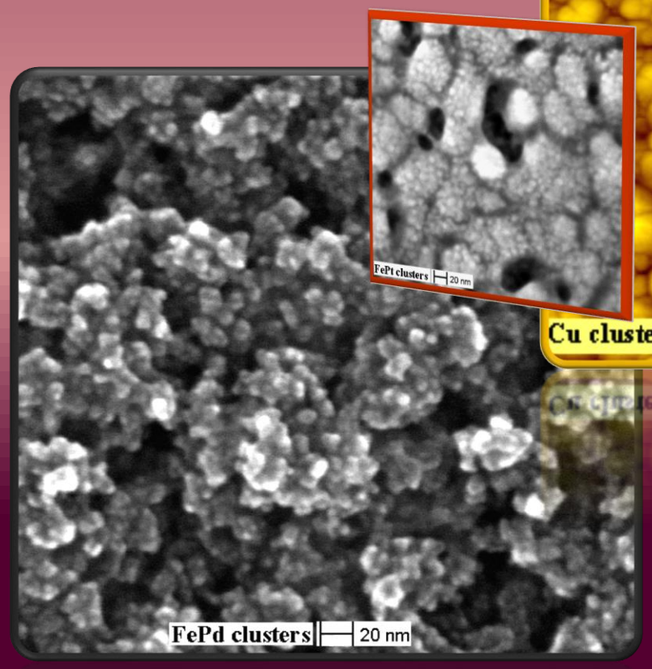

Ph.D. Thesis

THEJAL ABRAHAM

2014

Ph.D. Thesis

TRANSPORT POPERTIES OF NANOCLUSTER ASSEMBLED FILMS OF FeX (X= Au, Pd, Pt) and Cu, Ag, Au

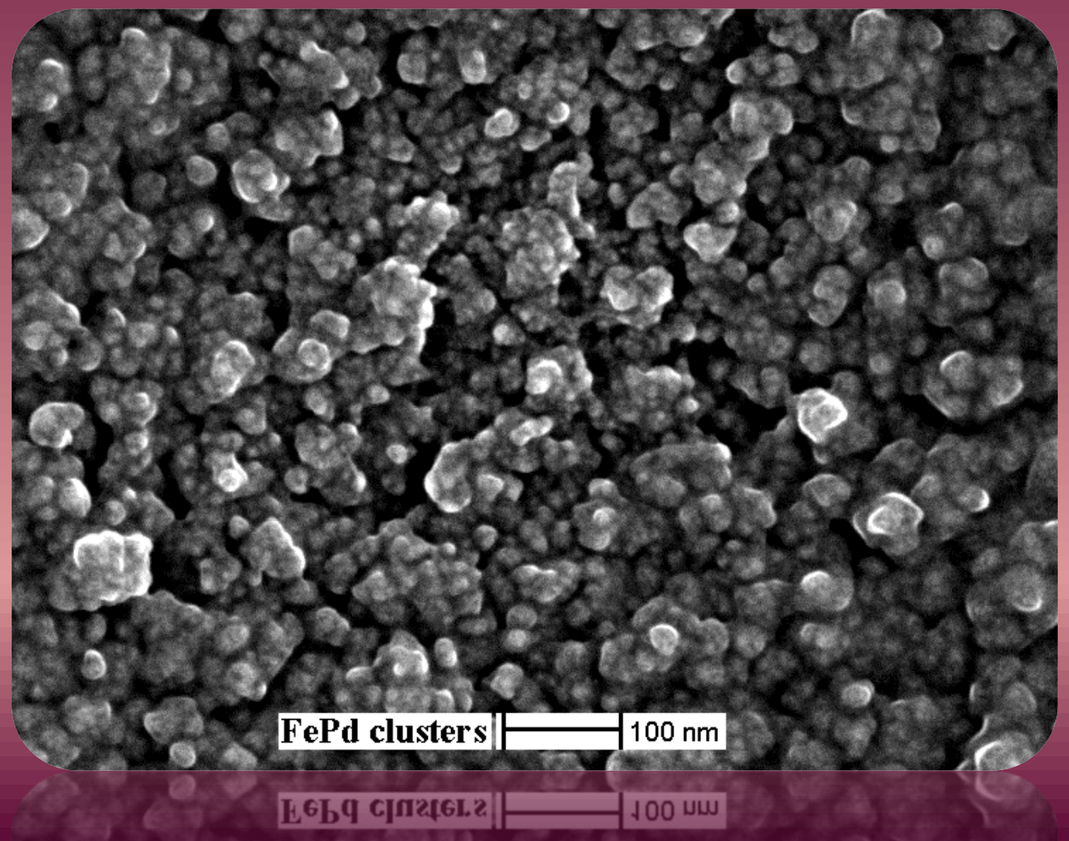

THEJAL ABRAHAM

School of Physics, University of Hyderabad.

TRANSPORT PROPERTIES OF NANOCLUSTER ASSEMBLED FILMS OF FeX (X=Au, Pd, Pt) AND Cu, Ag, Au

A thesis submitted for the degree of

Doctor of Philosophy

by

THEJAL ABRAHAM

School of Physics
University of Hyderabad
Hyderabad – 500046, India

July 2014

To
My Parents

DECLARATION

I hereby declare that the work reported in this thesis has been carried out by me under the supervision of ***Professor Chandrahas Bansal***, School of Physics, **University of Hyderabad**, Hyderabad, India. I also declare that this work has not been submitted to any university or institution for the award of any degree/diploma.

THEJAL ABRAHAM

Date: July, 2014

Place: Hyderabad

CERTIFICATE

This is to certify that the research work compiled in this thesis entitled **"Transport Properties of Nanocluster Assembled Films of FeX (X= Au, Pd and Pt) and Cu, Ag and Au"** has been carried out by **Mrs. THEJAL ABRAHAM** under our supervision and the same has not been submitted for the award of any degree of any university.

Prof. Chandrahas Bansal

RESEARCH SUPERVISOR
Professor, School of Physics
University of Hyderabad
Hyderabad

Dr. A. Rajani Kanth

CO-SUPERVISOR
Asst. Professor,
School of Physics
University of Hyderabad
Hyderabad

DEAN
School of Physics

ACKNOWLEDGEMENTS

At this moment in life, as I am submitting my thesis, it is with great delight I acknowledge heartfelt gratitude toward those who have been instrumental in helping me fulfill this venture. I thank Professor C. Bansal, my supervisor for his continuous guidance and encouragement during the entire course of my research work. It was altogether a different experience working with him. His approach to science is not only limited in solving research problems in view of future applications, but he is keenly interested in understanding the fundamental physics behind these endeavors. This has helped me gain a new perspective on how to approach a research problem and has encouraged me to take an exciting journey in understanding the fundamental mechanisms that are in play in this study. His critical analysis and keen mind for minute details has helped me to attain a better picture of the problem discussed here. I also extend my sincere thanks to Professor Ashok Chatterjee for his support and guidance. It was with the help of his theoretical knowledge and understanding that we could interpret the experimental results in the present work in detail. I thank him for the effort he has taken in sharpening my skills for a better understanding of Physics. I have also gained immensely from understanding his outlook on life and people. I sincerely thank both of them for being my teachers as they have contributed in different ways to prepare me for the life ahead.

I thank the Dean Prof. S. Chaturvedi and former Deans of School of Physics for permitting me to use the central facilities of the school required for the work reported in this thesis. I express my gratitude towards Prof. C.S. Sunandana for being my Doctoral Committee member and evaluating my

work at regular intervals. I also thank Dr. A. Rajani Kanth for kindly agreeing to be my Co-supervisor. I appreciate the kind support given to me by Prof. K. C. Jamesraju and all other faculty of the school. I sincerely thank Prof. J. Thampi Thanka Kumaran for his timely help in trouble shooting the nanocluster deposition system. I specially thank Prof. Rajan. K. John who motivated me to pursue research after my post-graduation. I express my thanks to all the technical staff as well as the non-teaching staff especially Mr. T. Abraham for the help and support I have received.

I wish to thank my juniors Venkata Krishnaya, Satya, Surya, Joshi and Jitu for their support and help. With gratitude I remember Swaroop, Kumar, Raji, Saritha, Uditha, Pushpa, KK, Farzana, for being there for me whenever I needed a friend. You have made my stay in the University a wonderful experience. I also thank my friends Ramudu, Alu, Sanjeev, Monisha and Shankar for their support. I wish to acknowledge all in School of Physics for their co-operation in carrying out my research work. I thank all the members of the church at Gachibowli, especially Prof. Joy David and Mrs. Clarice Joy David for their fervent prayers and support all along.

I am indebted to my parents for their unconditional support and prayers. Appa and Mummy you have believed in me all the way and I value that more than anything in my life. I wish to extend my thanks to my husband for making it possible for me even in the midst of difficult circumstances, to carry out this work. I gratefully remember my sister Sheethal, Aji and my nieces Diya and Daksha for their love and affection. I thank my in-laws, Pappa, Amma and Achachen, Cheduthy, Jake Suzzana and Jase. With love I remember my dear son Alden for making my life meaningful in every way. It is your presence in my life that gave me the courage and strength to bring this to culmination.

Above all I thank the Almighty for enabling me to carry out this work in a successful manner. I thank him for bestowing me with the knowledge required in understanding, even in a miniscule measure of what he has created in his infinite wisdom. "*I can do all things through Christ who strengthens me*." (Philippians 4: 13)

PLACE: HYDERABAD

DATE: (*Thejal Abraham*)

Page No.

CHAPTER 1

CHAPTER II

CHAPTER III

CHAPTER IV

CHAPTER 1

INTRODUCTION

1.1 Introduction

The dream of atomically engineered materials with desired properties for novel technologies is being fulfilled in leaps and bounds in different research laboratories all around the world. The journey of manipulating and controlling things in nanoscale has started as early as 1960. Scientists still find it difficult to grasp all the intricacies involved in creating these complex structures as well as unraveling its properties. In the natural world also, often it is observed that atoms assemble as molecules and further into nanostructures exhibiting a variety of properties. These structures are present in natural materials, in the biological arena, and in artificially designed materials. Thus nanotechnology transcends over different disciplines such as physics, chemistry, biology and engineering.

1.2 Importance of Nanostructured Materials

Before the advent of nanotechnology, our knowledge about the nature and its constituents has been restrained to certain scales of dimensions. To some extent we knew about atoms and molecules and also about bulk solids, but neither molecular nor bulk models could describe systems in nanoscale. In recent years there has been immense progress in the synthesis, characterization and understanding of nano-structured materials [1,2]. The research in nanomaterials has helped us to fill gaps in our fundamental understanding of matter and has opened a window to a new world of materials with unusual properties. It has also led to a number of new

technologies. This new world seems to be endless, spreading out in to almost all the established branches of science. Nanotechnology has been creating and is expected to create materials that could change the world and our lives completely. When manipulated with nanotechnology, ordinary materials become stronger, brighter and more durable [3]. Several size-dependent properties such as quantum confinement in semiconductor particles, surface plasmon resonance in some metal particles, superparamagnetism in magnetic materials and innumerable other effects are observed in nano structured materials. Quantum confinement effects significantly change the way the particles behave. This results in a change in conductivity, specific heat, an increase in energy band gap and variations in wavelengths of emitted light. Also, a change from bulk to nano-phase is sometimes accompanied by a change in the inter-atomic distances and crystal lattice constants. These materials have many outstanding properties such as high ductility, enhanced magnetic properties and improved hydrogen storage capacity to name a few of them. In elements such as Fe, Cr, Cd and Se a decrease in the particle size results in a loss of crystal structure and an appearance of amorphous structure [4-7].

However, why these materials gain such peculiar properties is a matter of extensive research. Our markets are already flooding with products enhanced by nanotechnology. These products play an important role in almost all branches of industry. They include more efficient catalysts, films for microelectronics, new magnetic materials, and protective coatings on metals, plastics and glasses. They are on their way to exceptional breakthroughs in all branches of science.

1.3 Origin of Novel Properties in Nanoscale.

The drastic changes observed in the properties, let it be electronic, magnetic or optical, when one ventures out from bulk to the nano-phase of materials is a problem that is investigated with keenest interest everywhere. Scientists are still baffled by questions regarding "Why nano structured materials exhibit peculiar properties?", but some of them are fairly answered.

Electronic properties of solids are altered with particle size. The quantum confinement effects experienced by the electrons as well as the resistance offered by the grain boundaries to the electronic motion contribute towards these effects. Thus interfaces play a very vital role in determining the properties of nano structures.

Since the surface to volume ratio of these materials is enormous, there are plenty of atoms available on the surface to help a reaction along. This gives nanomaterials high reactivity and enables them to serve as excellent catalysts. The high surface area to volume ratio of nanostructures provides a tremendous driving force for diffusion, especially at moderate temperatures. So sintering is possible for these materials at lower temperatures and over shorter durations than what is needed for bulk materials. The surface effects of nanoparticles also reduces the incipient melting temperature. With the reduction in the size of the particles, these materials have shown a decrease in the melting point in large number of studies: Sn [8,9], Bi [9], Pb [9-11], Pt [11], Ag [12,13], Al [11,13], Cu [13], Au [11,12,14-16], Na [17], Ga, In [10,11,18,19]. This effect is mostly observed when the particle size is below 10 nm.

Thus the exposure of large number of atoms to the surface environment, the presence of large number of interfaces as well as the change

in inter-particle spacing [20] all give rise to peculiar properties in nanostructures. A large number of surface atoms alter the surface energy and a variation in the surface energy leads to a change in the chemical potential. This in turn leads to changes in all thermodynamic properties [20].

1.4 Nanoclusters and Assembled Structures of Nanoclusters

Nanoclusters are entities made up of a few to thousands of atoms. Their dimensions are between 1-100 nanometers. Their properties are different from the atomic as well as the bulk properties and that is what makes them unique for fundamental studies as well as applications.

Organizing the clusters by an external force on to a substrate where the total energy of the system is minimized results in Nano Cluster Assembled (NCA) films or in other words stacking of clusters, during the deposition on to a substrate, produces the NCA films [21]. The physical and chemical properties of metallic clusters scale with the cluster sizes [22]. Assembling these mono-dispersed clusters as films can lead to materials with novel properties [23-25]. These systems express exotic physical properties concerning the electrical and magnetic measurements.

NCA films can be basically produced by a nanocluster deposition system, which consists of a nanocluster source with a DC magnetron sputtering system. It has an aggregation chamber and a deposition chamber in which the sputtered atoms condense to form clusters and are lead to be deposited on a substrate respectively. This method of preparation helps in minimizing the defects in nano structures. It gives a fairly mono-disperse cluster size and a choice in the kinetic energy of clusters during deposition. Thus the NCA films consist of atomic clusters, which have a small size

dispersion, having minimal defects, softly landed on the substrates and without any effect of nucleation and growth on substrates. Thus the method of preparation gives ample control on the parameters affecting the size and shape and after which these preformed clusters can be assembled on to the substrates. The aggregation time, which affects the size of the clusters and the deposition time that determines how densely packed they are, all play a decisive role in influencing the properties of NCA films. This work consists of investigations done on metallic and alloy cluster assembled films.

1.5 Ongoing Research in the Field of Nanoclusters

Metallic nanoclusters below 10 nm over a wide range of elements have been prepared and characterized in many labs over the world in the last decade. Investigations on the size distribution of various nanoclusters, their structural stability, adhesion to the substrate, coalescence, scaling of magnetic properties, electron transport, phonon density of states and surface roughness all has been under study.

There have been studies on the diffusion of Cu clusters after deposition, their size distribution, cluster-substrate interactions and cluster coalescence [26]. The geometry and stability of Niobium clusters, size-dependent structure of Molybdenum clusters, and magnetic properties of cobalt nanoclusters has all been reported in literature in detail [26]. Reports on the structural stability of Fe nanoclusters of 5nm revealed a thin oxide coating, which could be removed by annealing at a temperature almost equal to 1/3rd of the melting point of Iron. Annealing of clusters lead to the fusion and formation of larger clusters only if they were in contact, preserving their crystallographic structure [27]. Monolayer-thick films of self-assembled, size-selected, isolated $Fe_{1-x}Pt_x$ alloy nanoclusters have been reported to show

enhancement of phonon density of modes at low and high energies along with strong suppression of longitudinal and transverse acoustic phonon peaks in between [28]. Various studies on magnetic properties of nanocluster films by controlling the cluster parameters have been reported [29-32]. Electron transport in single-layer films made of Au clusters as small as 1.3 nm, placed between closely spaced electrodes has been studied. The cluster size was found to have an effect on the I-V characteristics and Coulomb blockade was found to be governing the system [33]. Apart from a few there are not many reports on the electron transport in the NCA films. This work is intended to fill this gap with detailed analysis of transport properties in these systems.

1.6 Motivation for the Present Work

The special properties of small particles were known to the ancient world and were exploited without understanding the reason behind it. Attempts on unraveling these properties and their causes in terms of applications are still going on in the present time. Though atomic aggregations or clusters of nano-size form a structure in-between isolated atoms and bulk solid, the properties revealed by these materials could not be explained simply by interpolating the bulk properties. When the size is reduced to nanoscale, quantum effects begin to dominate. There will be a great departure from the properties of bulk materials as novel properties emerge due to these effects.

As mentioned earlier, when the size of the cluster reduces, their surface to volume ratio increases tremendously. As the percentage of surface atoms increases, dominance of the behavior of atoms on the surface of a cluster over that of those in the interior occurs. This affects both the properties of the clusters in isolation and its interaction with other clusters. In

metals as the size decreases the number of grain boundaries increases. Thus an appreciable portion of the NCA material is subjected to forces related to interfaces and grain boundaries. Thus the mechanical, electrical, chemical, magnetic and optical properties of NCA structures are found to be different from their bulk counterparts. These properties are found to depend considerably on size, shape and the composition of these materials. Among them particle size is found to have the strongest effect on the properties of nanoclusters.

Grain size distribution and internal strains are crucial factors affecting the physical properties of NCA films. Therefore it is very important that there is proper control over the grain size distribution as well as the distribution of distances between nanoclusters while designing cluster-assembled materials with tailored properties.

The lattice vibrations or phonons and their transport through nanostructures are different from that in the bulk. Lattice vibrations couple with each other and can couple with structural defects such as grain boundaries, dislocations and point defects [34]. The high density of interfaces and grain boundaries in NCA materials affect the propagation of phonons in them. Thus transport properties in these nanostructures are found to be different from that of the bulk as the quantum effects will come in to play in reduced dimensions. Since the mean free path of charge carriers is much less than the structural dimensions in bulk, the charge transport is essentially diffusive, described by the Boltzmann Transport Equations whereas in NCA materials the quantum nature of the carrier states will begin to manifest themselves [34]. The transport in nanostructures is entirely dominated by the nature of quantum states and the manner in which these states carry current.

Effects such as quantization of motion due to confinement, Coulomb blockade, changes in the quasi particle energy and density of states all prevail in the nano dimensions. Phenomena such as quantum fluctuations, conductance quantization, localization of carriers and tunneling will be manifested as a result of quantum interference effects [34]. So the transport in NCA films has formed a crucial part of the present study.

A number of fascinating results on cluster size effects, quantum confinements of electrons and phonons and the resulting transport properties are described in this work. Growing randomly distributed nanometer-sized isolated Au clusters with specific electronic properties was also pursued. The morphology as well as the difference in the transport properties of Cu, Ag and Au as well as FeAu, FePd, and FePt NCA films from the bulk is investigated in detail.

The field of NCA structures is going to be revolutionary, transformative, powerful and potentially beneficial. We are approaching an era where each and every aspect of life will be enhanced by it in one form or another. Soon time will wipe away each and every challenge that is posed in its way. As an initial step towards this phase, all the fundamental questions regarding these materials are to be answered. In research or in any field, it is vital to establish the fundamentals. It is only on this basis that, future work can be carried out. The improvements made in the technology of probing devices has helped to resolve some of the questions regarding these materials. Creating the NCA structures with tailored properties with required dimensions is a real challenge. This work addresses the challenges in production as well as characterization of NCA films.

1.7 PLAN OF THE THESIS

This thesis is organized into six chapters. The contents of the chapters are as follows.

In this chapter we have already givena brief introduction to the nanostructured materials and their importance. It explains the origin of novel properties in nanoscale. We have defined nanoclusters as well as cluster assembled films and describes the superior properties possessed by NCA films produced from inert gas condensation technique, using a cluster source and a dc magnetron sputtering. A brief summary of the on-going research in the field of nanoclusters was presented. The objectives of the present work were discussed towards the end of this chapter. The aim of this study was to fabricate NCA films of desired cluster size and thickness. Also to study the cluster size distribution, morphology, structural stability and the response of NCA films to annealing. The transport properties of NCA films as well as isolated nanocluster assemblage were also investigated.

Chapter 2 discusses the experimental techniques used in this work. This includes the preparation of NCA films using a nanocluster deposition system based on the principle of inert gas phase condensation.The characterization methods of NCA films are also discussed. The optimum conditions for the preparation of metallic cluster films of different materials is discussed. The NCA films were characterized by investigating their structural, morphological, electrical and magnetic properties. The structural characterization was done using a Powder X-ray diffractometer. The composition was analyzed using an EDX. The morphological studies were done using an Atomic Force Microscope, Transmission Electron Microscope, Scanning Electron Microscope and a Field Emission Scanning Electron

Microscope. The magnetic measurements were done using a SQUID magnetometer. A four-probe dc resistivity measurement set up comprising a closed cycle refrigerator was used for the resistivity measurements.

Chapter 3 describes the preparation and characterization of alloy NCA films of FeAu, FePd, and FePt. Heat treatments were carried out on all the three systems to study their response to annealing temperatures of 350^0C and 300^0C for different durations of time. The composition analysis was done using Energy Dispersive X-ray Spectrometry and was found to be consistent with those in the starting material. The crystallographic structure was determined from the X-ray diffraction patterns and the presence of $Fe_{0.9}O$ oxide could be determined for the FePt films. The presence of oxide was later confirmed in all the samples from electron diffraction data. X-ray diffraction patterns were also used to estimate the average cluster size. The Atomic Force Microscopy images revealed the presence of agglomerates in the sample, which could be seen to split up to individual clusters with heat treatments. The TEM and FESEM pictures were analyzed to estimate the cluster size as well as the size distribution of NCA films. The distribution was found to be lognormal in these systems [35]. The cluster agglomerates were very clearly visible in the FESEM pictures. The oxide formed an insulating cloud around the agglomerates, isolating individual clusters while holding them together as a pack. The oxide layer formed a network kind of structure also connecting the agglomerates together.

The resistivity measurements of these alloy systems showed an activated behavior. This was understood in terms of the oxide cloud in the system which gives rise to Anderson localization. The resistivity was interpreted in terms of hopping conduction. The formalism of the Efros-

Shklovskii Variable Range Hopping (VRH), Mott VRH and Nearest Neighbor Hopping(NNH) are described in detail in this chapter. All these theories were employed in explaining the resistivity behavior in the case of as-sputtered and heat-treated FeAu films. Crossover from one mechanism to the other, were also observed in these samples. It was observed that with an increase in the duration of heat treatment at 350^0C, more and more oxide layer was getting removed from the system, which liberated the individual clusters that started spreading out into a wider area. The clusters still remained as agglomerates of very few numbers. With increased heat-treatment time the individual clusters started growing is size and the smaller agglomerates started coming into contact with each other. The oxide layer thickness around the clusters, their spacing with each other and the spacing between the agglomerates, their size, all are found to be deciding factors determining the conduction mechanism for FeAu NCA films.

The resistivity curves were analyzed using the Zabrodskii and Zenov'eva method [36]. The Efros-Shklovskii VRH was found to be the conduction mechanism in FePd and FePt films. The heat treatments carried out at 350^0C at 4 min and 7 min are found to bring about Metal- Insulator transitions in the FePd and FePt NCA films respectively. The transition temperature T_C is found to decrease with the increase in the duration of heat treatment. This was understood, as longer heat-treatments would result in thinner oxide layers which will allow the electron to hop from one cluster to the other with lower thermal energies and hence the decrease in T_C. The magnetic properties were analyzed by measuring the FC/ZFC curves using a SQUID magnetometer. These measurements confirmed the superparamagnetic nature of the NCA systems, which is typical of small nanoparticles. M-H loops of all the three NCA systems after field cooling

displayed exchange-bias [37]. The measurement results, the plots and micrographs are all discussed in detail in this chapter.

Chapter 4 talks about the preparation and characterization of metallic NCA films of Cu, Ag and Au. The preparation conditions of the NCA films are presented in the beginning of this chapter. The Au NCA films were found to have little adhesion to the glass-substrates used and found to be peeling off the substrates easily. X-ray diffraction patterns were used to characterize the crystallographic structure and to calculate the average cluster size in the NCA films. The Cu NCA films were found to be oxidized as the XRD pattern of the as-sputtered Cu films confirmed the presence of Cu_2O in the sample. This was also confirmed from the electron diffraction data. A heat-treatment under argon gas atmosphere at 350^0C for 5 min could remove this oxide [27]. Heat treatments were carried out on Cu and Ag NCA films to study their response to annealing temperatures between 100^0C-400^0C. The XRD patterns of heat-treated samples showed an increase in cluster size as cluster coalescence happens far below the bulk melting temperatures [21]. Microstructural characterization using Scanning Electron Microscopy allowed the study of the cluster size distribution of NCA films. The distribution was found to be lognormal for these systems. Atomic Force Microscopy revealed that the nanoclusters formed agglomerates of hundreds of nanometers and these agglomerates were disintegrating with heat-treatments. The measured resistivity was found to be a few orders of magnitude higher than the bulk resistivity. The increase in resistivity was interpreted in terms of phonon confinement effects in nanoscale as well as the increase in cluster boundaries, resulting in electron scattering as they propagate through the lattice. Because of the size confinement effects in nanostructures, the phonon spectrum is expected to vanish below a critical frequency [38,39]. This introduces a lower

limit of integration 'θ_0' in the Bloch Grüneisen formula, which is used for fitting the resistivity data of NCA films. From the resistivity fits, parameter θ_0 is found to decrease with an increase in the cluster size. The theoretical calculation of θ_0 and that obtained from the fits show a difference of one order of magnitude, the likely reasons for which is discussed. The temperature coefficient of resistance of NCA films is found to increase with an increase in the cluster size. These results are plotted and discussed in detail in this chapter and conclusions on the properties of Cu, Ag and Au NCA films are derived on the basis of these results.

Chapter 5 describes the preparation and electron transport in spatially separated Au nanocluster assemblies. The preparation conditions of isolated Au clusters are presented initially in this chapter. Scanning Electron Microscopy was employed to analyze the cluster size distribution of the system. The Transport measurements revealed a conductivity of NNH between the temperatures ranging from 230 K to 340 K. From 205 K to 230 K the conductivity behavior was identified as a logarithmic temperature dependence given by $\sigma = a + b \ln T$ (where σ is the conductance, T is the temperature and 'a' and 'b' are material dependent constants) [40]. The presence of Coulomb blockade was identified in the system for the temperatures below 280 K from non-linear I-V characteristics.

Chapter 6 gives the conclusions derived from the experimental data and analysis of the work described in this thesis and also discusses some directions for future work.

References

[1] Proceedings of the sixth international Conference on Small Particles and Inorganic Clusters, Z. Phys. D, Vol. 26, (1993).

[2] R. S. Averback, J. Bernholc, and D. L. Nelson, Eds. Mater. Res. Soc. Vol. 206, (1991).

[3] Valiev, and Ruslan, "Nanomaterial Advantage", Nature, 887 (2005).

[4] A. Hori, Chem. Econ. Eng. Rev. Vol. 7, 28 (1975).

[5] Yu. G. Morozov, A. N. Kostygov, V.I. Petinov, and P. E. Chizhov, Fiz. Nizkikh Temp. Vol. 1, 1407 (1975).

[6] Yu. G. Morozov, A. N. Kostygov, A. E. Petrov, P. E. Chizhov, and V.I. Petinov, Fiz. Tverd. Tela, Vol. 18, 1394 (1976).

[7] S. Fujime. Japan. J. Appl. Phys. Vol. 5, 1029 (1966).

[8] C. R. M. Wronski, Brit. J. Appl. Phys. Vol. 18, 1731 (1967).

[9] V. P. Skripov, V. P. Koverda and V. N. Skokov, Phys. Stat. Sol. (a) Vol. 66, 109 (1981).

[10] C. J. Coombes, J. Phys. F: Met. Phys. Vol. 2, 441 (1972).

[11] V. P. Koverda, V. N. Skokov and V. P. Skripov, Fiz. Metall. Metalloved., Vol. 51, 1238 (1981).

[12] T. Castro, R. Reifenberger, E. Choi and R. P. Andres, Phys. Rev. B, Vol. 42, 8548 (1990).

[13] N. T. Gladkikh, R. Niedermayer and K. Spiegel, Phy. Stat. Sol. Vol. 15, 181 (1966).

[14] R. Sambles, Proc. Roy. Soc. Londan A, Vol. 324, 339 (1971).

[15] M. Blackman, and J. R. Sambles, Nature, Vol. 226, 938 (1970).

[16] P. Buffat and J. Borel, Phys. Rev. A, Vol. 13, 2287 (1976).

[17] B. T. Boiko, A. T. Pugachev and V. M. Bratsykhin, Fiz. Tverd. Tela, Vol. 10, 3567-3570 (1968).

[18] V. N. Skokov, V. P. Koverda and V. P. Skripov, Fiz. Tverd. Tela, Vol. 24, 562 (1982).

[19] V. P. Koverda, V. N. Skokov and V. P. Skripov, Kristallografiya, Vol. 27, 358 (1982).

[20] Avery. N. Goldstein, "Handbook of Nanophase Materials", Marcel Dekker, Inc. New York, (1997).

[21] S. A. Koch, T. Vystavel, G. Palasantzas, J. Th. M. De Hosson. Encyl. Nano Sc. And Nano Tech., Ed. H. S. Nalwa, American Scientific Vol. 14, 457-496 (2011).

[22] U. Landman et al. Int. J. Mod. Phys. B, Vol. 6, 3623 (1992).

[23] J. M. Antonietti et al. Phys. Rev. Lett. Vol. 94, 213402 (2005).

[24] A. Sanchez et al. J. Phys. Chem. A, Vol. 103, 9573 (1999).

[25] J. T Lau et al. Phys. Rev. Lett. Vol. 89, 057201 (2002).

[26] H. S. Nalwa Ed. "Encyclopedia of Nanoscience and Nanotechnology", Vol. 14, 457-498 (2011).

[27] T. Vystavel, G. Palasantzas, S.A. Koch, and J. Th. M. De Hosson, Appl. Phy. Lett. Vol. 82, 197 (2003).

[28] B. Roldan Cuenya,Jason R. Croy,L. K. Ono, A. Naitabdi, H. Heinrich, W. Keune, J. Zhao, W. Sturhahn, E. E. Alp, and M. Hu, Phys. Rev. B, Vol. 80, 125412 (2009).

[29] David J. Sellmyer, Minglang Yan, Yingfan Xu, and Ralph Skomski, IEEE Transactions on Magnetics, Vol. 41, No: 2 (2005).

[30] Y. Xu, Z. G. Sun, Y. Qiang, and D. J. Sellmyer, J. Appl. Phys. Vol. 93, 8289 (2003).

[31] Y. Xu, Z. G. Sun, Y. Qiang and D. J. Sellmyer, J. Magn. Magn. Mater, Vol. 266, 164 (2003).

[32] Y. Xu, M. L.Yan, and D. J. Sellmyer, IEEE Trans. Magn. Vol. 40, No: 4, 2525–2527 (2004).

[33] M. G. Ancona, W. Kruppa, R. W. Rendell, A. W. Snow, D. Park, and J. B. Boos, Phys. Rev. B, Vol. 64, 033408 (2001).

[34] William A. Goddard et al. eds. "Handbook of Nanoscience Engineering and Technology" CRC Press, (2007).

[35] H. Hovel and I. Barke, Progr, Surf. Sci. Vol. 81, 53 (2003).

[36] Ralph Rosenbaum, Phys. Rev. B, Vol. 44, 3599 (1991).

[37] Y. K. Tang, Sun Y and Z. H. Heng, J. Appl. Phys. Vol. 100, 023914, (2006).

[38] H. S. Yang, S. P. Feofilov, D. K. William, J. C. Milora, B. M. Tissue, R. S. Meltzer and W. M. Dennis, Physica B, Vol. 263-264, 476 (1999).

[39] A. I. Gusev and A. A. Rampel, "Nanocrystalline Materials", Cambridge Int. Science, (2004).

[40] A. R. Akhmerov and A. S. Ioselevich, Condensed matter. JETP Lett. Vol. 83, (5)211–216 (2006).

CHAPTER II
EXPERIMENTAL TECHNIQUES

This chapter describes in detail the preparation method of nano cluster assembled (NCA) films, the experimental techniques used for characterizing them, and methods of transport measurements in the films.

2.1 NCA Film Preparation Method

We first describe the UHV cluster deposition system that was used for the synthesis of nanocluster films studied in this thesis.

2.1.1 Nanocluster Deposition System

The NCA films for the present work were prepared using the Nano Cluster Deposition System (NCDS) - Nanodep60 from the Oxford Applied Research, UK. The NCDS works under ultra-high vacuum and is designed specifically for the deposition of nanoclusters by the method of inert gas condensation. It is built around a nanocluster source NC200U that comprises of a dc magnetron and an aggregation chamber. Apart from these the NCDS include a deposition chamber, a dc ion source, facilities for internal bake out and pumping, an epicenter substrate holder with heater, pressure gauges and mass flow controllers. A schematic diagram of the NCDS is shown in Fig. 2.1. This system is an efficient tool for the study of nanoclusters as it can produce metallic, semiconducting, magnetic and compound nanoclusters. It offers optimal process flexibility by providing numerous entry ports for analysis tools. It is tailored for a deposition over $1cm^2$ substrates and is suitable for soft-landing clusters as well as for energetic cluster impact (ECI) studies. Emerging applications where NCDS is of use, include magnetic and optical

data storage, catalysis, ECI films, contact-hole filling [1] and fundamental studies of nanoparticles.

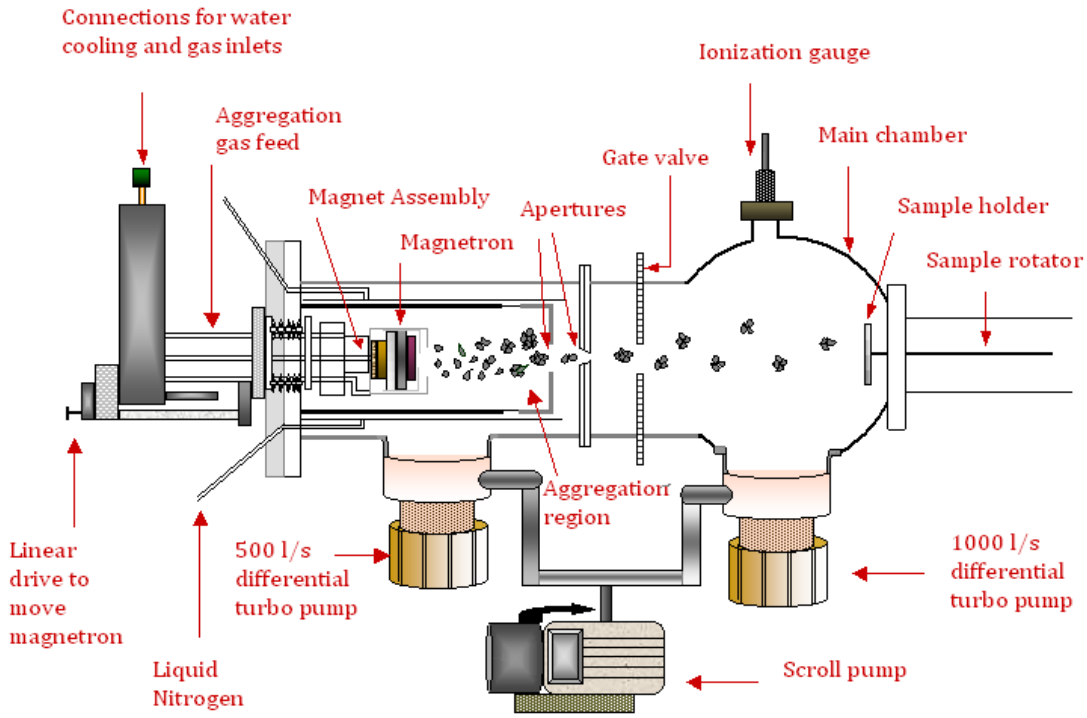

Fig. 2.1. A schematic diagram of the NCDS, showing the formation of clusters from sputtered atoms in the aggregation region, which is guided to be deposited on the substrates placed on the sample holder in the deposition chamber by differential pumping.

2.1.2 Nanocluster Source

The NC200U which is the nanocluster source, consists of the magnetron, a linear drive to move the magnetron, an aggregation region, a T-piece which is a differential pumping port, a pressure gauge and apertures opening to the deposition chamber. It uses a dc magnetron discharge to generate nanoclusters. The magnetron has been designed specifically for high operating pressures (up to 1 mbar) in the aggregation region, which yields

high sputtering rate. The distance between the magnetron and the apertures is adjusted using a linear motion drive that decides the dwelling time of the clusters in the aggregation region, which is a major parameter deciding the cluster size.

An enlarged view of the nanocluster source is given in Fig. 2.2 below:

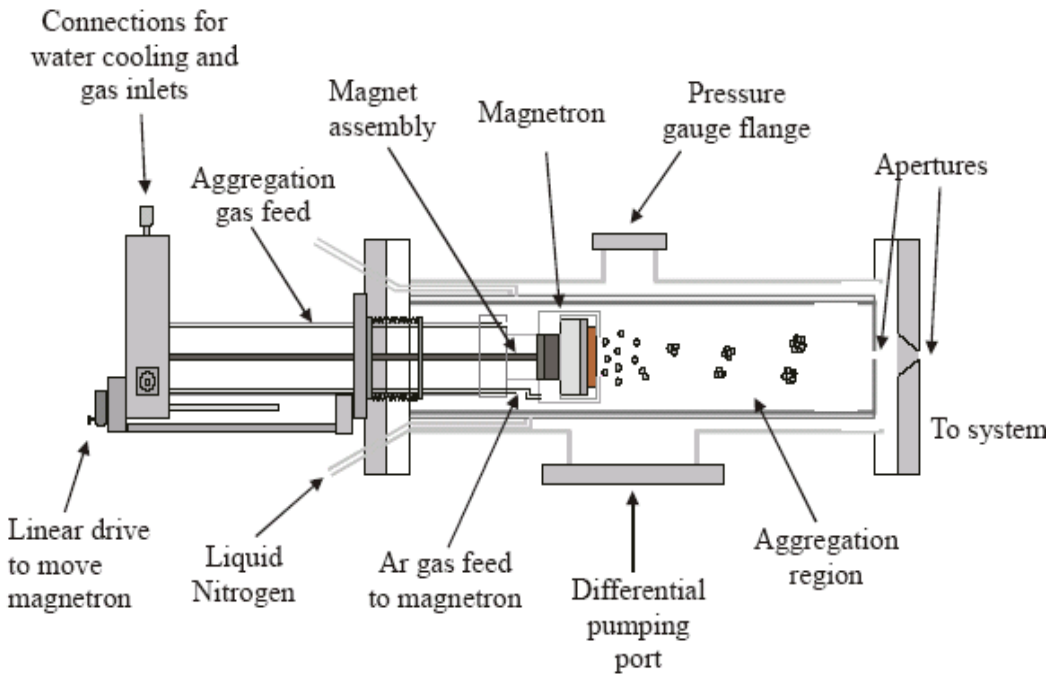

Fig. 2.2. A schematic diagram showing the enlarged view of NC200U nanocluster source.

Two gas inlets are provided to the NC200U, one is for Ar gas and is used for magnetron discharge. The other one is used for introducing gases in to the aggregation chamber. One of these is connected to the vacuum gauge monitoring the pressure in the aggregation region. The aggregation tube is cooled by water. The magnetron uses targets that are discs, which are of standard 50.8 mm diameter with a maximum 5 mm thickness. In the magnetron, rare earth magnets are positioned behind the target material and

the magnets are water-cooled. These magnets create magnetic fields to confine the electrons in the magnetron plasma. When using magnetic targets there is a possibility for these target materials to interfere with the magnetic field created for electron confinement. Therefore it is necessary to use thinner targets. Elements such as Fe should only have a target thickness of 1-2 mm, Co can have 2-3 mm and Ni about 2-4 mm. There are reports on successful deposition of Fe clusters even using targets of 0.8-0.9 mm [2]. A thin Molybdenum back plate is provided just behind the target to prevent the sputtering of the magnetron head in case the target is worn out. The target is held in place by the target holder, which is enclosed in the magnetron cover. The separation between the target holder and the magnetron cover should be normally around 0.3 mm whereas for magnetic materials this is reduced to 0.2 mm. A 500 l/s turbo pump is connected to the T-piece, which is a differential pumping port to reduce the gas load in the deposition chamber. The percentage of ionized clusters produced by NC200U (>30% for Cu) is very high. The ionized clusters can be manipulated electrostatically. An ionized beam can be accelerated towards substrate by biasing them to form highly adherent and uniform coatings [3]. This technique, the so-called ECI can be used to form dense films on otherwise-difficult materials, such as Teflon. The cluster source is capable of producing clusters consisting of a few tens of atoms up to particles with diameters greater than 10 nm. Compound clusters, can also be formed by using alloy targets or by adding the appropriate gas to the aggregation region during operation. The cluster size can be adjusted by varying three main source parameters: the aggregation length (the distance between the target and the apertures), the power to the magnetron and the flow of the aggregation gas.

2.1.3 Descriptions on Deposition Chamber and Differential Pumping

The nanocluster source with the aggregation region opens to the deposition chamber through the apertures. A 1000 l/s turbo pump is used to evacuate the deposition chamber whereas a 500 l/s turbo pump differentially pumps the T-piece of the nanocluster source. Both these pumps, are backed by a scroll pump. The deposition chamber is maintained at a lower pressure by this differential pumping. The NCDS is capable of producing a system base pressure of the order of 10^{-9} mbar. The apertures control the gas flow between the aggregation chamber and the deposition chamber. The aggregation zone is actually pumped through these small apertures through which the clusters pass. The aperture sizes can be varied from 3-6 mm. The aggregation region and the deposition region are separated by a gate valve, which can only be operated by hand. The deposition chamber is provided with the epicenter sample holder, a dc ion source, an ionization gauge and various ports for analysis tools. The epicenter controller is capable of sample heating, bias and rotation. It can apply a bias of ±5 kV to the sample. This also rotates the sample for a uniform deposition of clusters. The heater provided with the epicenter is capable of heating the sample up to a temperature of 800^0C. If the clusters are ionized, then an applied biasing voltage on the substrates can direct their paths. This can be used to the advantage of directing the clusters onto a substrate in a uniform fashion. Thus ionized clusters fly from the target in straight lines when the target is biased, resulting in ECI on substrate.

2.1.4 Working of NCDS

The turbo pumps connected to the aggregation as well as the deposition chamber together are capable of creating a vacuum of 10^{-9} mbar.

Once the desired vacuum is reached Ar gas is introduced and the target material is sputtered by the dc magnetron with Ar plasma. Ar or He gas is introduced in to the aggregation region through the second gas inlet. Now the pressure in the deposition chamber falls to a value of 10^{-5} mbar whereas the pressure in the aggregation region falls to 10^{-1} mbar. This is maintained by the differential pumping. The dc magnetron, sputters the target material into the high-pressure aggregation region. In the aggregation region, the sputtered atoms collide with the large population of inert gas atoms of argon or helium (or both) that act as moderators and move diffusively in the direction of gas flow, and condense by transferring their kinetic energy to the inert gas atoms. As they condense they start aggregating forming nano-sized clusters. The rare gases present sweep the atoms and clusters from the aggregation region towards the apertures. These clusters are channeled through the apertures into the deposition region because of the low pressure maintained there by differential pumping. The aggregation region in the nanocluster source is water-cooled. This stabilizes the deposition as well as reduces the mean cluster size.

Water is required for the cooling system and it is provided, for the nanocluster source, the dc ion source and the pumps. The incoming water temperature is to be maintained at 18^0C and the inlet water flow rate should be at least 3 l/min at a pressure of 2-3 bars. The Nanocluster source can be baked up to a temperature of 150^0C. The bake out should be extended to 4-5 hours for optimum results.

There are a number of parameters that can be varied to alter the cluster size using the NC200U cluster source, such as the magnetron power, the aperture size, Ar flow rate, He flow rate, aggregation region temperature

and the aggregation length. The relationship between cluster size and these parameters can be quite complex. Increasing the aggregation length increases the cluster size as it increases the dwelling time of the clusters in the aggregation region.

Fig. 2.3 shows the pressure produced in the deposition chamber with Ar gas flow alone and that which is produced with the He gas flow, while an Ar flow of 110 sccm is maintained. The depositions for Cu, Ag and Au were carried out at an Ar gas flow of 60-70 sccm and these points are also indicated in Fig. 2.3 and they agree with the expected pressures in the deposition chamber.

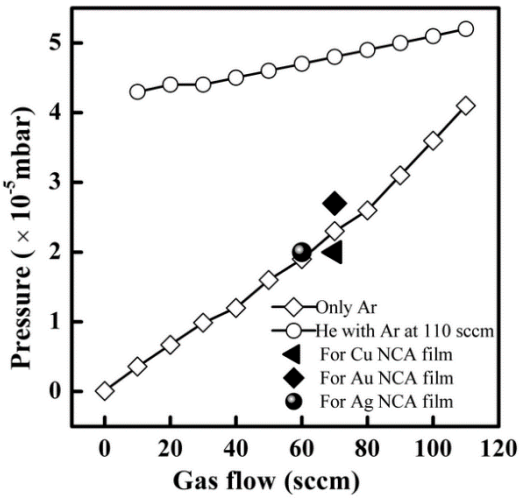

Fig. 2.3. Deposition chamber pressure vs. Ar and He flow. The pressure achieved during the deposition of NCA films with the corresponding Ar flow tally well with this data.

Fig. 2.4 shows the deposition rate as a function of Ar gas flow for different magnetron powers as given by the manufacturer. The maximum sputtering yield is obtained at an Ar flow of 70 sccm at 50 watt. Above 100 watt the sputtering rate increases with increasing Ar gas flow, whereas below

and at 100 watt the sputtering rate increases at first with the Ar flow reaching a maximum at 70 sccm and then falling down. The Cu films discussed in this work were deposited at 90 watts, at 70 sccm pressure and the observed rate of deposition agrees with the data shown in the Fig. 2.4.

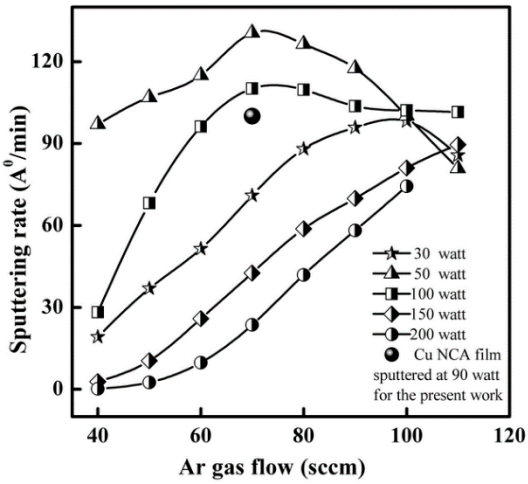

Fig. 2. 4. Effect of magnetron power on Cu deposition rate. The deposition rate of Cu NCA films for the present work agrees well with the data given by the manufacturer for the NCDS system.

The lifetime of a 5 mm thick cu target, using Ar as the sputtering gas is around 2 kWh when the magnetron power was maintained at 50 Watt and Ar gas flow rate was around 20 to 30 sccm [4]. The lifetime of a target will depend on the sputtering rate of a material. For different materials the lifetime will be different because of varying sputtering rates.

A summary of the cluster source specifications is given below:

Material Source	1 kW DC Magnetron (power supply incl.)
Target diameter	50.8 mm (2")
Target thickness	1- 5 mm
Mean cluster sizes	<0.4 nm to ~10 nm in diameter
Ar flow rate required	10-100 sccm

Beam diameter	5 mm to 40 mm (at a source-sample distance of 100 mm)
Aggregation length	65 – 205 mm
Maximum bake out temperature	150^0C

2.2 X-ray Diffractometer

The crystallographic structure as well as crystallite size of materials can be effectively investigated using X-ray diffraction [5]. X-ray diffractograms of NCA films were recorded in order to investigate the crystallographic structure of the systems. An X-ray diffractometer of Inel-make was used for this purpose.

The Inel x-ray diffraction system consisted of the Cobalt x-ray source, a gonio meter to rotate the sample and the detector. The X-ray generator XRG 3000 has a maximum power of 3000 Watts with a maximum current of 50 mA and a maximum voltage of 60 kV. It generated the Co K_α radiation with wavelength (λ) of 1.7889 A^0. The detector, Inel CPS-120 is a large angle position-sensitive detector (PSD) that consists of a curved chamber, which has a solid blade anode and a segmented cathode mounted in it. It is a proportional type detector. X-ray diffraction patterns are acquired at all angles simultaneously using this curved x-ray detector. It takes a snapshot of the entire diffraction pattern simultaneously i.e. all the data are recorded in "real time", at very high resolution. CPS 120 Model has got an angular range of detection of 120° / 2θ and its radius of curvature is 250 mm. The system can analyze a sample of area as small as 10 microns.

2.3 Transmission Electron Microscopy (TEM)

TEM makes use of a beam of monochromatic electrons, to obtain a magnified image of a specimen. The small de Broglie wavelength of the

electrons makes it possible to get a resolution in TEM, a thousand times better than a light microscope. This makes it possible for the TEM to examine fine details in a sample, of the order of a few angstroms, for e.g. a column of atoms. Thus TEM makes it possible to study the size, shape and arrangement of particles that make up a specimen as well as their relationship to each other on the scale of atomic diameters. The possibility for high magnifications makes TEM a valuable tool in medical, biological and material research.

An electron source placed at the top of a microscope emits electrons that travel through vacuum in the column of the microscope. Electromagnetic lenses are used to focus the electrons into a very thin beam. This electron beam is made to interact with an ultra-thin specimen while passing through, and some electrons are scattered and thus removed from the beam, depending on the density of the material present. At the bottom of the microscope the unscattered electrons, that go past unobstructed, is made to hit a fluorescent screen. Here the electrons are converted to light and an image is formed. This image of the specimen, formed from the interaction of the electrons transmitted through the specimen, has different parts displayed in varied lights according to the specimen density. The dark areas of the image correspond to areas on the specimen where fewer electrons were able to pass through and the lighter areas correspond to regions where more electrons could pass through. The variation in the amount of electrons that passed through a specimen, enable the user to see structures and gradients in it. The image can be studied directly or photographed with a camera. The transmission electron micrographs of NCA films were obtained using a model FEI Technai G^2 S-twin microscope of 200 kV. It can produce magnification up to 1000 KX with a resolution better than 10 A^0.

2.4 Atomic Force Microscopy (AFM)

AFM is used for imaging and measuring surfaces on a fine scale, down to groups of atoms [6,7]. They are designed to measure the topography of conductive as well as nonconductive samples. It can be used to measure the morphology, local resistivity, elasticity etc. AFM uses a tip made of Si to interrogate the shape of a sample surface. The tip is mounted on a flexible cantilever that allows it to follow the surface profile. When the tip moves in proximity to the investigated object, forces of interaction between the tip and the surface influence the movement of the cantilever. These movements are detected by selective sensors. The vertical and horizontal deflection of the cantilever is measured using an optical lever. The optical lever operates by reflecting a laser beam, off the back of the cantilever. This reflected beam strikes a position-sensitive photo-detector consisting of four side-by-side photodiodes. The difference between the four photodiode signals indicates the position of the laser spot on the detector and ultimately the tip. As the tip scans over the sample surface, the deflection of the cantilever reflects the topography of the surface. By collecting the height data for a succession of lines it is possible to form a three dimensional map of the surface features. AFM can operate in different modes, according to the force between the tip and the scanning surface. Among these the main modes are the contact mode and the non-contact mode.

In contact mode AFM tip makes a soft physical contact with the surface. The interaction force between the tip and the sample surface is repulsive. The tip is attached to the end of a cantilever with a low spring constant, lower than the spring constant holding the atoms together in a sample. As the scanner gently traces the sample under the tip, the contact force causes the cantilever

to bend to accommodate changes in topography. The resolution of AFM depends mainly on the sharpness of the tip.

In the non-contact mode the cantilever is held less than a few angstroms from the sample surface, and the interatomic force between the cantilever and sample is attractive. The non-contact mode of operation involves an oscillating cantilever. The attractive probe-sample interaction changes the spring constant of the cantilever and this modifies its resonant frequency. A modification of the resonant frequency will result in a change of the probe's oscillation amplitude which is fed to a feedback loop which in turn controls the movement of the tube scanner.

Different modes of operation are chosen based on the surface characteristics of interest and on the hardness or stickiness of the sample. Contact mode is most useful for hard surfaces where as non-contact mode is for soft surfaces. But the non-contact mode has the disadvantage of overlooking minute features of few nanometers on the sample and because of this NCA films in the present work were often scanned in the contact mode only using the model SPA 400 of Seiko Instruments.

2.5 Scanning Electron Microscopy (SEM)

SEM is a very important tool in the characterization of solid materials. It gives information about the external morphology and orientation of materials in a specimen. It consists of an electron gun, condensing lenses, scanning coils and the objective lens. A beam of electrons is generated in the electron gun located at the top of a column. This beam is attracted through an anode and the condensing lenses focus the electrons into a tight beam. The scanning coils or the magnetic lenses are energized by varying the voltage produced by a scan generator and this creates a magnetic field which deflects

the electron beam back and forth in a controlled pattern on the sample. The interaction between the electron beam and the specimen under study, results in the reflection of high-energy electrons by elastic scattering. Inelastic scattering of secondary electrons as well as the emission of electromagnetic radiation also occurs. Each of these can be detected by specialized detectors. Secondary electrons and backscattered electrons are commonly used for imaging samples. Secondary electrons are important in screening morphology and topography of samples and backscattered electrons helps in illustrating contrasts in composition in multiphase samples. The detectors convert the gathered information to voltage signals, amplify them and feed them to the display where the final image is created. The SEM model used for this study is ESEM XL-30 of FEI Netherlands make.

The In-lens field emission scanning electron microscopy (FESEM) provides topographical information at magnifications of 250 X to 1000 KX with virtually unlimited depth of field. In-lens FESEM produces clearer, less electrostatically distorted images than SEM with spatial resolution down to 0.6 nanometers. In an FESEM, a field emission cathode in an electron gun provides probing beams which are narrower than that in an SEM, at a wide range of electron energies. This will bring about improved spatial resolution and minimize the sample charging and damage.

Electrons, which are liberated from a field emission source, are accelerated in a high electrical field gradient. The primary electrons are focused and deflected by electronic lenses within a high vacuum column, to produce a narrow scan beam. The sample is bombarded with this beam. Each point on the sample will then emit secondary electrons. The angle and velocity of these secondary electrons correspond to the surface structure of the sample. These secondary electrons are recorded and converted in to

electronic signals by a detector. This signal is amplified and transferred to a video scan image that can be saved and processed.

In the present work, FESEM of model Ultra 55, Carl Zeiss-make was employed for obtaining the micrographs. The working distance for most of the samples was in the range of 4 - 10 mm. The charging effects of the electron beam on the samples coated with oxide layers were reduced by coating them with a thin layer of gold.

2.6 Resistivity Set-up

Four-probe dc resistivity measurements were carried out on the NCA films between temperature ranges of 20 K to 350 K.

The four-probe method is a standard way of measuring the resistivity. In this method the errors in the measured resistance due to contacts, which will be significant in electrical measurements, is overcome by using two extra contacts for putting current through the sample. The influence of the contact resistance between the voltage electrodes and the sample can be eliminated due to the high impedance of the voltage measuring device. Using proper correction factors based on sample geometries quiet accurate measurements of the sample resistance is possible by this method.

The Fig. 2.5 shows the resistivity set-up consisting of a closed cycle refrigerator and the temperature controller along with the current sources and the voltmeters. A water cooler attached to the compressor, and a vacuum pump for the sample space makes the set-up complete. The NCA films were mounted on the sample holder as shown in Fig. 2.6 that goes in to the sample well. A small current is applied to the sample by the current source, Keithley 6621 and voltage developed is measured using the nanovoltmeter, Keithley 2182A. The temperature near the sample is measured using a platinum resistor thermometer PT-100. A current source, Lakeshore 120 and a digital

multimeter, Keithley 195A is used for applying current and measuring voltage respectively on the platinum sensor.

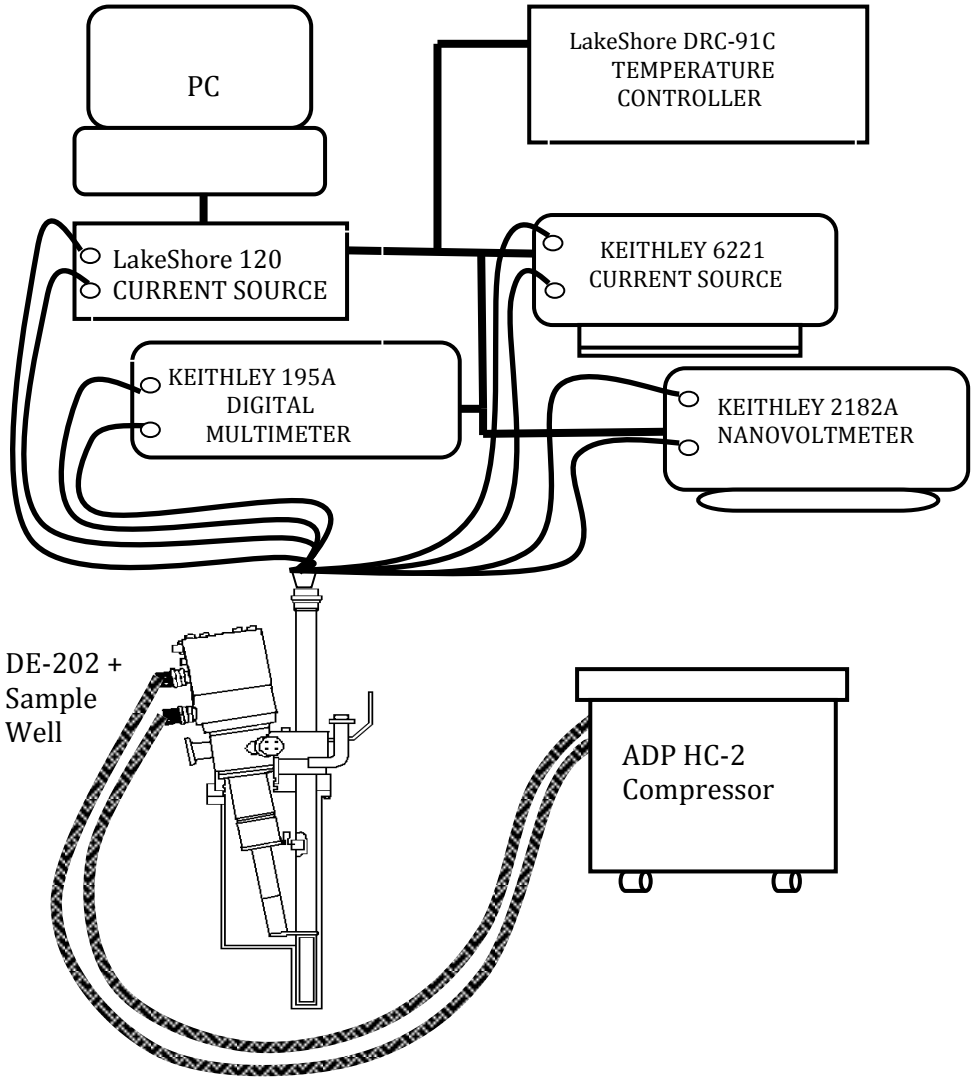

Fig. 2.5. Block diagram showing the DE-202 expander, the sample well and the compressor along with connections to various instruments in the resistivity set-up.

The closed cycle refrigerator used for the investigation of NCA films consists of APD DE-202, which includes an expander and a vacuum shroud

and an HC-2 helium compressor. This operates on the Gifford-McMahon principle. The great advantage of this principle is that the compressor as well as the expansion unit can function separately, connected by the gas lines. This increases the flexibility of the whole system as the cold head or the expander unit can be operated in any mounting position. In addition to these major components it consists of several electrical feed-throughs. A temperature controller was connected to the system to adjust and measure the sample temperature.

The Gifford-McMahon refrigeration cycle takes place in the expander, shown in Fig. 2.7, which is a two stage cryogenic refrigerator. It is connected to a compressor by the helium gas lines and an electrical power cable. One gas line takes the high-pressure helium gas from the compressor to the expander while the other line returns the low-pressure helium gas from the expander back to the compressor. The expander uses the helium gas from this helium compressor to produce the cold temperatures. The compressor provides the necessary helium gas flow rate at the high and low pressure for the expander, which helps it to function at the desired refrigeration capacity. A vacuum shroud appears on the cold end of the expander surrounding it. Once the vacuum is achieved the vacuum shroud limits the heat load on the expander caused by conduction and convection.

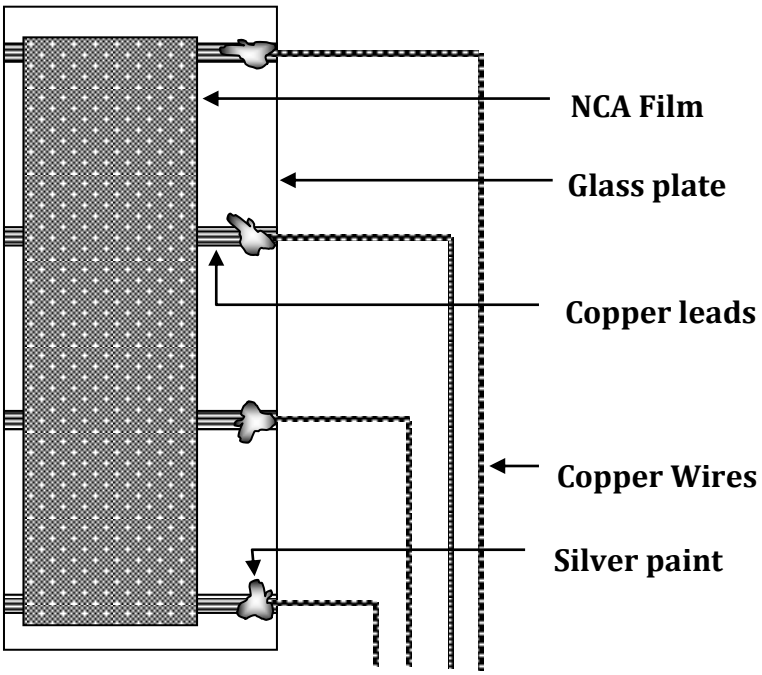

Fig. 2.6. A representation of how the sample is mounted on the sample holder.

HC-2 compressor is a single stage, water-cooled rotary compressor that delivers high-pressure oil free helium gas to the cryogenic refrigerator. When in a closed cycle system the compressor injects the low-pressure helium gas that enters through the return line with oil. Then the gas is compressed and cleaned by removing oil and moisture.

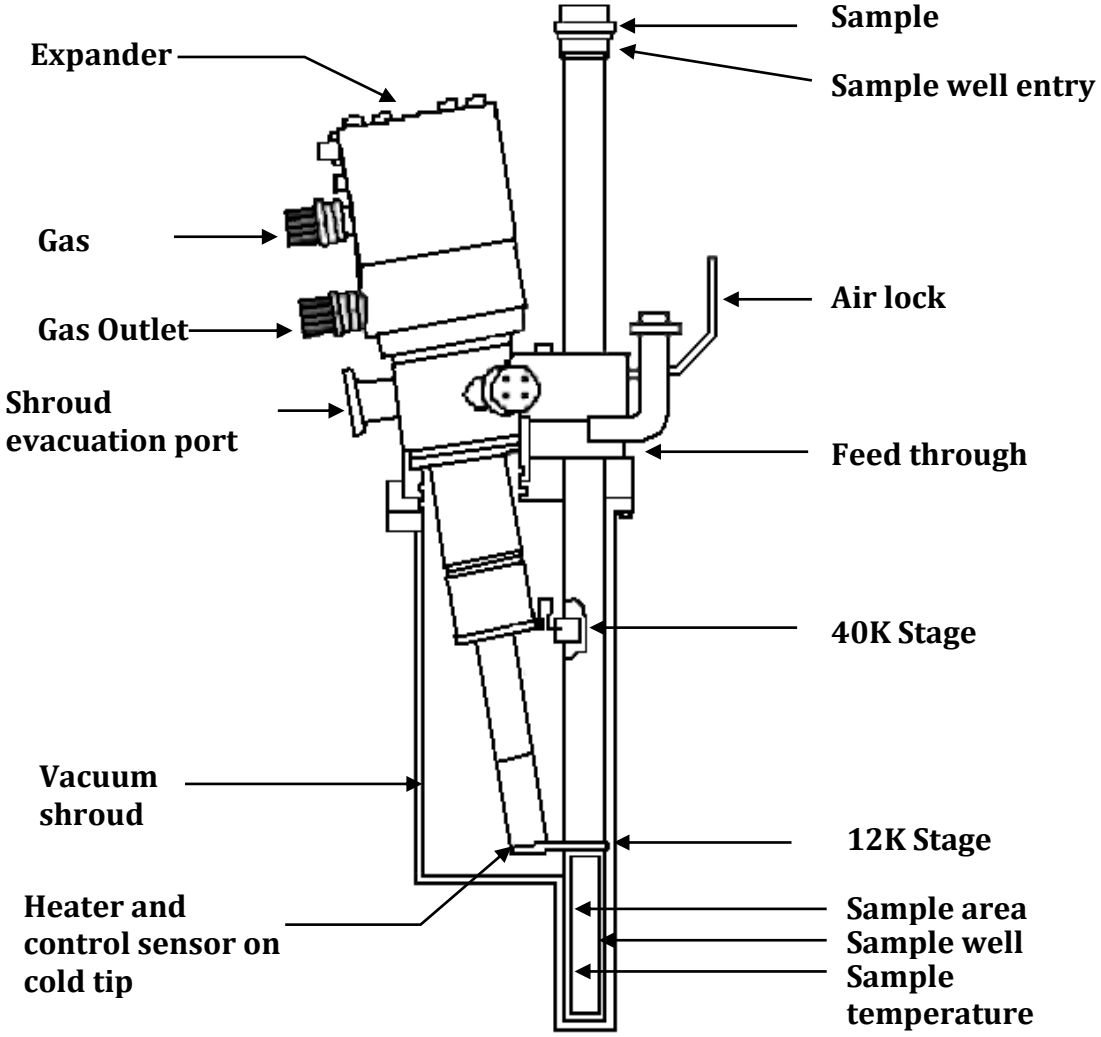

Fig. 2.7. DE 202 expander with the sample well.

This high pressure, oil free helium gas is then delivered back to the expander. In this compressor a gas line containing a relief valve that connects the high pressure gas line to the low pressure gas line allows the compressor to operate independently, without being connected to the expander.

Before refrigeration, the sample well is purged of any air using the helium gas. Then the insulating vacuum shroud has to be evacuated to 0.5 torr. The evacuation is done using an oil pump. In order to prevent back streaming oil contamination from the pump, a long hose longer than 3 feet is used. Also while cooling when the expander temperature reaches 220 K, the connection to the pump is closed using a shut off valve. A temperature scan of 20 K to 350 K was done on the NCA films. The whole system was interfaced using a program in LabView and the data directly entered in to files of given name.

The general details of the experimental techniques used in the present work were described in this chapter. Specifics of actual methods and parameters will be given if required in the respective chapters.

References

[1] H. Haberland et al. J.Vac.Sci.Technol A Vol. 12, 2925 (1994).

[2] S. A. Koch, T. Vystavel, G. Palasantzas and J. Th. M. De Hosson. Encyl. NanoSc. And Nano Tech., Ed. H. S. Nalwa, Am. Sci. Vol. 14, 457-496 (2011).

[3] H. Haberlandet al. J.Vac. Sci. Technol. A, Vol. 10, 3266 (1992).

[4] Nanocluster Deposition System Manual. Oxford Applied research.

[5] Charles Kittel, "Introduction to Solid State Physics", John Wiley & Sons (2005).

[6] R. Wiesendanger, "Scanning Probe Microscopy and Spectroscopy: Methods and Applications", Cambridge University Press, (1998).

[7] D. Bonnell Ed. "Scanning Probe Microscopy and Spectroscopy: Theory, Techniques, and Applications", 2nd ed. Wiley-VCH, New York, (2001).

CHAPTER III

ELECTRON TRANSPORT AND MAGNETISM IN FeX (X=Au, Pd and Pt) ALLOY NANOCLUSTER ASSEMBLED FILMS

3.1 Introduction

Metallic nanoclusters are quite important as they exhibit interesting size dependent chemical and physical properties [1]. Size effects become significant when the critical length scales of physical phenomena become comparable with the characteristic size of a particle. When small enough, the physical properties of nanoclusters are scalable even with respect to the amount of atomic subunits present in them i.e. size effects are all the more prominent in them. Understanding high-surface area materials derived from nanoclusters is essential in designing and controlling their material properties for applications. Metallic alloy nanoparticles are important in research fields concerning catalytic action as well as optical and magnetic properties [2]. Properties of metallic systems can be greatly enhanced by preparing inter-metallic compounds and alloys. Thus alloys present us with the opportunity to create finely tuned materials, which make binary alloy nanoclusters an important candidate for research and application [3]. The properties of alloy nanoclusters can also be tuned by their composition. Thus compared with nanoclusters of a single metal, alloy clusters have more extensive applications [4-6]. These facts triggered the study of equi-atomic alloy clusters of FeAu, FePd and FePt, of a few nanometers. These systems also come under nano-magnetic materials, a research area, which is vigorously active.

3.2 Importance of FeAu, FePd, and FePt Nano-Alloys

Magnetic nano-alloys have potential uses in magnetic recording devices, biomedical applications, magneto-optical systems, and in numerous other areas [7]. Alloys of FeAu, FePd, and FePt in nano scale find applications in recording devices. FePt [8] and FePd alloys are important for ultra-high-density magnetic data storage [9]. FePt has captured great attention because of its large magneto crystalline anisotropy, good chemical stability [10, 11] and resistance to oxidation [11-14], which can be used for permanent data storage [15]. FeAu nanoparticles are found to exhibit magnetic as well as optical properties [2]. FeAu also finds applications in recording media, magnetic sensors, high-density data storage and high performance permanent magnets [2]. It has interesting chemical, optical, magnetic, and biomedical applications [16-20].

This chapter deals with the study of composition, size, structure, morphology as well as electrical and magnetic properties of the nanostructures made up of atomic cluster assemblies in the form of films. It mainly concentrates on the behavior of the transport properties of these alloy films. Heat treating the as-sputtered films for different durations has resulted in nanostructured films of various cluster sizes ranging from 2 nm to 14 nm. The mechanisms of electron transport in these cluster-assembled films are addressed in terms of existing theories of nearest neighbor hopping (NNH) and variable range electron hopping (VRH), which were originally applied to heavily doped semiconductors and granular metal composites.

3.3 Sample Preparation

Alloy nanoclusters assembled as films were prepared using a nanocluster deposition system (NANODEP 60). This system helps in growing well-organized cluster films tailored with specific electronic, mechanical and

tribological properties. It also helps in the synthesis of fairly mono-disperse nanoclusters, which is important owing to size-dependent properties. Finding the optimum conditions for controlled self-assembly of these artificial nanostructures is a challenging task. As clusters are formed in the agglomeration chamber, before reaching the substrate, choosing appropriate preparation conditions will allow us to tailor the functional film properties.

3.3.1 Preparation of Alloy Nanocluster Films

The Nano Cluster Assembled (NCA) films were deposited on high purity borosilicate glass substrates of rectangular shape. The sputter targets were equi-atomic alloys of 2 inch diameter and 1/16 inch thickness. The substrates were kept at room temperature without any bias. Before deposition of cluster films, four copper leads having a breadth of 1 mm and 4 mm apart, were made on the glass substrates by RF sputtering, to ensure electrical contacts. The preparation conditions are tabulated below.

Table 3.1. Preparation conditions of NCA films

	FePd	FePt	FeAu
Argon gas flow	60 sccm	70 sccm	70 sccm
Aggregation Distance	155 mm	155 mm	155 mm
Base Pressure	2.8×10^{-8} mbar	8.2×10^{-7} mbar	2×10^{-8} mbar
Working pressure	2.4×10^{-5} mbar	2.9×10^{-5} mbar	2×10^{-5} mbar
Power	87.5 watts	84.25 watts	92.5 watts
Duration of Deposition	30 min	50 min	90 min
Apertures used	5 mm & 6 mm	5 mm & 6 mm	5 mm & 6 mm
Target thickness	1.59 mm	1.59 mm	1.59 mm

3.3.2 Heat Treatments

The as-deposited NCA films were heat-treated under Ar atmosphere at temperatures of 300^0C and 350^0C for the time ranging from a few minutes to 2

hours. This was done in order to study the response of alloy clusters to high temperature annealing and to obtain clusters with various sizes exhibiting a range of size dependent properties. The heat treatments done on the NCA films are tabulated below.

Table 3.2. Heat treatments done on FeAu NCA films

Temperature	Duration
350^0C	30 min
350^0C	1 hr
350^0C	2 hr

Table 3.3. Heat treatments done on FePdNCA films

Temperature	Duration
350^0C	4 min
350^0C	7 min
350^0C	15 min
350^0C	20 min
350^0C	1 hr

Table 3.4. Heat treatments done on FePt NCA films

Temperature	Duration
300^0C	9 min
300^0C	15 min
350^0C	7 min
350^0C	25 min

As nanoclusters have large surface areas, in order to minimize the total surface or interfacial energy, they often form agglomerates resulting from attractive vander Waals forces. The as-deposited NCA films of all the three systems exhibited cluster agglomeration, which was evident from AFM, TEM and FESEM pictures [21]. Also the XRD, TEM and FESEM analysis revealed, a thin oxide layer formation around the nanoclusters. This thin oxide layer, formed around the clusters, breaks down upon annealing at relatively low

temperatures. Annealing post deposition usually leads to cluster size growth through inter-cluster coalescence. This also results in loss of mono-dispersity and regularity of the cluster arrangement in films. In NCA systems, annealing at low temperatures brought about disintegration of cluster agglomerates, which had interesting consequences in their transport behavior. Thus larger clusters which got disintegrated from agglomerates, that preserved their crystallographic structures [22] from the as-deposited state and also with reduced oxide shell thickness, were formed in films after heat treatments.

3.4 Preliminary Observations

All the NCA films exhibited their respective metallic luster. These films showed good adhesion to the borosilicate glass substrates. The primary observation of electrical resistance measured for the alloy NCA films was unusually high for metallic films. The resistivity vs. temperature data of all the three alloys displayed a negative temperature coefficient of resistance. The resistivity values were in the range of 10^{-3} Ω-cm to 10^{+3} Ω-cm. The high values of resistivity of these as-deposited and heat-treated films reflected the presence of oxides in the system. Further experiments lead to the conclusion that the nanoclusters consisted of a metal core and an oxide shell structure.

3.5 Measurements

Different measurements were carried out on NCA films in order to understand their structure, morphology and transport characteristics. Composition and structure determination was done using EDX, XRD and TEM. AFM, SEM and FESEM were employed to understand the morphology of the systems. Four-probe resistivity measurements were carried out to understand the transport properties of the NCA films. The dependence of these

measurements on parameters like composition, size, temperature etc. are investigated.

3.5.1 Determination of Composition and Crystallographic Structure

The elemental investigation of the alloy NCA films was done using the attachment for energy dispersive X-ray analysis, which was available with the FESEM. The X-ray diffraction patterns obtained at grazing angles with 0.05^0 oscillation revealed the crystallographic structure of the NCA films.

3.5.1.1 EDX

Energy Dispersive X-ray Spectrometry (EDX) analysis on the NCA films were conducted and the mole fraction of each element determined. The EDX spectrum of FeAu, FePd and FePt NCA films is shown in Fig. 3.1, Fig. 3.2 and Fig. 3.3 respectively. The analysis revealed that in FeAu films atomic fraction of Fe and Au came about 48.2 % and 51.8 % respectively, for FePd it was 48.2 % of Fe and 51.8 % of Au. FePt films showed an atomic fraction of Fe and Pt about 47.53 % and 52.47 % respectively.

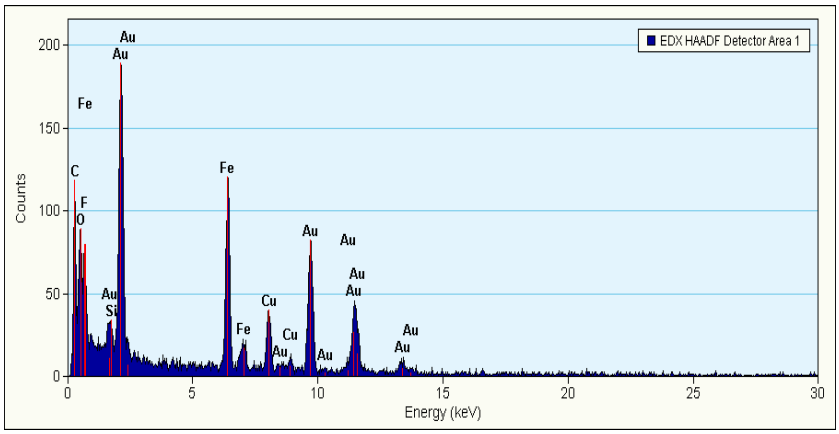

Fig. 3.1. EDX spectrum revealing the elemental ratio outputs for FeAu NCA films. The film consists of 51.8 at. % of Au and 48.2 at. % of Fe.

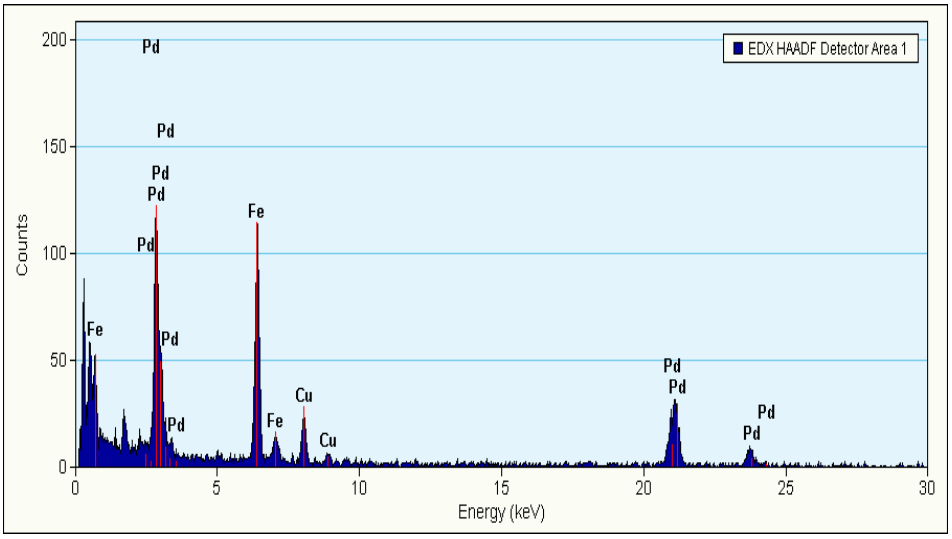

Fig. 3.2. The EDX spectrum of FePd NCA films. For FePd films the atomic fraction of Fe and Pd was around 47.8 % and 52.2% respectively.

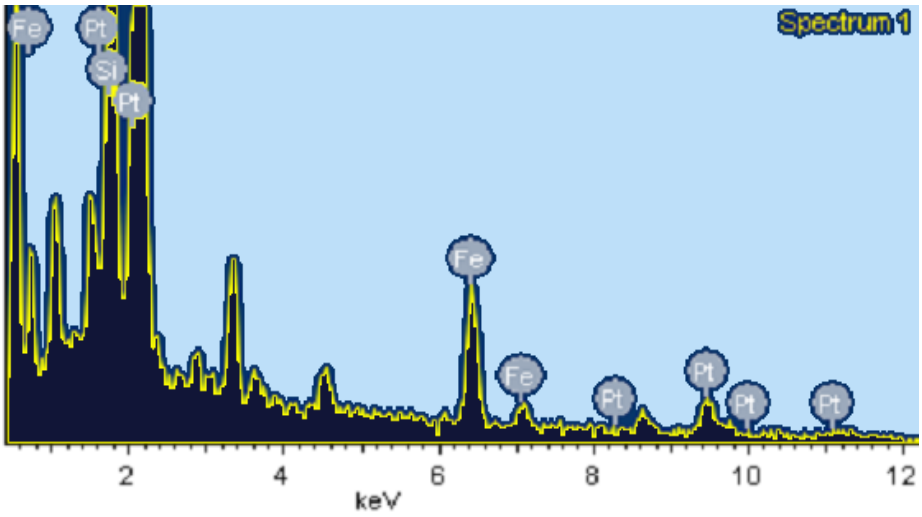

Fig. 3.3. The EDX spectrum of FePt NCA films. For FePt films the atomic fraction of Fe and Pt was around 52.47 % and 47.53 % respectively.

The compositions of the NCA Films were consistent with those in the starting material. This established the formation of alloy nanoclusters and confirmed their compositions.

3.5.1.2 X-ray Diffraction Measurements.

X-Ray diffraction patterns of as-deposited FeAu, FePd and FePt NCA systems along with the heat-treated samples were taken to determine their lattice structures as well as their cluster sizes. With heat-treated samples the XRD peaks have grown sharper indicating enlargement in the cluster sizes. As many of the properties of the nanocluster assembled materials depend exclusively on the size of its clusters, accurate measurement of the cluster size is extremely important. XRD gives an average value of cluster size for these films but no information on the size distribution.

The X-ray diffraction patterns for FeAu films revealed all the fcc peaks, whereas for FePd and FePt films only the fundamental peaks were visible as shown in Fig. 3.4. The indexing of the lines in the XRD patterns is done using the equation below.

$$\mathrm{Sin}^2\theta / (h^2+k^2+l^2) = \lambda^2 / 4\,a^2 \qquad (1)$$

where θ is the glancing angle, h, k, l are the Miller indices, λ, the wavelength of X–ray and 'a', the lattice constant. The as-sputtered FePt films revealed the presence of the oxide $Fe_{0.9}O$ as shown in Fig. 3.4 which was later confirmed in all the samples by electron diffraction data.

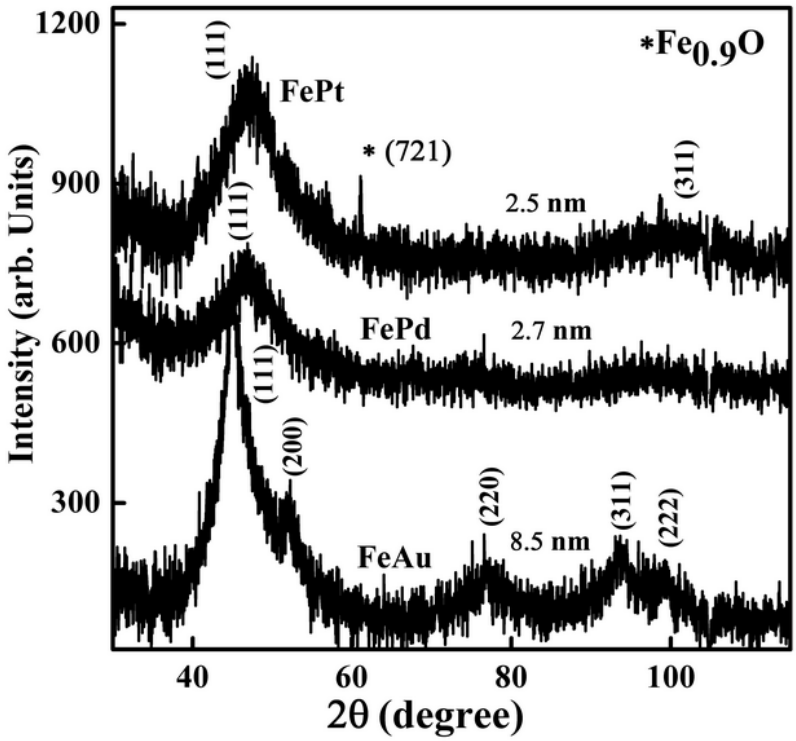

Fig. 3.4. X-ray diffractograms of as-deposited FeAu, FePd and FePt films.

The Cluster sizes from XRD patterns were calculated using the Scherrer formula $d = k \lambda / B \cos \theta$. Here the constant k is taken as 0.9. 'k' depends on the shape of the cluster, which is assumed to be circular here. λ is the wavelength of the Co Kα radiation, which is 1.7889 A^0, B is the broadening of the diffraction line at half its maximum intensity, and θ is the glancing angle. The size calculated from the Scherrer formula will be an average over all the crystallite sizes. This method does not provide any information on the distribution of cluster sizes in the sample. For the system FeAu the positions of the reflections in the XRD as shown in Fig. 3.5 are identical with those of pure Au. It has been understood that for multi elemental nanocrystalline materials the positions and intensities of the XRD reflections do not necessarily reflect

the nominal composition but depends on other factors like surface segregation [23].

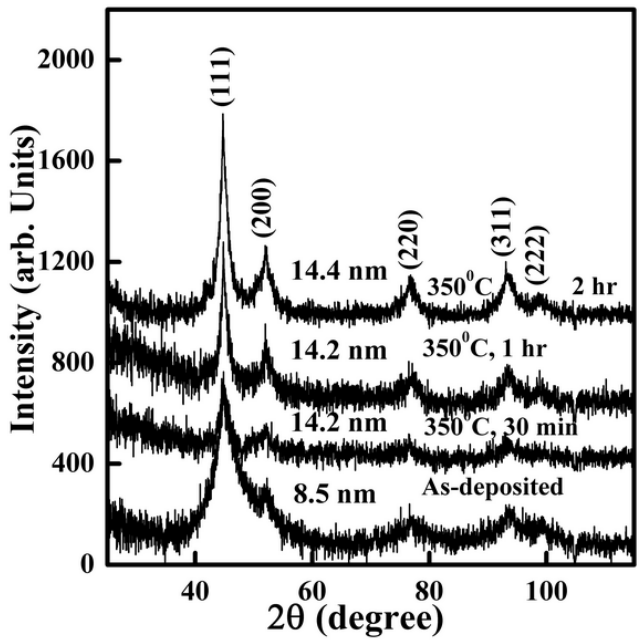

Fig. 3.5. X-ray diffractograms of FeAu films with different cluster sizes.

The XRD patterns of as-sputtered and heat-treated FeAu alloy films confirmed that the bravais lattice was face centered cubic lattice. This is consistent with the X-ray diffraction studies on bulk alloys which have shown that Fe_xAu_{100-x} forms the crystal structure of bcc for x > 75 at. % and fcc for x < 75 at. % [23]. The lattice constant obtained for FeAu NCA systems is displayed in Table 3.5. The cluster sizes were calculated using the Scherrer equation [24, 25] as discussed above.

Table 3.5. Results of XRD measurements on FeAu films

System: FeAu	2θ (deg)	FWHM (deg)	Cluster Size (nm)	Lattice Constant (A^0)
As-deposited	45.025 ± 0.039	1.241	8.5 ± 0.2	4.046 ± 0.002
350^0C, 30 min	44.658 ± 0.024	0.773	14.2 ± 0.2	4.078 ± 0.004
350^0C, 1 hr	44.797 ± 0.018	0.772	14.2 ± 0.1	4.066 ± 0.001
350^0C, 2 hrs	44.844 ± 0.010	0.762	14.4 ± 0.1	4.062 ± 0.002

The cluster size estimated from XRD patterns for FeAu NCA system is also displayed in Table 3.5. For bulk FeAu with cubic structure, a lattice parameter a = 3.9634 ± 0.0012 A^0 has been reported [26]. The lattice parameter observed for FeAu clusters in the as formed disordered fcc phase is reported to be 4.17 A^0 [27]. Only a heat treatment at 600^0C followed by a slow cooling could bring about a transition to an ordered $L1_0$ structure with a lattice parameter a =3.75 ± 0.03 A^0 and c = 3.61 ± 0.1 A^0 [27]. The observed value of lattice parameter for NCA films shown in Table 3.5 are in agreement with the disordered fcc phase. For the heat-treated FeAu films XRD patterns showed an increase in cluster size with a heat treatment of 350^0C for 30 min. An increase in the duration of heat treatment further for the same temperature did not have any effect on the cluster size i.e. the increase in cluster size reached a plateau. As the substrate of films was borosilicate glass, it was not considered appropriate to cross a temperature of 350^0C.

In the case of FePd NCA system the 2θ value of the peak positions in Fig. 3.6 agrees well with that reported for nanoparticles with $Fe_{47.1}Pd_{52.9}$ and $Fe_{49.1}Pd_{50.9}$ confirming the alloy formation [28]. Both these nanoparticle systems were reported to display fcc lattice structure [28]. The XRD patterns of alloy FePd NCA system revealed only the (111) peaks of the fcc structure.

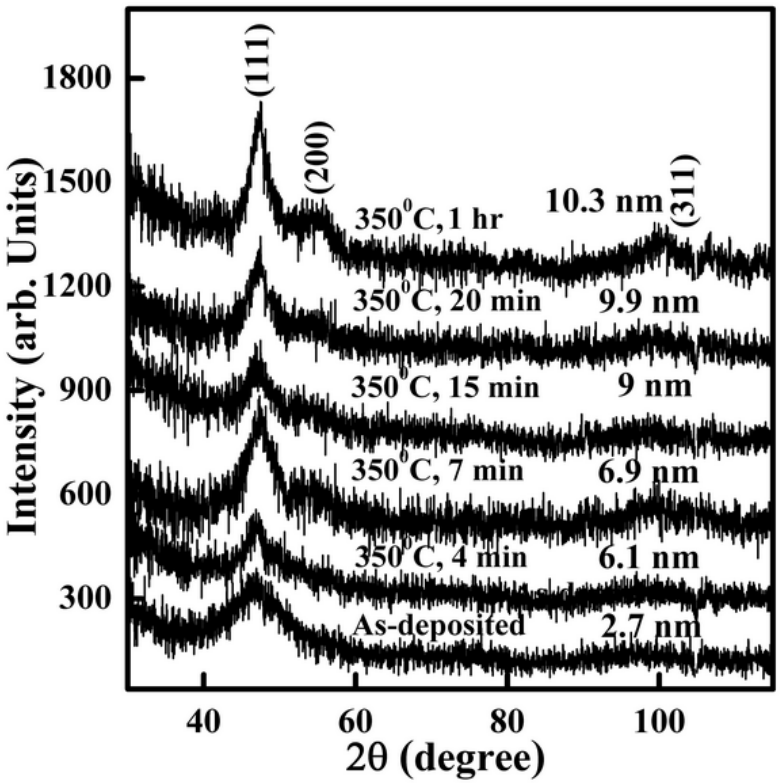

Fig. 3.6. X-ray diffractograms of as-deposited as well as heat-treated FePd films.

The lattice constants observed for $Fe_{47.1}Pd_{52.9}$ nanoparticles in reference [28] with a particle size of 8.4 nm was 3.869 A^0. For bulk FePd alloy the lattice constant is reported to be around 3.88 A^0 [29]. These reported values are in good agreement with the estimated lattice constants for NCA FePd films in the present work. In NCA FePd system with nanoclusters of a comparable size of 9 nm, the lattice constant was estimated to be 3.892 ± 0.0082 A^0.

Table 3.6. Results of XRD measurements on FePd films

System: FePd	2θ (deg)	FWHM (deg)	Cluster Size (nm)	Lattice Constant (A^0)
As-deposited	46.936 ± 0.075	3.871	2.7 ± 0.1	3.893 ± 0.011
350^0C, 4 min	46.855 ± 0.121	1.718	6.1 ± 0.3	3.899 ± 0.018
350^0C, 7 min	47.331 ± 0.041	1.491	6.9 ± 0.1	3.863 ± 0.001
350^0C, 15 min	46.950 ± 0.064	1.183	9 ± 0.3	3.892 ± 0.010
350^0C, 20 min	47.174 ± 0.044	1.085	9.9 ± 0.2	3.875 ± 0.002
350^0C, 1 hr	47.258 ± 0.025	1.050	10.3 ± 0.1	3.868 ± 0.001

In FePd nanoclusters, the lattice constant is found to decrease with an increase in cluster size i.e. with increasing annealing temperature. For $Fe_{54.5}Pd_{45.5}$ nanoparticles synthesized by polyol process using dioctyl ether, a decrease in lattice constant, with increasing annealing temperature has been reported [28]. The stresses inside a thin film with increased grain boundary regions are suggested as the reason behind the change in the d spacing which intern changes the lattice constant of a material [28].

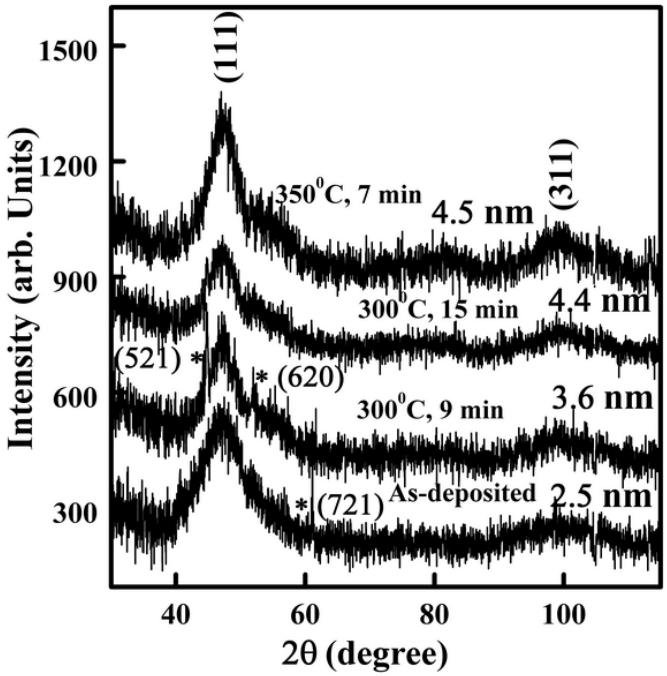

Fig. 3.7. X-ray diffractograms of as-sputtered as well as heat-treated FePt films. Since Fe nanoparticles are easily oxidized [2] some oxide peaks are also seen in the XRD pattern. The satellite peaks denoted with '* 'corresponds to $Fe_{0.9}O$ indicating the presence of oxide shell around the clusters.

Table 3.7. Results of XRD measurements on FePt films

System: FePt	2θ (deg)	FWHM (deg)	Cluster Size (nm)	Lattice Constant (A^0)
As Sputtered	47.019 ± 0.064	4.124	2.5 ± 0.1	3.887 ± 0.002
300^{0}C 9 min	46.906 ± 0.078	2.838	3.6 ± 0.1	3.896 ± 0.003
300^{0}C 15 min	47.169 ± 0.068	2.288	4.4 ± 0.1	3.875 ± 0.002
350^{0}C 7 min	47.062 ± 0.049	2.362	4.5 ± 0.1	3.883 ± 0.002

The XRD patterns of FePt NCA films could record the presence of only two peaks as shown in Fig. 3.7. For the as-sputtered films with a particle of size 2.5 ± 0.2 nm the fundamental peak position was identified to be 47.019 ± 0.049^0. The lattice constant for this system was found to be 3.887 ± 0.002 A^0. In fcc FePt nanoparticles of 3 nm and 9 nm sizes the lattice constant is found to be 3.84 A^0 [30]. This confirms the alloy formation in the NCA FePt system with fcc lattice structure.

The additional peaks observed for as-sputtered as well as heat-treated XRD patterns of FePt system was also indexed. The peak positions were identified to be 44.711 ± 0.019^0, 51.962 ± 0.002^0 and 61.106 ± 0.004^0 corresponding to the (h k l) values (521), (620) and (721) of $Fe_{0.9}O$ [31]. This confirms the presence of the oxide layer around the clusters, which acts like a shell structure. The electron diffraction studies of these systems also showed the presence of $Fe_{0.9}O$. This oxide shell could be removed from all the three alloy systems by heat treatments at optimum temperatures.

3.5.1.3 Electron Diffraction Measurements

In the case of the X-ray diffraction of as-sputtered films only the diffraction patterns of FePt showed a peak corresponding to (721) plane of $Fe_{0.9}O$ whereas that for FeAu and FePd did not show any presence of oxide. But the electron diffraction data for all the films revealed the presence of oxides in the sample. The selected area electron diffraction pattern from these nanoparticles revealed a diffuse ring structure with spots superimposed on them.

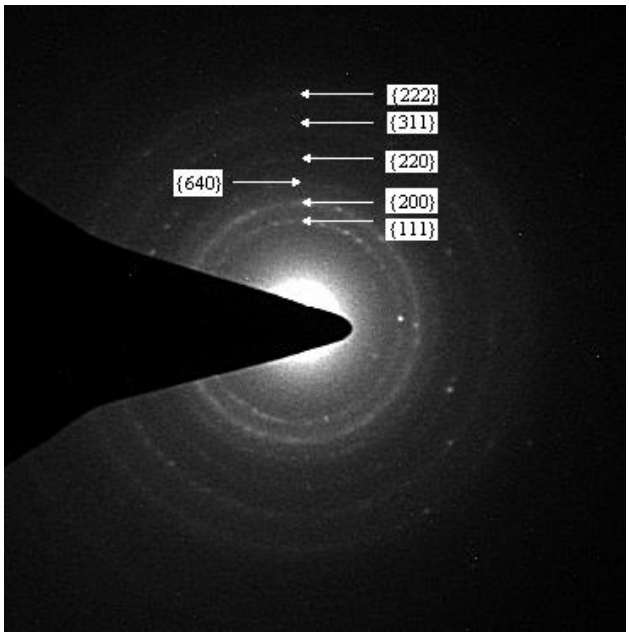

Fig. 3.8. Electron diffraction of 3.61 ± 0.06 nm FePt nanoclusters showing fcc FePt pattern. The {640} of $Fe_{0.9}O$ is also seen in the pattern.

The d values calculated from the positions of the electron diffraction rings agreed well with the d values reported for fcc structure of the alloy films. The electron diffraction pattern for FePt revealed a d spacing corresponding to {640} of $Fe_{0.9}O$ as shown in the Fig. 3.8. Also the electron diffraction patterns of both the FeAu and FePd films clearly showed the d spacing corresponding to {332} of $Fe_{0.9}O$ which are shown in Fig. 3.9 and Fig. 3.10.

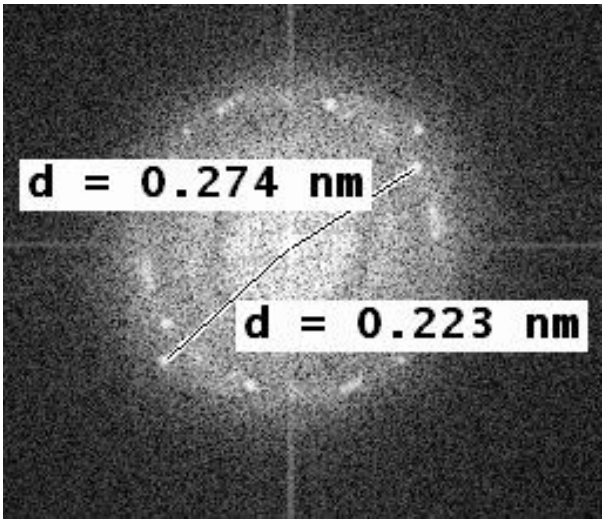

Fig. 3.9. Electron diffraction of 5.1 ± 0.1 nm FePd nanoclusters showing {111} of fcc FePd pattern and {332} of $Fe_{0.9}O$.

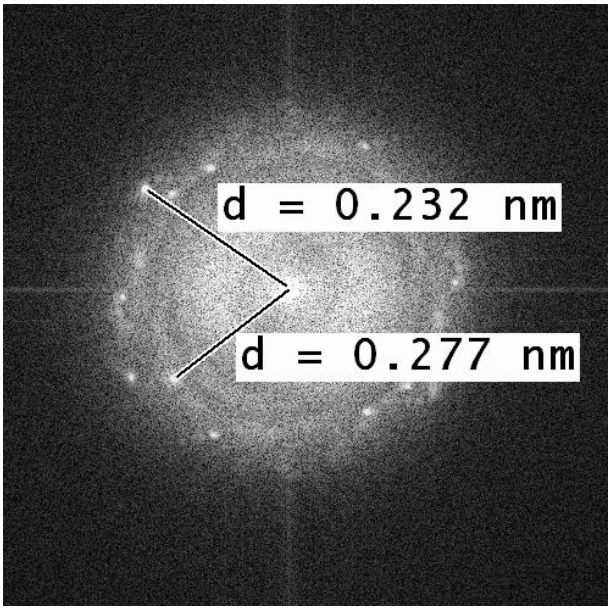

Fig. 3.10. Electron diffraction of 6.4 ± 0.2 nm FeAu nanoclusters showing {111} of fcc FeAu pattern and {332} of $Fe_{0.9}O$.

3.5.2 Microstructural Characterization

The morphology and microstructure of as-deposited as well as heat-treated alloy NCA films were investigated by Atomic Force Microscopy (AFM), Transmission Electron Microscopy (TEM), Scanning Electron Microscopy (SEM) and Field Emission Scanning Electron Microscopy (FESEM). To confirm the oxide layer formation around the clusters as well as to check the diameter of the alloy nanoclusters High Resolution Transmission Electron Microscopy (HRTEM) investigations were also performed. The shape of the clusters, their sizes and interconnections as well as the structure and porosity of the films, all these have been investigated. The results from different measurement techniques give an overall picture from which the true nature of the system can be deduced.

3.5.2.1 Atomic Force Microscopy

We have obtained AFM images of as-deposited FeAu clusters at 1-6 μm resolutions, which is shown in Fig. 3.11. The images revealed a dense film of spherical particles with a size distribution. The particle size fall in the range of 42 to 168 nm, which gives an indication that the particles are cluster agglomerates and not individual clusters. AFM could not reveal individual clusters due to its poor resolution. The spherical agglomerates in AFM pictures were found to be touching each other indicating a well-connected structure.

AFM images of as-deposited as well as heat-treated samples of FePd NCA films of 4 μm resolution are shown in Fig. 3.12. The as-deposited film images revealed almost spherical particles with a narrow size distribution. Each particle was an agglomerate of atomic clusters.

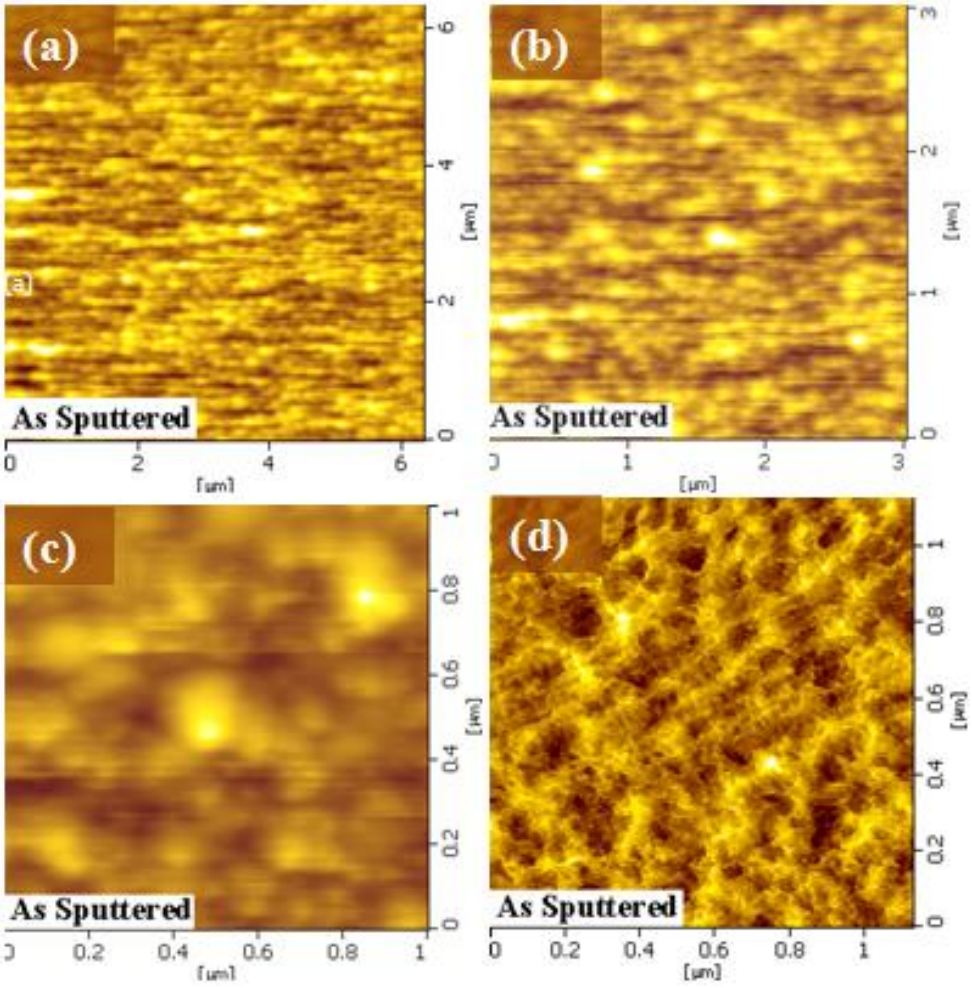

Fig. 3.11. AFM images of as-sputtered FeAu NCA films. (a), (b) and (c) depicts topographic images of the as-deposited film at different magnifications whereas the image (d) shows a phase image of the as-deposited film. The topographic image gives us details of the cluster agglomerates regardless of the roughness of the NCA film. The phase image highlights cluster agglomerate positioning and how they are interconnected giving an indication of the surface roughness.

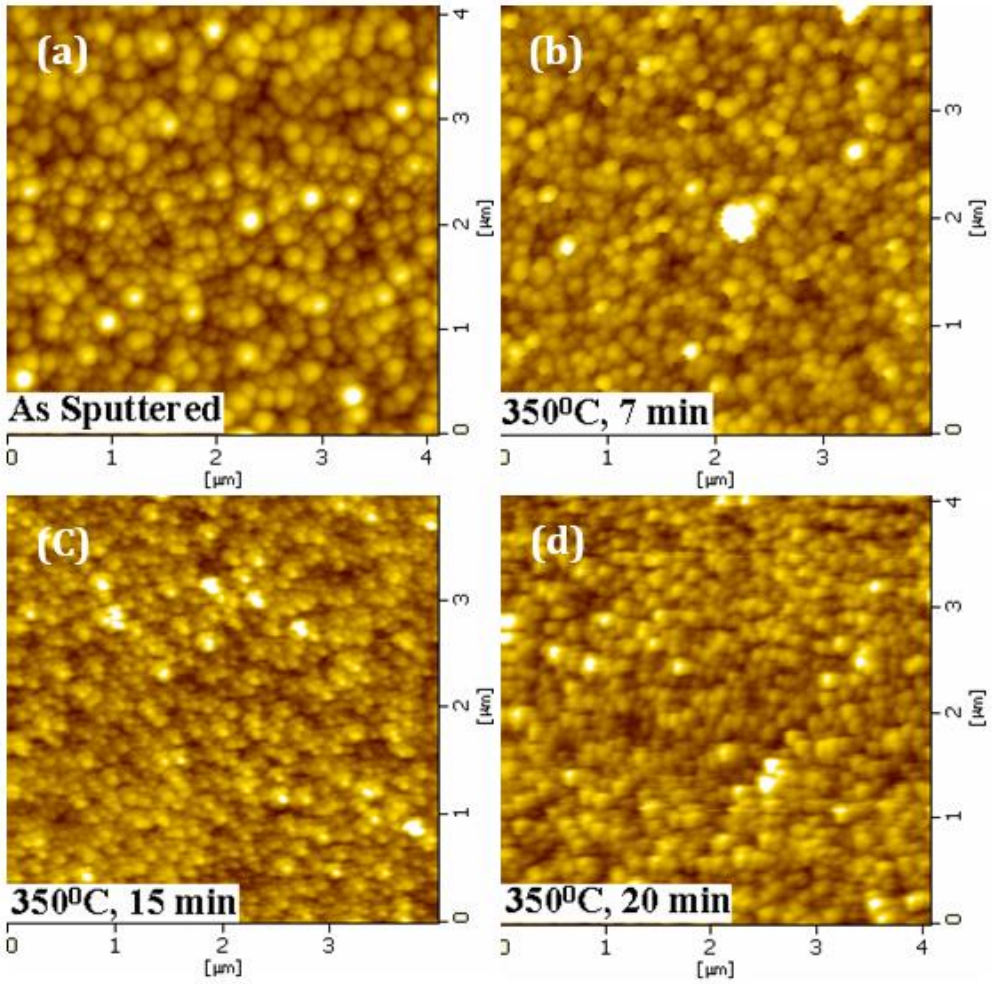

Fig. 3.12. AFM images of the as-deposited and heat-treated FePd NCA films. (a) shows the image of the as-deposited film whereas (b),(c) and (d) show the heat-treated films at 350^{0}C for different durations.

The films looked porous and the particles were seen well connected with each other for electric conduction. The particle sizes of the as-deposited films fall in the range of 90 nm to 200 nm. The heat-treated film images at the same magnification as that of the as-deposited cluster films reveal that the particle size decreases with increasing duration of heat treatment. This looked

rather unusual as one expects an increase in the particle size with heat treatment.

Later it was understood that with increasing heat treatment the cluster agglomerates dissociate and the spherical particles look reduced in size. The reduction in the individual particle size is tabulated in Table 3.8.

Table 3.8. Reduction in cluster agglomerate Size with heat treatment for FePd films.

System	Cluster Agglomerate size range
FePd As-deposited	90-200 nm
FePd 350^0C, 7 min	80-160 nm
FePd 350^0C, 15 min	52-102 nm

AFM images of as-deposited and heat-treated FePt clusters at 4 μm resolution are shown in Fig. 3.13. These images also show a dense cluster film with almost spherical particles. The size of the particles seen from these images also give indications of the formation of cluster agglomerates. The cluster agglomerate sizes of FePt films fall in the range of 42 to 95 nm. The agglomerates are found to reduce in size with increase in the duration of heat treatments. Also the particles are found to line up for a few nanometers, with heat treatment. Due to poor resolution, AFM does not distinguish between individual clusters and cluster agglomerates, which are formed in NCA films. So it was thought appropriate to carry out further investigation on the shape as well as the size of clusters with TEM in order to have a clear understanding of these structures.

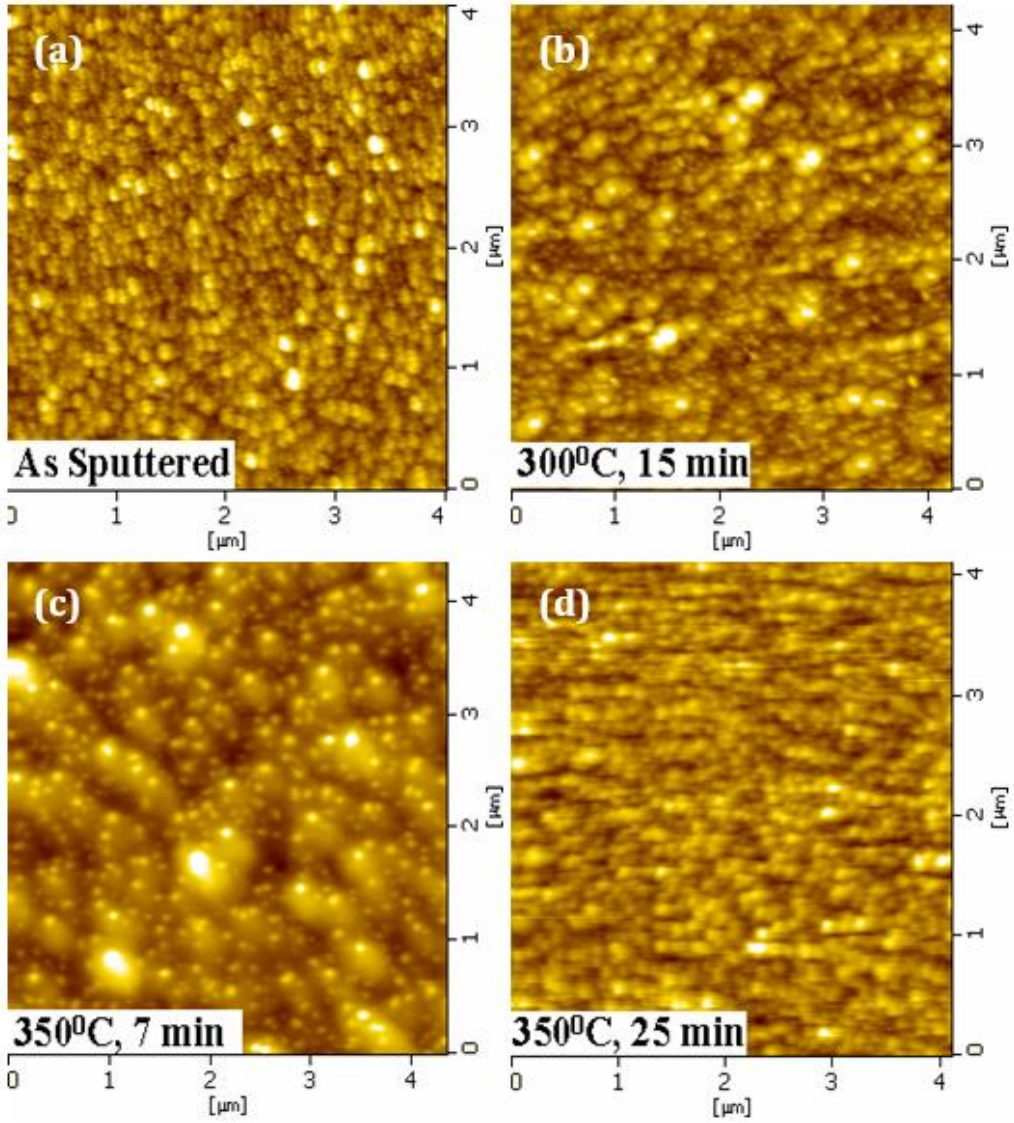

Fig. 3.13. AFM images of FePt NCA films. (a), (b) (c) and (d) depicts the images of as-deposited and heat-treated FePt films, where a reduction in the cluster agglomerate size is observed with increase in heat treatment.

3.5.2.2 TEM

TEM samples were prepared by depositing onto the carbon-coated TEM grids. Cluster agglomerates of FeAu, FePt and FePd systems which were seen as individual spherical particles became evident with trasmission electron

microscopy and the micrographs are displayed in Fig. 3.14. For all these systems TEM reveals individual atomic clusters of a few nanometers connected with eachother to form cluster agglomerates. Big cluster agglomerates of around 90 nm can also be observed in these pictures. The atomic clusters look spherical in shape. TEM images show that there is a size distribution of a few naometers present in the NCA films. Measurements show that the cluster sizes for all the systems are below 5 nm (Fig. 3.15, Fig. 3.16 & Fig. 3.17) and the values are tabulated in Table 3.9. The distribution for cluster size is lognormal. The atomic clusters captured in the AFM images were spherical in shape, but in TEM pictures the agglomerates are irregular in shape and reveal a nucleation site around which the agglomeration happens. So cluster agglomerates are observed to have a core which is densely packed with atomic clusters and towards the outer region they become sparse. For all the three systems the formation of cluster agglomerates leads to a nanoporous structure, which is displayed in these transmission electron micrographs.

Table 3.9. Cluster Sizes estimated for the NCA films from TEM.

System	Cluster Size (nm)
FeAu	4.2 ± 0.9
FePd	2.0 ± 0.1
FePt	2.3 ± 0.1

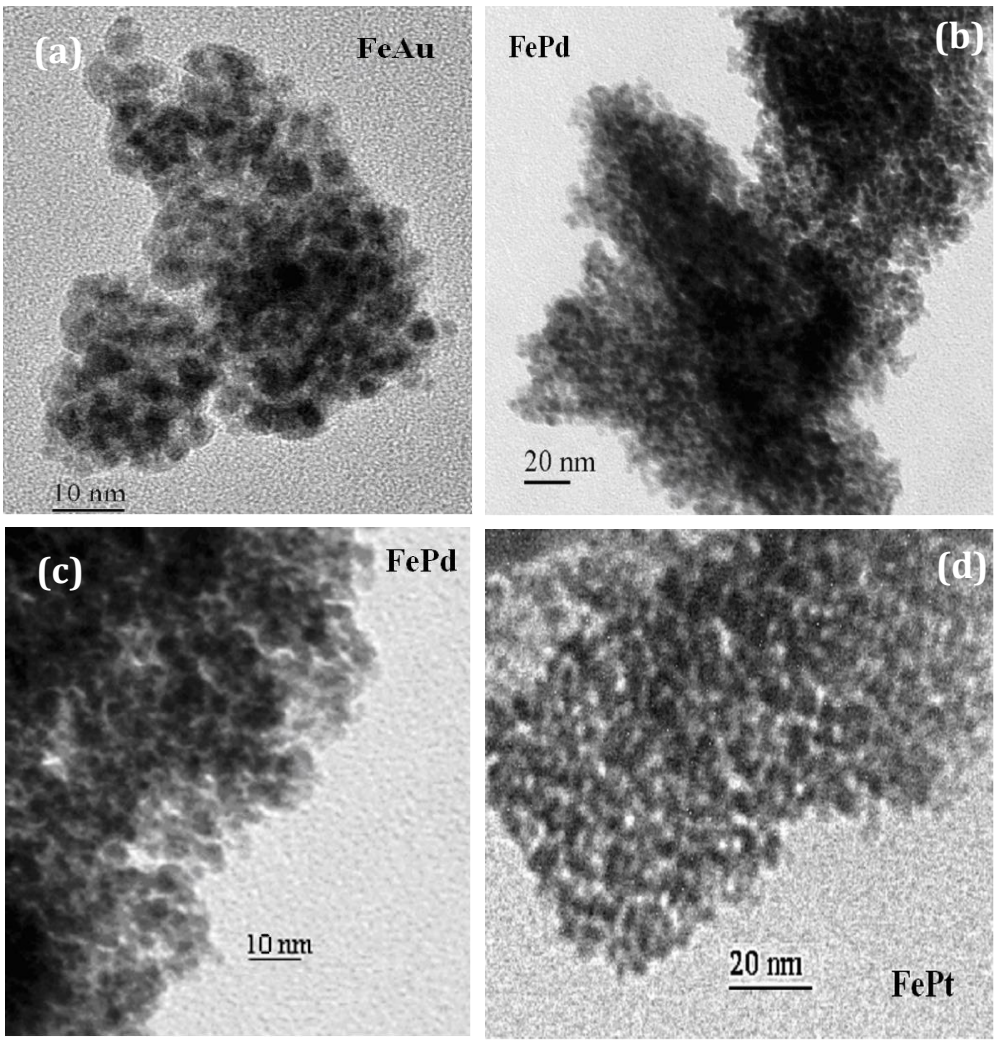

Fig. 3.14. TEM pictures of FeAu, FePd and FePt showing smaller individual clusters with a size distribution within bigger cluster agglomerates are presented in (a), (b) and (d). (C) shows a larger magnification of the FePd clusters.

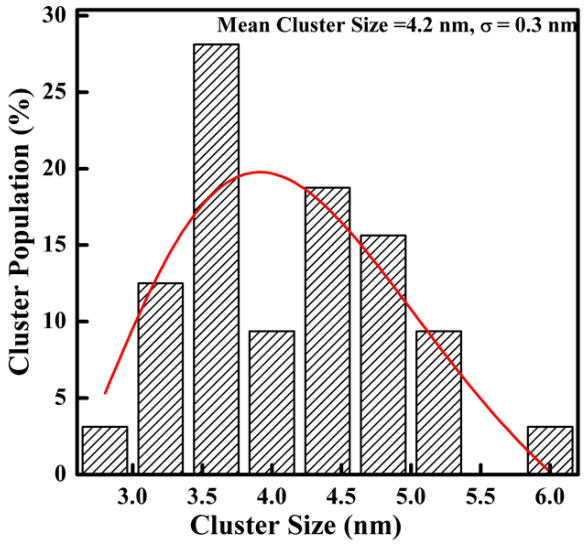

Fig. 3.15. Cluster size distribution for the as-deposited FeAu alloy clusters from TEM data. The curve fit represents a lognormal distribution. σ is the standard deviation of the distribution of logarithm of size.

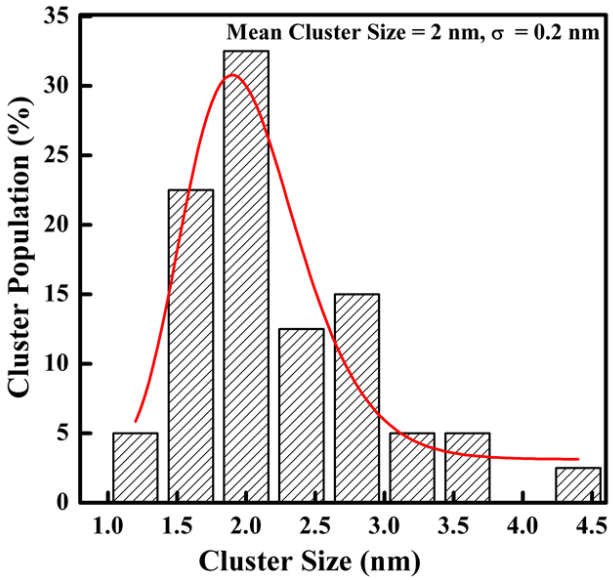

Fig. 3.16. Cluster size distribution for the as-deposited FePd alloy clusters from TEM data. The curve fit represents a lognormal distribution. σ is the standard deviation of the distribution of logarithm of size.

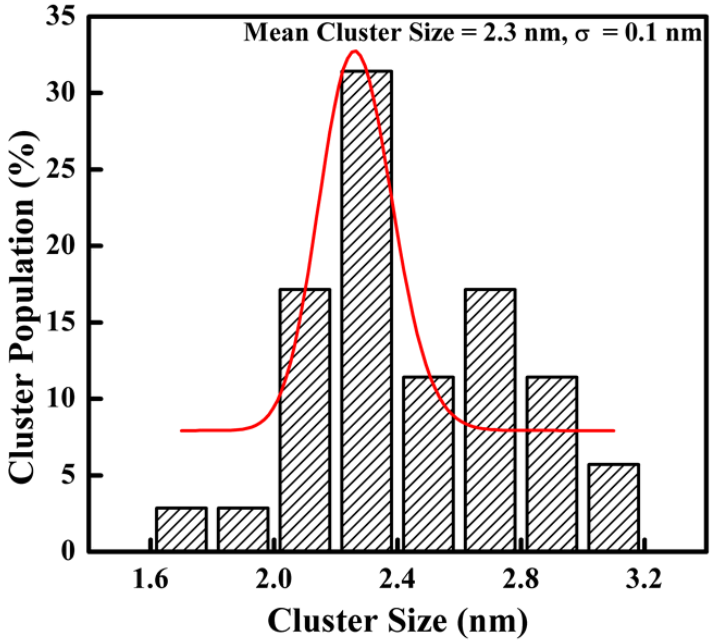

Fig. 3.17. Cluster size distribution for the as-deposited FePt alloy clusters from TEM data. The curve fit represents a lognormal distribution. σ is the standard deviation of the distribution of logarithm of size.

TEM measurements may tend to slightly underestimate nanocluster sizes, since it can be difficult to observe surface layers in TEM.

3.5.2.3 HRTEM

The high-resolution TEM images of FeAu and FePt nanoclusters are shown in the Fig. 3.18. The pictures show spherical nanoclusters as part of bigger agglomerates. The highlighted lines reveal the (111) planes of both FeAu and FePd nanoclusters in their respective images. The average cluster sizes calculated from these images are 4.9 nm for FeAu and 2.2 nm for FePd.

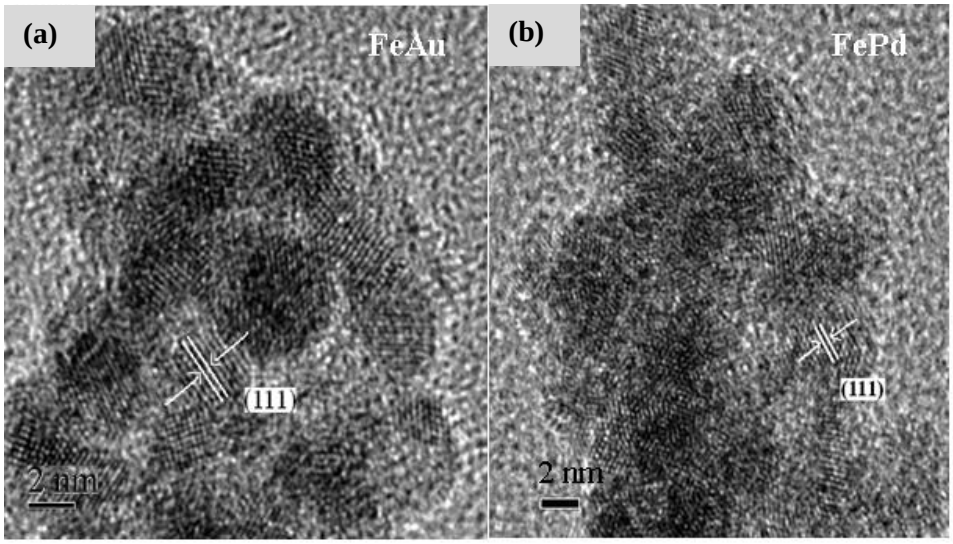

Fig. 3.18. HRTEM pictures of FeAu and FePd enlarged nanoclusters showing lattice fringes. (a) The (111) planes of the fcc structured FeAu clusters is highlighted in the picture. (b) The (111) planes of fcc structured FePd clusters is highlighted in the HRTEM Image.

3.5.2.4 SEM and FESEM

Though SEM has less resolution, the magnification it produces is more useful than the TEM data in many ways. The dramatic three-dimensional images of alloy NCA films that is produced here yields more information about shape, size and surface topography of these films. Representative micrographs of the alloy films are shown in Fig. 3.19, Fig. 3.21 and Fig. 3.23. It can be seen that the observed NCA thin films cover the substrates. Small individual nanoclusters can be seen in the FESEM pictures that form a part of bigger agglomerates. The clusters are seen to be sticking to each other and are found to be well connected. The cluster size distribution is observed to be narrow. The agglomerates look like a coral structure with the clusters sticking to it forming small branches on it and the system is very porous. All together these pictures enhance our understanding of an oxide shell making the clusters stick together

forming agglomerates and results in the disintegration of clusters when they undergo heat treatment as that will remove the oxide layer.

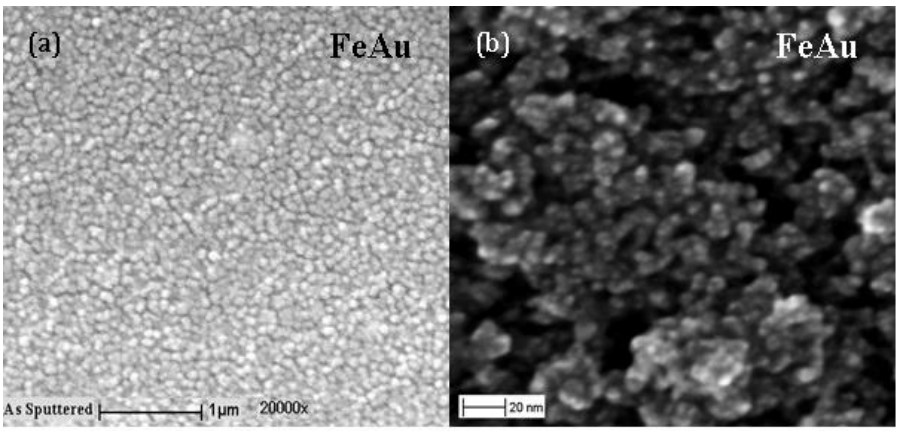

Fig. 3.19. (a) SEM image of as-deposited FeAu Films showing the cluster agglomerates. (b) Magnified FESEM images of the same films illustrating the individual atomic clusters in agglomerates.

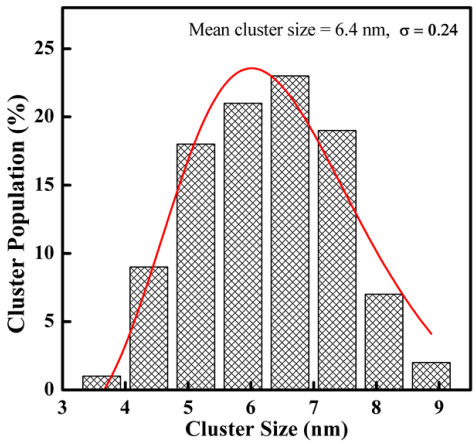

Fig. 3.20. Cluster size distribution for the as sputtered FeAu clusters from TEM data. The curve fit represents a lognormal distribution. σ is the standard deviation of the distribution of logarithm of size.

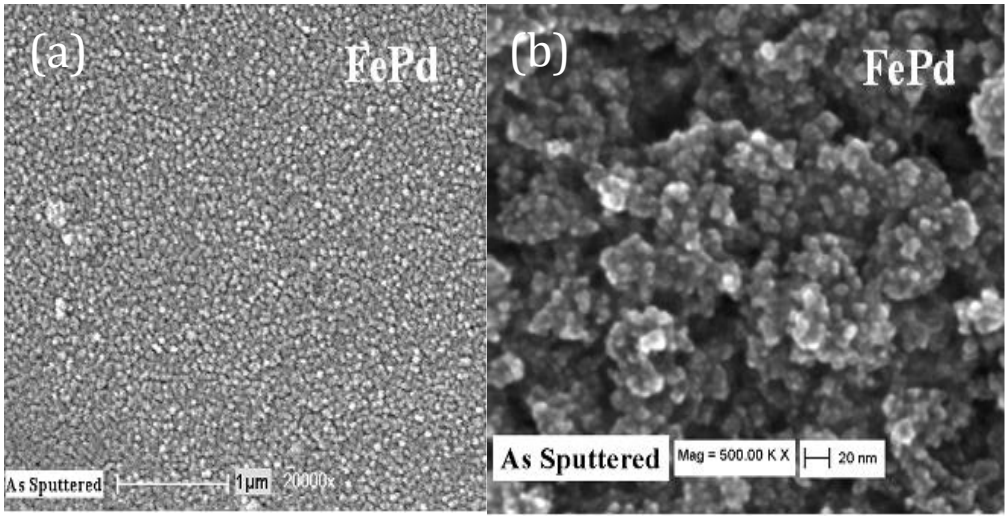

Fig. 3.21. (a) SEM Image of as-deposited FePd films illustrating the cluster agglomerates. (b) The FESEM image of the same film showing the individual atomic clusters in the cluster agglomerates.

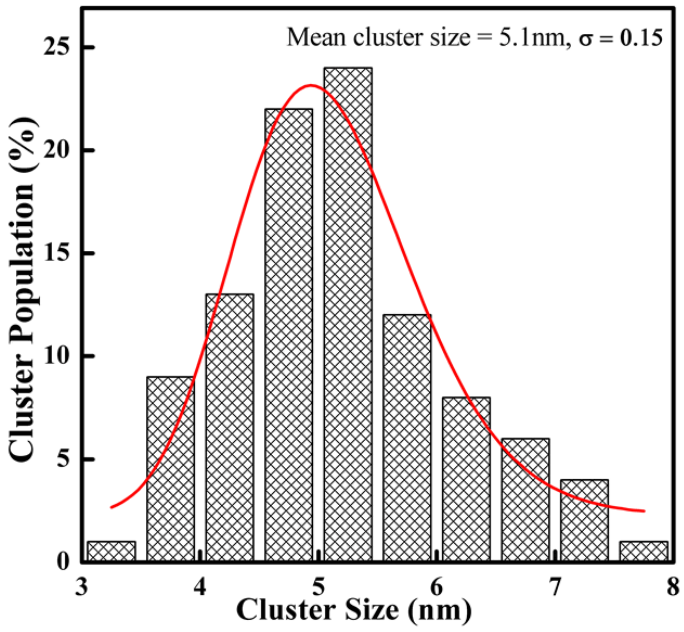

Fig. 3.22. Cluster size distribution for the as sputtered FePd clusters from FESEM data. The curve fit represents a lognormal distribution. σ is the standard deviation of the distribution of logarithm of size.

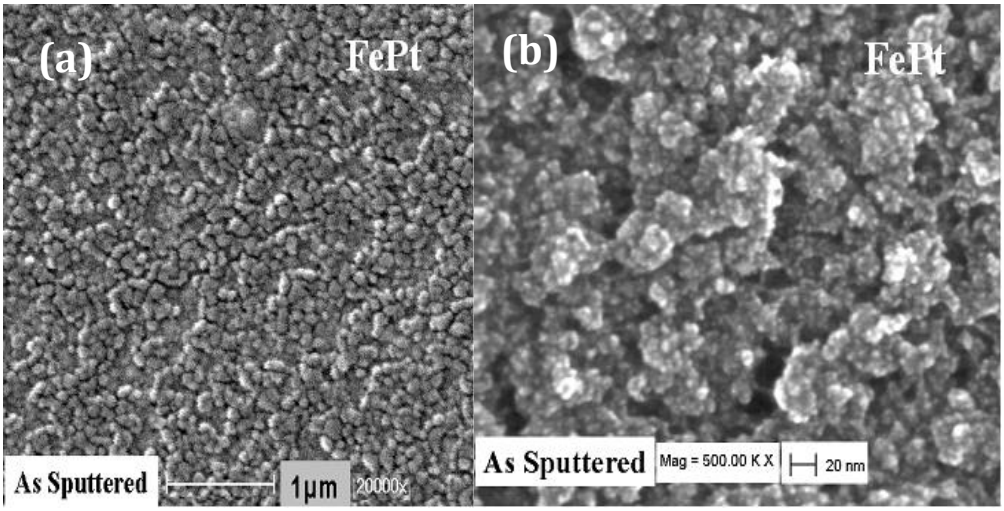

Fig. 3.23. (a) SEM Image of as-deposited FePt films illustrating the cluster agglomerates. (b) The FESEM image of the same film showing the individual atomic clusters in agglomerates.

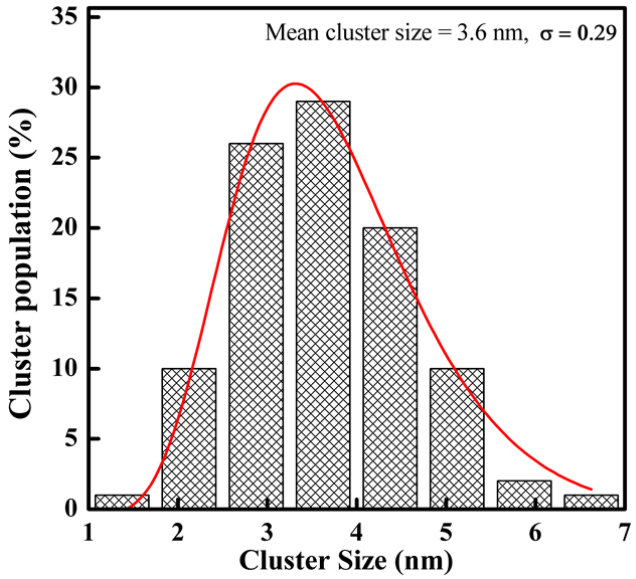

Fig. 3.24. Cluster size distribution for the as sputtered FePt clusters from FESEM data. The curve fit represents a lognormal distribution. σ is the standard deviation of the distribution of logarithm of size.

The FESEM pictures reveal the small sized clusters below 10 nm. The cluster size is measured from these pictures and the average value is calculated from the bar diagrams shown in Fig. 3.20, Fig. 3.22 and Fig. 3.24, by fitting them to the lognormal distribution curves. The calculated cluster sizes are tabulated below.

Table 3.10. Comparison of Cluster Sizes estimated for the NCA films.

System	Cluster Size (nm) XRD	Cluster Size (nm) TEM	Cluster Size (nm) FESEM
FeAu	8.5 ± 0.1	4.2 ± 0.9	6.4 ± 0.2
FePd	2.7 ± 0.1	2.0 ± 0.1	5.1 ± 0.1
FePt	2.5 ± 0.2	2.3 ± 0.1	3.6 ± 0.1

3.5.3 Transport Measurements on Nanocluster Assembled Films.

Resistivity scans were done for rectangular samples of cluster-assembled films through temperatures ranging from 350 K down to 25 K (Fig. 3.25). Temperature increments of 1 K below 130 K and 5 K above 130 K were used in these measurements. A non-linear temperature dependence of resistivity was observed for all the films and the resulting curves showed an insulating behavior. Thus the measured resistivity values for all the systems were found to decrease with an increase in temperature for the whole temperature range mentioned above. From these values the temperature coefficient of the resistivity was calculated and found to be negative ($d\rho/dT < 0$) for all the films. By further analyzing the resistivity curves the electrical conduction is interpreted as by hopping mechanism [32,33].

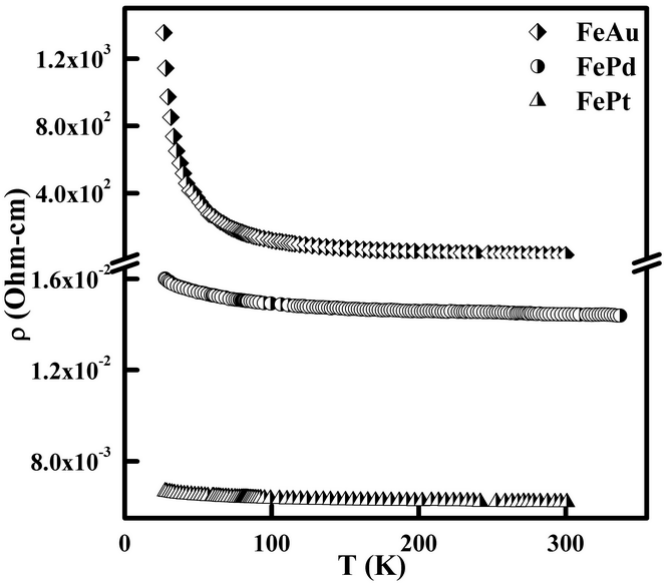

Fig. 3.25. The resistivity plots for alloy NCA films in the temperature range of 25 K to 350 K.

The conduction mechanism initiated by hopping is usually observed in granular metals. The important question here is, how this kind of a conduction mechanism can be applicable to metallic alloy cluster films. This behavior also suggests the existence of an insulating barrier between the metallic clusters, which can give rise to localization of electronic wave functions known as Anderson localization. This will give rise to a resistivity behavior induced by electron hopping between the localized states. The XRD as well as the electron diffraction data gives evidence for the presence of $Fe_{0.9}O$ in the alloy cluster assembled films. Also the FESEM data obtained for the alloy clusters shows a network kind of structure around a group of atomic clusters, forming cluster agglomerates. Effectively the oxide is found to form a shell structure around the metallic core of the cluster. Fig. 3.26 represents schematically this oxide layer that separates individual atomic clusters from each other while holding a few clusters together to form cluster agglomerates. This suggests that the electron

transport mechanism in alloy NCA films can be interpreted in terms of hopping conduction.

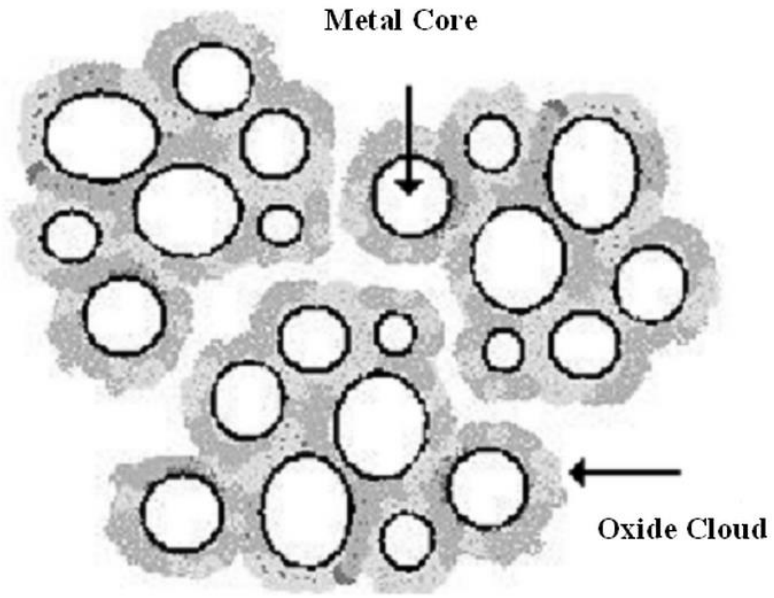

Fig. 3.26. Representation of oxide layer separating individual atomic clusters and forming cluster agglomerates.

The study of the conductance of electrons is a very basic problem in material science. For electronic conduction quantum theory gives the picture of electrons diffusing through the solid and occasionally getting scattered from defects in the lattice, which ushers in the concept of electron mean free path. The electronic conductivity will be directly proportional to the mean free path. But how the degree of disorder in a system affects the mean free path as well as its conductivity was addressed by P. W. Anderson in his famous 1958 paper and this initiated the concept of Anderson Localization [34].

3.5.3.1 Anderson Localization

What makes the electrons flow in metals and what holds them back in insulators is a question that baffled many scientists for a long time. In 1958 Anderson in his famous paper “Absence of Diffusion in Certain Random Lattices" described that the electronic wave function in a random potential will be altered, if the randomness or the disorder in the system is high. With high degree of disorder, the electrons will have localized eigen states. These electrons would not have the ability to transport charge or energy, which is assumed in the theory of metals [35] as they would undergo multiple scattering. When the electron scattering by defects increases beyond a critical value, it no longer diffuses through the lattice. Thus the diffusion is suppressed and the electrons are localized. We may make the statement that with strong disorder the electron wave function becomes localized.

From the date of its introduction till today Anderson localization in disordered systems continues to be an active research field. Localization finds its origin in interference effects [36]. This phenomenon is actually due to the destructive interference of randomly scattered partial waves. The localizing effect of a random potential on quantum particles or classical waves can be interpreted as the interference between multiple scatterings of wave components, scattered by randomly positioned centers or defects in the potential. This alters the eigen modes from being extended (Bloch waves) to exponentially localized [37]. When placed in a sufficiently strong disordered lattice, an electron may become immobile [34] and the envelope of the electron wave function decays exponentially. Once localization is attained the particles can’t move beyond the localization length [37].

Mott along with Ioffe and Regel predicted that in 3D systems the mean free path 'ℓ' reduces with increasing disorder and the Anderson localization occurs when the electron mean free path 'ℓ' becomes smaller than its De Broglie wavelength [38, 39]. This amounts to the condition $K_F\ell < 1$ in metals, where K_F is the Fermi wave number given by $K_F = 2\pi/\lambda_F$ and λ_F is the Fermi wavelength at low temperatures. This is a direct consequence of the quantum nature of particles for transport. In a classical system, the shortest possible mean free path is always given by the average distance between the scattering centers, irrespective of the particle energy. Thus for energies near the band edge, λ_F may be much larger than the lattice spacing but for electrons in the center of the band the wavelength 'λ_F' is of the order of a. For electrons in strongly disordered systems, the quantum nature is reflected in the fact that the mean free path ℓ of electrons scattering off imperfections in the crystal lattice, cannot become shorter than the wavelength of the particles [39]. When a matter wave's mean free path becomes shorter than its De Broglie wavelength, there is not much to wave and the electron don't go anywhere. If the disorder is increased beyond the point where $\ell \approx \lambda_F$, or else if the energy of the electrons (and hence $1/\lambda_F$) is decreased for a fixed disorder, the nature of the electronic states is expected to change from extended to localized. Then the electrical conductivity of the system is expected to go to zero [40]. In 1D or 2D systems ℓ may be much longer than the wavelength and even then the particles are nonetheless localized [39].

Anderson argued that in a tight-binding model of electrons on a lattice with randomly varying site energies, electrons of a given energy would become localized if the spread of the energies V_0 (i.e. the disorder) is sufficiently large [41]. In other words, the electronic states would change drastically from extended to localized states. The localization of electronic states occurs when

the criteria $V_0/I \geq \sqrt{32}\ \pi$ [41] is satisfied, where I is the electron transfer integral given by I = B/2z, where z is the co-ordination number and B is the electron band width. Then the criteria for localization becomes

$$V_0/B \geq (\sqrt{32}\ \pi)/2z \qquad (2)$$

In the case of a cubic lattice the criteria becomes

$$V_0/B \geq 0.83 \qquad (3)$$

So when V_0/B exceeds the value 0.83 for cubic lattice the electronic states become localized.

Anderson localization could be applied to explain the many relevant features of the disordered systems. As mentioned above Anderson localization can result in the transition of a material from conductor to an insulator [42]. Larger the disorder in a system, larger is the localization and also larger the system, less disorder is required for localization.

3.5.3.2 Anderson localization and Hopping Conduction in NCA Films

In the Nanocluster assembled films the cluster size distribution as well as the distribution in the oxide shell thickness gives rise to disorder in the system. This will give rise to a scenario of an array of potential wells of varying depths i.e. a spread of energies for the electron. The Fig. 3.27 shows a representation of nanoclusters with an oxide shell and a metallic core along with an illustration of lattice site energies with a V_0 energy spread, which will result in Anderson localization.

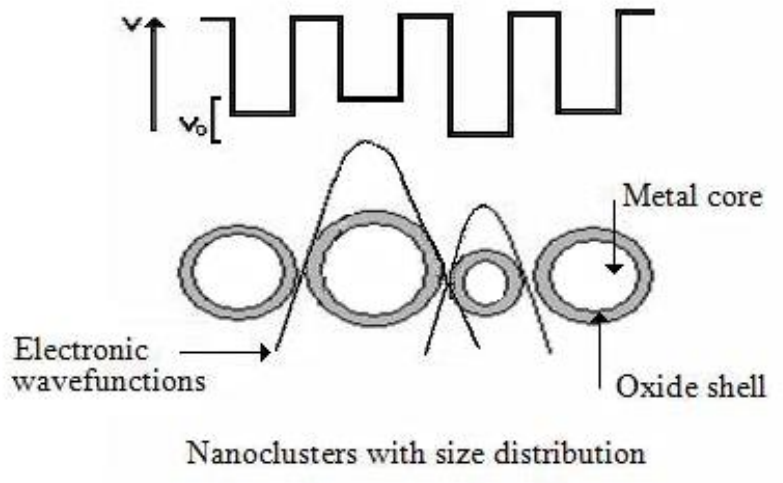

Fig. 3.27. Representation of Anderson localization in a crystal lattice with the spread of the energies V_0 in comparison with the scenario presented by alloy NCA systems.

I. Nearest Neighbor Hopping

In systems were localization persists, the transport of electrons require a conduction mechanism through localized states only. As the electronic states are localized, electrons transport current only if energy is available to enable them to hop from one localized state to another. This hopping can take place by two different mechanisms: nearest neighbor hopping (NNH) and variable range hopping (VRH). If the system has a finite density of states (DOS) at the Fermi level $N(E_F)$, at sufficiently high temperatures the mechanism of conduction and electron transfer is by thermally activated hopping. As a result electrical conductivity decreases exponentially as the temperature goes to zero [43]. With strong localization, the electrons jump to a place nearest in space because the electron wave function falls of rapidly with distance [41]. This is known as the NNH.

In NNH the lattice provides the energy necessary for electrons to hop over the potential barriers, which are randomly distributed between localized states. In this conduction mechanism an electron in a localized state acquires energy and hops to a nearest localized state with a higher energy i.e. an electron in an occupied state with energy below E_F receives energy from a phonon, enabling it to move to a nearby state above E_F. A process of this kind was first described by Miller and Abrahams [44], and was called 'nearest-neighbor' hopping. Because of very strong localization, the hopping of the electrons is limited only by the distance and electrons are supposed always to move to the nearest empty center. Here the conduction rate is limited by the thermal energy of electrons. In NNH the average hopping length is of the order of average distance between localized states and does not vary with temperature.

When there is not enough thermal energy, electrons in localized states cannot be activated to the conduction band. The energy difference of two neighboring localized states usually is smaller than the activation energy required for the electron to jump from a localized state to the conduction band. When electron hops from one localized state to another, there could be phonons absorbed or emitted.

In disordered systems the temperature dependence of conductivity results from two factors. One is the hopping rate, which is a function of energy mismatch (activation energy) ΔE, the distance R between the donor and acceptor site and the temperature T. The second factor is the statistical relation between the distance and activation energy among two hopping sites, R (ΔE) [45]. Activation energy ΔE is associated with the process of absorption of phonons. The average distance R, which is the distance to a nearest neighbor

depends on the concentration of the localized states N_{LS} as $R = [3/4\pi N_{LS}]^{1/3}$. Then the NNH conduction is given as [45]

$$\sigma = \sigma_0 e^{-(2\alpha R)} e^{-(\frac{\Delta E}{K_B T})} \quad (4)$$

Where σ_0 is a constant independent of temperature, α is the inverse of the localization length or the spatial extend of the wave function; R is the average distance between neighbors. ΔE is the thermal activation energy. K_B is the Boltzmann's constant and T is the temperature. The first exponential term is determined by the wave function overlap, which is independent of the temperature and the second exponential term is determined by the thermal activation energy.

II. Mott Variable Range Hopping

At low temperatures and with large localization distances the transport properties of disordered materials are governed by VRH between localized states. This relation for the temperature dependence of conductivity for the case in which, the DOS, near the Fermi energy is constant or varying slowly was put forward by Mott and Davis [41].

Hopping conductivity is governed primarily by the hopping probability between localized sites. At relatively high temperatures, the hopping probability is dominated by the random spatial distribution of localized states. As a result the hopping conductivity is determined by NNH. At lower temperatures, typical resistances between nearest-neighbor sites become larger than those states, whose energy levels lie within a few units of the Fermi level. Then the probability of electron thermal activation between states that are close in space but far in energy becomes smaller than that of electron

hopping between some remote states whose energy levels happen to be very close to each other. Therefore, electron hops between remote states rather than the nearest neighbors, dominate the conductivity. The fact that the localized states with levels close in energy may not necessarily be the nearest in spatial positions, results in a different hopping length, for each hop. This is named as the variable-range hopping (VRH) [46]. It is a general conduction mechanism in systems with strongly localized carriers at sufficiently low temperatures. As the temperature decreases the available thermal activation energy ΔE also decreases. This means that only the electrons with energy states close to the Fermi level are allowed to hop. The activation energy available will be spent for the hop from an occupied to an empty localized state of the system. Empty energy states, which are ΔE closer to the Fermi level, are quite rare and are separated by greater spatial distances. The lower the temperature is, the fewer energetically affordable sites there are, and the bigger is their spatial separation [47]. Therefore in this regime of VRH, the characteristic hopping length increases with decreasing temperature.

The thermally activated hopping conduction through the localized states in a small energy interval near the Fermi level depends on the hopping probability. The hopping probability per unit time is obtained by multiplying the following factors:

1. The Boltzmann factor $e^{-\Delta E/K_B T}$, where ΔE is the difference in energies of the two states.
2. A factor depending on the frequency of the phonon spectrum ν_{ph}.
3. A factor depending on the overlap of electron wave function $e^{-2\alpha R}$, where α is the inverse of the localization length and R is the hopping distance.

Only electrons with energies within a range of K_BT at the Fermi level need to be considered as taking part in the conduction as those with lower energies need more activation energy to hop to an empty state. The number of electrons per unit volume within the range K_BT of the Fermi energy is given by 2 N (E_F) K_BT, where N(E_F) is the DOS at the Fermi level.

For finding out the conductivity we need to consider hopping probabilities in positive and negative directions and their difference per unit time is given by

$$\nu_{hop} = \nu_{ph} e^{-(2\alpha R)} e^{-(\frac{\Delta E + eRF}{K_B T})} - \nu_{ph} e^{-(2\alpha R)} e^{-(\frac{\Delta E - eRF}{K_B T})} \qquad (5)$$

The term 'eRF' is due to the presence of a field 'F' in the direction of the flow of current. The above equation simplifies to

$$\nu_{hop} = \nu_{ph} e^{-(2\alpha R)} e^{-(\frac{\Delta E}{K_B T})} sinh \frac{eRF}{K_B T} \qquad (6)$$

When eRF << K_BT

$$\nu_{hop} = \nu_{ph} e^{-(2\alpha R)} e^{-(\frac{\Delta E}{K_B T})} \frac{eRF}{K_B T} \qquad (7)$$

The current density 'j' is obtained by multiplying the probability rate by 2N(E_F)K_BT, e and R.

$$j = 2e^2 R^2 F N(E_F) \nu_{ph} e^{-(2\alpha R)} e^{-(\frac{\Delta E}{K_B T})} \qquad (8)$$

Therefore conductivity is given as

$$\sigma = 2e^2 R^2 N(E_F) \nu_{ph} e^{-(2\alpha R)} e^{-(\frac{\Delta E}{K_B T})} \qquad (9)$$

Equation (9) can be written as

$$\sigma = \sigma_0 e^{-(\frac{\Delta E}{K_B T})} \quad (10)$$

with $$\sigma_0 = 2e^2 R^2 N(E_F) \nu_{ph} e^{-(2\alpha R)} \quad (11)$$

which is the expression for NNH.

There is a competition between the two exponential terms of equation (9) that, whether the overlap of the wave functions or the thermal activation energy will dominate the conductivity.

It was Mott [41,48] who first pointed out that at low temperatures ($\Delta E/k_B T \gg 1$) the most probable hopping mechanism would not be the NNH, as the process is also limited by the spread of the energies. It would be more convenient to hop to a site at longer distance R, having a smaller energy difference ΔE, than to a closer one with a larger ΔE. Therefore, the maximum hopping rate can be for a combination of the optimal energy difference ΔE and a distance R.

By expressing both the exponential factors in (9) in terms of the average hopping length R' and then differentiating (9) with respect to R and equating to zero, the minimum of the resistivity exponent can be found. This corresponds to a situation where there is an equal contribution to the resistivity from thermal activation and from tunneling between the sites. Then we get the maximum hopping rate. By further inserting R back in (7) a general expression of the temperature dependent hopping conductivity is obtained as shown in what follows.

The hopping probability/unit time is given by

$$\nu_{hop} = \nu_{ph} e^{-(2\alpha R)} e^{-(\frac{\Delta E}{K_B T})} \quad (12)$$

Consider the sites, which are uniformly distributed in energy close to the Fermi energy E_F, with a concentration $N(E_F)$. A sphere of radius R will on an average contain $4\pi R^3 N(E_F)/3$ sites giving an average energy separation of ΔE. This will decrease with increasing R as more sites become available, the probability of finding energy close to that of the occupied site increases.

Within a range R of a given site, the DOS per unit energy range n(E), near the Fermi energy, is

$$n(E_F) = \frac{4\pi}{3} R^3 N(E_F) \quad (13)$$

Then the value of ΔE is given as

$$\Delta E = \frac{1}{\frac{4\pi}{3} R^3 N(E_F)} \quad (14)$$

The full sphere radius in (12) i.e. the radius of the sphere within which the hopping occurs should be replaced by the average hopping distance Ŕ, defined as [49]

$$\acute{R} = \frac{\int_0^R r^3 dr}{\int_0^R r^2 dr} = \frac{3R}{4} \quad (15)$$

Substituting ΔE and R' in (12) we get

$$\nu_{hop} = \nu_{ph} e^{-(\frac{3\alpha R}{4})} e^{-(\frac{3}{4\pi R^3 N(E_F) K_B T})} \quad (16)$$

The combined factors within the exponential terms in (16) are then differentiated with respect to R, to find the value at which the hopping probability has a maximum. This will occur when the term

$$2\alpha R + \frac{1}{\frac{4\pi}{3}R^3 N(E_F) K_B T} \tag{17}$$

has its minimum value. Then we get the hopping distance as

$$R = \left(\frac{3}{2\pi N(E_F) K_B T \alpha}\right)^{\frac{1}{4}} \tag{18}$$

Substituting this back in the hopping probability/ unit time we get

$$\nu_{hop} = \nu_{ph} e^{-\left(\frac{B}{T^{1/4}}\right)} \tag{19}$$

$$B = B_0 \left(\frac{\alpha^3}{N(E_F) K_B}\right)^{1/4} \tag{20}$$

where $$B_0 = 2\left(\frac{3}{2\pi}\right)^{1/4} = 1.66 \tag{21}$$

Comparing (19) with the equation (9), conductivity is obtained by multiplying (19) by $2e^2N(E_F)R^2$

$$\sigma = 2e^2 R^2 N(E_F) \nu_{ph} e^{-\left(\frac{B}{T^{1/4}}\right)} \tag{22}$$

Thus from (22) we obtain

$$\boldsymbol{\sigma = \sigma_0 e^{-\left(\frac{T_0}{T}\right)^{1/4}}} \tag{23}$$

and the average hopping distance is given by

$$R \approx \left(\frac{T_0}{\alpha T}\right)^{1/4} \tag{24}$$

Equation (23) is the temperature dependence of conductivity described by Mott's VRH.

From the above results the characteristic temperature T_0 as well as the residual resistivity ρ_0 can be calculated as follows.

$$T_0 = B_0{}^4\left(\frac{\alpha^3}{N(E_F)K_B}\right) \tag{25}$$

Where

$$B_0 = 2\left(\frac{3}{2\pi}\right)^{1/4} = 1.66 \tag{26}$$

Where

$$\rho_0 = \frac{1}{D}\left(\frac{T_0}{T}\right)^{-1/4} \tag{27}$$

$$D = \left(\frac{3}{2^4}\right)^{1/2}\left(\frac{e^2 \nu_{ph} N(E_F)}{\alpha^2}\right) \tag{28}$$

The value of the factor B and D varies considerably, but is generally found in the range 2.5- 1.7 [18]. In the 2D and 1D cases, the factor 1/4 in equation (23) is replaced by 1/3 and 1/2, respectively [50].

III. Efros-Shklovskii Variable Range Hopping

As we have already seen, low temperature transport properties of disordered materials are governed by VRH between the localized states. A study on the effect of interactions on the single-particle states lead to the concept of a gap, which was predicted, by Efros and Shklovskii in 1975 [51]. This actually resulted from the suppression of the single-particle DOS near the Fermi level. It is well established that in disordered metals the electron-electron interaction lead to a singular negative correction to the single particle DOS near the Fermi level [52]. In the insulating regime these Coulomb correlations cause a gap in the DOS called the Coulomb gap [51, 53]. This changes the temperature dependence of the DC electrical conductivity at very

low temperatures. In other words Efros Shklovskii Variable Range Hopping (ES-VRH) occurs when the DOS near the Fermi energy tends to zero, yielding a parabolic coulomb gap resulting from the long-range Coulomb interactions between localized electron states [53]. The Efros-Shklovskii (ES) hopping theory is valid at low temperatures depending on the size of the coulomb gap [54].

III. (a). The Concept of Coulomb Gap

Coulomb gap is present in systems where there is considerable interaction of charged particles. Consider two energy levels ϵ_i and ϵ_j near the Fermi level as shown in Fig. 3.28. These are separated by a distance r_{ij}.

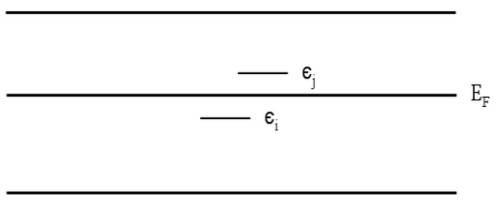

Fig. 3.28. Representation of energy levels where electron interaction results in coulomb gap.

The energy required for an electron to jump from energy levels ϵ_i to ϵ_j is given as

$$\Delta E = \epsilon_j - \epsilon_i \tag{29}$$

In the presence of a hole the energy required will become

$$\Delta E = \epsilon_j - (\epsilon_i + \frac{e^2}{\varepsilon_0 \varepsilon_r r_{ij}}) \tag{30}$$

where ε_r is the relative permittivity of the medium.

When the distance r_{ij} is very small, $e^2/\varepsilon_0\varepsilon_r r_{ij}$ will be large making

$$\Delta E = \epsilon_j - (\epsilon_i + \frac{e^2}{\varepsilon_0 \varepsilon_r r_{ij}}) < 0 \quad (31)$$

Such a situation will mean that the state above Fermi level ϵ_j is of lower energy than ϵ_i, which is not possible. Thus near the Fermi level states are possible only when the condition $\Delta E = \epsilon_j - (\epsilon_i + e^2/\varepsilon_0\varepsilon_r r_{ij}) > 0$ is satisfied. This results in the absence of energy states near the Fermi level till r_{ij} will have a considerable value, which will satisfy the above-mentioned condition. Till certain distance r_{ij}, until ΔE becomes positive, there won't be any electronic states available. This absence of energy levels near the Fermi level due to Coulomb interaction of electrons is called the Coulomb gap.

The suggestion that the Coulomb interactions lead to a Coulomb Gap in the DOS at the Fermi energy came first from Pollok [55]. Later Efros and Shklovskii showed that the DOS takes the following form in the vicinity of E_F.

$$g(E) = g_0 |\mathrm{E} - \mathrm{E}_F|^{D-1} \quad (32)$$

Where D is the dimensionality of the system and g_0 is given by

$$g_0 \approx \frac{3}{\pi} \left(\frac{\varepsilon_0 \varepsilon_r}{e^2}\right)^3 \quad (33)$$

This gives a parabolic form for the DOS in three dimensions. The resistivity then follows ES-VRH, the expression for which is derived below.

The Derivation of Conductivity for ES-VRH

Starting with equation (12) and substituting the Coulomb energy ΔE

$$\Delta E = \frac{e^2}{4\pi\varepsilon_0\varepsilon_r R} \tag{34}$$

we get the hopping probability as

$$\nu_{hop} = \nu_{ph} e^{-(2\alpha R)} e^{-(\frac{e^2}{4\pi\varepsilon_0\varepsilon_r R K_B T})} \tag{35}$$

Maximizing (35) with respect to the hopping length R will lead to the term

$$-2\alpha + \frac{e^2}{4\pi\varepsilon_0\varepsilon_r K_B T R^2} = 0 \tag{36}$$

which gives the temperature dependence of R as follows:

$$R = (\frac{e^2}{4\pi\alpha\varepsilon_0\varepsilon_r K_B T})^{\frac{1}{2}} \tag{37}$$

The hopping length R in terms of the localization length ξ, where $\xi=1/\alpha$ is

$$R = (\frac{e^2\xi}{4\pi\varepsilon_0\varepsilon_r K_B T})^{\frac{1}{2}} \tag{38}$$

Substituting R back in to (35) and multiplying with $2e^2R^2N(E_F)$ will ultimately yield the conductivity

$$\boldsymbol{\sigma = \sigma_0 e^{-(\frac{T_{ES}}{T})^{1/2}}} \tag{39}$$

where T_{ES} is the ES characteristic temperature and σ_0, T_{ES} and ξ are given by

$$\sigma_0 = \frac{4e^4 \xi N(E_F) \nu_{ph}}{3\varepsilon_0 \varepsilon_r K_B T} \quad (40)$$

$$T_{ES} = \frac{\beta_{Es} e^2}{\xi \varepsilon_0 \varepsilon_r K_B} \quad (41)$$

where β_{ES} =2.8 [53] is the numerical value of the coefficient appearing in T_{ES}.

From (41), $$\xi = \frac{\beta_{Es} e^2}{\varepsilon_0 \varepsilon_r T_{ES} K_B} \quad (42)$$

Equations (39)-(42) describe the temperature dependence of conductivity by ES-VRH. The resistivity data are now analyzed in terms of these models.

3.5.3.3 Analysis of Resistivity data

The resistivity values of the alloy NCA films at 273 K are given in Table 3.11. The highest value of resistivity at this temperature was observed for FeAu whereas the lowest value was noted for FePt. For FeAu, as the sample goes from 350 K to 25 K there is a two-order increase in the observed resistivity value. For FePd and FePt films the resistivity value was of the same order in the entire temperature range as shown earlier in Fig. 3.25.

Table 3.11. The resistivity values of alloy NCA films at 273 K.

NCA Films	Cluster Size (nm)	ρ at 273 K (Ω-cm)
FeAu (As-sputtered)	8.5 ± 0.1	3.65×10^{2}
FePd (As-sputtered)	2.7 ± 0.1	1.45×10^{-2}
FePt (As-sputtered)	2.5 ± 0.2	6.21×10^{-3}

From (10), (23) and (39) the resistivity behavior in hopping mechanism is given by the equation

$$\rho = \rho_0 e^{(\frac{T_0}{T})^x} \quad (43)$$

where ρ is the resistivity at T, ρ_0 is the pre-exponential factor and 'x' is the exponent. As explained earlier in section (I) in 3.5.4.2 when localization is strong, at high temperatures the hopping mechanism is NNH and x takes the value 1. We have also shown in section (II) in 3.5.4.2 that a competition between the thermal activation energy and localization length results in Mott VRH mechanism[56, 57] in the absence of electronic interaction where the exponent x has the value $1/4$ (please see equation (43)). In the ES model we have taken into consideration the Coulomb interaction and showed that the presence of a soft gap in the electron DOS at the Fermi level gives a depletion of low-lying excitations [51, 53]. This modifies the equation (43) to $\rho = \rho_0 \exp (T_0/T)^{1/2}$ yielding a larger resistivity.

I. FeAu System

The order of resistivity for the as-deposited FeAu films varied from 1.3 kΩ-cm to 30 Ω-cm with increasing temperature. This is around nine orders of magnitude higher than the material's bulk resistivity. Confirming the presence of $Fe_{0.9}O$ in the alloy films left no ambiguity in understanding the source of this unusually high resistivity. The resistivity vs. temperature data was analyzed using a procedure [58] suggested by Zabrodskii and Zinov'eva (Z-Z). Assuming that the resistivity follows the general hopping law:

$$\rho(T) = BT^{-m} \exp (T_0/T)^{x} \quad (44)$$

Taking the logarithm of both sides and differentiating we get

$$(\partial \ln \rho / \partial \ln T) = -m - x\,(T_0/T)^{x} \qquad (45)$$

Defining $W(T) = -(\partial \ln \rho / \partial \ln T)$

Then equation (45) becomes, $W(T) = m + x\,(T_0/T)^{x}$

and the exponent in the general hopping law has to be estimated using the equation (45). In a system with exponential hopping dependence of ρ, the term $m \ll x\,(T_0/T)^{x}$ and hence 'm' can be neglected. The temperature dependent pre-factor is omitted because of its weak dependence compared to the strong temperature dependence of the exponential term [59].

This yields $W(T) = x\,(T_0/T)^{x}$

$$\ln W(T) = \ln x\,(T_0)^{x} - x \ln T \qquad (46)$$

The equation (46) is that of a straight line and the slope of the straight line obtained by plotting ln W and ln T will yield the value of the exponent *x*. The characteristic temperature can be obtained as $T_0 = (e^{A}/x)^{1/x}$ where $A = \ln[x(T_0)^{x}]$ is the intercept of the straight line. This method suggested by Z-Z helps to determine the appropriate value of the exponent in the hopping law [55].

Plot of ln W vs. ln T for FeAu is shown in Fig. 3.29. It was observed that the slope of the low temperature region was considerably higher than the slope of the high temperature region. The straight line fits to these data yielded an exponent of 0.49 ± 0.04 for the low temperature region confirming ES-VRH where as it yielded the value of 0.21 ± 0.09 for the high temperature region corresponding to MVRH.

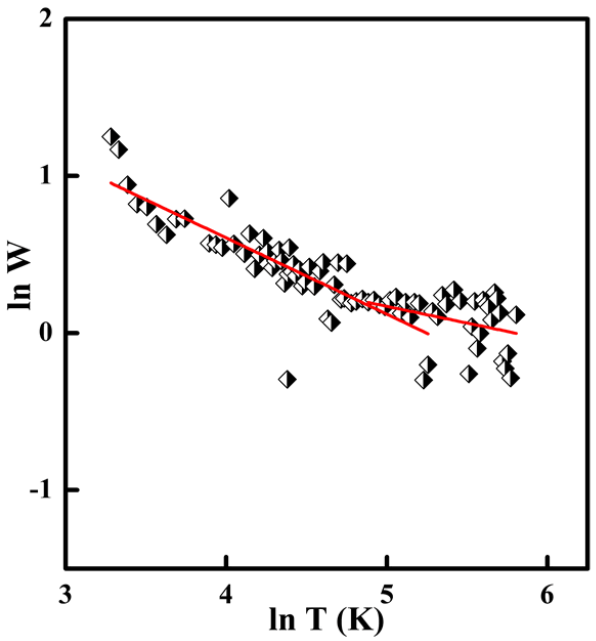

Fig. 3.29. Plot of lnW vs. lnT, for as-deposited FeAu films, with the Z-Z method of analysis. The solid lines are the least square fits to the data.

The fitting parameters x and T_0 are shown in Table 3.12. The intersection of the best fits for both ES-VRH and MVRH defines a cross over temperature T_{cross} which was found to be at 132 K. At this temperature the resistivity curve of FeAu undergoes a cross over from ES-VRH to MVRH. This kind of a cross over from ES-VRH to MVRH has been reported in many cases for disordered system [60,61,62].

Table 3.12. Fitting parameters obtained for lnW vs. lnT plots for as-deposited FeAu films (Z- Z method). The parameters x and T_0 for the two regions are displayed.

Low Temperature Resistivity		High Temperature Resistivity	
x	$T_0 = T_{ES}$ (K)	x	$T_0 = T_{Mott}$ (K)
0.49 ± 0.04	$7.88 \times 10^2 \pm 1.67$	0.21 ± 0.09	$6.02 \times 10^5 \pm 5.36 \times 10^{+1}$

The resistivity vs. temperature curves for FeAu films were also fitted to the equation $\rho(T)=\rho_0 \exp (T_0/T)^x$, separating the region above and below 132 K. The values obtained for the exponent *x* from the Z-Z method was given as the initial fitting parameters and the fits are shown in Fig. 3.30. The parameters obtained from the fits are displayed in the Table 3.13. These values are found to coincide with the fitting parameters obtained from the Z-Z fits, confirming the ES-VRH and MVRH as well as the cross over from one mechanism to the other in FeAu films.

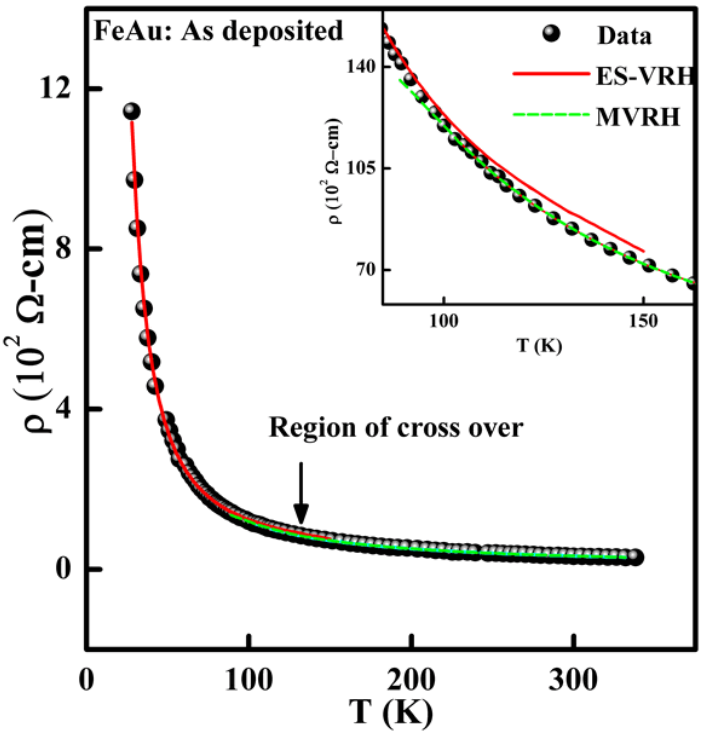

Fig. 3.30. Resistivity vs. temperature plots for as-deposited FeAu alloy NCA films. The fits are for the equation $\rho = \rho_0 \exp (T_0/T)^x$ which shows the region of cross over at 132 K. At this temperature it crosses over from ES to Mott VRH.

Table 3.13. Fitting parameters obtained for the hopping law $\rho = \rho_0 \exp(T_0/T)^x$ for as-deposited FeAu films. The parameters x, T_0 and ρ_0 for the high temperature as well as the low temperature are displayed below.

Low Temperature Resistivity			High Temperature Resistivity		
x	$T_0 = T_{ES}$ (K)	ρ_0 (Ω-cm)	x	$T_0 = T_{Mott}$ (K)	ρ_0(Ω-cm)
0.49 ± 0.03	668.37 ± 16.3	9.9 ± 2.3	0.22± 0.02	$3.35\times10^{+5}$ ± $2.22\times10^{+2}$	0.3 ± 0.13

The plot between ln ρ and T^{-x} with x = 1/2 and x = 1/4 are displayed in Fig. 3.31. The presence of a cross- over from ES-VRH to MVRH is evident from these plots. From Fig. 3.31 (a) the low temperature part is found to follow the ES-VRH mechanism where as a deviation is seen towards the end of the high temperature region. Fig. 3.31 (b) shows that the high temperature region follows the MVRH which deviates from this behavior coming towards the low temperature.

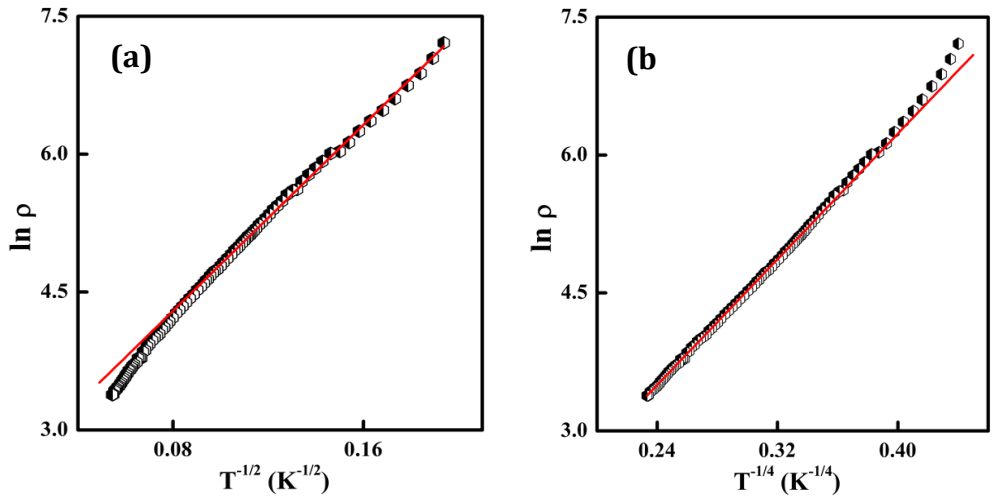

Fig. 3.31. Plot of ln ρ vs. T^{-x}, for as-deposited FeAu films. (a) The deviation from ES-VRH can be seen towards high temperatures. (b) The high temperature part fits to MVRH and the deviation of the data from this hopping mechanism can be seen towards the lower temperatures.

The FESEM pictures of FeAu films showed the formation of cluster agglomerates in these films. In order to understand how the cluster agglomerates evolve in elevated temperatures, the films were heat-treated. The temperature and the duration of heat treatment is as tabulated in Table 3.2. The resistivity vs. temperature data for as-deposited as well as heat-treated films of FeAu are shown in Fig. 3.32.

The FeAu films heat-treated at 350^0 for 30 min showed a resistivity higher than the as-deposited films. The as-deposited FeAu sample was once again sealed and heat-treated at the same temperature and duration in order to rule out the possibility of continued oxidation. The same results were repeated. FeAu films were further heat-treated at the same temperature for durations such as 1 hr and 2 hr and the resistivity values started decreasing compared with the as-deposited films. Although the resistivity behavior seemed puzzling at first, the SEM and FESEM pictures of as-deposited as well as heat-treated samples suggested some possible answers.

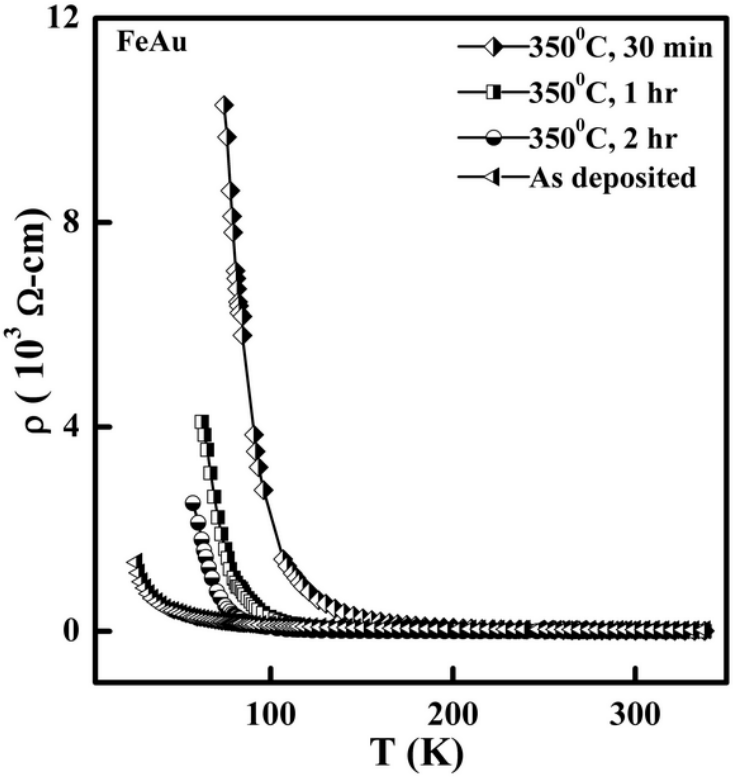

Fig. 3.32. Resistivity vs. temperature plots for FeAu films.

A clear understanding of the evolution of particle size in the SEM and FESEM (Fig. 3.33, Fig. 3.34 and Fig. 3.35) pictures helped to realize the reason behind the variation in resistivity in the FeAu films. From the SEM pictures shown in Fig. 3.33 the average particle size was estimated to be 51.5 nm, 50.8 nm, 47.7 nm and 46.4 nm for as deposited as well as heat treated samples at 350^{0}C for 30 min, 1 hr and 2 hr respectively. These sizes were much larger than the cluster sizes obtained from the XRD which confirmed that these are cluster agglomerates. Also it was evident that the particle size decreased with the increase in the duration of the heat treatment.

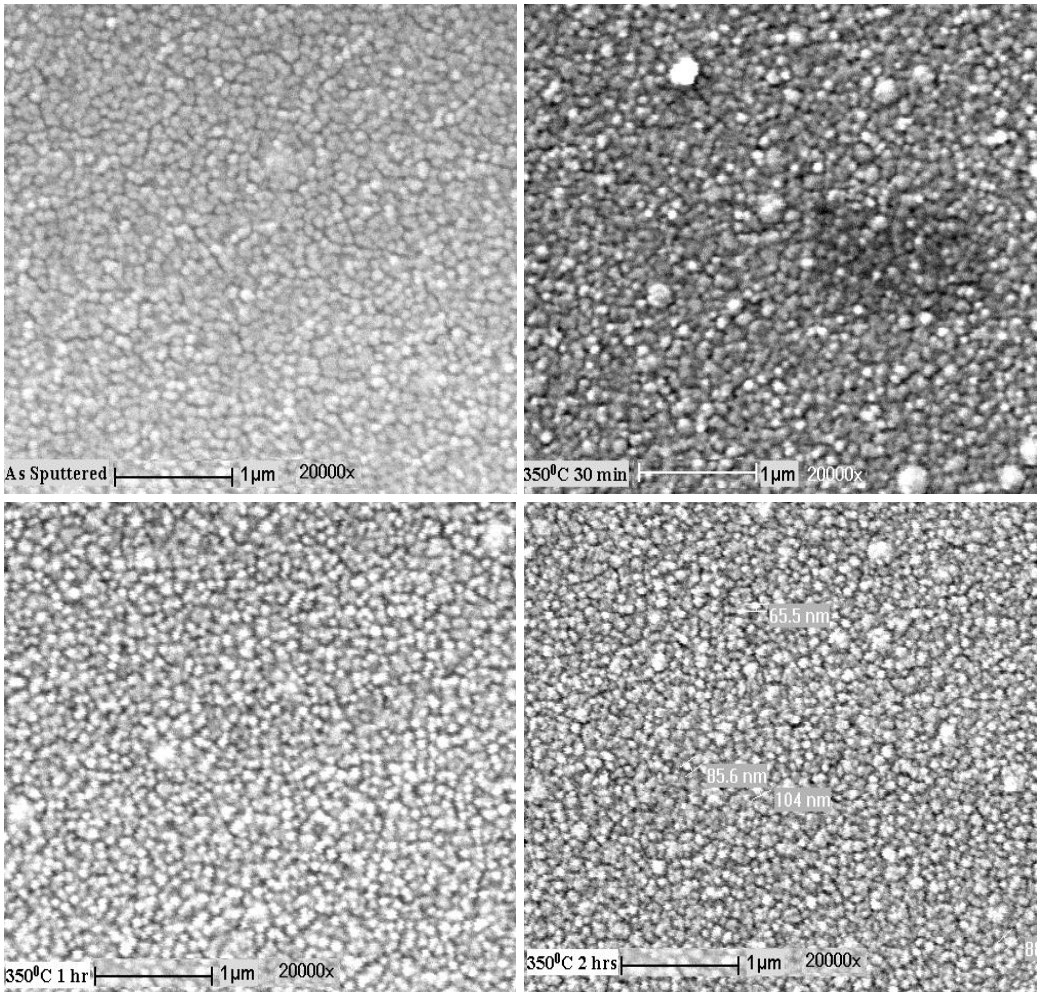

Fig. 3.33. SEM micrographs of as-deposited as well as heat-treated FeAu films.

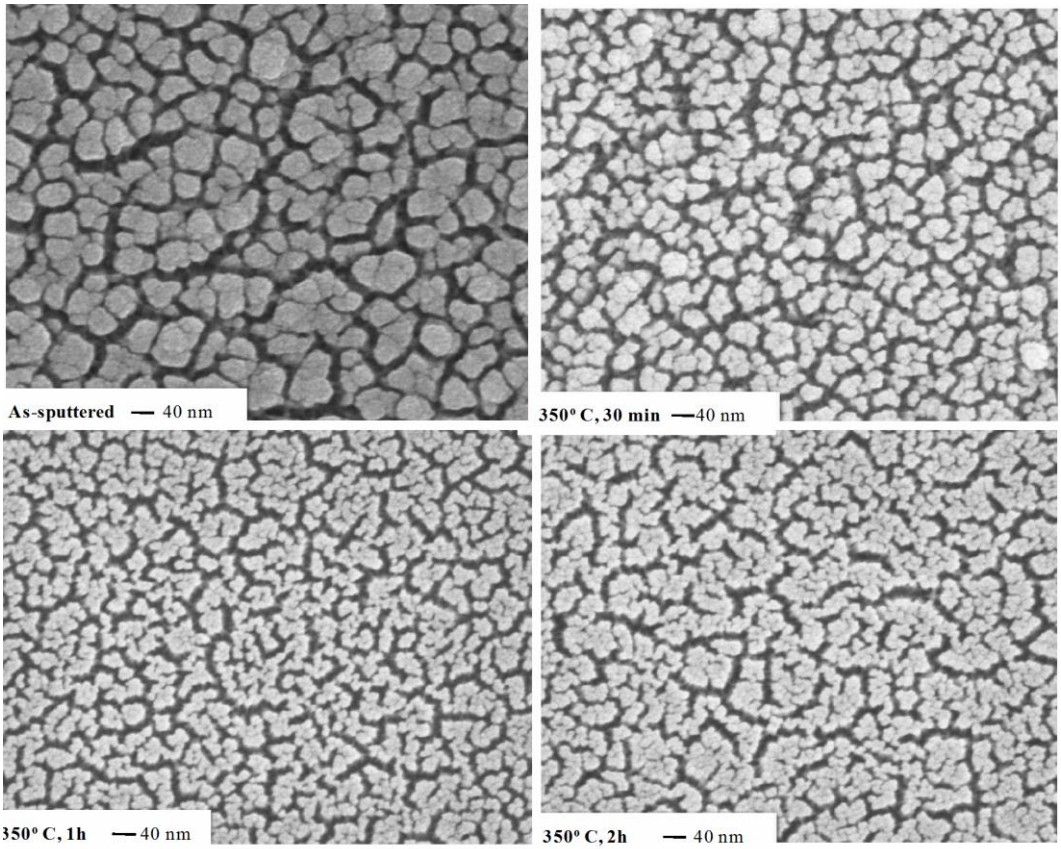

Fig. 3.34. FESEM micrographs of as-deposited as well as heat-treated FeAu films of magnification 200 KX.

The FESEM images in Fig. 3.34 and Fig. 3.35 helps us to understand the evolution of cluster agglomerates. The as-deposited samples show groups of 3-4 cluster agglomerates with an average size of 56 nm. On close reexamination individual atomic clusters are also visible inside these cluster agglomerates.

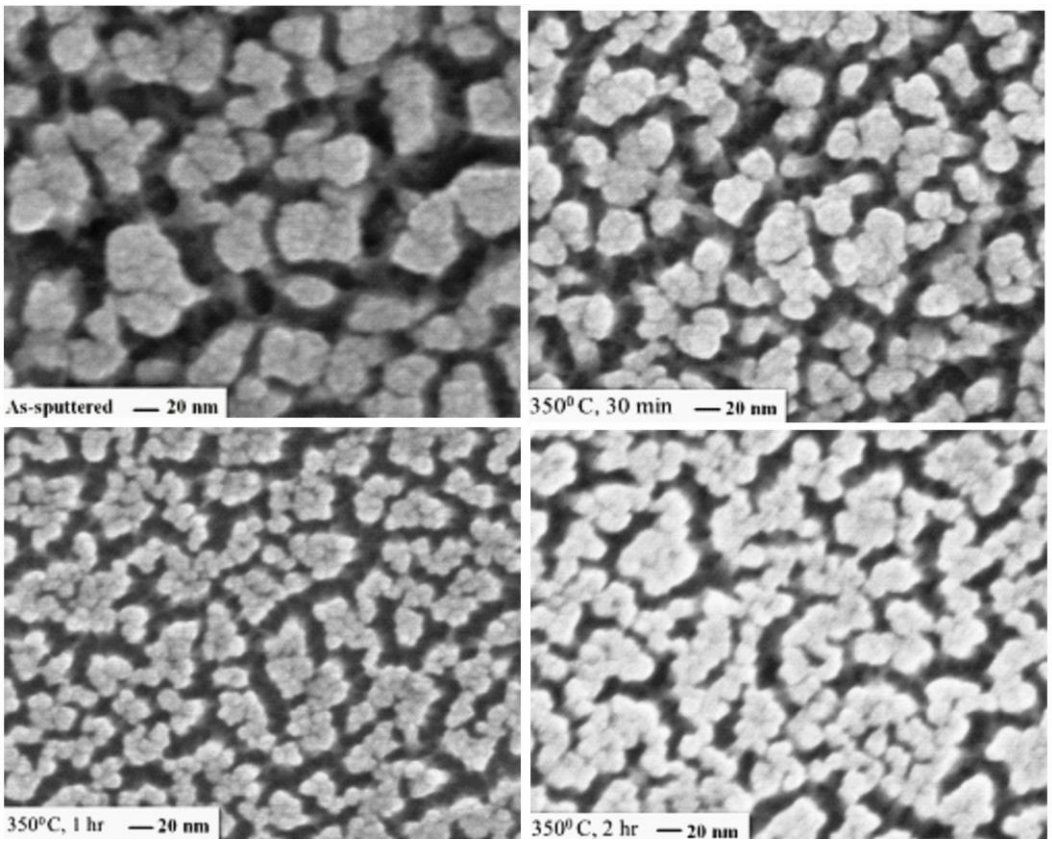

Fig. 3.35. SEM micrographs of as-deposited as well as heat-treated FeAu films.

With a heat treatment of 350^0C for 30 min the cluster agglomerates are found to reduce in size to smaller aggregates of 41 nm by the disintegration of clusters. Further increase in the duration of heat treatment to 1 hr and 2 hr reduces the agglomerate sizes and the clusters are found to separate and spread out, ultimately coming together with more and more nanoclusters connected to each other forming a continuous structure. From these micrographs we could infer that there was not much growth in cluster size, which agrees well with the XRD data. The cluster size from FESEM was found to vary from 9 to 14 nm with heat treatment, which coincides with the cluster size estimated from XRD.

From the FESEM pictures as well as from the resistivity curves we can infer that there are three mechanisms, which are in play, when the NCA films are heat-treated, that affect their resistivity. (1) There is reduction in the oxide layer thickness that covers the surfaces of the nanoclusters. (2) There is disintegration of cluster agglomerates to individual atomic clusters, which increases the distance between them. (3) Then there is increase in the individual atomic cluster sizes. The observed resistivity is a result of all the three processes.

With a heat treatment of 350^0C for 30 min the resistivity is found to increase as compared to the as-deposited films. A further increase in the duration of heat treatment for 1 hr and 2 hr brought about a reduction in the resistivity values.

From the FESEM pictures it could be inferred that after 30 min heat treatment disintegration of cluster agglomerates occurs in FeAu films which is due to the removal of oxide layer. This results in the formation of many smaller cluster agglomerates separated from each other. FeAu films were more oxidized than FePd and FePt films because the resistivity values where almost 6 orders higher for FeAu comparing with FePd and FePt. Also as we shall see later while discussing the data of FePd and FePt films, that the heat treatments at 350^0C for 4 min and 7 min could bring about a change in the conduction from insulating type to metallic type (metal insulator transition (MI)) respectively whereas no such transition occurred in FeAu films even after a heat treatment of 2 hr at the same temperature. So the thickness of the oxide layer is more around FeAu nanoclusters and the removal of these oxides results in the disintegration of clusters with separations which are larger and with almost no medium in between. This makes it difficult for electrons to hop or tunnel

through which results in an increase in resistivity. An increase in the duration of heat treatment to 1 hr and 2 hr results in the dissolution of atomic clusters and individual atomic clusters started getting unbound from each other, spreading spatially and ultimately touching each other helping the electrons to hop from one atomic cluster to the other which brings down the resistivity. A schematic diagram of the disintegration of clusters is shown in Fig. 3.36.

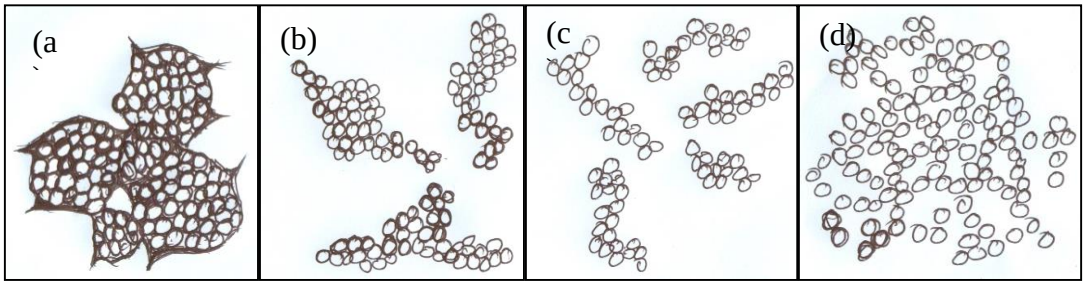

Fig. 3.36. Different stages of cluster agglomerate disintegration. (a) Clusters with the oxide layer. (b) & (c) Reduction in agglomerate size with increase in their distance of separation. (d) Spreading of the clusters with few of them getting connected to one another.

As shown in Fig. 3.32 the resistivity data for the heat-treated samples of FeAu also show an activated behaviour. The resistivity curve of FeAu film heat-treated for 350^0C for 30 min was analyzed using the Z-Z method. The best fit to the data points for ln (W) vs. ln(T) shows that the slope of the entire temperature region from 25 K to 350 K remains the same. This straight-line fit yielded an exponent of 0.24 ± 0.05 corresponding to MVRH (Fig. 3.37). The fitting parameters are shown in Table 3.14 where the values of the exponent x, the characteristic temperature T_0 are displayed. The entire region of resistivity vs. temperature curves for FeAu films were also fitted to the equation $\rho(T) = \rho_0 \exp (T_0/T)^x$ as shown in (Fig. 3. 38). ln ρ vs. $T^{-1/4}$ is also plotted in Fig. 3.39 which shows that the MVRH mechanism suits the entire temperature range. The values obtained from the fits are displayed in the Table 3.14. These values

coincided with the fitting parameters obtained from the Z-Z fits which confirms the conduction mechanism to be MVRH.

In the case of FeAu films heat-treated at 350^0C for 1 hr the resistivity data showed a cross over at 138 K (Fig. 3.40, Fig. 3.41 & Fig. 3.42). The lower temperature part yielded a slope of 0.23 ± 0.15 which corresponds to the MVRH and the higher temperature part of the resistivity displayed a slope of 0.99 ± 0.12 corresponding to NNH. The FeAu film heat-treated at 350^0C for 2 hr showed no cross over and yielded a slope of 0.93 ± 0.04 corresponding to NNH (Fig. 3.43, Fig. 3.44 & Fig. 3.45). The FESEM pictures for the heat-treated sample at 350^0C for 1 hr and 2 hr shows a disintegration of cluster agglomerates which makes the clusters spread out. The absence of MI transition even after heat treatments in these films show that the oxide was only partially removed and a part of it still remains in the system. The presence of the oxide layer as well as the increase in distance between the nanoclusters in these systems will usher in the hopping mechanism for conduction and the thermal energy available can make the electron hop through their localized states. According to the degree of localization of the system, different hopping mechanisms are exhibited.

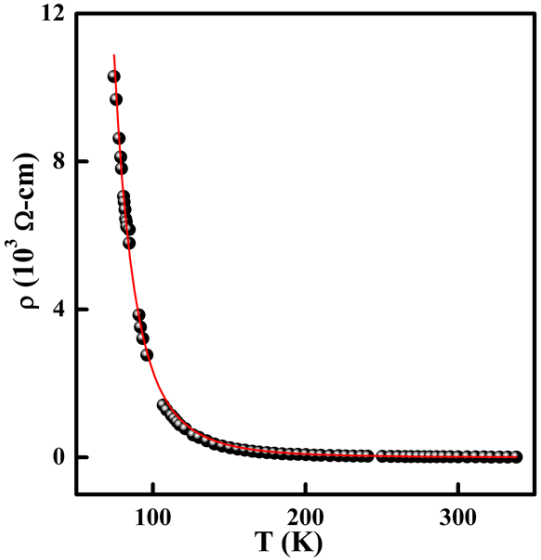

Fig. 3.37. Resistivity vs. temperature plots for 350^{0}C, 30 min heat-treated FeAu films. The fits are for the equation $\rho = \rho_0 \exp (T_0/T)^x$.

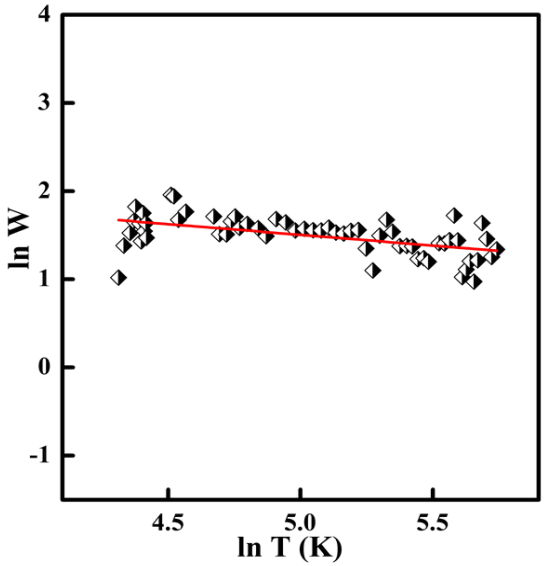

Fig. 3.38. Plot of ln W vs. ln T, for 350^{0}C, 30 min heat-treated FeAu films, with the Z-Z method of analysis. The solid lines are the best fits to the data. The slope of the solid lines yields the hopping exponent *x*, and the intercept is related to the characteristic hopping temperature.

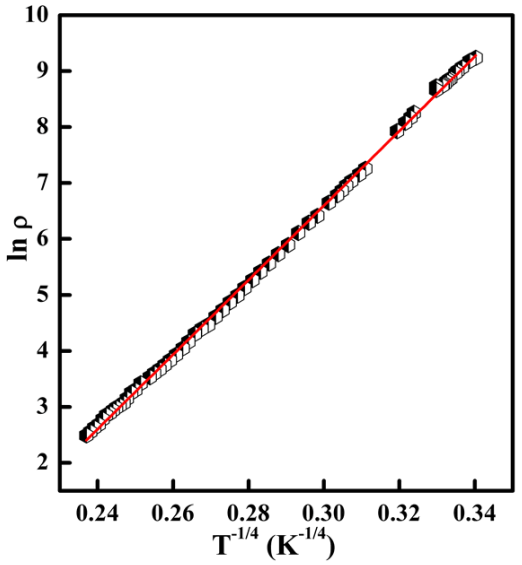

Fig. 3.39. Plot of ln ρ vs. $T^{-1/4}$, for 350^{0}C, 30 min heat-treated FeAu films. The whole range of data comes under the Mott VRH.

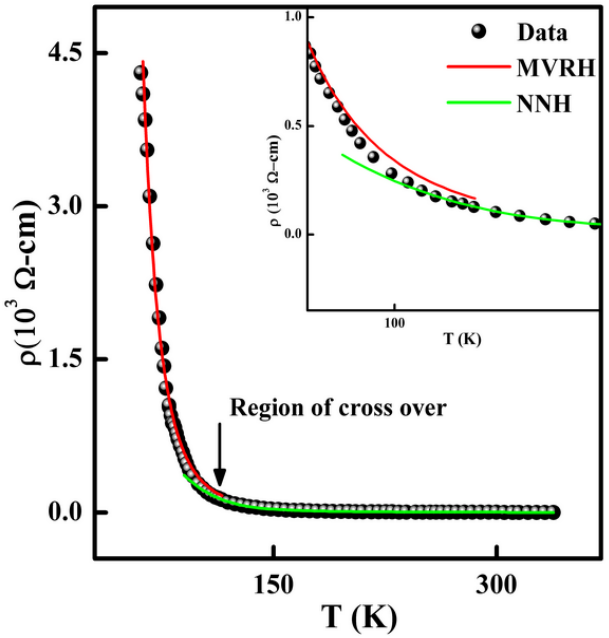

Fig. 3.40. Resistivity vs. temperature plots for 350^{0}C, 1 hr heat-treated FeAu films. The fits are for the equation $\rho = \rho_0 \exp (T_0/T)^x$ which shows the region of cross over at 138 K. At this temperature it crosses over from Mott VRH to NNH.

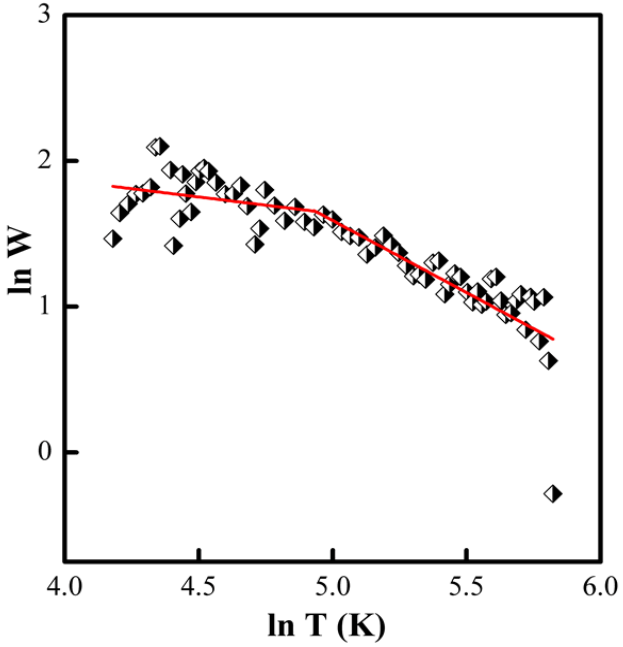

Fig. 3.41. Plot of ln W vs. ln T, for 350^{0}C, 1 hr heat-treated FeAu films, with the Z-Z method of analysis. The solid lines are the best fits to the data. The slope of the solid line yields the hopping exponent *x*. A cross over can be seen at 138 K.

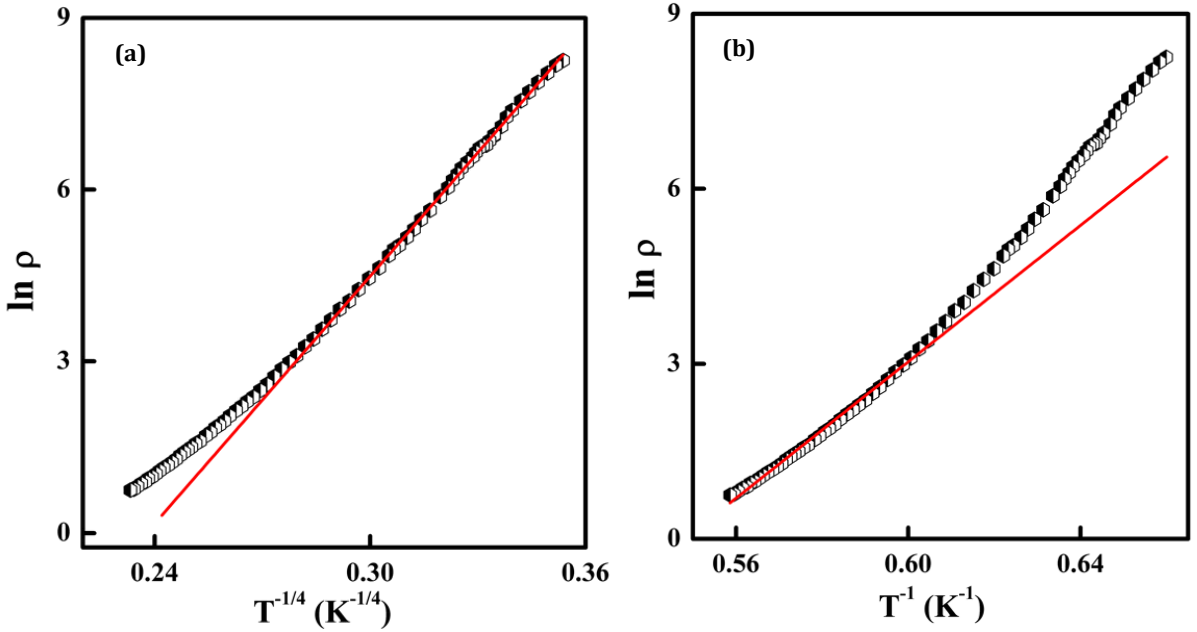

Fig. 3.42. Plot of ln ρ vs. T^{-x}, for 350^{0}C, 1 hr heat-treated FeAu films. (a) The deviation from MVRH can be seen towards the high temperatures. (b) The high temperature part fits to the NNH.

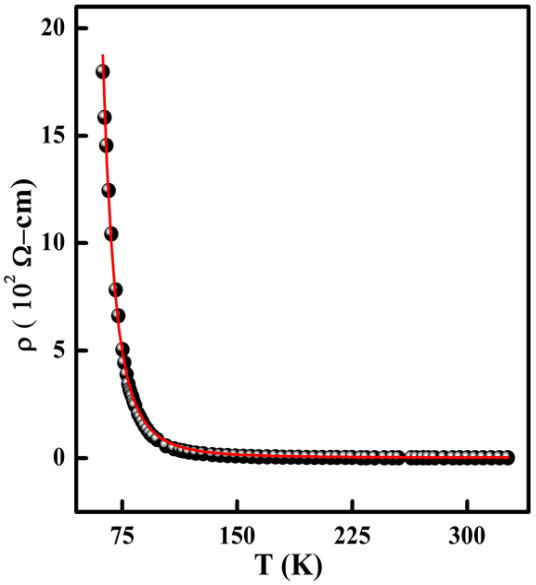

Fig. 3.43. Resistivity vs. temperature plots for 350^{0}C, 2 hr heat-treated FeAu films. The fits are for the equation $\rho = \rho_0 \exp (T_0/T)^x$.

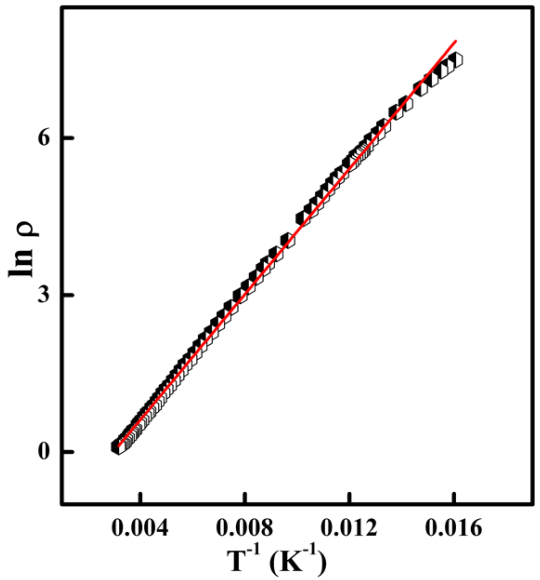

Fig. 3.44. Plot of ln ρ vs. T^{-1}, for 350^{0}C, 2 hr heat-treated FeAu films. The whole range of data comes under the NNH. Only there is a slight deviation towards the high temperature part, which gives an indication of a transition. This could not be verified due to the lack of data points in that region.

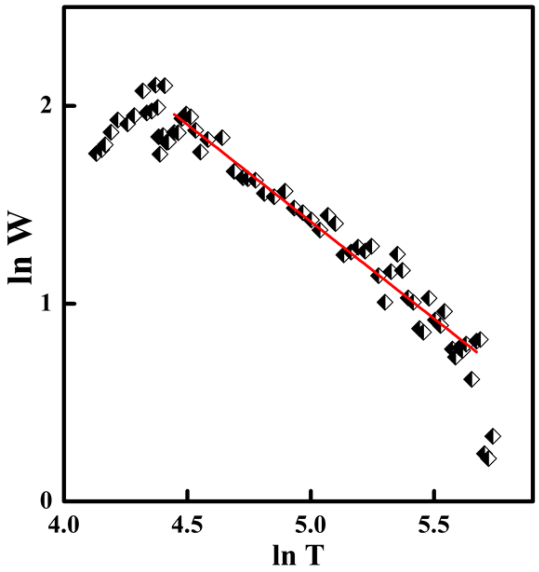

Fig. 3.45. Plot of ln W vs. ln T, for 350^{0}C, 2 hr heat-treated FeAu films, with the Z-Z method of analysis. The solid lines are the least square fits to the data. The slope of the solid lines yields the hopping exponent *x*, and the intercept is related to the characteristic hopping temperature.

Table 3.14. Comparison of the Fitting parameters obtained for lnW vs. lnT plots for FeAu film heat-treated at 350^{0}C for various periods (Z-Z method). The parameters x and T_0 and T_{cross} are displayed below.

FeAu	x (ES)	$T_0 = T_{ES}$ (K)	x (Mott)	$T_0 = T_{Mott}$ (K)	x (NNH)	T_0 (NNH)	T_{cross} (K)
As-deposited	0.49 ± 0.04	788 ± 16.7	0.21 ± 0.09	$6.02 \times 10^5 \pm 53.6$	____	_____	132 K
350^{0}C, 30 min	_____	_____	0.24 ± 0.05	$3.18 \times 10^7 \pm 25.8$	____	_____	____
350^{0}C, 1 hr	_____	_____	0.23 ± 0.15	$1.01 \times 10^9 \pm 678$	0.99 ± 0.12	744 ± 6.74	138 K
350^{0}C, 2 hr	_____	_____	_____	____	0.93 ± 0.04	676 ± 1.74	_____

Table 3.15. Comparison of the Fitting parameters obtained for the hopping law $\rho = \rho_0 \exp (T_0/T)^x$ for FeAu films heat-treated at 350^{0}C for various periods. The parameters *x*, T_0 and ρ_0 are displayed below.

FeAu	*x* (ES)	$T_0 = T_{ES}$ (K)	ρ_0 (Ω-cm) (ES)	*x* (Mott)	$T_0 = T_{Mott}$ (K)	ρ_0 (Ω-cm) (Mott)	*x* (NNH)	T_0 (NNH)	ρ_0 (Ω-cm) (NNH)	T_{cross} (K)
As-deposited	0.49 ± 0.03	668 ± 16.3	9.9 ± 2.3	0.22 ± 0.02	3.351×10^5 ± 222	0.3 ± 0.13	____	_____		132 K
350^{0}C, 30 min	_____	_____	_____	0.25 ± 0.13	1.27×10^7 ± 186	$5.3 \times 10^{-6} \pm 5.2 \times 10^{-7}$	____	_____		____
350^{0}C, 1 hr	_____	_____	_____	0.24 ± 0.09	3.4×10^7 ± 200	$2.1 \times 10^{-7} \pm 5.2 \times 10^{-8}$	0.92 ± 0.03	884 ± 58	0.2 ± 0.03	138 K
350^{0}C, 2 hr	_____	_____	_____	_____	____	_____	0.90 ± 0.1	682 ± 96	0.35 ± 0.08	_____

II. FePd System

The resistivity values of FePd films were not as high as FeAu films. The order of resistivity for as-deposited FePd films was around 1×10^{-2} Ω-cm. This order remained throughout the temperature range of 25 K to 350 K. The resistivity vs. temperature data analysis was also done using Z-Z method and is shown in Fig. 3.46. The straight-line fits to the ln W vs. ln T plots yield a slope of 0.52 ± 0.09, which is the exponent value corresponding to ES-VRH mechanism. The fitting parameters are given in Table 3.16. The resistivity vs. temperature curves were also fitted to the equation $\rho = \rho_0 \exp (T_0/T)^x$ (Fig. 3.47) and the values obtained are displayed in Table 3.17, These values are in agreement with each other. In the Fig. 3.48 the plot of ln ρ vs. $T^{-1/2}$ shows that the slope of the straight line remains the same for the entire temperature range confirming there was no crossover from one conduction mechanism to another.

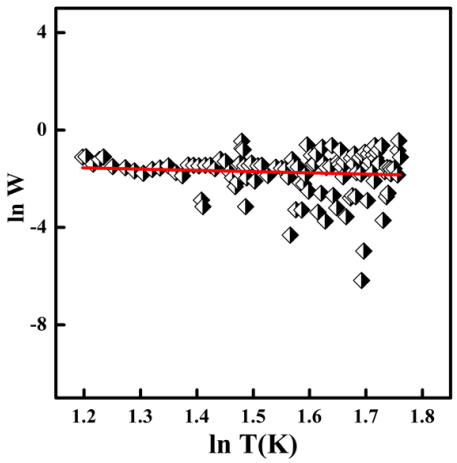

Fig. 3.46. Plot of ln W vs. ln T for as-deposited FePd alloy films, with the Z-Z method of analysis. The solid lines are the least square fits to the data. The slope of the solid line yields the hopping exponent *x*, and the intercept is related to the characteristic hopping temperature.

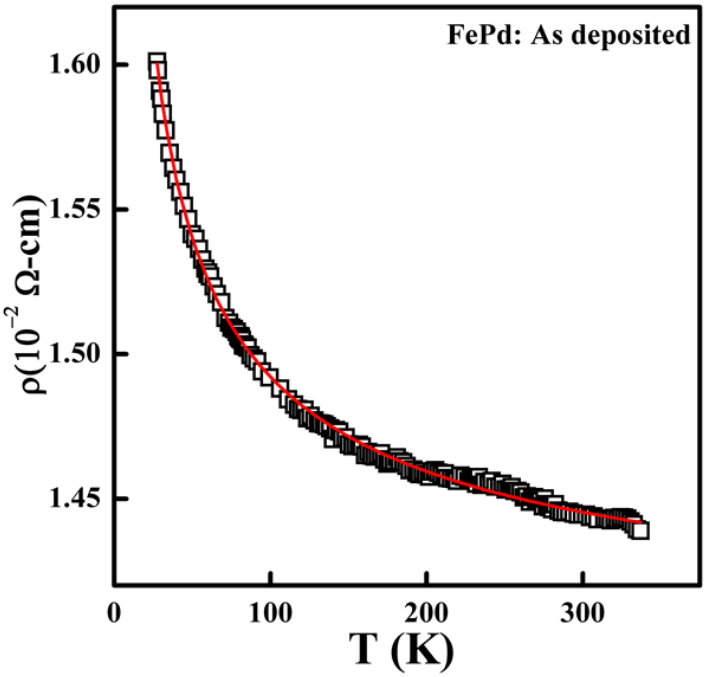

Fig. 3.47. Resistivity vs. temperature plots for as-deposited FePd alloy NCA films. The fits are for the equation $\rho = \rho_0 \exp (T_0/T)^x$.

Table 3.16. Fitting parameters obtained for lnW vs. lnT plots for as-deposited FePd film (Z- Z method). The parameters *x*, and T_0 are given in the table below.

x	$T_0 = T_{ES}$ (K)
0.52 ± 0.09	$5.86 \times 10^{-1} \pm 0.08$

Table 3.17. Fitting parameters obtained for the hopping law $\rho = \rho_0 \exp (T_0/T)^x$ for as-deposited FePd films. The parameters x, T_0 and ρ_0 are given in the table.

x	$T_0 = T_{ES}$ (K)	ρ_0 (Ω-cm)
0.52 ± 0.01	$8.89 \times 10^{-1} \pm 0.02$	$(1.39 \pm 0.002) \times 10^{-2}$

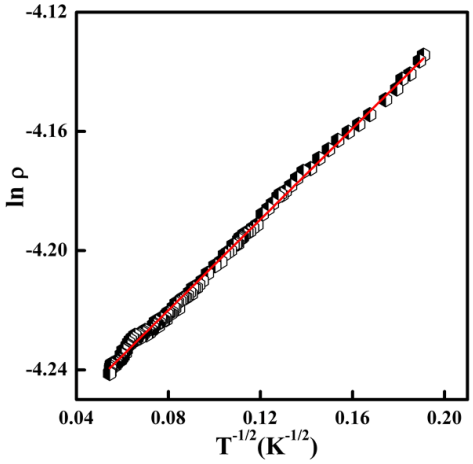

Fig. 4.48. Plot of ln ρ vs. $T^{-1/2}$, for as-deposited FePd films. The resistivity in the whole temperature range is seen to follow ES-VRH.

We now discuss the results for FePd films that were heat-treated at a temperature of 350^0C, for different durations of time. The duration of heat treatment is tabulated in Table 3.3 and the resistivity data is displayed in Fig. 3.49. The order of resistivity for heat-treated films were one order less than that of the as-deposited ones. The samples heat-treated for 4 min and 7 min show lower resistivity values than the as-deposited film. The resistivity starts increasing with 15 min heat treatment and increases further as the duration of heat treatment is increased to 20 min. continuing the heat treatment for 1 hr ultimately brings the resistivity down as seen from Fig. 3.49.

As discussed earlier the oxide layer in FePd films were thinner compared to that of FeAu films. In FePd at first with the 4 min heat treatment the thin oxide layer starts getting removed, but because of the short duration of time no considerable inter-cluster separation (due to cluster agglomerate disintegration) happens. Then the electron finds it possible to hop from one cluster to the other and the resistivity comes down. The heat treatment of 7 min is able to reduce the resistivity further as more oxide is removed. With 15 min heat treatment the cluster agglomerates disintegrate and the clusters start getting separated from each other which increases the resistivity. Longer durations of heat-treatment now increases the separation between clusters which results in higher resistivity values. Ultimately with a 1 hr heat treatment the clusters spread out and touch each other, fusing together (as seen from the FESEM pictures in Fig. 3.51 and Fig. 3.52) which brings down the resistivity. The resistivity for this particular sample displays more of a metallic behavior because of the increased oxide removal (Fig. 3.49).

All the heat-treated samples showed MI transitions at some transition temperature T_C. This was because below T_C the oxide layer that remains in the sample acts as barrier for hopping electrons and above T_C however, the electron does not see the barrier as enough thermal energy is available to overcome the barrier. The metal to insulator transition temperature T_C was found to shift towards lower temperatures with an increase in the duration of heat treatment as shown in Fig. 3.53 and Fig. 3.54. For the 4 min heat-treated sample the T_C was around 82.6 K and it reduced to 49.8 K with a 1 hr heat treatment. This is understandable, as longer heat treatment would result in thinner oxide layers, enabling the electrons to overcome the oxide layer barrier with lower thermal energies.

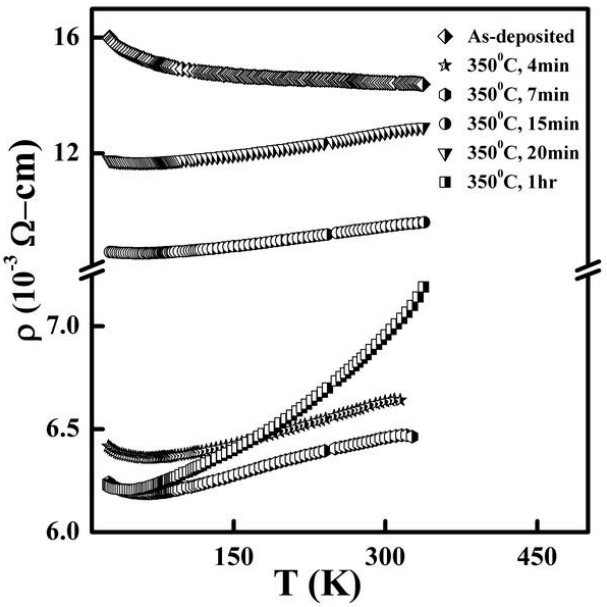

Fig. 3.49. Resistivity vs. temperature plots for FePd films. The heat-treated samples exhibit a resistivity lower than that of as-deposited film because of the removal of the oxide layer.

The micrographs in Fig. 3.50, Fig. 3.51 and Fig. 3.52 show that the agglomerates reduce in size which depict the dissociation of cluster agglomerates in to smaller aggregates with an increase in the duration of heat treatment. The individual cluster size is found to increase from the FESEM as well as XRD data. All these progressions are clear from the micrographs of the FePd films. Thus we see that there are several processes at work such as removal of the oxide layer, the disintegration of cluster agglomerates and the increase in cluster size, which determine the value of resistivity in these films.

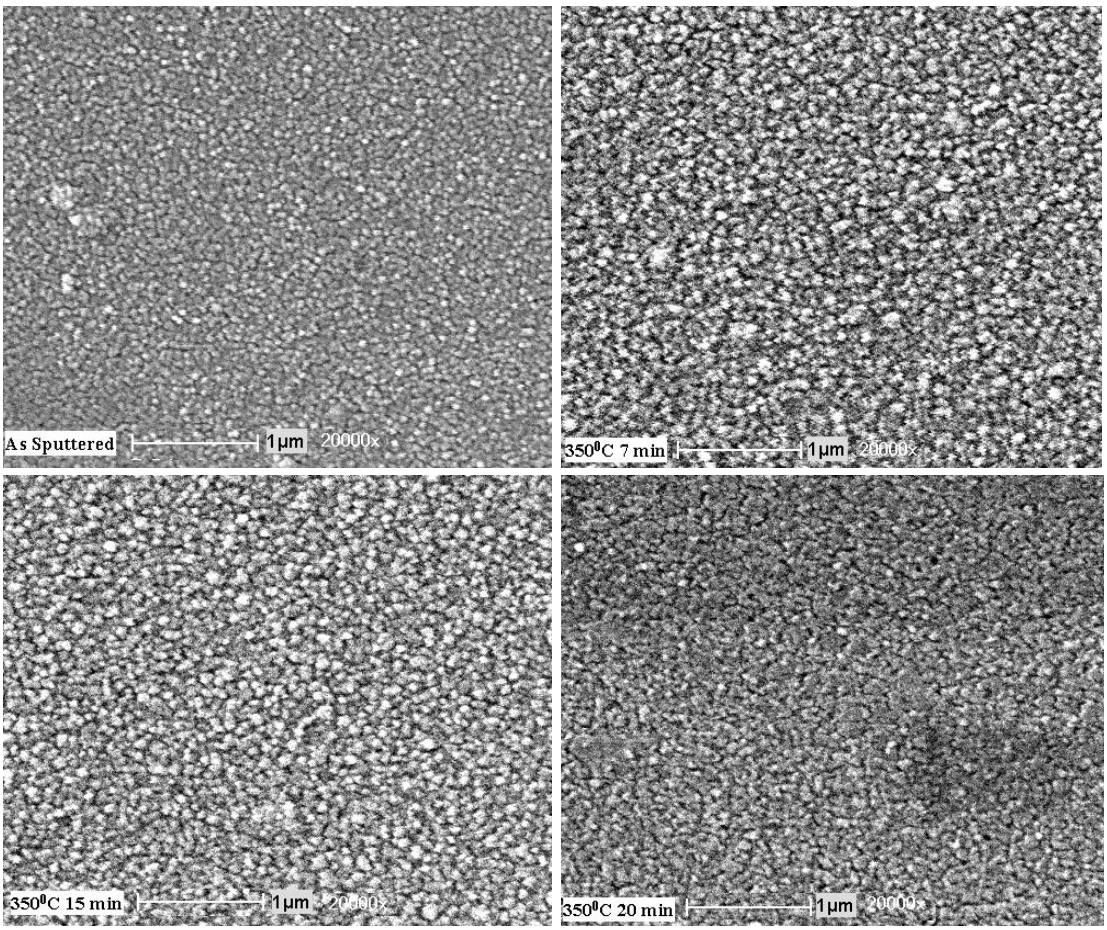

Fig. 3.50. SEM images of as-deposited as well as heat-treated FePd films. The particles seen are cluster agglomerates. The agglomerates are found to reduce in size with increase in the duration of heat treatments.

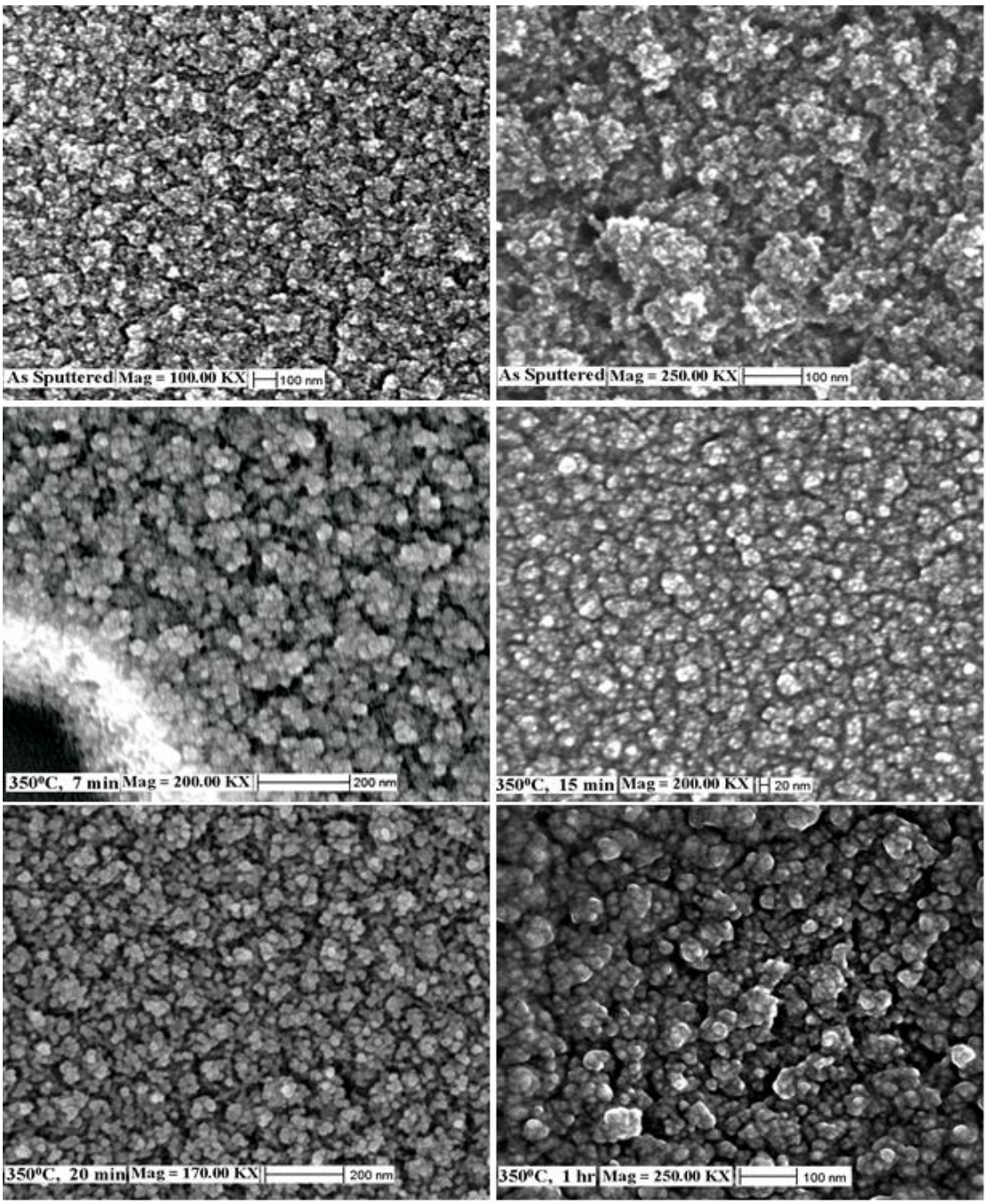

Fig. 3.51. FESEM images of as-deposited as well as heat-treated FePd films of magnification 200 KX.

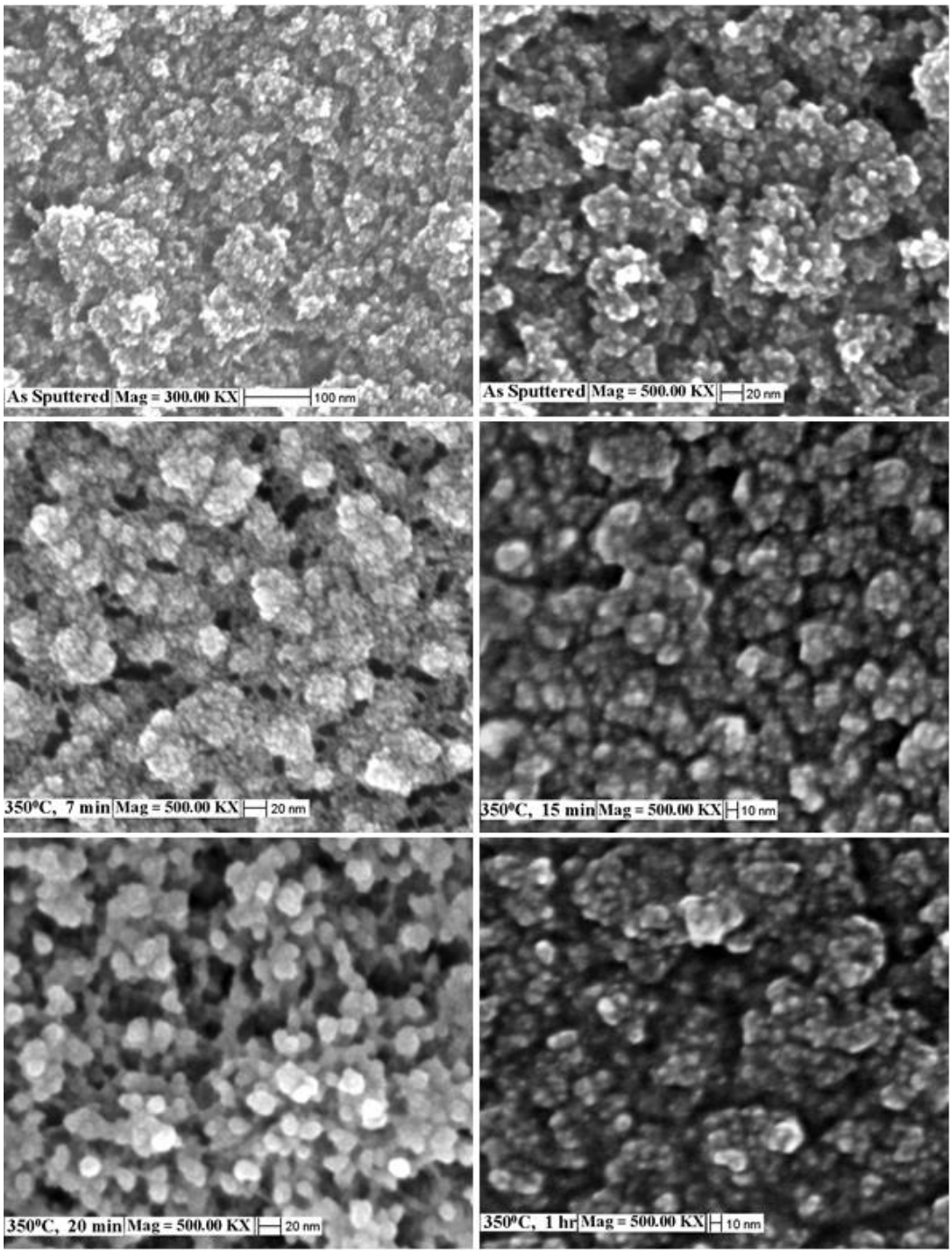

Fig. 3.52. FESEM images of as-deposited as well as heat-treated FePd films of magnification 500 KX.

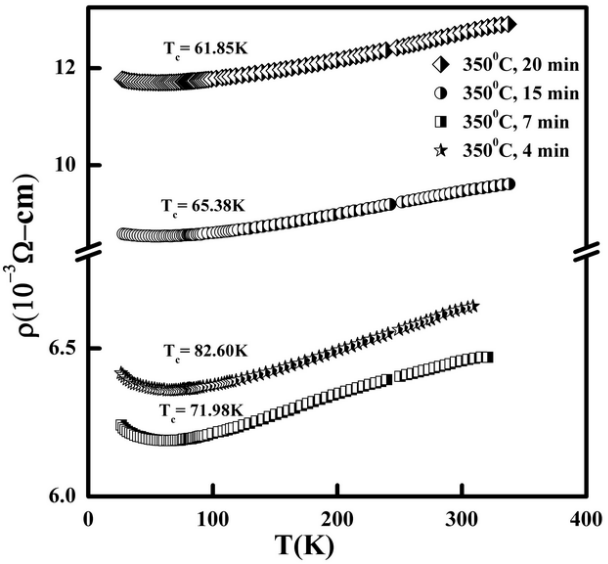

Fig. 3.53. Insulator to metal transition observed for FePd films, by decreasing the oxide layer surrounding the nanoclusters. The transition temperature T_C is found to decrease with an increase in the duration of heat treatment.

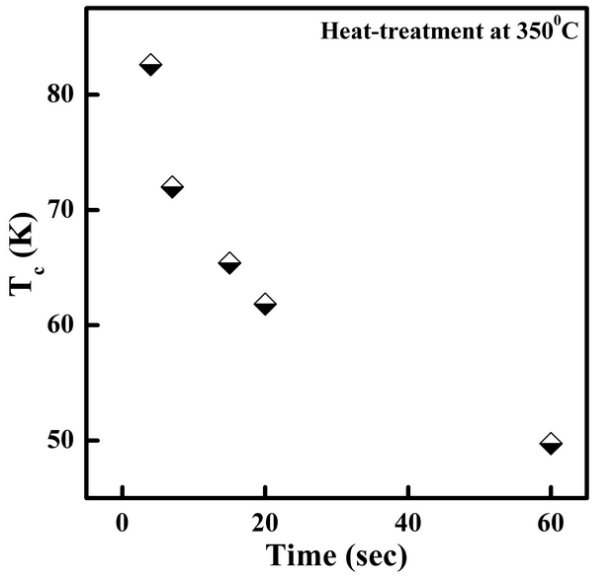

Fig. 3.54. Variation of T_C with the duration of heat treatment at 350^0C for FePd films.

III. FePt System

The FePt films showed resistivity values that were least among the three systems. The order of resistivity for as-deposited FePt films was around 1×10^{-3} Ω-cm. There was no change in the order of this value throughout the temperature range of 25 K to 350 K.

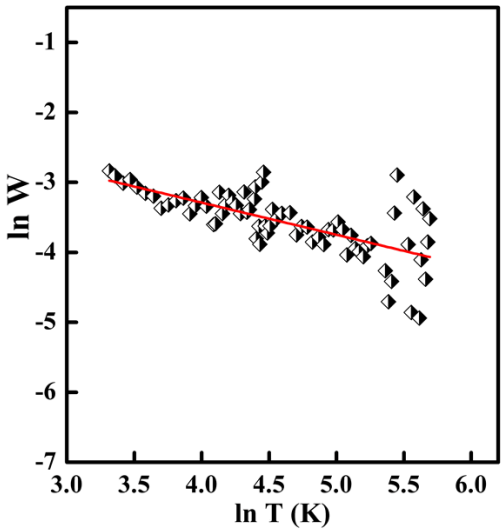

Fig. 3.55. Plot of ln W vs ln T, for as-deposited FePd alloy films, with the Z-Z method of analysis. The solid lines are the least square fits to the data. The slope of the solid line yields the hopping exponent *x*, and the intercept is related to the characteristic hopping temperature.

Table 3.18. Fitting parameters obtained for lnW vs. lnT plots for as-deposited FePt film (Z-Z method). The parameters *x*, and T_0 are given in the table below.

x	$T_0 = T_{ES}$ (K)
0.46 ± 0.06	$4.29 \times 10^{-2} \pm 2.7 \times 10^{-3}$

The resistivity vs. temperature data analysis was done using Z-Z method and is shown in Fig. 3.55. The straight-line fits to the ln W vs. ln T plots yield a slope of 0.46 ± 0.06, value corresponding to ES-VRH mechanism. The fitting parameters are given in Table 3.18. The resistivity vs. temperature curves were also fitted to the equation $\rho = \rho_0 \exp (T_0/T)^x$ (Fig. 3.56) and the values obtained are displayed in Table 3.19, These values are in agreement with each other. The plot of ln ρ vs. $T^{-1/2}$ (Fig. 3.57) shows that the slope of the straight line remains the same for the entire temperature range confirming that the entire range is governed by ES-VRH.

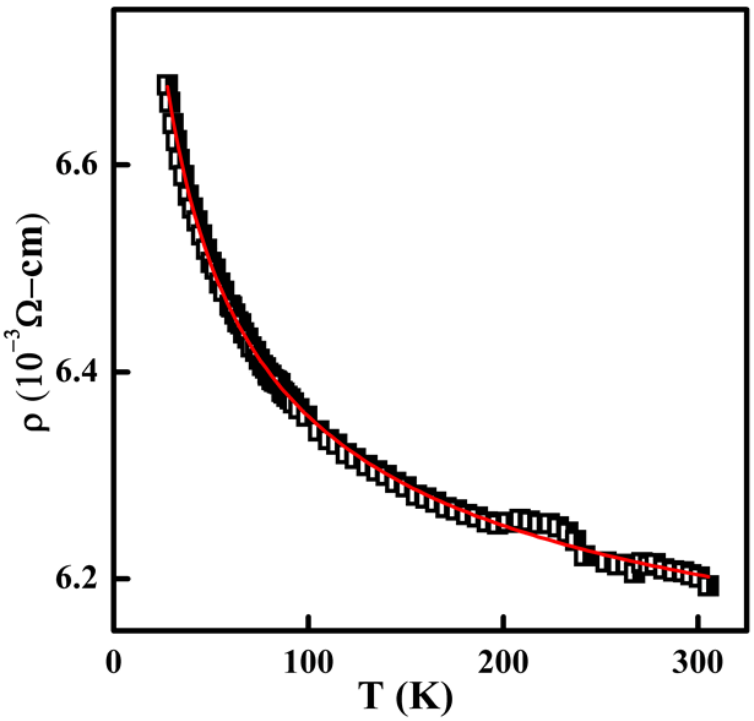

Fig. 3.56. Resistivity vs. temperature plots for as-deposited FePt NCA films. The fits are for the equation $\rho = \rho_0 \exp (T_0/T)^{1/2}$ which is the ES-VRH.

Table 3.19. Fitting parameters obtained for the hopping law $\rho = \rho_0 \exp(T_0/T)^x$ for as-deposited FePt films. The parameters *x*, T_0 and ρ_0 are given in the table.

x	$T_0 = T_{ES}$ (K)	ρ_0 (Ω-cm)
0.45 ± 0.01	$7.27 \times 10^{-1} \pm 0.02$	$(5.97 \pm 0.001) \times 10^{-2}$

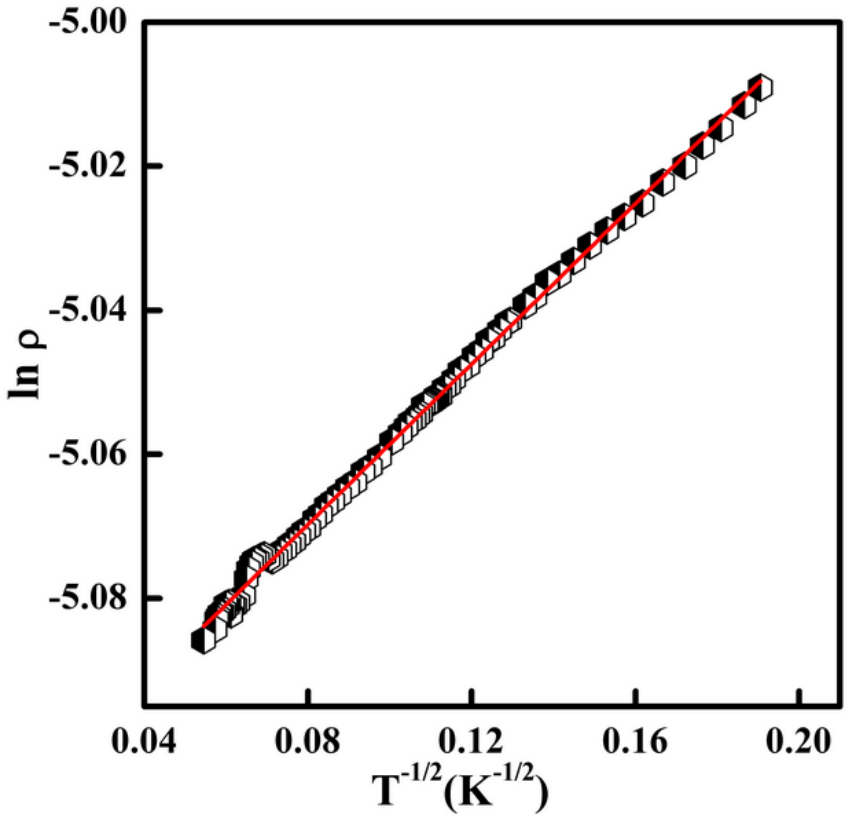

Fig. 3.57. Plot of ln ρ vs $T^{-1/2}$, for as-deposited FePt. The resistivity in the whole region is seen to follow ES-VRH.

The resistivity vs. temperature plots for 300^0C and 350^0C heat treatments for different durations of time are shown in Fig. 3.58. The duration of heat treatment is tabulated in Table 3.4. The order of resistivity for heat-

treated films remained the same as that of the as-deposited ones. The sample heat-treated at 300^0C for 9 min shows a lower resistivity value than the as sputtered film. The resistivity starts increasing with a 15 min heat treatment and increases further as the duration of heat treatment is increased to 25 min. A heat treatment at 350^0C for 7 min also reduces the resistivity which increases with a 25 min heat treatment.

In FePt films also the oxide layer was thinner compared to that of FeAu films as was explained earlier. In this system with a 9 min heat treatment the thin oxide layer started getting removed, but the short time duration of heat treatment could not bring about any inter cluster separation, which enables the electron to hop between clusters reducing the resistivity. At heat treatment of 15 min the cluster agglomerate disintegration happens resulting in an increased resistivity. A further increase in resistivity is seen with 25 min heat treatment, because of larger inter-cluster separation. The same pattern of reduction in resistivity and an increase in its values is repeated for heat treatments at 350^0 for 7 min and 25 min respectively for the reasons explained above. The SEM and FESEM micrographs in Fig. 3.59, Fig. 3.60 and Fig. 3.61 show the reduction in the size of the cluster agglomerates, with an increase in the duration of heat treatment.

Thus during heat treatment, while the oxide layers around the metallic core of the clusters go away partially, the cluster agglomerates break into smaller aggregates. Heat treatment for a longer time does reduce the size of the agglomerates, increase the inter-cluster separation while increasing the individual cluster sizes. All these processes explained here are clear from the SEM pictures of the FePt films.

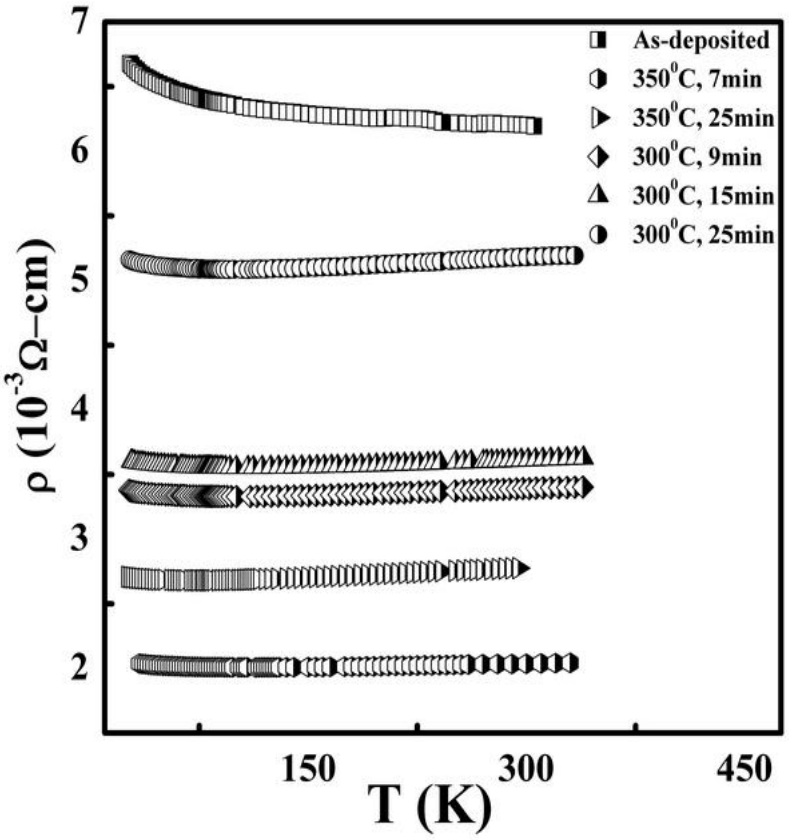

Fig. 3.58. Resistivity vs. temperature plots for FePt films. The heat-treated samples exhibit a resistivity lower than that of as-deposited film because of the removal of the oxide layer.

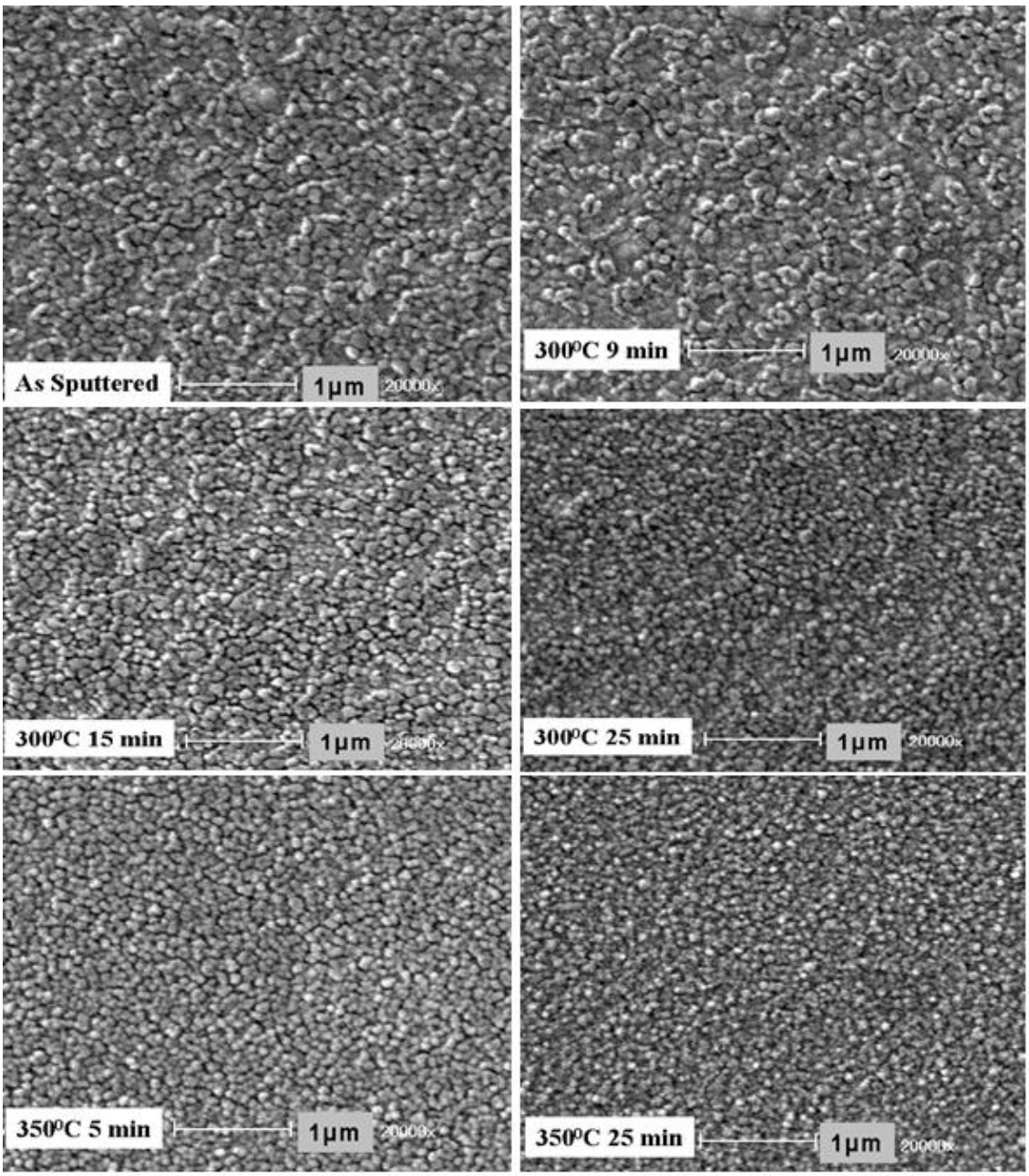

Fig. 3.59. SEM images of as-deposited as well as heat-treated FePt films. The particles seen are cluster agglomerates. The agglomerates are found to reduce in size with increase in heat treatments.

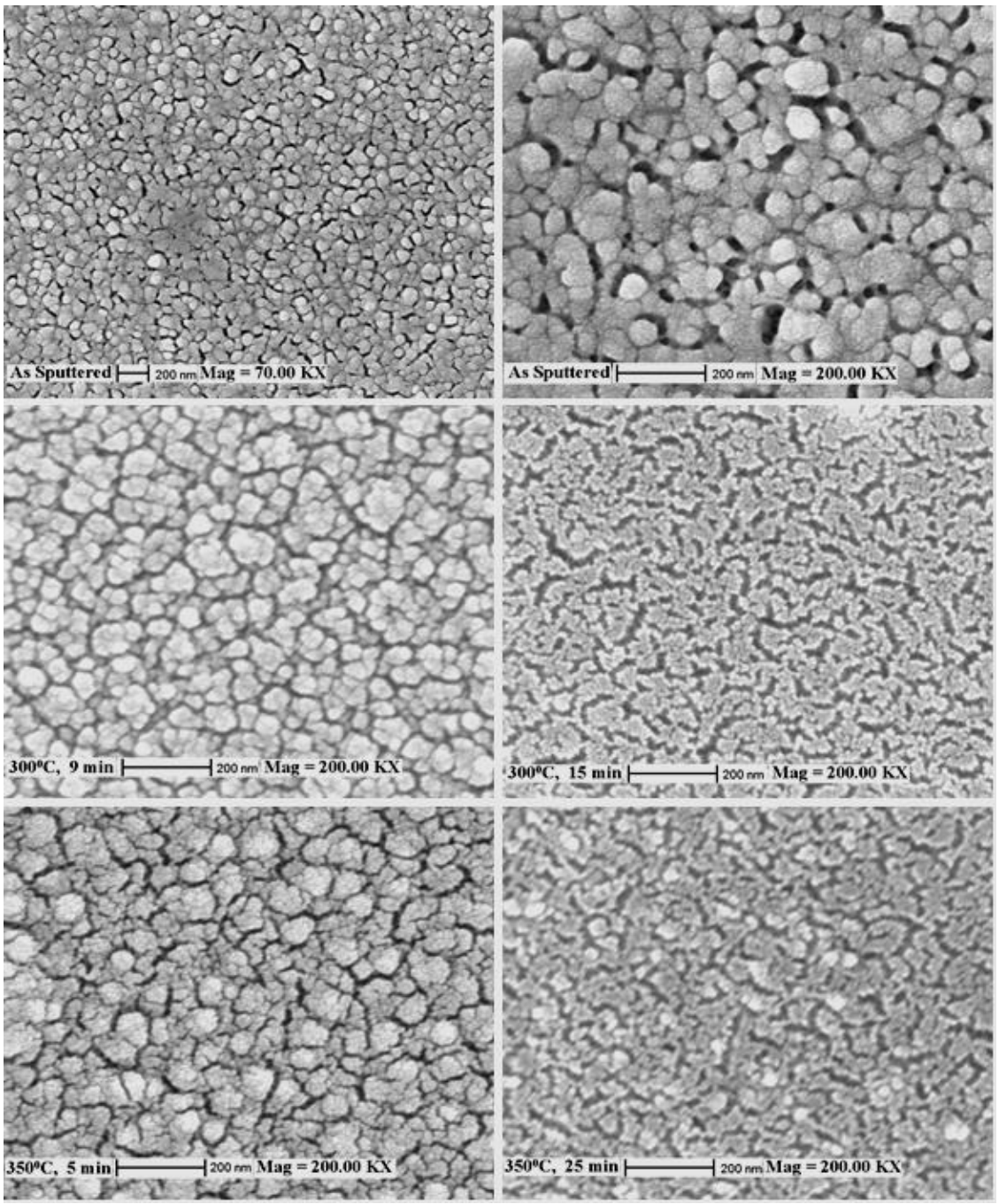

Fig. 3.60. FESEM images of as-deposited as well as heat-treated FePd films of magnification 200 KX.

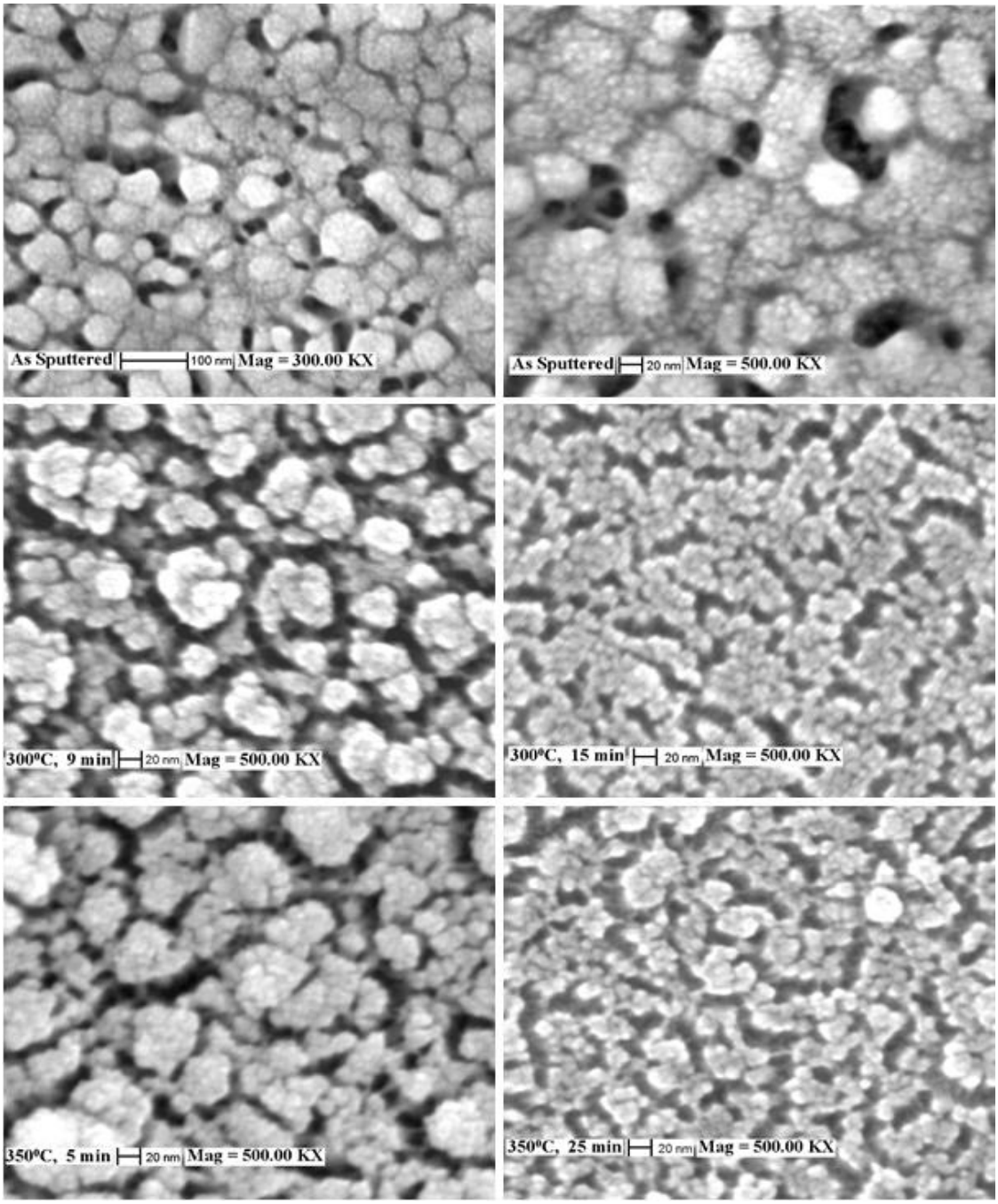

Fig. 3.61. FESEM images of as-deposited as well as heat-treated FePt films of magnification 500 KX.

In the case of FePt films also it was found that, as the duration of heat treatment increases the temperature at which metal insulator transition occurs, decreases as shown in Fig. 3.62 and Fig. 3.63. As explained in the case of FePd, with the increased removal of the oxide layer, less and less thermal energy can bring about M-I transitions.

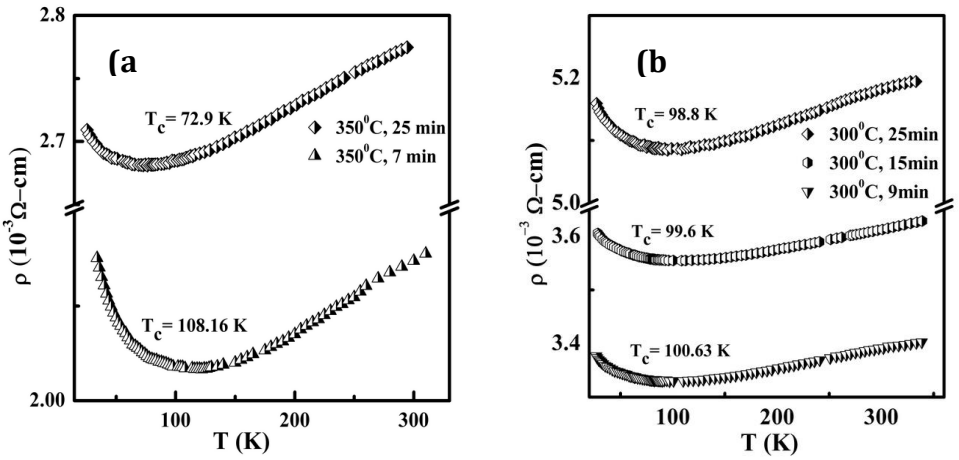

Fig. 3.62. Insulator to metal transition observed for FePt films, by decreasing the oxide layer surrounding the nanoclusters. The transition temperature T_C is found to decrease with an increase in the duration of heat treatment.

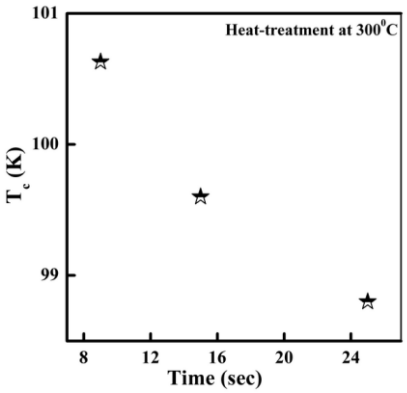

Fig. 3.63. Variation of T_C with the duration of heat treatment at 300^{0}C for FePt films.

IV. Calculation of localization length and hopping length

In VRH, the hopping length is expected to be larger than the localization length. According to equation (42), with the knowledge of the characteristic temperature as well as the dielectric constant of a material the localization length can be calculated. The dielectric constant ε_r of all the samples were measured using Split Post Dielectric Resonator. For the sample FeAu 'ε_r' was found to be 29.74. This is agreeable as for many metallic oxide films the relative permittivity ranges between $10< \varepsilon_r < 30$ [63]. For FePt and FePd it was not possible to measure ε_r as the resonant peak itself was vanishing indicating that the samples are far from the insulating regime. The value of dielectric constant is unknown for disordered metal films, but if we assume a value $\varepsilon_r \sim 10^4$ which is much larger than the insulating value of $\varepsilon_r \sim 10$ as was assumed by Butko and et. al. [63], then we can calculate the localization length (ξ) for ES-VRH using the equations (42) and hopping length (R) using (38).

The ratio of these two characteristic lengths is

$$\frac{R}{\xi} = \frac{1}{4}\left(\frac{T_{ES}}{T}\right)^{1/2} \tag{43}$$

and the hopping energy [60] is given by:

$$\Delta E_{hopp} = \frac{1}{2} K_B T \left(\frac{T_{ES}}{T}\right)^{1/2} \tag{44}$$

Considering a parabolic DOS near the Fermi energy for ES-VRH (32) becomes

$$g(E) = g_0 |\mathrm{E} - \mathrm{E}_F|^2 \tag{45}$$

where g_0 is given by (33).

Substituting the values of $\varepsilon_0\varepsilon_r$ from (42) in terms of T_{ES} and ξ we get g_0

$$g_0 = \frac{3}{\pi}\left(\frac{\beta_{Es}}{\xi T_{ES}}\right)^3 \quad (46)$$

The value of g_0 obtained for all the three systems is given in Table 3.20. For systems FePt and FePd, the value of g_0 is several orders of magnitude higher than that of FeAu making it evident that in the above two systems, the number of states available is much higher. This clearly gives an indication that these systems are near insulator metal transitions.

Table 3.20. Hopping parameters obtained for ES-VRH for as-deposited NCA films.

System (As-deposited)	ES-VRH parameters			
	ξ (A^0)	R at 100 K (A^0)	g_0(cm^{-3} K^{-3})	ΔE_{hopp} at 100 K (mev)
FeAu	0.035	1.4	2.71×10^9	11.1
FePt	59.1	3.14	1.03×10^{17}	0.41
FePd	88.4	3.84	1.03×10^{17}	0.38

For MVRH the hopping length R_{Mott} and the hopping energy $\Delta E_{hopp,\ Mott}$ are given by the following equations.

$$\frac{R_{Mott}}{\xi} = \frac{3}{4}\left(\frac{T_{Mott}}{T}\right)^{1/4} \quad (47)$$

$$\Delta E_{hopp} = \frac{1}{24} K_B T (\frac{T_{Mott}}{T})^{1/4} \quad (48)$$

The calculated value of R/ξ as a function of temperature using (43) and (47) are shown in Fig. 3.64.

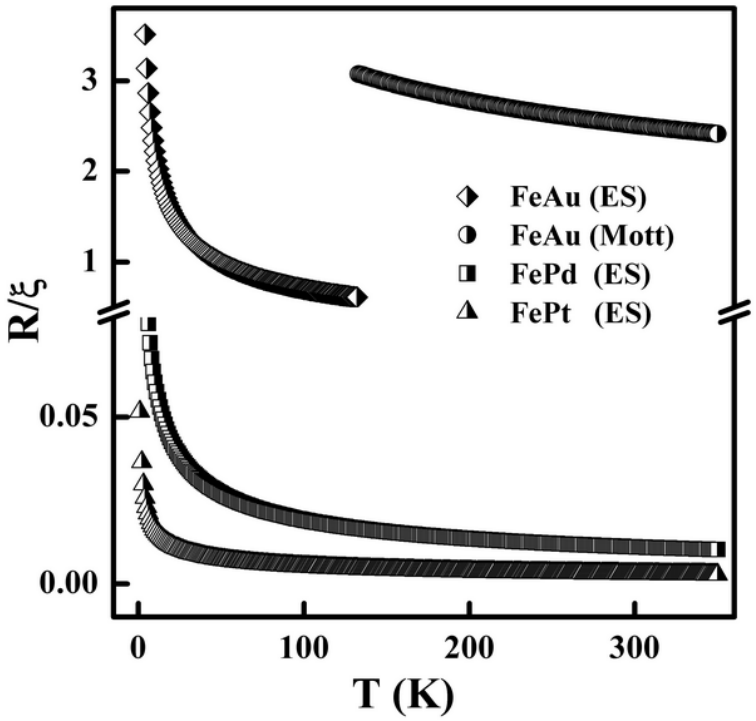

Fig. 3.64. The behavior of the ratio of hopping distance R to localization length ξ as a function of temperature for the NCA films.

3.5.4 Magnetic Measurements

3.5.4.1 Introduction

The magnetic properties of nanoparticles are very sensitive to the composition, structure, lattice defects, size, shape, morphology as well as their immediate surroundings. By varying the size, shape, composition or structure

of the nanoparticles, one can control, to some extent the magnetic characteristics of these materials.

The unique magnetic properties exhibited by nanoparticles are usually inherent in those with a size ranging from 2-30 nm. This size coincides with, or is less than the magnetic domain size in most bulk materials, which results in the formation of single domains in nanoparticles. The reason behind this is that, when the grains reach a critical size, the domain wall formation is not supported energetically. In fact the magnetization of these single domains and their interactions form the reason behind most of the unique magnetic properties exhibited by nanoparticles. Improved physical properties such as giant magneto-resistance, superparamagnetism, large coercivity, and low saturation magnetization [64-70] are critical for enhancing magnetic devices. The future research in nanoclusters would need to be focused on designing suitable nanostructures.

3.5.4.2 Measurements

In order to investigate the magnetic properties of NCA alloy films FC/ZFC measurements were taken using a SQUID magnetometer. The films were cooled to 5 K in zero applied field (ZFC). Then the samples were warmed up while applying a constant field and the temperature dependence of ZFC magnetization was measured from 5 K to 320 K. For field-cooled magnetization the sample was cooled down to 5 K under a constant field and the magnetization was measured while warming up, in the same field. These measurements were taken with a magnetic field of 2 kOe for FeAu and FePt and 1 kOe for FePd. The magnetic relaxation curves of the cluster-assembled films are shown in Fig. 3.65, Fig. 3.66 and Fig. 3.67.

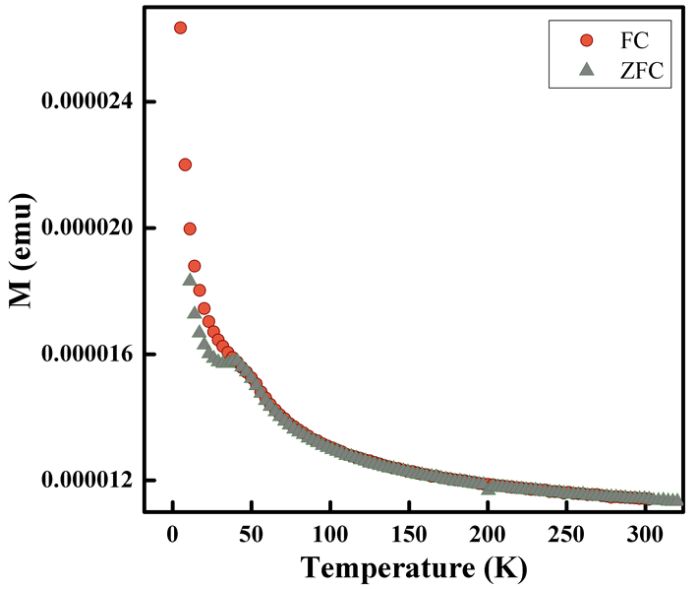

Fig. 3.65. Magnetization vs. temperature curves of FeAu NCA films under FC and ZFC conditions in a magnetic field of 2 kOe.

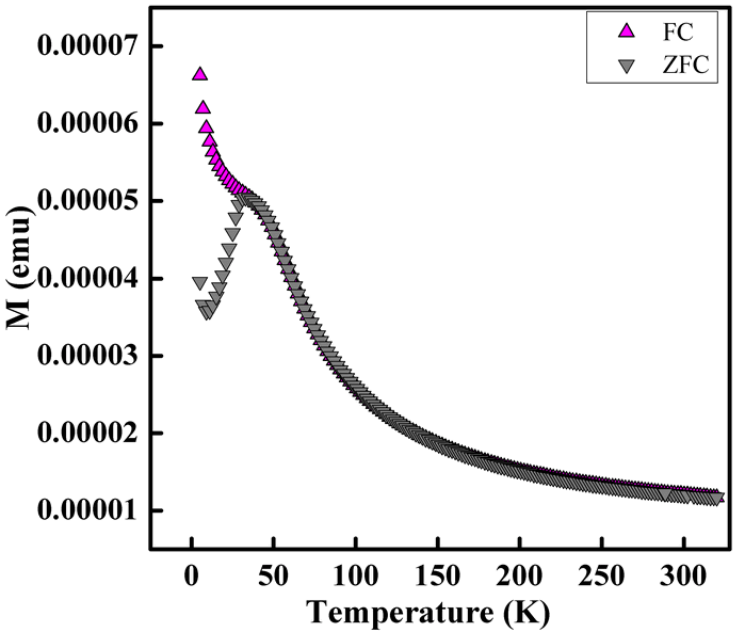

Fig. 3.66. Magnetization vs. temperature curves of FePd NCA films under FC and ZFC conditions in a magnetic field of 1 kOe.

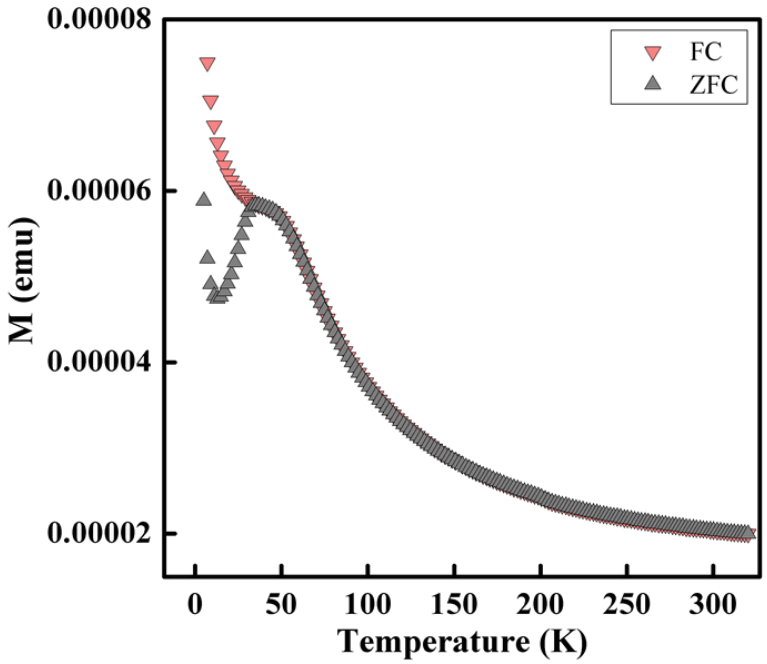

Fig. 3.67. Magnetization vs. temperature curves of FePt NCA films under FC and ZFC conditions in a magnetic field of 2 kOe.

Ferromagnetic particles below a certain size regime exhibit superparamagnetism or in other words superparamagnetism is a size effect of ferromagnetism. The characteristic features of superparamagnetism include: i) the ZFC magnetization vs. temperature curve, (measured using low magnetic fields) displays a maximum at certain temperature called the blocking temperature denoted as T_B ii) divergence in the ZFC/FC magnetization curves below the blocking temperature and iii) presence of magnetic hysteresis and remnant magnetization below T_B whereas magnetic hysteresis disappears above T_B.

The ferromagnetic to super paramagnetic transitions were evident in the FC/ZFC curves. The FC/ZFC curves coincided with each other till T_B, indicating the superparamagnetic state of the systems at high temperatures. Then the curves tend to diverge, where the irreversibility sets in. This temperature is found to be 41 K, 36.9 K and 38.9 K for FeAu, FePt and FePd respectively. It is the magnetic anisotropy that causes the divergence in the FC and ZFC magnetization measurements [71]. After the point of irreversibility the ZFC curve reaches a maximum, which is typical of superparamagnetism. The temperature at which this maximum occurs is known as the blocking temperature (T_B) for superparamagnetic particles [72,73,74]. It is a characteristic of single domain materials. This blocking temperature corresponds to the thermal energy to unblock the largest particle in the sample. Below this temperature, the material shows ferromagnetic properties. The width of the ZFC curve peak reflects the distribution in the particle sizes. A sharp peak represents a narrow size distribution where as a wide peak represents a broad particle size distribution. The NCA alloy films have a distribution in the particle sizes which is reflected in the width of the peak. The blocking temperatures for FeAu, FePd and FePt are found to be 38 K, 33 K and 35 K respectively.

In the case of the ZFC curves at low temperatures below the blocking temperature, the magnetic anisotropy will align the magnetization direction of each nanocluster with its easy axis. The easy axis, which is an energetically favorable direction of moments, has random orientation for nanoparticles. Below T_B when the thermal energy available is less than the anisotropy energy barrier, it prevents the magnetization direction from flipping. In other words the orientation of the magnetic moments of the particles is frozen in random directions and cannot rotate freely. Therefore the magnetization of

the samples becomes very small at low temperatures. The magnetic anisotropy energy is not uniform in the nanoparticles and there exists a distribution in this energy [71]. As the temperature increases the thermal activation energy starts overcoming the anisotropy energy barrier in some nanoclusters, and these particles are unblocked. Consequently the magnetization of the sample increases. At the blocking temperature, anisotropy of almost every nanoparticle is overcome and all particles are unblocked. Then the magnetization becomes maximal. Above blocking temperature the magnetic moment of the unblocked particles fluctuates due to thermal energy, and the particles are in the superparamagnetic state. The magnetic order still exists in each of the nanoparticles, but the direction of spins of each particle randomly flip, lowering the net value of magnetization. Consequently above the blocking temperature the magnetization of the sample decreases with increasing temperature. The superparamagnetic nanoparticles do not display any magnetization hysteresis above the blocking temperature. In the case of FC curve the total magnetization increased with decreasing temperature because the individual nanoclusters tend to orient along the field at low temperatures. At high temperatures thermal fluctuations took over, randomly orienting the moments of the particles, which results in a decrease in the magnetic moments with increasing temperature. There is the presence of a rise in the ZFC/FC curves in the low temperature range of 5 K to 35 K. At first below T_B, the value of magnetization of ZFC curve decreases with decreasing temperature. Then it is found to shoot up along with the FC curve as the temperature decreases further. A similar feature was previously observed for electrodeposited Co-Re films and attributed to the presence of extremely small clusters [75,76,77]. This shooting up of magnetization in the

ZFC curve happens at temperatures 32 K, 13 K and 9 K for FeAu, FePd and FePt respectively.

The larger the particles, a larger thermal energy i.e. k_BT is required for superparamagnetism. Therefore, T_B increases with increasing particle size. Also when a stronger magnetic field is applied, the magnetization direction of the nanoparticles becomes easier to switch to the field direction, and less assistance is required from the thermal activation. Consequently, the blocking temperature decreases with a larger applied field. It is known that the blocking temperature is actually related to the size of the magnetic particles and the magneto-crystalline anisotropy constant (K) by the equation [78,79].

$$K \approx 25 k_B T_B / V \qquad (49)$$

where k_B and V are the Boltzmann constant and the volume of a single particle, respectively and T_B is the blocking temperature. The particle size for FeAu, FePt and FePd from FESEM images are 8.5 nm, 2.5 nm and 2.7 nm respectively. By substituting the value of Boltzmann constant 1.38×10^{-16} ergs K^{-1} as well as the values of T_B obtained from the ZFC curves, we deduce the approximate values of K to be 4×10^5 erg cm^{-3} 1.5×10^7 erg cm^{-3} and 1.2×10^7 erg cm^{-3} for FeAu, FePt and FePd respectively. This is comparable to that of bulk value of these systems, which is 6.6×10^7 erg cm^{-3} for FePt [80] and 1.8×10^7 erg cm^{-3} for FePd [81]. The difference between the values is expected due to several phenomena related to the nanoscale regime such as the structural disorder, surface anisotropy, non-magnetic or weak magnetic interfaces, the lack of surface coordination for the surface magnetic atoms and the electron exchange between the capping agent and surface atoms that are known to influence these values [82].

Magnetic hysteresis measurements at different temperatures from 5 K to 150 K of all the samples were performed in order to obtain further information about magnetic properties of nanoclusters. Fig. 3.68, Fig. 3.69 and Fig. 3.70 show the evolution of magnetic hysteresis loops with varying temperatures for FePt, FePd and FeAu respectively.

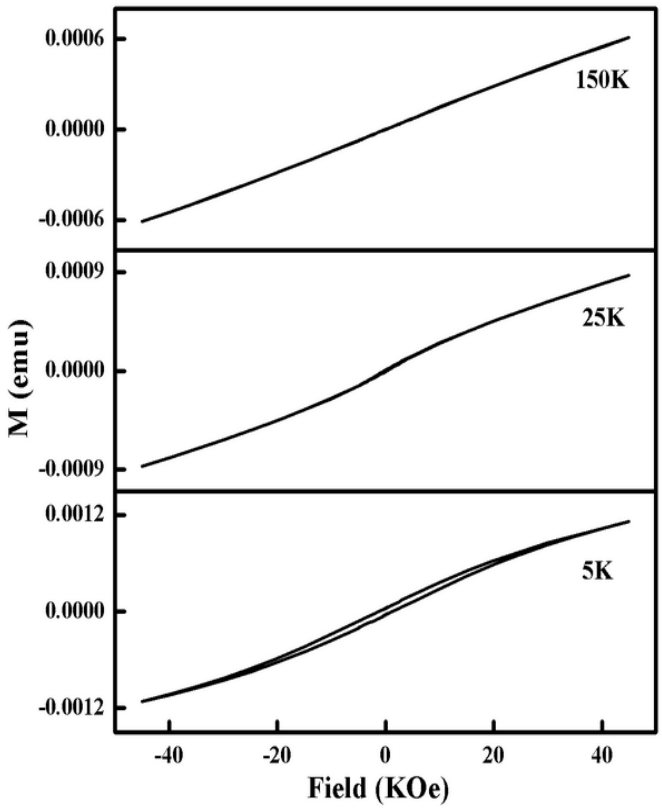

Fig. 3.68. Field dependence of Magnetization at varying temperatures for FePt films.

As expected, ferromagnetic hysteresis loops could not be observed above the respective blocking temperatures of each sample. The field dependence of magnetization recorded at temperatures below blocking

temperature exhibit a finite value of the coercivity. But the magnetization curves measured above the blocking temperature of the samples confirmed the superparamagnetic relaxation of spins, by the vanishing of coercivity and decrease in saturation magnetization. The coercive field is decreased to zero when a sample becomes superparamagnetic because the thermal fluctuations erase each nanocluster's memory of its history.

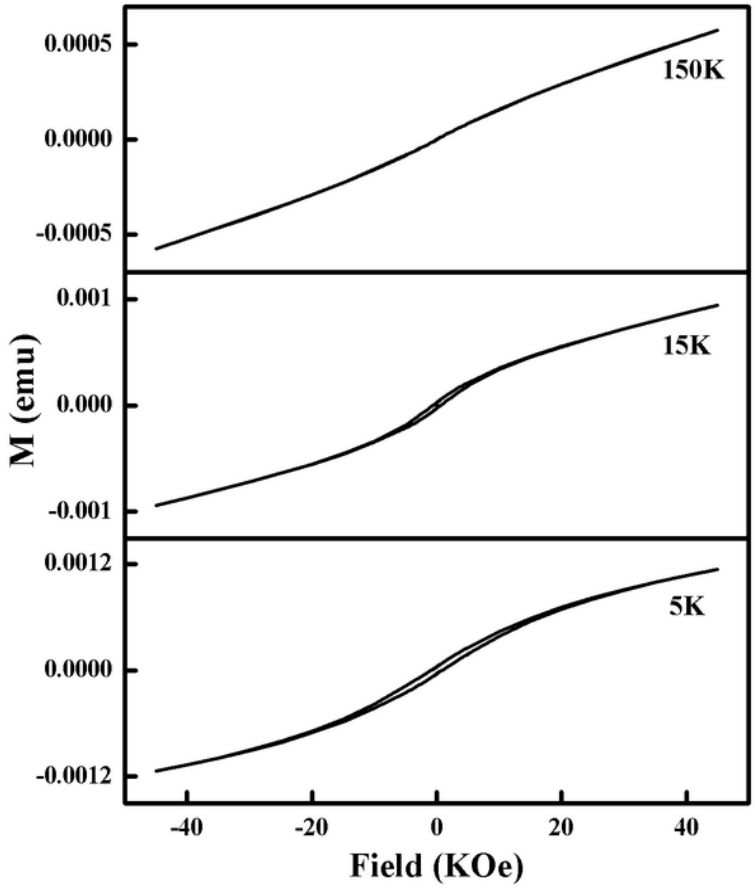

Fig. 3.69. Field dependence of Magnetization at varying temperatures for FePd films.

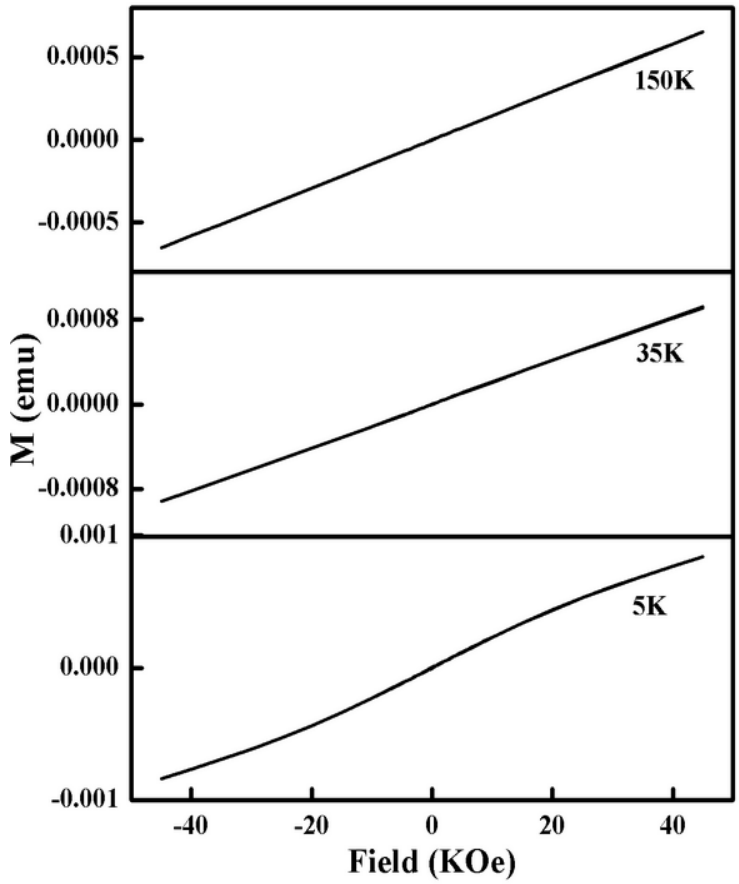

Fig. 3.70. Field dependence of Magnetization at varying temperatures for FeAu films.

The alloy nanoclusters of FeAu, FePd and FePt NCA films have metallic cores surrounded by the $Fe_{0.9}O$ oxide layer corresponding to a shell structure. This was evident from the FESEM pictures and was confirmed by the XRD as well as the electron diffraction data. FeAu [83,84,85], FePd [86,87,88] and FePt [87,89,90] metallic alloys have ferromagnetic behavior whereas $Fe_{0.9}O$ is antiferromagnetic in nature [91]. The antiferromagnetic shell structure of $Fe_{0.9}O$ on top of a ferromagnetic core of metallic alloys in these nanoparticles

results in a coupling between these two materials, which gives rise to exchange biasing.

The effect of exchange bias is manifested as the shifting and broadening of a magnetic hysteresis loop of a sample cooled under an applied magnetic field [92,93,94]. It has been reported extensively in nanoparticles with core/shell structure where a ferromagnetic (FM)/ anti-ferromagnetic (AFM) interface is present [95-97]. The interface exchange coupling between FM and AFM is considered to be the origin of the exchange bias [98].

This phenomenon was first observed in nanoparticles consisting of a core of FM cobalt covered by a shell of AFM CoO [93]. Mieckeljohn and Bean have given a simple model, explaining exchange bias [93]. In a system of FM and AFM layers, when the field is applied at a temperature which is less than the curie temperature of the FM layer and is above the Ne`el temperature of the AFM layer, the low anisotropy spins of the FM material align with the applied field. When the system is cooled through the Ne`el temperature of the AFM layer its spins align with respect to each other. They may also couple with the FM spins depending upon the interfacial exchange coupling between the two layers. Thus a uniaxial anisotropy parallel to the cooling field direction is produced. The large anisotropy of the AFM layer prevents the AFM spin rotation and these in turn prevent the FM spins in turning away from the cooling direction.

To observe the exchange bias, first the samples were field cooled from 320 K to 5 K. Then the M-H loops were measured in a dc field of 2 kOe for FeAu and FePt and 1 kOe for FePd at 5 K, a temperature below T_B. It is below

the blocking temperature T_B that the anti-ferromagnetic order sets in, initializing the exchange bias. The FC magnetization curves in all the samples exhibited the typical features of an exchange bias system, namely a shift H_{EB} of the hysteresis loop towards negative magnetic fields and enhancement of coercivity. This shift occurs because, a hard magnetization behavior of an anti-ferromagnetic layer causes a shift in the soft magnetization curve of the ferromagnetic layer. It is seen in Fig. 3.71, Fig. 3.72 and Fig. 3.73. The value of the shift defines directly the exchange bias field of the system.

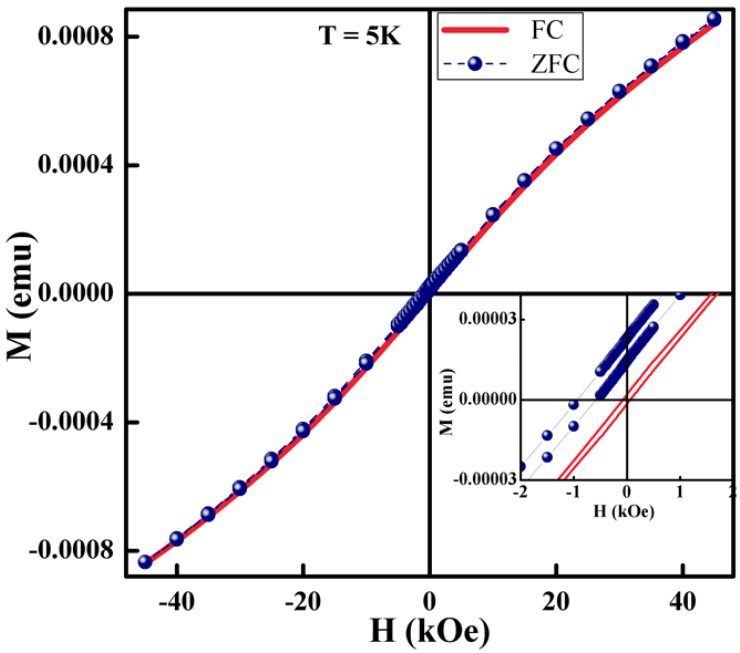

Fig. 3.71. Hysteresis loops of FeAu nanoclusters.

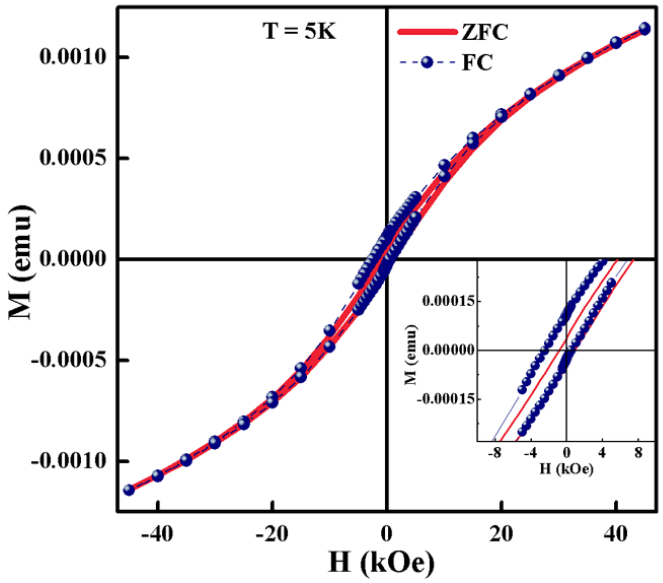

Fig. 3.72. Hysteresis loops of FePd nanoclusters.

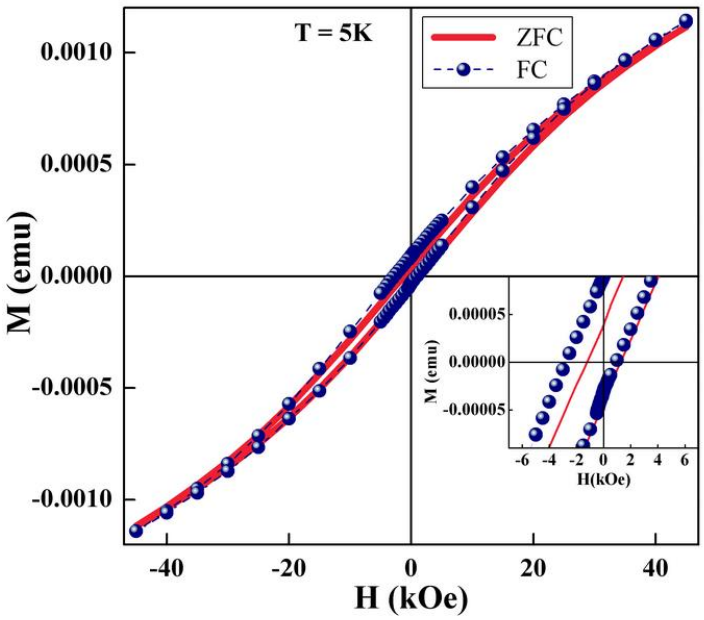

Fig. 3.73. Hysteresis loops of FePt nanoclusters.

The exchange bias field was estimated from field-cooled hysteresis loop by the standard procedure [99,100] using equation

$$H_{EB}=(H^{FC}_{C+} - H^{FC}_{C-})/2 \quad (50)$$

where H^{FC}_{C+} and $H^{FC}_{C-}$are the absolute values of positive and the negative coercive fields. The exchange bias field calculated using the above equation for FeAu, FePd and FePt are 0.067 kOe, 0.84 kOe and 1.24 kOe respectively.

3.6 Conclusion

The NCA films of FeAu, FePt and FePd could be successfully prepared by the Nanocluster Deposition System. The morphology studies revealed that the atomic clusters showed strong tendency to agglomerate by sticking to each other and the presence of oxide could be confirmed in these system. The oxide was found to form a layer around the atomic clusters, separating them from each other while holding them together as agglomerates of 50 to 100 clusters. The presence of Anderson localization of electrons in the metallic core of the nanoclusters surrounded by the oxide could be established in the NCA films. The observed resistivity behavior of the NCA systems was shown to follow the variable range hopping mechanism which could be confirmed from the Zabrodskii and Zinov'eva analysis. The FeAu system showed a crossover from the ES-VRH to MVRH as a function of temperature. The FePd and FePt systems exhibited the ES-VRH conduction for the entire temperature range. The oxide layer in FePd and FePt systems could be reduced by a heat treatment at 350^0C under Ar atmosphere, but no significant reduction was observed in FeAu films. When the oxide shell around the metallic clusters is reduced by the heat treatment, the nanocluster films showed a transition from the insulating state to a conducting state. There was no signature of insulator

to metal transitions in FeAu NCA films even with a 2 hr heat treatment at 350^0C. In this system, the removal of oxide layer resulted in the disintegration of cluster agglomerates to smaller agglomerates and ultimately to individual nanoclusters. With a variation in the distance separating the clusters the conduction mechanism was found to vary from ES-VRH to MVRH and then to NNH as a function of temperature.

The magnetic properties of these nanocluster films were also investigated. The superparamagnetic behavior was observed and the blocking temperatures were determined. The anisotropy energies were estimated from the blocking temperatures and an order of magnitude agreement with bulk values was observed. The exchange bias effect due to the presence of surface oxides was also observed in these systems.

References

[1] H. J. Freund, Surf. Sci. Vol. 500, 271 (2002).

[2] I. Chen Chiang and Dong Hwang Chen, Adv. Funct. Mater. Vol. 17, 1311-1316 (2007).

[3] Geoffrey C. Bond, Platinum Metals Rev. Vol. 52, 107–109 (2008).

[4] Riccardo Ferrando, Julius Jellinek and Roy L. Johnston, Chem. Rev. Vol. 108, No.3, 845-910 (2008).

[5] Deendayal Mandal, Mark E. Bolander, Debabrata Mukhopadhyay, Gobinda Sarkar and Priyabrata Mukherjee, Appl. Microbiol. Biotechnol. Vol. 69, 485-492 (2006).

[6] T.C. Deivaraj and J.Y. Lee, J. Power Sources, Vol. 142, 43–49 (2005).

[7] K. J. Klabunde, "Nanoscale Materials in Chemistry'', John Wiley & Sons, New York, (2001), D. L. Peng, T. Hihara and K. Sumiyama, J. Magn. Magn. Mater. Vol. 277, 201 (2004).

[8] David J. Sellmyer, Minglang Yan, Yingfan Xu and Ralph Skomski, IEEE Trans. Magn. Vol. 41, NO. 2, 560-565 (2005).

[9] S. C. Hern´andez, B. Y. Yoo, E. Stefanescu, S. Khizroev and N. V. Myung, Electrochim Acta. Vol. 53, 5621–5627 (2008).

[10] D. Weller and A. Moser, IEEE Trans. Magn. Vol. 35, 4423(1999).

[11] S. Sun, C. B. Murray, D. Weller, L. Folks and A. Moser, Science, Vol. 287, No.5460, 1989-1992 (2000).

[12] S. H. Sun, S. Anders, T. Thomson, J. E. E. Baglin, M. F. Toney, H. F. Hamann, C. B. Murray and B. D. Terris, J. Phys. Chem. B, Vol. 107, 5419 (2003).

[13] Y. H. Huang, Y. Zhang, G. C. Hadjipanayis and D. Weller, J. Appl. Phys. Vol. 93, 7172 (2003).

[14] M. Chen, J. P. Liu and S. H. Sun, J. Am. Chem. Soc. Vol. 126, 8394 (2004).

[15] Ed. M. Plumer, J. Van Ek and D. Weller, "Physics of Ultra-High-Density Magnetic Recording", Springer, New York, (2001).

[16] R. M. Finch, N. A. Hodge, G. J. Hutchings, A. Meagher, Q. A. Pankhurst, M. R. H. Siddiqui, F. E. Wagner and R. Whyman, Phys. Chem. Chem. Phys. Vol. 1, 485 (1999).

[17] Q. Sun, A. K. Kandalam, Q. Wang, P. Jena, Y. Kawazoe and M. Marquez, Phys. Rev. B, Vol. 73, 134409 (2006).

[18] Y. P. Lee, Y. V. Kudryavtsev, V. V. Nemoshkalenko, R. Gontarz, and J. Y.Rhee, Phys. Rev. B, Vol. 67, 104424 (2003).

[19] K. Takanashi, S. Mitani, K. Himi, and H. Fujimori, Appl. Phys. Lett. Vol. 72, 737 (1998).

[20] B. Roldan Cuenya, L. K. Ono, J. R. Croy, A. Naitabdi, H. Heinrich, J. Zhao, E. E. Alp, W. Sturhahn, and W. Keune. Appl. Phys. Lett. Vol. 95, 143103-3 (2009).

[21] Carl. C. Koch, "Nanostructured materials Processing, Properties and Applications", William Andrew Publishing, Norwich, NY, U.S.A.

[22] T. Vystavel, G. Palasantzas, S. A. Koch, and J. Th. M. De Hossona, Appl. Phys. Lett. Vol. 82, No.2, 197-199 (2003).

[23] J. Pielaszek and J. Barczynska, Mat. Sci. Forum, Vol. 139, 79-82 (1991).

[24] B. E. Warren, "X-Ray Diffraction", New York, Dover Publ. (1990).

[25] P. Scherrer, Nachr. Ges, and Wiss. Goetingen. Math-Phys. Kl. Vol. 2, 96, (1918).

[26] Y. H. Ko, K. J. Kim, C. K. Han, C. Petrovic, Rongwei Hu, H. H. Lee and Y. Lee, Proceedings of the XLVIIth European High Pressure Research Group (EHPRG 47) Meeting, Paris, 6–11 (2009).

[27] P. Mukherjee, Y. Zhang, M. J. Kramer, L. H. Lewis and J. E. Shield, Appl. Phys. Lett. Vol. 100, 211911 (2012).

[28] Keita Watanabe, Hiroaki Kura and Tetsuya Sato Sci. Technol. Adv. Mater. Vol. 7, 145–149 (2006).

[29] T. Mehaddene, J.M. Sanchez, R. Caudron, M. Zemirli and V. Pierron-Bohnes, Eur. Phys. J. B, Vol. 41, 207–212 (2004).

[30] M S Seehra et. al. J. Phys. D: Appl. Phys. Vol. 43, 145002 (2010).

[31] JCPDS-International Centre for Diffraction Data. (Id-00-086-2316) (1999).

[32] R. K. Joshi and H. Sehgal, Physica E. Vol. 23, 168 (2004).

[33] S. B. Concari and R. H. Buitrago, J. Appl. Phys. Vol. 9(4), 2417 (2003).

[34] P.W. Anderson, Phys. Rev. Vol. 109, 1492–1505 (1958).

[35] R Abou-Chacra, P W Anderson and D J Thouless, J. Phys. C: Solid State Phys. Vol. 6, 1734 (1973).

[36] B. A. van Tiggelen, A. Lagendijk and D. S. Wiersma, Phys. Rev. Lett. Vol. 84, N0.19 (2000).

[37] Patrik A Lee and T. V. Ramakrishnan, Rev. Mod. Phys. Vol. 57, 287–337 (1985).

[38] Nevill Mott, Rev. Mod. Phys. Vol. 40, 677-683 (1968).

[39] A. F. Ioffe and A. R. Regel, Prog. Semicond. Vol. 4, 237 (1960).

[40] Dieter Vollhardt and Peter Wolfle, Electronic Phase Transitions, Ed. W. Hanke and Yu. V. Kopaev, Elsevier Science Publishers B.V, (1992).

[41] N.F. Mott and E. A. Davis, “Electronic Processes in Non-Crystalline Materials”, Clarendon Press, Oxford, (1979).

[42] Tal Schwartz, Guy Bartal, Shmuel Fishman and Mordechai Segev, Nature, Vol. 446, 7131, 52-55(2007).

[43] D. J. Thouless. Phys. Rev. Lett. Vol. 39, No: 18 (1977).

[44] A. Miller and E. Abrahams, Phys. Rev. Vol. 120, No:3, 745–755 (1960).

[45] Arjan J. Houtepen, Daan Kockmann, and Danie Vanmaekelbergh, Nano Lett. Vol. 8, (10) 3516-3520 (2008).

[46] Jiaping Han, Mingrong Shen, and Wenwu Cao, A. M. R. Senos and P. Q. Mantas, Appl. Phys.Lett. Vol. 82, No.1, (2003).

[47] Aurora Voje, Thesis, University of Oslo, June (2009).

[48] N.F.Mott, "Conduction in non-crystalline materials", Clarendon Press, Oxford (1987).

[49] Ed. Rainer kassing, "Functinal properties of nanostructured materials", springer, (2006).

[50] R. Casalini, "Organic thin films: a comparison of their electrical and gas sensitivity", Theses, Durham University. Available at Durham E-Theses Online: http://etheses.dur.ac.uk/4477/ (1999).

[51] A. L. Efros and B. I. Shoklovskii, J. Phys. C: Solid State Phys. Vol. 8, (1975)

[52] B. L. Althsuler and A. G. Arnov, Sol. St. Comm. Vol. 30, 115 (1979). B. L. Althsuler and A. G. Arnov, Sov. Phys. JEPT, Vol. 50, 968 (1979).

[53] B. I. Shoklovskii and A. L. Efros, "Electronic Properties of Doped semiconductors", Solid State Series , Springer-Verlag, Berlin-Heidelberg, Vol. 45, (1984).

[54] M. Ghosh, A. Barman, S.K. De and S. Chatterjee. Synth. Met. Vol. 97, 23-29 (1998).

[55] M.Pollak, Discuss. Faraday Soc. Vol. 50, 13-19 (1970).

[56] N. F. Mott, "Conduction in Glasses Containing Transition Metal Ions, Journal of Non-Crystalline Solids", Vol. 1, No.11-17 (1968).

[57] N. F. Mott, "Metal-Insulator transitions", Taylor and Francis Ltd. London, (1974).

[58] Ralph Rosenbaum, Phys. Rev. B, Vol. 44, 3599 (1991).

[59] S. Bogdanovich et al. Phys. Rev. B, Vol. 60, 2286-2291 (1999).

[60] Ralph Rosenbaum, Nguyen V. Lien, Mark R. Graham and Mike Witcomb, J. Phys. Condens. Matt., Vol. 9, 6247-6256 (1997).

[61] M. Iqbal, J. Galibert, J. Leotin, S. Waffenschmidtahd and H. V. Lohenysen. Phil. Mag. B, Vol. 79, No. 10, 1591-1601 (1999)

[62] Hung-Cheng Fang, Tzung-I Su and Shui-Tien Lin, J. Non-cryst. Solids, Vol. 334 & 335, 417-420 (2004).

[63] V. Yu. Butko, J. F. DiTusa and P.W. Adams, Phys. Rev. Lett., Vol. 84, No.7, 1543-1546 (2000).

[64] A.P. Alivisatos, Science, Vol. 271, 933 (1996).

[65] C. B. Murry, C. R. Kagan and M. G. Bawendi, Science, Vol. 270, 1335 (1995).

[66] V. F. Puntes, K. M. Krishnan and A.P. Alivisatos, Appl. Phys. Lett. Vol. 78, 2187 (2001).

[67] J. L. Dorman, D. Fiorani and E. Tronc, Adv. Chem. Phys., Vol. 98, 283 (1997).

[68] A. S. Edelstein and R. C. Cammarata, Nanomaterials: Synthesis, Properties and Applications, IOP, Bristol (1998).

[69] W. Luo, S. R. Nagel, T. F. Rosenbaum and R. E. Rosensweig, Phys. Rev. Lett. Vol. 67, 2721 (1991).

[70] R. W. Chantrell, N. S. Walmsey, J. Gore and M. Maylin, Appl. Phys. Lett. Vol. 85, 4320 (1999).

[71] Adam J. Rondinone, Anna C. S. Samia, and Z. John Zhang, J. Phys. Chem. B. Vol. 103, No. 33, 6876–6880 (1999).

[72] B. H. Sohn, R. E. Cohen, and G. C. Papaefthymiou, J. Magn. Magn. Mater. Vol. 182, No .216 (1996).

[73] D. K. Kim, Y. Zhang, W. Voit, K. V. Rao, and M. Muhammed, J. Magn. Magn. Mater. Vol. 225, 30 (2001).

[74] Lei Zhang, Georgia C. Papaefthymiou, and Jackie Y. Ying, J. Phys. Chem. B, Vol. 105, 7414 (2001).

[75] H. J. Blyte and V. M. Fedivetosyuk, J. Magn. Mater. Vol. 155, 352 (1996).

[76] Thomas Tsakalakos, Illya A. Ovid'koAsuri and K. Vasudevan, "Nanostructures: Synthesis, functional properties and applications", Springer Science and Business Media (2003).

[77] G.A. Jones, C.A. Faunce, D. Ravinder, H.J. Blythe and V.M. Fedosyuk, J. Magn. Magn. Mater. Vol. 28, 184 (1998).

[78] TanushreeBala, S. D. Bhame, P. A. Joy, B. L. V. Prasad and Murali Sastry. J.Mater. Chem. Vol. 14, 2941 – 2945 (2004).

[79] J.Nogue´s, V.Skumryev, J.Sort, S.Stoyanov and D.Givord, Phys. Rev. Lett. Vol. 97, 157203(2006).

[80] J. P. Liu, Y. Liu, C. P. Luo, Z. S. Shan, and D. J. Sellmyer, J. Appl. Phys. Vol. 81, No. 8 (1997).

[81] M. Perzanowski, Y. Zabila, J. Morgiel, A. Polita, M. Krupinski, A. Dobrowolska and M. Marszałek. Acta Phys. Pol. A, Vol. 117, 423-426 (2010).

[82] D. H. Chen and S. H. Wu, Chem. Mater, Vol. 12, 1354 (2000).

[83] HongLing Liu, Peng Hou and JunHua Wu, J. Mater. Res. Vol. 26, 2040-2049 (2011).

[84] M. Yamaguchi, T. Kusakabe, K. Kyuno and S. Asano, Physica B, Vol. 270, 17-34, (1999).

[85] S. Lucatero, W. H. Fowle, and E. J. Podlaha, Electrochem. Solid-State Lett. Vol. 12, (12) D96-D100 (2009).

[86] Yoichi Kishi, ZenjiroYajimaTeiko Okazaki, YasubumiFuruya and Manfred Wuttig, Adv. Sci. Tech. Vol. 59, 24-29 (2008).

[87] C. Clavero, J. M. García-Martín, G. Armelles, and A. Cebollada, J. Appl. Phys. Vol. 99, 073903 (2006).

[88] Lisha Wang, Zhaohui Fan, Anup G. Roy, and David E. Laughlin, J. Appl. Phys. Vol. 95, No.11 (2004).

[89] Chuan-bing Rong, Vikas Nandwana, Narayan Poudyal, Girija S. Chaubey and J. Ping Liu. IEEE Trans. Nanotechnol. Vol. 8, NO. 4 (2009).

[90] Narayan Poudyal, Girija S. Chaubey, Chuan-bing Rong, and J. Ping Liua, J. Appl. Phys. Vol. 105, 07A749 (2009).

[91] M. Gheisari, M. Mozaffari, M. Acet and J. Amighian, J. Magn. Magn. Mater. Vol. 320, 2618– 2621(2008).

[92] J. Nogues, J. Sort, V. Langlais, V. Skumryev, S. Surinach, J. S. Munoz and M. D. Baro, Phys. Rep. Vol. 422, 65-117 (2005).

[93] W.H. Meiklejohn and C.P. Bean, Phys. Rev. Vol. 105, 904 (1957) and W.H. Meiklejohn and C.P. Bean, Phys. Rev. Vol. 102, 1413 (1956).

[94] Berkowitz AE and Takano K, J. Magn. Magn. Mater. Vol. 200, 552-570 (1999).

[95] G. Salazar-Alvarez, J. Sort, S. Surinach, M. D. Baro and J. Nogues, J. Am. Chem. Soc. Vol. 129, 9102-9108 (2007).

[96] D.W. Kavich, J.H.Dickerson, S.V.Mahajan, S.A.Hasan and J.H.Park, Phys. Rev. B, Vol. 78, 174414 (2008).

[97] P. Hajra, S. Basu, S. Dutta, P. Brahma and D.Chakravorty, J. Magn. Magn. Mater. Vol. 321, 2269-2275 (2009).

[98] Y. K. Tang, Y. Sun and Z. H. Heng, J. Appl. Phys. Vol. 100, 023914 (2006).

[99] S.A. Makhlouf, H.A. Attar and R.H. Kodama, Solid State Commun. Vol. 145, 1 (2008).

[100] N. Domingo, A.M. Testa, D. Fiorani, Ch. Binns, S. Baker and J. Tejada, J. Magn. Magn. Mater. Vol. 316, 155 (2007).

CHAPTER IV

ELECTRONIC CONDUCTION IN NANOCLUSTER ASSEMBLED Cu, Ag AND Au FILMS

4.1 Introduction

Cu, Ag and Au are indispensable in today's technologies and are essential in a variety of applications and industries. Copper is the third most important industrial metal which has huge role in the development of electrical and electronic applications. Excellent conductivity, ideal mechanical properties at low, ambient and elevated temperatures, hardness and tensile strength when alloyed with other metals all make it invaluable. Silver is used in printed circuits and other electronic applications and plays a prominent role from photovoltaic cells to high power explosives. Metallic silver is used as a catalyst for several oxidation reactions. Gold finds applications in the area of electronics, particularly in telecommunication and information technology. Gold bonding wires and gold plated contacts are used extensively within semiconductor packages. It has very good solder wetting properties and has excellent biocompatibility, malleability and resistance to corrosion. As gold is an inactive metal, it is even used for biomedical applications. A comparison of the physical properties of these metals in bulk form is given in the Table 4.1.

The nanoclusters of all the three metals find applications in microelectronics, sensors, catalysis, nonlinear optics and biomedicine. So an experimental investigation to find out the properties of assembled nanostructures of these metals is relevant in today's technology.

Table 4.1. Comparison of properties of Cu, Ag and Au

	Cu	Ag	Au
Atomic number	29	47	79
Lattice structure	fcc	fcc	fcc
Lattice constant	0.361 nm	0.408 nm	0.408 nm
Fermi energy	7.0 eV	5.49 eV	5.53 eV
Electrical Resistivity	1.683 μΩ-cm	1.62 μΩ-cm	2.44 μΩ-cm
Electron mean free path	39.22 nm	53.03 nm	34.57 nm
Temperature coefficient of resistance	0.00393 per °C	0.0038 per °C	0.0034 per °C
Thermal conductivity	0.923 cal/cm-s-K	0.974 cal/cm-s-K	0.7003 cal/cm-s-K
Melting point	1083°C	961°C	1063°C
Hardness	3 Moh	2.7 Moh	2.5 Moh
Young's modulus	16 x 10^6 psi	10.3 x 10^6 psi	11.3 x 10^6 psi

A proper understanding of the transport behavior is important, in order to take advantage of the unusual properties of Nano Cluster Assembled (NCA) structures in technological developments. A lot of material properties depend on a system's electron transport mechanism. In this chapter we describe a few metallic NCA structures realized in the form of films and investigate their electron transport properties. Metals such as Cu, Ag and Au were chosen for this study, as they are good examples of free electron metals.

All elements in nano-dimensions have increased reactivity due to their large surface to volume ratio. This increases the risk of oxidation of the prepared samples in nanophase, as was seen in the case of alloy clusters. It was to avoid the risk of oxidation of noble metals like Ag and Au besides Cu were chosen for this study. Their low reactivity, helps in reducing the oxidation of nanoclusters, post preparation, to some extent. The transport

behavior of these metals in their bulk form has been thoroughly understood, which helps in understanding the unique properties of their nanocluster counterparts.

4.2 Preparation of NCA films

The NCA structures of Cu, Ag and Au in the form of films were prepared using the Nanocluster Deposition System as described in detail in chapter 2. The details of the preparation conditions of all the three metal films are listed in the Table 4.2.

Table 4.2. Preparation conditions of NCA films.

Sample	Cu	Ag	Au
Argon gas flow	70 sccm	60 sccm	70 sccm
Aggregation Distance	140 mm	140 mm	155 mm
Base Pressure	2×10^{-8} mbar	8×10^{-7} mbar	2.8×10^{-8} mbar
Working pressure	2×10^{-5} mbar	2×10^{-5} mbar	2.7×10^{-5} mbar
Power	90 Watts	125 Watts	83 Watts
Duration of Deposition	1 hour	50 minutes	30 minutes
Substrate	Glass	Glass	Glass
Target thickness	5 mm	5 mm	3 mm

4.3 Initial Observations

The nanocluster assemblies of each metal exhibited their respective metallic luster, except the Cu films. The Cu films on exposure to the atmosphere instantly got oxidized. These films appeared black in color due to

the oxidation layer. The resistivity of Cu films at room temperature was found to be in the semi-conducting regime; around 1.152 x 10^3 Ω-cm, whereas for Ag and Au it was metallic. When taken out of the deposition chamber, Cu and Ag films were uniformly coated and fixed to the substrate, whereas the Au films crumbled in to small flakes with very little adhesion to the substrate.

4.4 Annealing of Nanocluster Assembled Films

Heat-treatments were carried out on NCA films specifically to study its effect on the morphology and on the transport properties of these systems. The as-prepared films were heat-treated in sealed glass tubes under argon atmosphere. For Cu films, the heat treatment resulted in the removal of the oxide layer and the films regained their metallic copper color. As expected the heat treatments caused enlargement of initial cluster sizes which were determined by the cluster deposition system parameters. This increase was proportional to the temperature as well as the duration of the heat treatments. The cluster size is known to have the strongest effect on the properties of NCA materials. The Cu and Ag NCA films were heat treated for various periods of time to investigate the transport properties that scale with the cluster size. The temperature and the duration of heat-treatments for Cu and Ag films are tabulated in Table 4.3 and Table 4.4 respectively.

Table 4.3. Heat treatments done on Cu NCA film

Temperature	Time
350^0C	5 min
350^0C	15 min
400^0C	1.5 hr
400^0C	6.5 hr

Table 4.4. Heat treatments done on Ag NCA film

Temperature	Time
100^0C	45 min
100^0C	1 hr
100^0C	3.5 hr
100^0C	6 hr
100^0C	12 hr

4.5 Measurements from X-ray diffraction patterns

X-ray diffraction patterns for NCA films were recorded. These diffraction patterns were used to characterize the crystallographic structure and to calculate the average cluster sizes. X-ray patterns of the as-sputtered and the heat-treated samples of Cu and Ag films after indexing are shown in the Fig. 4.1 and Fig. 4.2.

In the XRD patterns of all nanocluster assembled films the lines with mixed odd and even indices were absent which confirmed that the Bravais lattices of the specimens under consideration were face centered. Cu, Ag and Au have fcc structures in their bulk forms and no significant change in the structure is expected in their nanocluster counter parts unless the clusters are less than 2 nm [1]. The XRD pattern of as-sputtered Cu films, which appeared black in color, confirmed the presence of Cu_2O peak along with the fundamental (111) peak of Cu. This proved that the highly reactive Cu nanoclusters were oxidized, while being taken out of the ultra-high vacuum chamber. This phenomenon is quite common for the metallic films [2]. The presence of Cu_2O explains the high resistivity observed in the as deposited Cu

films. No oxide lines were present in the XRD patterns of the noble metal films.

4.5.1 Removal of the oxide layer in Cu films

The as-sputtered Cu films did not show metallic conduction as the highly reactive clusters have undergone oxidation which was confirmed by their X- ray diffraction patterns. In order to remove this oxide, copper films were heat treated under argon gas atmosphere at 350^0C (which is ~⅓ of the melting temperature of copper) for 5 minutes [2]. This process could remove the oxide that was present. The XRD pattern after heat treatment showed no oxide peak. Also the resistivity at room temperature of the heat-treated sample was found to reduce to 1.33×10^{-3} Ω-cm, and showed a metallic behavior over the temperature range of 300 K to 20 K. All the more after the heat-treatment the films regained their metallic copper color. This process of oxidation of clusters and its removal by heat treatment is consistent with previous reports.

An important thing that was noticed was the temperature at which the oxide could be removed. The melting point of copper is 1084.62^0C, but the oxide was removed, at a much lower temperature, i.e. at 350^0C. The reason could possibly be that the oxide Cu_2O might have formed only a layer around the surface with dangling bonds. This would be easily removed with a heat treatment at lower temperatures. Another possibility is the lowering of the melting point in NCA Cu films. The melting point of a material tends to decrease much lower than its bulk value, when the particle size is in nano range.

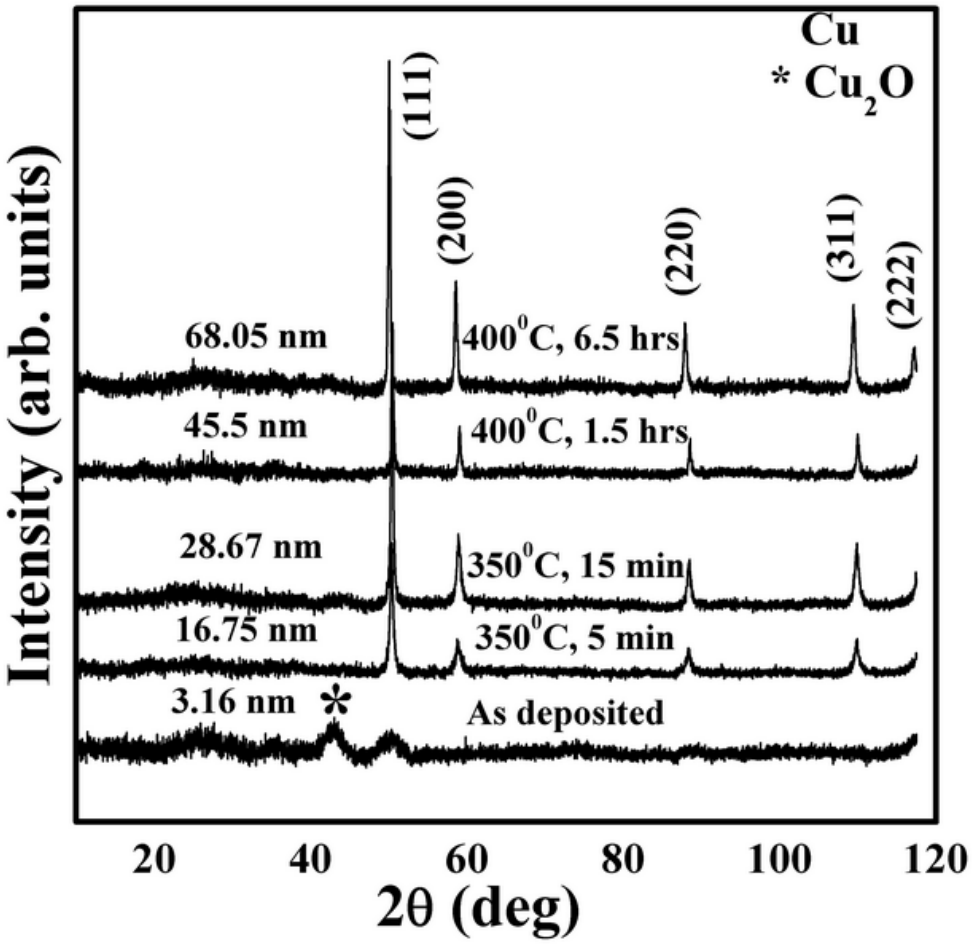

Fig. 4.1. XRD patterns of the NCA Cu films showing the increase in cluster size with various sintering temperatures and durations.

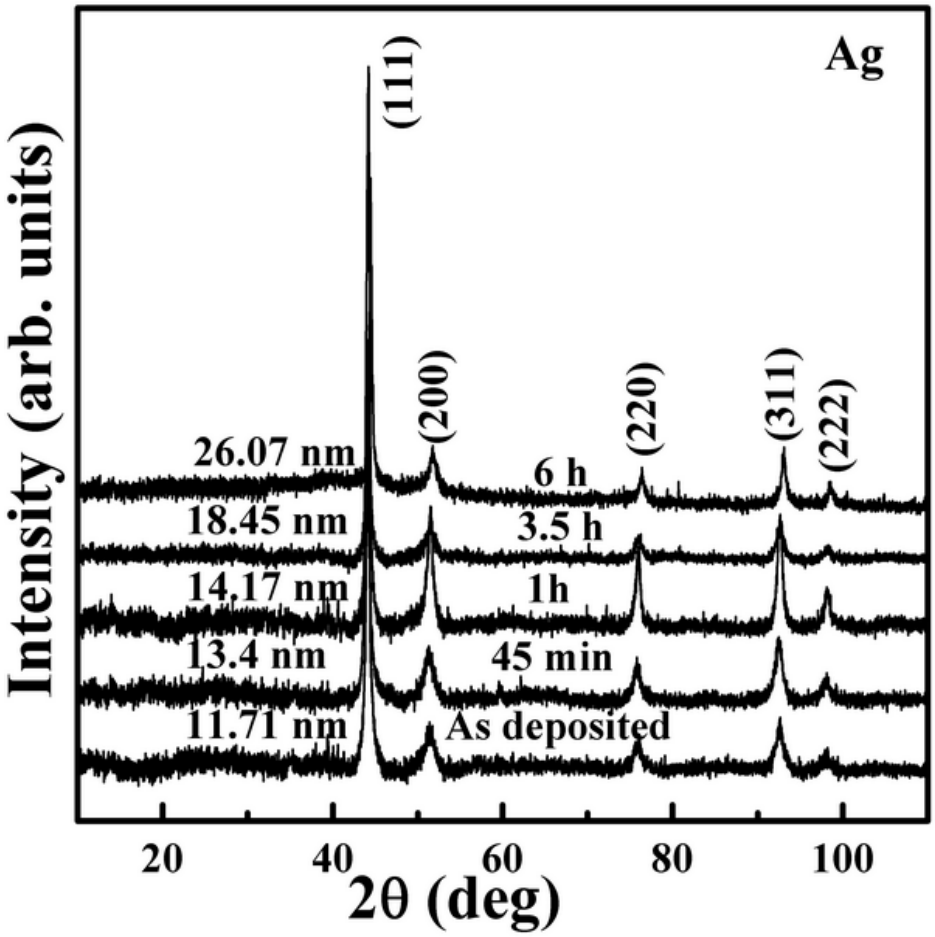

Fig. 4.2. XRD patterns of the NCA Ag films depicting the increase in cluster size with a sintering temperature of 100^0C, for durations from 45 min to 6 hr.

I. Reduction in the Melting Point in Nanostructures

In nanostructures the ratio of surface atoms to that of interior atoms is very high compared to the bulk. For instance a gold particle of 4 nm has almost 25% of its atoms on the surface and these surface atoms form a substantial part of the nanomaterials. The atoms at the surface have fewer neighbors than the interior atoms or in other words the surface atoms are poorly coordinated. In small clusters there is only limited interaction between

the surface and the interior atoms resulting in a reduced surface energy. This results in a lower melting temperature of the surface layers. Thus in nanomaterials the presence of large number of surface atoms result in a drastic decrease in the melting temperature. This reduction is reported in literature for various materials. The melting point of 2.5 nm particles of CdS is found to be around 673 K which is ~⅓ of its bulk melting temperature (1873 K) [3].The melting point of 2.5 nm gold particles is reported to be about 930 K, which is much lower than its bulk value (1336 K) [4].Thus reduced cluster size in Cu NCA films might have resulted in the reduction of the melting temperature of the surface layers, which made the oxide removal possible. This also gives us an indication that the as-sputtered copper clusters are only of a few nanometers in size as was observed from X-ray diffraction data which is reported below.

4.5.2 Variation of Cluster Sizes with Annealing Temperature and Time Duration as Observed from XRD

In all XRD patterns except the as-sputtered Cu, only pure metal diffraction lines are present without any oxide phase. The cluster growth at every stage of heat treatment is evident from the continuous decrease in the line width of the fundamental lines (Fig. 4.1 and Fig. 4.2). The corresponding cluster size after the heat treatments is indicated in Tables 4.5 and 4.6. The cluster sizes fall in the range of 3-70 nm. Because of the poor adhesion on the substrates these measurements could not be carried out on Au films.

The patterns of as-sputtered Cu and Ag films showed very broad peaks which indicated very small cluster sizes. The average cluster size determined from the broad peak of as-sputtered Cu was 3.2 ± 0.1 nm and the as-sputtered Ag was 11.7 ± 0.2 nm. Heat-treated samples of both Cu and Ag films showed a

decrease in the line width with increasing temperature and duration of heat-treatment. This reduction in line width, of course, occurred due to an increase in the cluster size. The Cluster sizes from XRD patterns were estimated using the Scherrer formula and so it does not provide any information on the distribution of cluster sizes in the sample.

When transitions occur from bulk to nano phase, sometimes there will be slight changes in inter atomic distances and crystal lattice constants [5-9]. There are reports on the size dependence of the lattice constant of Cu clusters when the diameter is below 5 nm [10]. The size dependence of lattice constant of Ag particles around 3 nm is also reported in literature [11]. The nanocluster assembled Ag film after a 6 hour heat treatment at 100^0C, was observed to possess a lattice constant equal to that of the bulk material. For other cluster sizes, there were slight changes in the lattice constant. The data however do not suggest any systematic variation of the lattice constant on the cluster size.

Table 4.5. Cluster size and lattice constant calculated from XRD for Cu films.

Heat Treatment	Cluster Size (nm)	Lattice constant (A^0)
As-sputtered	3.2 ± 0.1	3.61 ± 0.007
350^0C, 5 min	16.8 ± 0.2	3.64 ± 0.0081
350^0C, 15 min	28.8 ± 0.7	3.64 ± 0.0046
400^0C, 1.5 hr	45.5 ± 2.3	3.63 ± 0.0054
400^0C, 6.5 hr	68.1 ± 2.5	3.66 ± 0.0035

Table 4.6. Cluster size and lattice constant calculated from XRD for Ag films.

Heat Treatment	Cluster Size (nm)	Lattice constant (A^0)
As-sputtered	11.7 ± 0.2	4.12 ± 0.0122
100^0C, 45 min	13.4 ± 0.2	4.13 ± 0.0097
100^0C, 1 hr	14.2 ± 0.20	4.12 ± 0.0122
100^0C, 1.5 hr	18.5 ± 0.2	4.12 ± 0.007
100^0C, 6 hr	26.1 ± 0.7	4.09 ± 0.012

4.6 Microstructural characterization.

The microstructures of the nano-cluster assembled films were investigated using SEM, AFM and TEM.

4.6.1 Scanning Electron Microscopy

Fig. 4.3 shows the FESEM images of the as-sputtered Cu films. The image displays a narrow distribution of the cluster size. The size of the individual clusters is found to be in the range 2.5 to 6.8 nm. The distribution of cluster size shown in the histogram in Fig. 4.4 is slightly asymmetric towards the larger cluster sizes and can be described by the lognormal distribution function [12]. The mean cluster size obtained from the curve fit is around 4.2 ± 0.2 nm for the as-sputtered Cu nanocluster assembled films. The XRD pattern revealed a cluster size of 3.2 ± 0.1 nm for this specimen. The individual clusters are found to agglomerate together in small numbers in this image. These agglomerates are loosely bound to each other giving rise to a porous structure to the system.

The SEM pictures of Ag films in Fig. 4.5 clearly show the individual spherical clusters formed with distinct boundaries. The Ag clusters also follow the lognormal distribution shown in Fig. 4.6 and the mean value for the cluster size from the curve fit is found to be 14.5 ± 0.4 nm. The cluster size, which was calculated from the XRD pattern for the same sample, was 11.7 ± 0.2 nm. The clusters were connected to each other just enough, to make the film continuous. Few agglomerates of 2 to 3 atomic clusters can be seen in the picture. The porous structure of these films is also evident from these images. Structural features such as pores and other crystal lattice defects do play an important role in the properties of materials.

From the SEM picture of Au nanocluster assembled films in Fig. 4.7 it could be observed that, Au clusters in the as-sputtered films are under 10 nm in size. The size distribution was lognormal and the average size obtained from the curve fit shown in Fig. 4.8 was 9.3 ± 0.2 nm. It is reported that for nano particles below 10 nm, a strong decrease in melting temperature, caused by size effect is observed [13-15]. Therefore the peeling off, of Au films from the substrate as mentioned earlier can also happen due to a lowering of melting temperature of Au clusters. The gold nanoparticles did not show any change in color indicating that the sample is free of oxides. This was confirmed by the resistivity data, which showed a metallic behavior.

The SEM data revealed that all the three systems showed lognormal behavior in the distribution of cluster sizes. In vapor-phase synthesis, always coalescence forms the dominant mechanism in the formation of nanoclusters. During nanocluster deposition, metal atoms lose their kinetic energy, after colliding with each other and with gas atoms. These atoms come together following nucleation and the growth happens through coalescence.

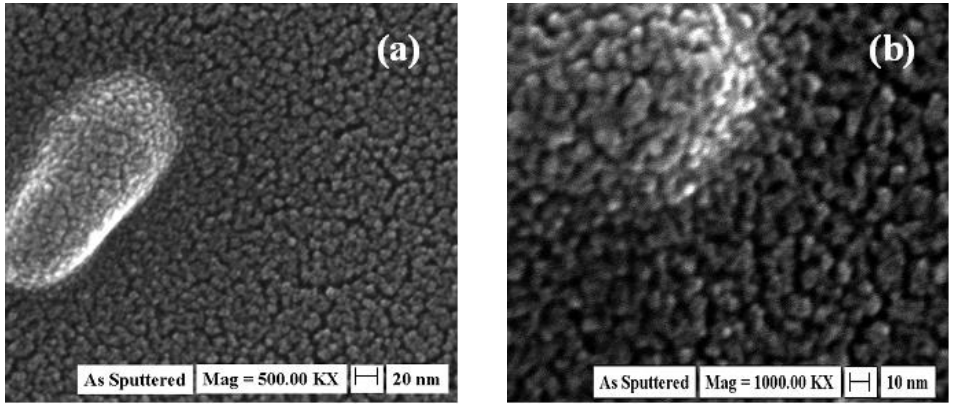

Fig. 4.3. FESEM images obtained for the as-sputtered copper clusters. (a) At a magnification of 500 KX. (b) At a magnification of 1000 KX.

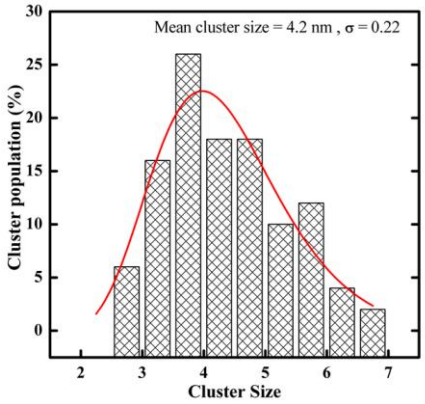

Fig. 4.4. Cluster size distribution for the as-sputtered Cu clusters. The curve fit represents a lognormal distribution. σ is the standard deviation of the distribution of the logarithm of size.

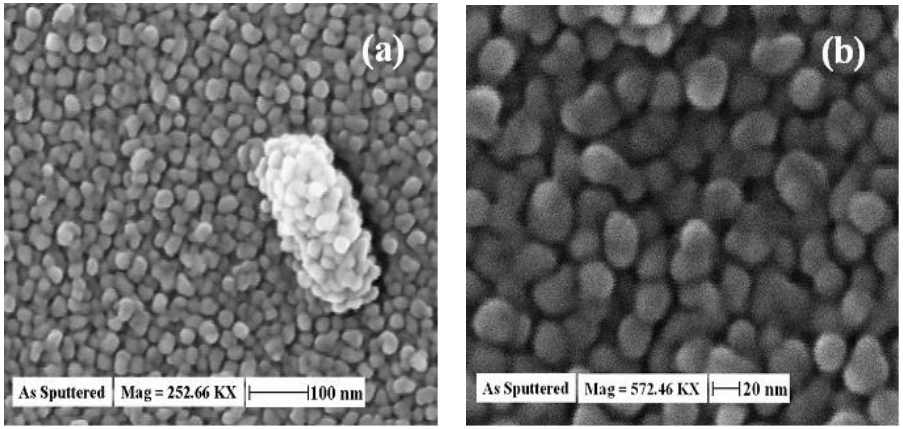

Fig. 4.5. SEM images of as-sputtered Ag clusters. (a) At a magnification of 252 KX. (b) At a magnification of 572 KX

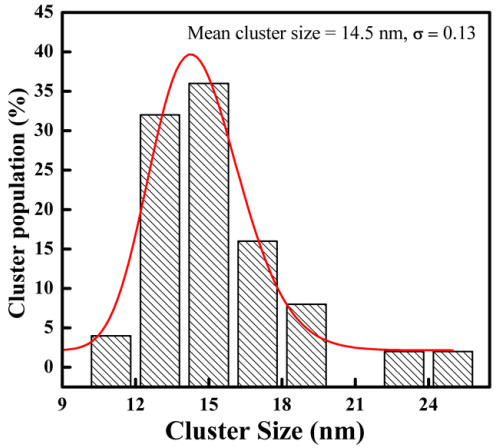

Fig. 4.6. Cluster size distribution for as-sputtered Ag clusters from SEM data. The curve represents a lognormal distribution. σ is the standard deviation of the distribution of the logarithm of size.

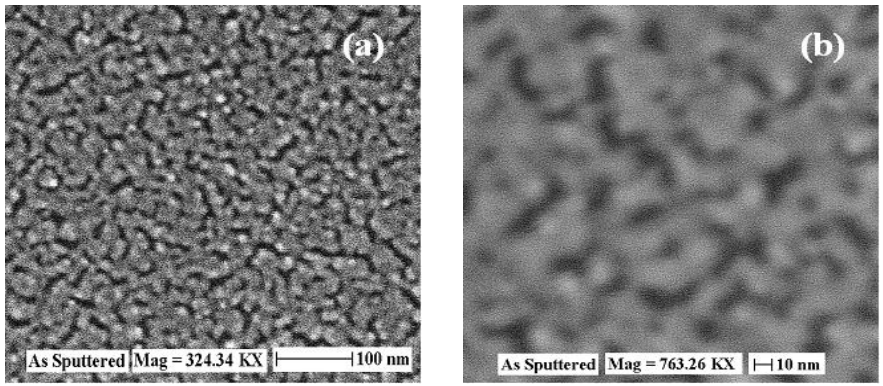

Fig. 4.7. SEM images of as-sputtered Au clusters. (a) At a magnification of 324 KX. (b) At a magnification of 763 KX.

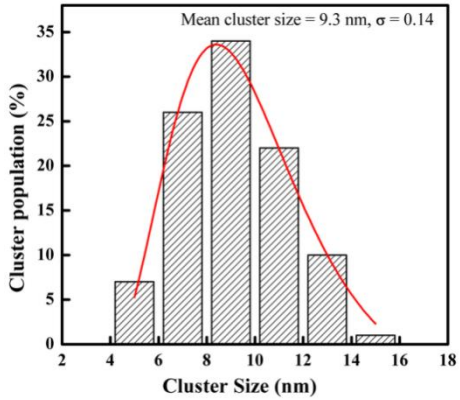

Fig. 4.8. Cluster size distribution for as-sputtered Au clusters from SEM data. The curve represents a lognormal distribution. σ is the standard deviation of the distribution of the logarithm of size.

Coalescence always leads to a lognormal distribution of the particles, which has been explained by Granqvist and Burhman [16]. This was found true for all the three nanocluster-assembled systems.

4.6.2 Transmission Electron Microscopy

The TEM images obtained for the as-sputtered Cu films are shown in the Fig. 4.9. The presence of Cu_2O in the electron diffraction data of as-sputtered Cu films confirms the oxidation as can be seen from Fig. 4.9 (b). The cluster size measured from the TEM data was around 4.7 ± 0.2 nm. This was in agreement with the size obtained from XRD and the FESEM.

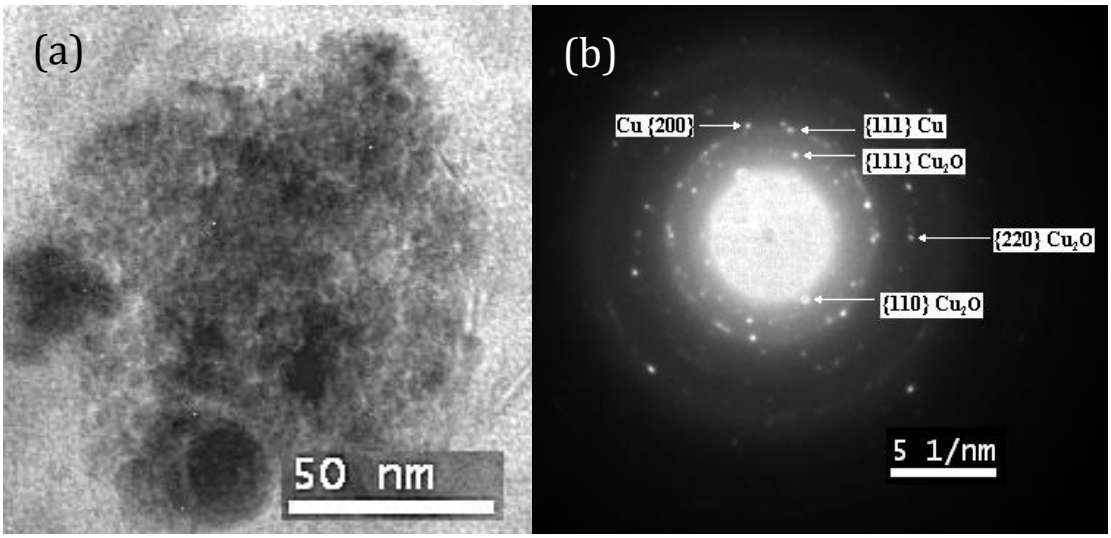

Fig. 4.9. (a) TEM image of as-sputtered NCA Copper films. **b)** Electron diffraction of 4.7 ± 0.2 nm Cu nanoclusters showing {111} and {200} lines of Cu and {111}, {220} and {110} lines of Cu_2O.

4.6.3 Atomic Force Microscopy

I. Cu NCA system

The AFM picture of the as-sputtered Cu film in Fig. 4.10 recorded at a lower resolution exhibit particles in the range of 130 to 300 nm. They were

spherical in shape with a size distribution. The average size of these particles was found to be 192.6 ± 4.2 nm. This was much larger than the average cluster size obtained from FESEM, XRD and TEM data, which was around 3-4 nm.

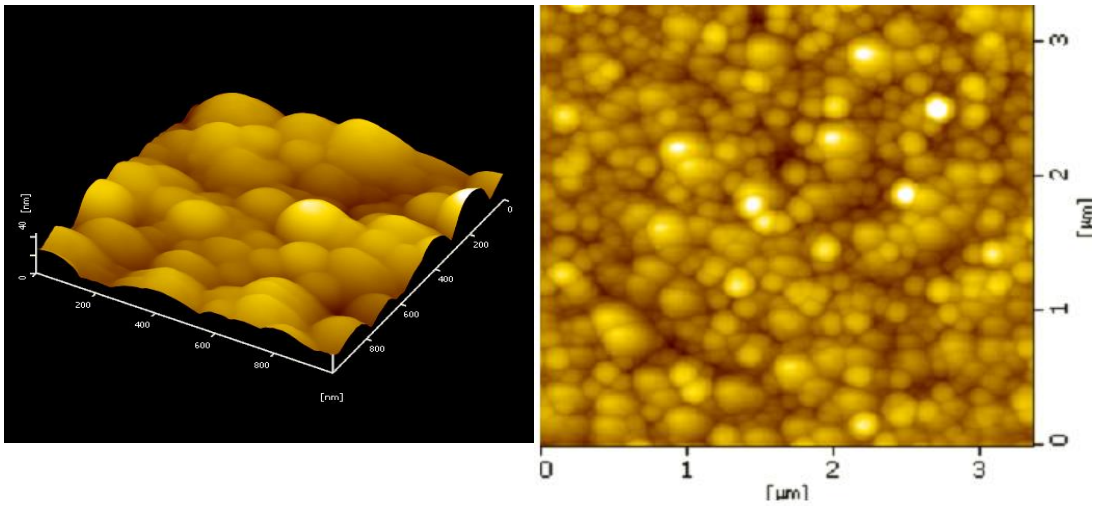

Fig. 4.10. AFM pictures of as-sputtered nano-cluster assembled Copper films.

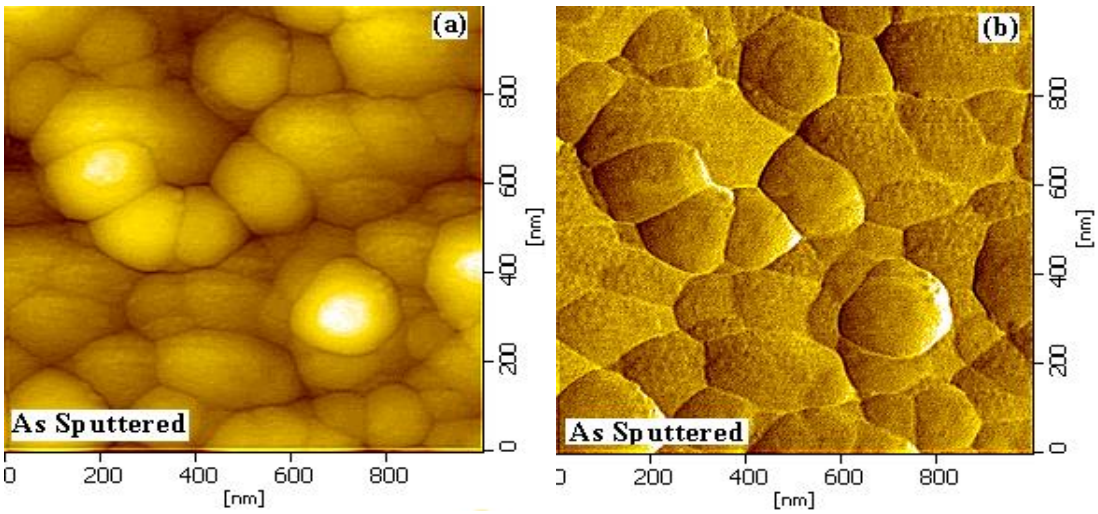

Fig. 4.11. AFM pictures of as-sputtered nano-cluster assembled Copper films in higher resolution. (a) Image showing small atomic clusters as mosaic like pattern. (b) AFM images taken with frictional force scan.

The AFM images in Fig. 4.11with higher resolution revealed along with big particles, the real atomic clusters of 3-4 nm. This looked as a mosaic like

pattern on the surface of the big particles. Mosaic like chips that were seen on the surface of these big particles were actually the atomic clusters that were formed in the aggregation chamber during deposition. Over all it gave the impression that the atomic clusters are packed in sacs of 200 nm size and several such sacs are put together. This helped us to confirm that, the big particles were not individual atomic clusters but cluster agglomerates. After deposition the atomic clusters combined together to form the big agglomerates retaining their cluster boundaries. The AFM was unable to reveal the individual clusters at first clearly because of its poor resolution.

I. (a). Why Do Atomic Clusters Form Agglomerates?

Materials in the nanophase have large surface to volume ratio. In every system the tendency is always to minimize the total surface or interfacial energy. So the atomic clusters often form agglomerates as a result of attractive vander Waals forces. It has been reported that at low temperatures, after the formation of atomic clusters, loose cluster agglomerates with quite open structures are formed [17]. This happens when the coalescence is negligibly slow. Agglomeration of these clusters may occur during synthesis or subsequent processing. All NCA samples were deposited at room temperature and so the possibility of agglomeration of clusters is very much present and also in our case it happened during synthesis itself.

The AFM images of heat-treated nano cluster films (Fig. 4.12) did not show the presence of any cluster agglomerates. Measuring the size of the particles and comparing them with size obtained from XRD revealed that only atomic clusters were present in these heat-treated samples.

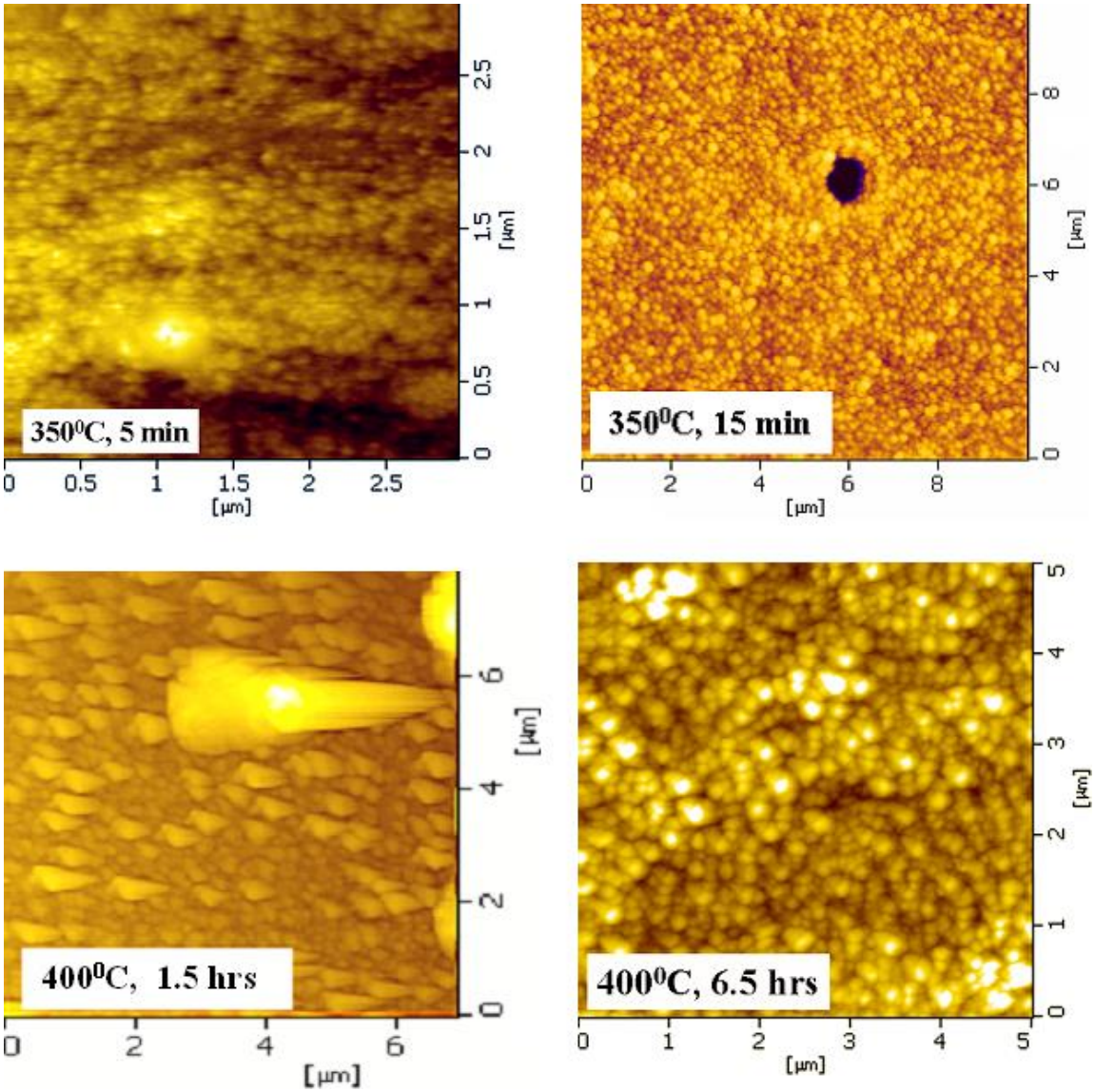

Fig. 4.12. The AFM Images of heat-treated NCA Copper films.

As-sputtered Cu films clearly showed the presence of cluster agglomerates around 200 nm, whereas in all the Cu samples after heat-treatment, they disappeared. Also the XRD pattern of as-sputtered Cu films showed the presence of Cu_2O whereas in films after heat-treatment, there was no

presence of any oxide. This suggested the possibility of the oxide forming a shell around the clusters holding them together as agglomerates in the as-sputtered films as was the case in the alloy films in chapter 3. Once the oxide was removed with the heat treatment, the agglomerates disintegrated in to individual atomic clusters. The heat treatment at 350^0C for 5 min removed the oxide layer but also resulted in an increase in the size of atomic Cu clusters. At 350^0C, 5 min heat-treatment the clusters in the Fig. 4.12 (a) seem to be more or less identical in size, with a very narrow size distribution. The oxide layer forming big agglomerates disappeared and the clusters got dispersed. The remaining energy has been spent on increasing the cluster size. It can be seen from Fig. 4.12 (b) that with the heat treatment at 350^0C, 15 min the size has increased uniformly. But Fig. 4.12 (c) and (d) makes it clear that, with increasing temperature and duration of heat treatment the size distribution widens. Small clusters fuse together and the grain boundaries between them disappear forming bigger spherical clusters. The average sizes obtained for Cu films heat-treated for350^0C-5 min, 350^0C-15 min, 400^0C-1.5 hr and 400^0C-6.5 hr were respectively 20 nm, 31 nm, 56 nm and 80.7 nm. These values were in agreement with the values calculated from the XRD pattern.

I. (b). Cluster growth in Cu films heat-treated at temperatures below 350^0C (⅓ of the melting temperature).

For Cu films with a heat treatment of 350^0C, for 5 min the atomic clusters got dispersed from the cluster agglomerates and started increasing in size. Since cluster boundaries are regions of high energy, reduction in boundary area reduces the energy of a system and the cluster growth happens by the movement of these boundaries. At heat treatments above 350^0C the atomic clusters fused together, forming bigger spherical clusters. But the

picture of cluster growth is entirely different for heat treatments at lower temperatures for longer durations.

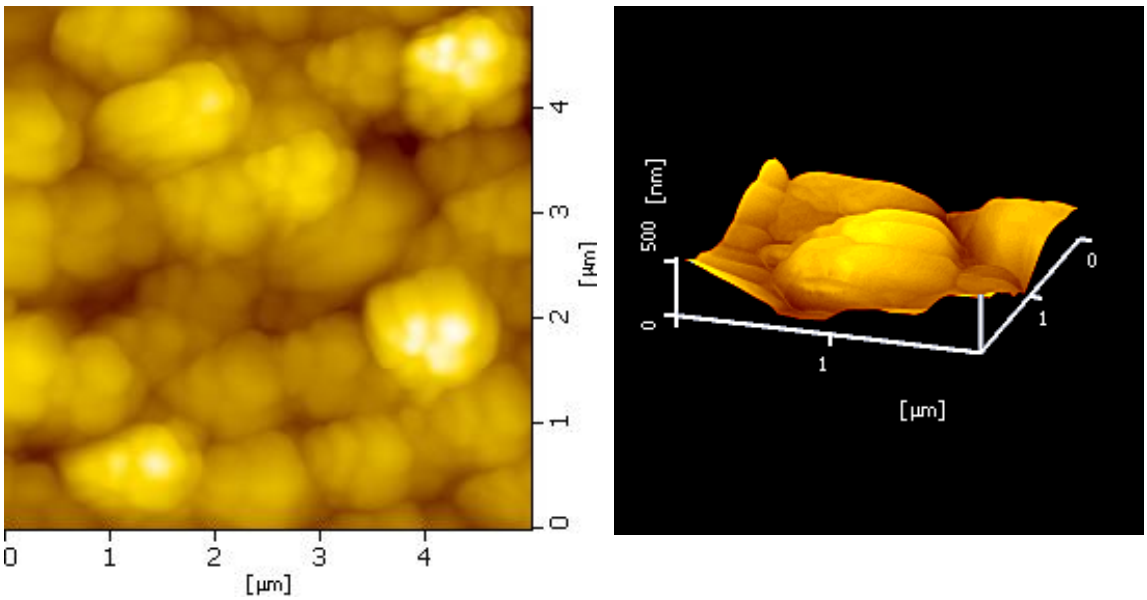

Fig. 4.13. The AFM Images of Cu films heat treated at 300^{0}C for 3 hr.

As-sputtered Cu clusters were heat-treated 300^{0}C for 3 hr, 6.5 hr, 10.5 hr and 200^{0}C for 20.5 hr. At these lower temperatures there was no disintegration of cluster agglomerates into individual clusters. The AFM pictures revealed groups of 8-9 agglomerates sticking together and growing in a cylindrical fashion. At 300^{0}C, 3 hr heat treatment (Fig. 4.13) the cluster agglomerates increased in size up to 450 nm resulting in a cylindrical shape. At 300 ^{0}C, 6.5 hr (Fig. 4. 14 (a)) the size increased to 1800 nm. With increasing durations of heat-treatment i.e. at 300^{0}C, 10.5 hr (Fig. 4.14 (b)) the agglomerates fused together to form individual cylindrical columns with an average size of 2500 nm. At 200^{0}C, 20.5 hr (Fig. 4.14 (c)) the cylindrical agglomerates were only of an average size of 650 nm.

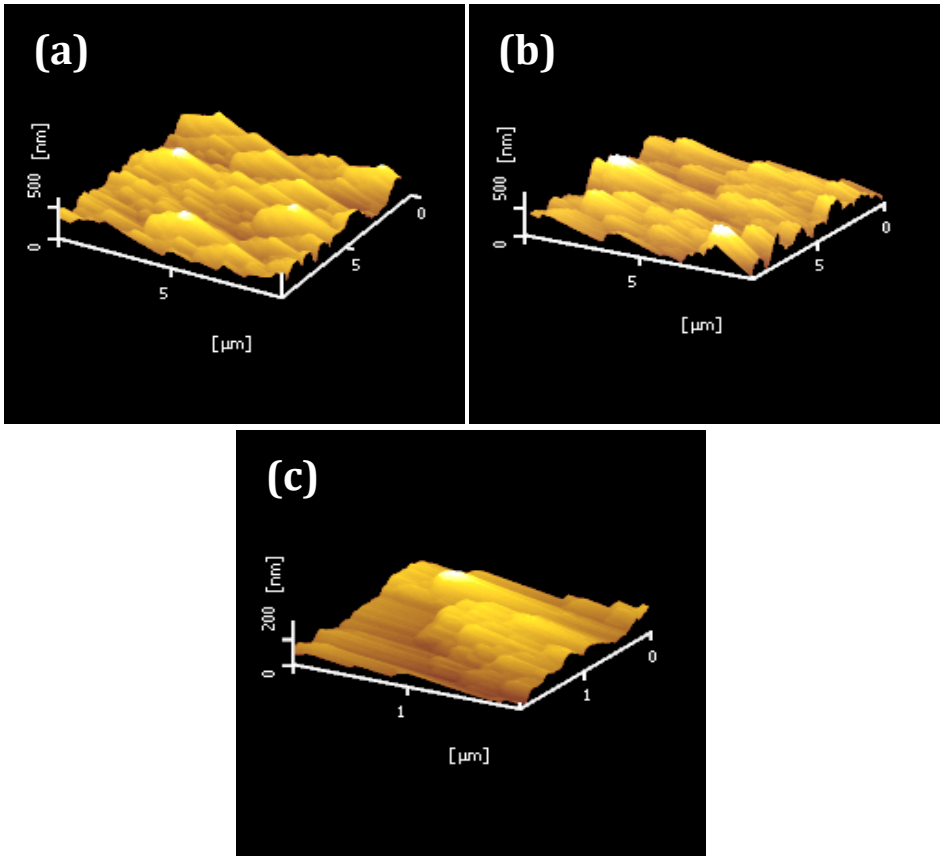

Fig. 4.14. The AFM Images of heat-treated NCA Cu films. (a) 300^0C for 6.5 hr. (b) 300^0C for 10.5 hr. (a) 200^0C for 20.5 hr.

II. Ag NCA System

The AFM picture of the as-sputtered Ag films, in Fig. 4.15 also exhibited big particles in the range of 20 to 60 nm. The average size of these agglomerates was found to be 27.3 ± 0.7 nm, and again this was larger than the average cluster size obtained from SEM and XRD data, around14.5 ± 0.4 nm and 11.7 ± 0.2 nm respectively. These are possibly agglomerates of 2-3 atomic clusters. These agglomerates also exhibited a lognormal size distribution.

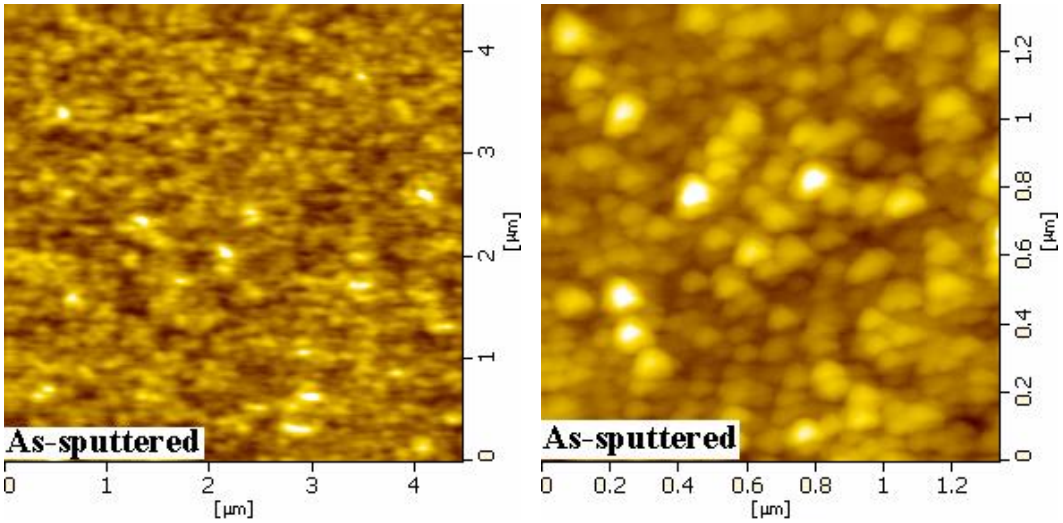

Fig. 4.15. AFM pictures of as-sputtered nano-cluster assembled Ag films.

4.7 Resistivity Measurements on NCA films

The resistivity measurements of NCA films were carried out in the temperature range of 23–300 K. In the case of as-sputtered Cu, the resistivity value, at room temperature fell in the semiconducting regime due to the presence of oxide layer as discussed previously. So the Cu films were heat-treated and the oxide layer was removed before measuring the resistivity versus temperature behavior. After heat treatment the Cu samples showed a much lower resistivity than in the as-sputtered state and displayed a metallic behavior with temperature, confirming the removal of oxide. So, for Cu, the resistivity data discussed in the following sections refer to the samples from where the oxide layer was removed. The resistivity of these films were found to increases with temperature in the entire temperature range. The temperature dependence was non-linear, with the resistivity curves showing a metallic behavior with a positive temperature coefficient ($d\rho/dT > 0$) of resistance. The measured resistivity at 273 K are given in Table 4.7 together

with the cluster size. The absolute values of resistivity of NCA films are found to be a few orders higher compared to bulk coarse-grained resistivity.

Table 4.7. The resistivity values of NCA systems at 273 K.

NCA Films	Cluster Size (nm)	ρ at 273 K (Ω-cm)	% of increase in ρ at 273 K (ratio with bulk value)
Au (As-sputtered)	9.3 ± 0.2	2.64×10^{-5}	1301
Ag (As-sputtered)	11.7 ± 0.2	1.58×10^{-5}	1077
Cu (350^0C, 5 min)	16.8 ± 0.2	2.09×10^{-3}	13562

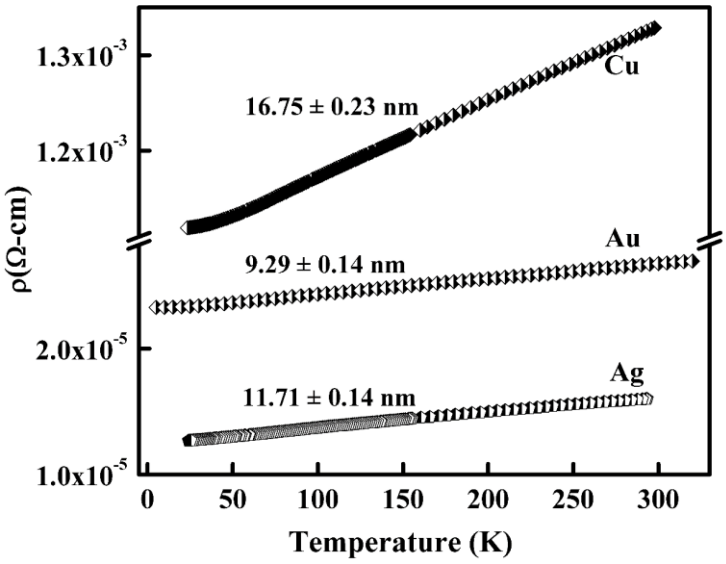

Fig. 4.16. Comparison of resistivity of nano-cluster assembled Cu, Ag and Au films.

The temperature dependence of Cu, Ag and Au NCA films are displayed in Fig. 4.16. With the cluster size around 16.8 ± 0.2 nm, the resistivity of copper was found to be around 3 orders of magnitude higher than the bulk

resistivity at roomtemperature and around 6 orders higher at low temperatures (25 K). For both Au and Ag films with a cluster size around 9.3 ± 0.2 nm and 11.7 ± 0.2 nm, the room temperature resistivity was only one order of magnitude higher while resistivity around 25 K was around 3 orders of magnitude higher compared to the corresponding bulk coarse-grained values.

Resistivity in metals is attributed to the scattering of conduction electrons, which takes place by two mechanisms. The scattering that happens due to the lattice imperfections, which is temperature independent, and the scattering due to the lattice vibrations or phonons, which is temperature dependent. Since the two mechanisms are independent of each other the Matthiessen's rule tells that they are additive. In this work on NCA films, we try to understand how the reduced dimensions affect the temperature dependent as well as the temperature independent part of the resistivity.

4.7.1 Resistivity due to Phonons

The phonons play a determinant role in the electrical properties of a material as they form a very important source of scattering, in electron transport, inside a crystal lattice. When electrons are scattered by the lattice, the interaction ends up creating or destroying phonons. In the case of NCA films within the temperature range in which the resistivity measurements were conducted, only the acoustic phonons need to be considered. The range of optical phonon energies are quite large (~30-60 meV) i.e. around 350 K to 700 K and at the low temperatures where we have conducted the experiments, optical phonon number is negligible. Inorder to understand the temperature dependent part of resistivity, the ratio of total resistivity to the residual resistivity (ρ/ρ_0) has been taken. The ρ_0 is approximated as the

resistivity at 23 K. Thus in the ratio ρ/ρ_0 the effect of intrinsic resistivity has been removed. The slope of these curves tells us the rate at which phonons are created in the crystal lattice of NCA films. The increase in resistivity with temperature now is only the effect of phonons. It is worthwhile to note that the absolute values of the resistivity of the NCA films are rather large, but the ratio of total to residual resistivity is relatively low. It can be seen from Fig. 4.17 that the rate of increase of resistivity with temperature due to phonons is much higher in Ag NCA films than in Cu films or in the case of Au films.

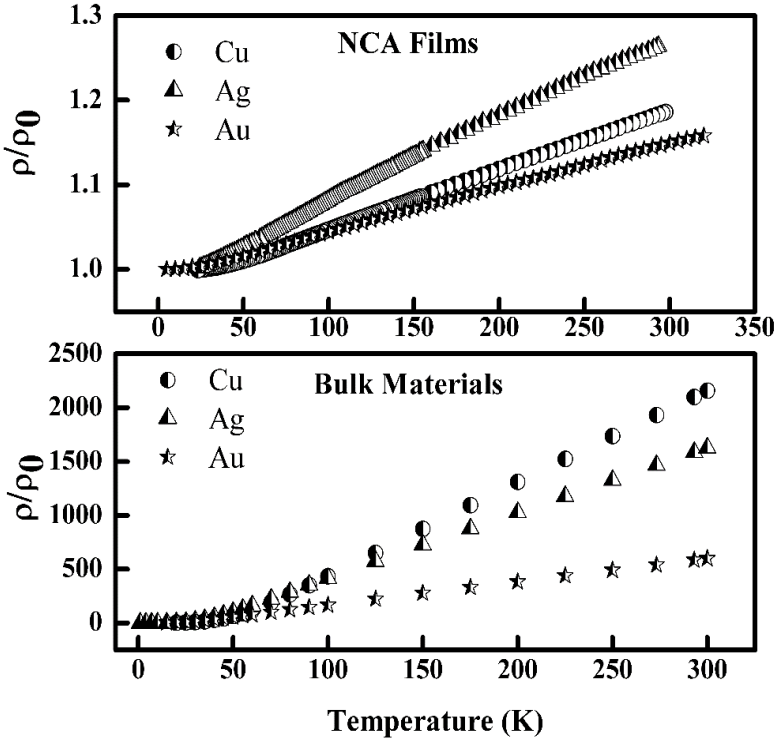

Fig. 4.17. Comparison of temperature dependent part of the resistivity of NCA films of Cu, Ag and Au.

The slopes of the curves tell us that the rate of increase of phonon resistivity is much less in the case of NCA films when compared with the bulk. The ratio ρ/ρ_0 makes it clear that in NCA films intrinsic part rather than that from phonons forms a major fraction of the resistivity. The rate of phonon

admittance into the crystal given by the slope of the curve is shown in the Table 4.8 below.

Table 4.8. The rate of admittance of phonons into the crystal lattice of NCA films with temperature.

System	Slopes of the curves ρ/ρ_0 vs. T	
	Bulk	**NCA Film**
Cu	8.63 ± 0.02	$7.07\times10^{-4} \pm 9.\times10^{-7}$
Ag	6.06 ± 0.02	$9.71\times10^{-4} \pm 4.5\times10^{-6}$
Au	2.16 ± 0.004	$5.22\times10^{-4} \pm 1.4\times10^{-6}$

4.7.2 Resistivity due to Cluster Boundaries.

In the case of films, the film thickness, grain boundaries and other defects all contribute towards its resistivity. Since the thicknesses of the NCA films were much higher than their respective electron mean free paths, the electrons are not limited by the film thickness. Thus the film thickness doesn't have a contribution towards the resistivity of the NCA films. The high resistivity of NCA films at lower temperature regions, where the temperature dependent phonon contribution ceases, clearly indicates that predominant contribution to the resistivity arises from the residual resistivity coming from the electron scattering at the defects or grain/cluster boundaries.

For the bulk materials below 50 K the resistivity falls down by many orders rapidly. In the temperature range where T/Θ_D is less than 1, usually only long wavelength phonons are exited, as there is energy available only for them. Due to the limited phonon spectrum available, in pure bulk materials

with minimal defects and with micro sized grains, at temperatures below 50 K there is hardly anything that results in the scattering of electrons. In the case of NCA films, no such rapid falling off of the resistivity is observed. The resistively almost remains the same order of magnitude, in the range of 20 K to 300 K. This gives us clear indication that electron scattering is due to cluster boundaries or defects. Plasma assisted deposition is known to avoid impurity, so defects due to impurity can be ruled out. But when a grain boundary is encountered in a polycrystalline material, electron propagation is interrupted. Grain boundaries have long been known to affect the electrical properties of metals [18]. But in bulk polycrystalline metals with micro size grains, the volume fraction of grain boundaries is relatively small and therefore their effect is only significant at low temperatures [19-22]. At smaller grain sizes the volume fraction of the interfaces becomes comparable to the volume fraction of the crystalline regions. Such materials are characterized by a large number of interfaces in which the atomic arrangements are different from those of the crystal lattice [23]. When the grain size is reduced to less than 10 nm almost 50% of the atoms reside in the grain boundary area whereas it is 1-3% when the grain size is around 100 nm [24, 25]. Therefore at reduced grain sizes a significant volume fraction of atoms reside at the grain boundaries and the mean free path is limited mainly by these boundaries in the sample.

Thus nanostructures are found to have remarkable influence on the electrical resistivity of a system due to their finite size effect and large fraction of grain boundaries in them. Usually in bulk materials the grain boundary effect is considered to be important for electrical conductivity only at low temperatures where the probability of electron-phonon scattering decreases. But in nano-materials the contribution of grain boundary scattering to

electrical conductivity is relatively more important throughout all temperature ranges, since it forms a major portion of the total resistivity. AFM, TEM, SEM and XRD measurements indicate that the Cu, Ag and Au NCA films have nano-grain structures with mean grain sizes of about 16.8 ± 0.2, 11.7 ± 0.2 and 9.3 ± 0.2 nm respectively.

These NCA films can be regarded as crystalline regions of nanometer-size surrounded by regions of cluster boundaries. A decrease of the cluster size of the NCA films leads to the enhancement of the cluster boundary volume. The cluster boundaries with a higher degree of discontinuity, will block the carrier transition, which will result in an increase of the resistivity. Thicker the cluster boundary, more the atoms in the material that are in a state of disorder. Thus nano-clustered material has a higher electrical resistivity due to the high ratio of the cluster-boundary volume to the crystalline volume. The effect of finite size on resistivity has been reported in many studies of nanocrystalline metals such as Ni [26], Cu, Fe [24]) and noble metals such as Pt [27,28], Au, Pd [24]. This phenomena is also observed in a few nanocrystalline alloys [29–32].

The electron mean-free paths of Cu, Ag and Au are respectively, 39.2 nm, 53.03 nm and 34.6 nm at room temperature. In the literature for nano-crystalline Ag with grain sizes 38.5 nm and 25 nm, the electron mean free path at room temperature was evaluated using the model of grain boundary reflection, and found to be 44 and 33 nm respectively [17]. Not all grain boundaries affect resistivity in the same way. In zone-refined Aluminum, considerable differences were observed in the electrical resistivity for structurally different grain boundaries [33]. Since atomic clusters are formed on its way to the substrate, they do have well defined boundaries, which are structurally different from the grain boundaries in nanocrystalline materials.

So the electrons will be strongly deflected from the cluster boundaries than the grain boundaries in nanocrystalline materials. The cluster sizes in all the systems under consideration vary between 10 nm to 70 nm. In all these samples the cluster size is comparable with the electron mean free path of the bulk. Thus the transport phenomena in these systems are strongly influenced by the electron scattering on the grain boundaries in agreement with the Mayadas-Shatzkes model [34]. This very well explains the increase in the residual resistivity of these systems.

Thus the temperature independent part of the resistivity, which constitutes 79% of the total resistivity at 300 K for Ag, 84% for Cu and 87% for Au, results mainly from the cluster-boundary scattering of the electrons in the nanocluster systems.

4.7.3 The Temperature Dependence of Resistivity in NCA films

The scattering of electrons caused by the thermal vibrations or phonons at finite temperatures form the main source of resistivity in metals. The temperature dependent electrical resistivity of non-magnetic metallic crystalline solids is given by the Bloch-Grüneisen equation [35-37]. This is an approximate solution of the Bloch-Boltzmann equation with the additional approximation of a Debye phonon spectrum. It is based on a spherical free electron band structure and a spherical Debye phonon spectrum of a single longitudinal branch.

Bloch Grüneisen formula in its general form is suitable when the temperature range is around or within Θ_D (Debye temperature) values of the system. The Θ_D values of Cu, Ag and Au are 343 K, 225 K and 170 K respectively and the resistivity experiments were done in the temperature

range of 23 K to 300 K which covers a range from low to temperatures above Θ_D. So a modification of the Bloch Grüneisen form, which works for the representation of resistivity at low as well as high temperatures as given by Matula [35] is used to fit the resistivity curves of Cu, Ag and Au NCA films:

$$\rho(T) = \rho_0 + A\left[1 + \left(\frac{B}{x}\right) + (Dx^p)\right]\left[\frac{4}{x^5}\int_0^x \frac{z^5 e^z}{(e^z-1)2}dz\right] \qquad (1)$$

where x = (Θ_D - CT) / T, Θ_D is the Debye temperature, 'C' is the constant related to the anharmonicity of the system, ρ_0 is the residual resistivity arising predominantly due to grain boundary scattering, 'A' is a constatnt of the metallic system consisting of Debye radius, Fermi velocity etc, 'B' is the constant related to electron coupling to the lattice anharmonic vibrations and thermal expansion, 'D' and 'p' are the constants related to e^- - e^- interaction at low temperatures giving rise to a temperature variation of resistivity following a $T^{(5-p)}$ law instead of T^5 Bloch-Grüneisen law.

It is the Debye temperature that sets the boundary between high temperature and low temperature behavior in electron phonon scattering. At high temperatures the resistivity of a metal ρ is proportional to temperature T. At Debye temperature Θ_D, all phonon modes are excited. Above Θ_D the phonon population in any given mode is proportional to T, hence the number of scatterers and the resistivity are proportional to T [38]. Below the Debye temperature, the phonon modes begin to "freeze out," and the resistivity of the metal drops down rapidly. The resistivity is expected to drop as $\rho(T) \sim T^5$ which is the Bloch Grüneisen regime [37, 39]. Both these cases are represented in Fig. 4.18.

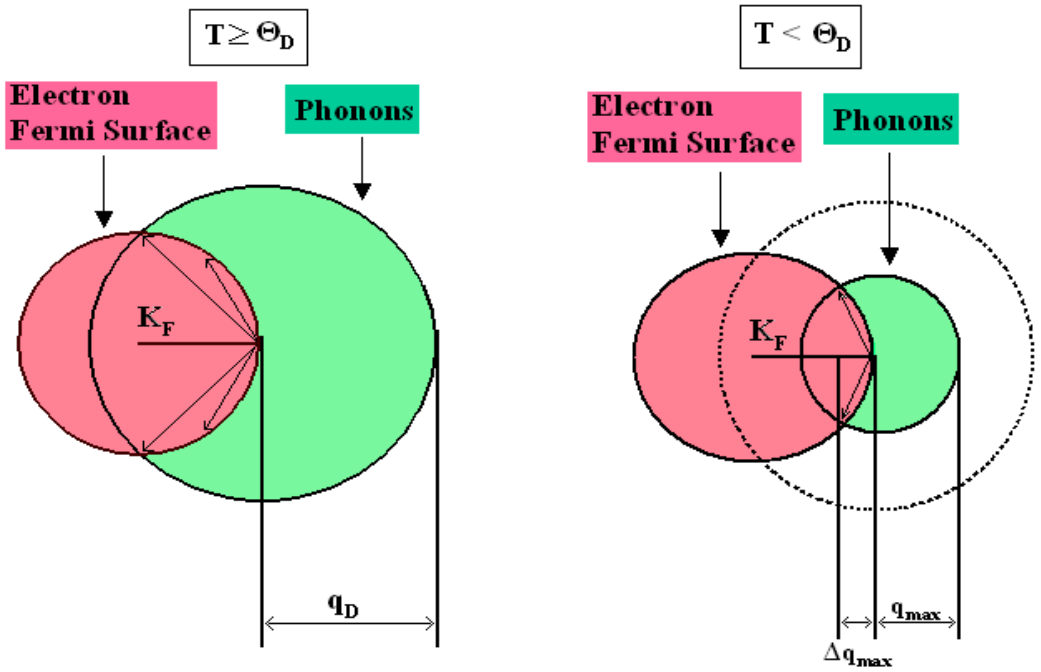

Fig. 4.18. Phonon spectrum available in a material for scattering above and below the Debye temperature Θ_D.

In this Bloch-Grüneisen regime, the area of the Fermi surface available for scattering shrinks as $q^2_{max} \sim T^2$ and as the allowed scattering angle becomes small, the momentum lost by a scattering event decreases as $\Delta q_{max} \sim q^2_{max} \sim T^2$. The electron-phonon coupling constant is also proportional to q_{max}, leading to an additional factor of T in the resistivity, and the result is that in the Bloch-Grüneisen regime $\rho(T) \sim T^5$.

The electron scattering processes are strongly dependent on the phonon occupation number or the phonon density of states (DOS), which tells us how many phonons occupy a given state of energy. DOS is a key characteristic of atomic dynamics and it gives the frequency spectrum of the modes of vibrations. All the elastic and thermodynamic properties of a material depend on the phonon DOS.

The equation governing the phonon DOS in a crystalline lattice can be derived as follows:

The number of states in K space within a sphere of radius K is given by

$$N_K = \frac{4\pi}{3} K^3 \times \frac{V}{8\pi^3} \tag{2}$$

where K is the wave vector and V the volume of the crystal. Then the density of states for phonons is

$$D\ (\omega) = \frac{dN_K}{d\omega} = \frac{dN_K}{dK}\frac{dK}{d\omega} = \frac{VK^2}{2\pi^2}\frac{dK}{d\omega} \tag{3}$$

According to Debye model

$$\omega = v_s K \tag{4}$$

where ω is the frequency, υ_s is the sound velocity, which is considered constant and K is the wave vector. Hence DOS is given as

$$D(\omega) = \frac{V\omega^2}{2\pi^2 v_s^2} \tag{5}$$

With N primitive cells in the crystal, the total number of acoustic phonon modes is Nfor each polarization. This helps to calculate the cutoff frequency called the Debye frequency:

$$\omega_D = \left(\frac{6\pi^2 v_{sN}^3}{V}\right)^{1/3} \tag{6}$$

This tells us that all modes with frequencies less than ω_D are allowed in the crystal. Fig. 4.19 shows all the allowed modes of phonon frequencies in bulk materials with the cut off frequency ω_D.

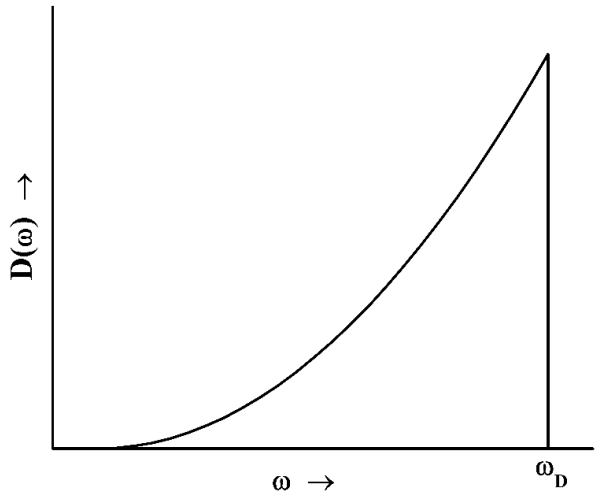

Fig. 4.19. The phonon density of states, as a function of frequency for a solid according to Debye model is shown in the figure.

The estimations performed here are based on Debye model for acoustic phonons up to Debye frequency ω_D. Thus we can see that the density of states depends on the volume, frequency as well as the velocity of the acoustic phonons. It is a known fact that in the case of nanomaterials the velocity of sound waves is reduced [40]. A nanocrystalline sample of silicon with 30 nm crystal size is found to exhibit a sound velocity reduced by 8.75% than the velocity in the bulk silicon [40]. This reduction in the velocity increases the density of states in the allowed frequency ranges.

Also reference [41,42] indicates there is a lower cut off frequency for nanomaterials i.e. the phonon spectrum of nano sized particles of diameter 'd' does not contain low frequency modes that are present in the spectra of bulk crystals. So the phonon spectrum can be considered as restricted by some minimum frequency ω_0 as shown in Fig. 4.20 which we shall see in the next section, is given by the equation

$$\omega_0 = \frac{2\pi v_s}{2d} \qquad (7)$$

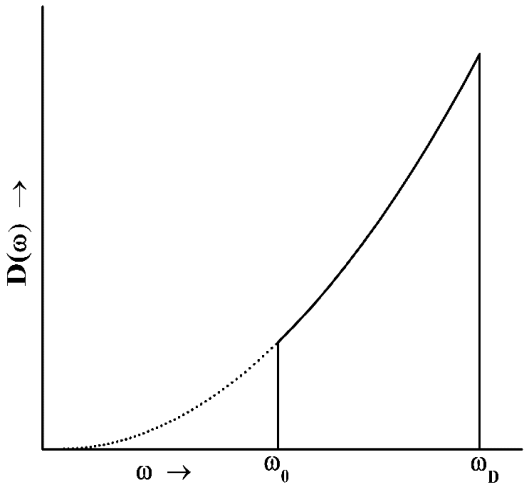

Fig. 4.20. The phonon density of states as a function of frequency, for a nano material, with limiting frequency ω_0 that is determined by the size of the clusters/grains in the material.

I. Origin of Minimum Cut off frequency in Nanomaterials

In an isolated cluster the phonon can get reflected from the boundaries and remain confined within the cluster. The consequences of phonon confinement are noticeable in the vibrational spectra only when the grain size is smaller than typically 20 lattice parameters. Although the average cluster size in our samples are above this limit, because of the distribution in the size of the clusters, this effect cannot be completely ruled out.

The highest frequency i.e. the smallest wavelength of a phonon that can be excited in a system is always determined by the inter-atomic distance 'a' i.e. $\lambda_{min} = 2a$. When it comes to the maximum phonon wavelength, bulk materials with micro sized grains pose no limit to the entire phonon spectrum available at any particular temperature.

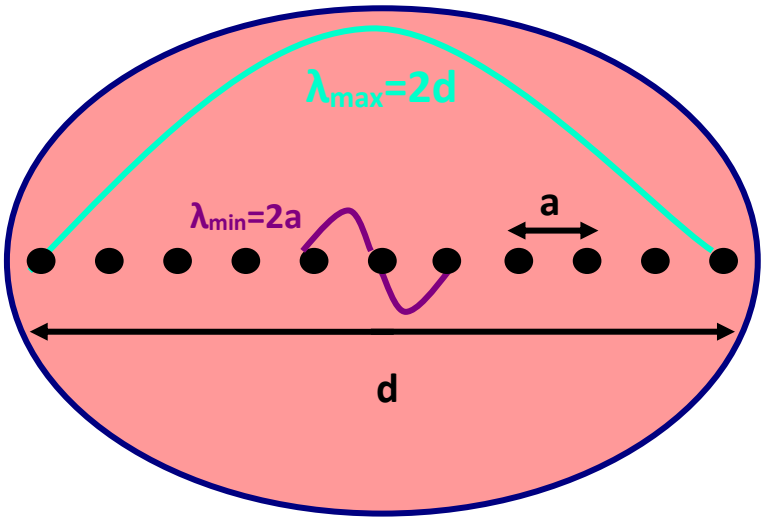

Fig. 4.21. Picture showing the maximum and minimum wavelength that can be sustained in a cluster of diameter d.

However in the case of nano materials the size comes into picture. The maximum wavelength that will be sustained in a cluster of diameter 'd' will be equal to twice its diameter, λ_{max} = 2d as shown in Fig. 4.21. This means that there is a lower limit to the frequency of the phonons exited in the material because of the size:

$$\nu_{min} = \frac{v_s}{\lambda_{min}} \qquad (8)$$

Where υ_s is the velocity of sound propagating through the nanostructures and the minimum value of Θ would be given by

$$K_B\theta_0 = h\nu_{min} \qquad (9)$$

where K_B is the Boltzmann's constant and h is the Plank's constant. With λ_{max} = 2d, where d is the diameter of the cluster. Using (7), (8) and (9) we get:

$$\theta_0 = \frac{h\nu_s}{2dK_B} \qquad (10)$$

Introduction of this limiting frequency as the lower limit of integration gives the Bloch Grüneisen formula the form given below. This formula is used to fit the data, introducing the parameter Θ_0 to be obtained from the fits to the data.

$$\rho(T) = \rho_0 + A\left[1 + \left(\frac{B}{x}\right) + (Dx^p)\right]\left[\frac{4}{x^5}\int_{\theta_0}^{x}\frac{z^5 e^z}{(e^z-1)2}dz\right] \qquad (11)$$

Since the contribution from anharmonicity of lattice vibtations are diminutive, the constants B and C are neglected (x = (Θ_D - CT) / T= Θ_D/T). This gives the above equation the form:

$$\rho(T) = \rho_0 + A[1 + (Dx^p)]\left[\frac{4}{x^5}\int_{\theta_0}^{x}\frac{z^5 e^z}{(e^z-1)2}dz\right] \qquad (12)$$

4.7.4 Resistivity Data Fits

The resistivity data are fitted using equation (12) for the NCA films. The initial value for each fitting parameter has been the corresponding bulk values obtained from the reference [35]. Curve fitting done by floating all parameters revealed that there is no substantial change in the Debye temperature value for NCA films from their bulk value. The value of Debye temperature obtained from the fits lie within 6% of the bulk value for all the films. Many researchers dealing with nanomaterials have observed a reduction in the Debye temperature associated with a decrease in particle size [41,44,45]. However the determination of Debye temperature by Mossbauer

effect for Au and Fe particles of 5-7 nm reveal that the Debye temperature of these particles remain the same as that of the bulk crystals [46,47]. These reports are in agreement with our observation from curve fitting. Holding the parameter Θ_D, i.e. the upper limit of the integration in equation (12) at the corresponding bulk value, while floating all other parameters provided a better fit of the data especially at lower temperatures from 25K to 50K.The values obtained from the fits are given in Tables4.9 - 4.11.The fitted curves are also shown in Fig. 4.22, Fig. 4.23 and Fig. 4.24. The fittings were reasonably good with a root mean square deviation value of about 0.1%. The electron-phonon coupling constant 'A' for the nanocluster assembled films are found to vary slightly from that of the bulk. The lower limit of integration θ_0 was observed to vary according to the cluster size of the films.

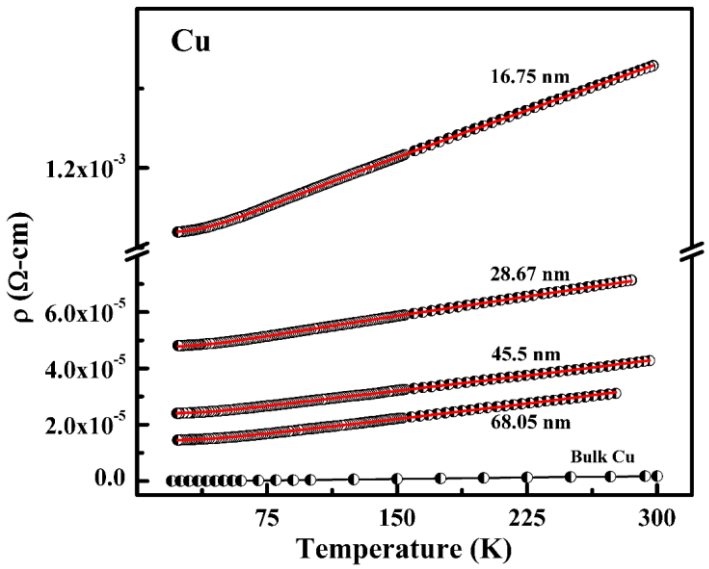

Fig. 4.22. Variation of resistivity of NCA Cu films with Temperature. Resistivity data along with fits are shown.

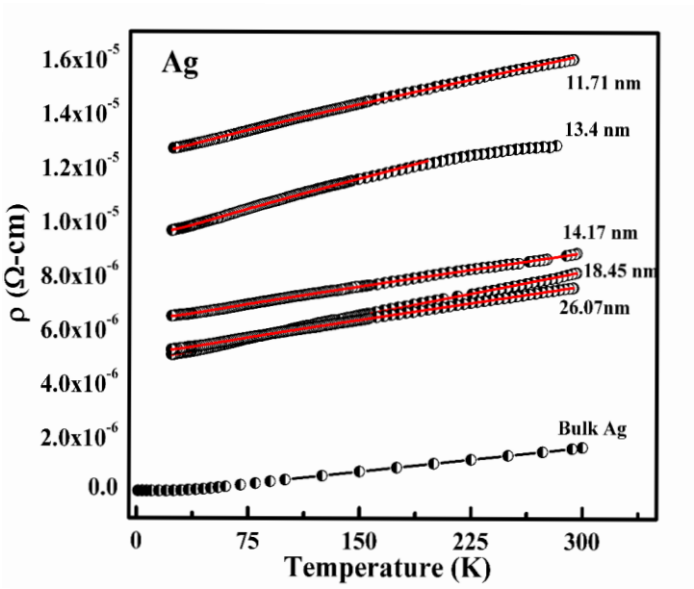

Fig. 4.23. Variation of resistivity of NCA Ag films with Temperature. Resistivity data along with fits are shown.

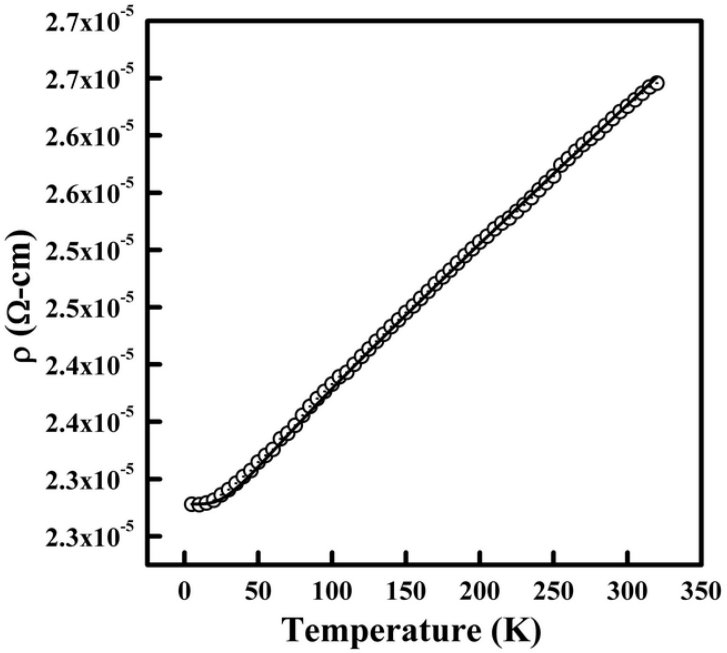

Fig. 4.24. Variation of resistivity of NCA Au film with temperature. Resistivity data along with fit is shown

Table 4.9. Parameters of resistivity fits for Cu films fixing Θ_D at the bulk value (343K).

Cluster Size (nm)	ρ_0 (Ohm-cm)	A (Ohm-cm)	θ_0 (K)	D	P
16.8 ± 0.2	1.118×10^{-3}	8.401×10^{-2}	47.38	4.09×10^{-2}	1.855
28.7 ± 0.7	4.8×10^{-5}	1.005×10^{-2}	44.28	1.79×10^{-2}	2.104
45.5 ± 2.3	2.402×10^{-5}	7.604×10^{-3}	42.96	1.77×10^{-2}	2.098
68.1 ± 2.5	1.456×10^{-5}	7.505×10^{-3}	39.73	9.2×10^{-2}	2.095

Table 4.10. Parameters of resistivity fits for Ag films fixing Θ_D at the bulk value (225K)

Cluster Size (nm)	ρ_0 (Ohm-cm)	A	θ_0 (K)	D	P
11.7 ± 0.2	1.267×10^{-5}	6.29×10^{-4}	79.14	1.437×10^{-2}	2.316
13.4 ± 0.2	9.539×10^{-6}	7.449×10^{-4}	76.76	3.01×10^{-2}	2.221
14.2 ± 0.2	6.46×10^{-6}	4.143×10^{-4}	72.88	1.658×10^{-2}	2.2
18.5 ± 0.2	4.97×10^{-6}	5.52×10^{-4}	68.2	2.60×10^{-2}	2.26
26.1 ± 0.7	5.24×10^{-6}	4.092×10^{-4}	62.32	1.438×10^{-2}	2.126

Table 4.11. Parameters of resistivity fits for Au films fixing Θ_D at the bulk value (170 K).

Cluster Size (nm)	ρ_0 (Ohm-cm)	A	θ_0 (K)	D	P
9.3 ± 0.2	2.33×10^{-5}	3.51×10^{-4}	34	6.67×10^{-9}	1.8

4.7.4.1. Variation of θ_0 with cluster size

Values of θ_0 obtained from the resistivity curve fits for the systems Cu and Ag as shown in Fig. 4. 25 affirms the understanding that θ_0 scales with the cluster size. The value of θ_0 is found to decrease with an increase in the cluster size for both Cu and Ag films. This supports the idea that θ_0 tends to the limit zero as the clusters approaches the size of bulk crystalline grains.

Now the value υ_s has been approximated to the velocity of sound waves in the bulk Cu, Ag and Au, which are 3901 m/sec, 2680 m/sec and 3240 m/sec respectively. The values yielded from this calculation using (10) for Cu and Ag has been displayed in Table 4.12 and 4.13 along with the values of θ_0 obtained from fit.

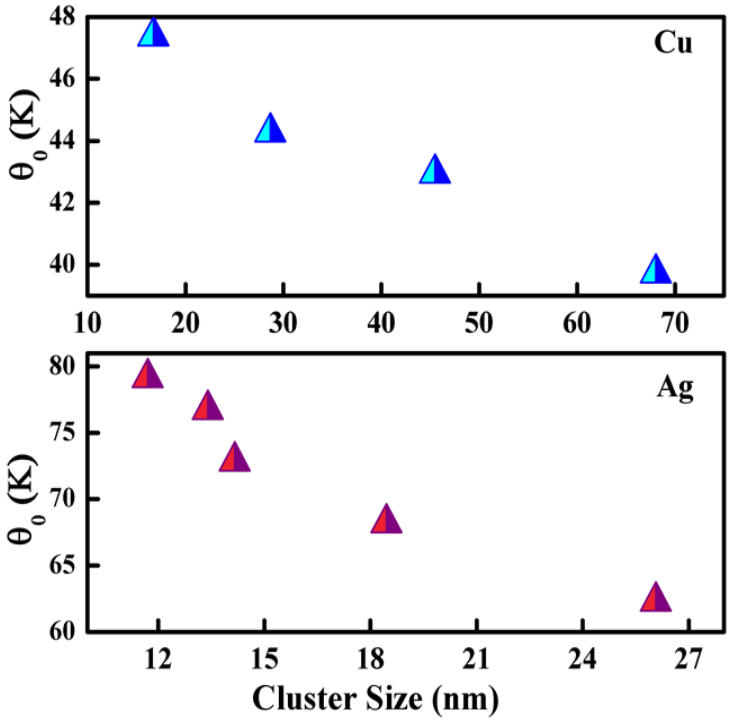

Fig. 4.25. θ_0 scales with cluster size for NCA Cu and Ag films.

Table 4.12. Comparison of θ_0 calculated and that obtained from the fit for Cu

Cluster Size	θ_0 (K)	θ_0 from fit (K)
16.8 ± 0.2	5.59	47.38
28.7 ± 0.7	3.34	44.28
45.5 ± 2.3	2.06	42.96
68.1 ± 2.5	1.38	39.73

Table 4.13. Comparison of θ_0 calculated and that obtained from the fit for Ag

Cluster Size	θ_0 (K)	θ_0 from fit (K)
11.7 ± 0.2	5.49	79.14
13.4 ± 0.2	4.8	76.76
14.2 ± 0.2	4.54	72.88
18.5 ± 0.2	3.49	68.2
26.1± 0.7	2.47	62.32

The values of θ_0 calculated using the above equation is much smaller than that obtained from the resistivity curve fits. There is almost one order difference between these values. However the variation in θ_0 with the cluster size is found to be consistent in the Cu as well as Ag NCA films. The θ_0 values obtained from the fits, do not tally with the cluster sizes reported here, but correspond to a size below 3 nm. The cluster size that is used for the calculation is an average value obtained from XRD. As there is a wide distribution of cluster sizes in the NCA films, this will definitely have an effect

on the lowest frequency that is propagated in the clusters, which may result in a lower θ_0 value.

Thus nanomaterials vary from the bulk in their distribution function of the frequency modes of atomic vibrations. There are reports indicating that the size confinement of nanocrystals modifies the phonon density of states at low frequencies which results in changing the optical and thermal properties of the given nanocrystals [48, 49]. The size confinement effect is expected to make the phonon spectrum vanish below a critical frequency for isolated nanocrystals [50]. In nanomaterials this limit on the lower frequency may result in displacing the phonon spectrum to the range of high frequencies [51], i.e. the missing modes can accumulate near the upper frequency cutoff.

The experimentally-determined DOS for nanocrystalline systems reveal striking anomalies when compared with the bulk DOS [52-57]. The main differences in the DOS was the broadening of the phonon peaks and enhancement of the phonon states at low energies [53-57], as well as at the high energies [57-61]. It was found that in the energy range lower than 15 meV the density of vibrational states of nanocrystalline materials is higher than coarse grained crystals [51]. This is quite unexpected as size confinement theoretically leads to a lower cut off frequency. Thus in the low frequency region the vibrational spectra of nanocrystalline materials differ from the bulk mainly in its form because of the excess density of states. This excess density of states appears as a kink for nanocrystalline Ni of 10 nm [51]. An enhancement in the vibration density of states at low frequencies and an overall shift of the high frequency band beyond the top of the bulk phonons was observed in the case of Ag nanocrystals [62]. As mentioned above, experimental observations indicate that for nanomaterials there is increased intensity of the phonon DOS at energies below 15 meV whereas this excess

intensity diminishes after the material is annealed at higher temperatures [63].

The enhancement of phonon spectrum at low frequencies may be due to the oscillations of clusters, which are metastable atomic groupings, with increased local stability [51]. The calculation of phonon DOS in nanocrystalline bcc Fe reveals an anisotropic stiffening in the interatomic force constants which lead to the shrinking of nearest-neighbor distances [64]. This results in additional vibrational modes above the bulk phonons near the bottom of the phonon band. Also the anomalies that are found in the phonon density of states is believed to result not from the atoms at the interior of grains [65] but from the atom at the grain boundaries which consists of a significant volume of the material. That is, the anomalies originate from the DOS of the interfaces. A grain of 2 nm size can amount to ~65% of the total volume of the nanomaterial at the interfaces. Also broadening of the DOS in the nanocrystalline materials is put forward as due to the anharmonic, inter-atomic potentials in un-relaxed grain boundaries [63].

The surface to volume ratio is much higher in nanoclusters. The density of states in nanocluster systems is mostly determined by the contributions from the surface atoms. The limited spatial extent of the clusters is expected to suppress the existence of long wavelength modes but it is found that the surface atoms broaden the DOS of the clusters, leading to an enhanced DOS at low and high frequencies [66]. Calculations of the local vibrational DOS inside a Ag531 cluster show a shift to higher energies compared to bulk Ag and this shift is attributed to the capillary pressure that builds up inside the clusters [66].

The residual resistivity obtained from the fits for both NCA Cu and Ag films are much higher than their corresponding bulk values. This is represented in Fig. 4.26.

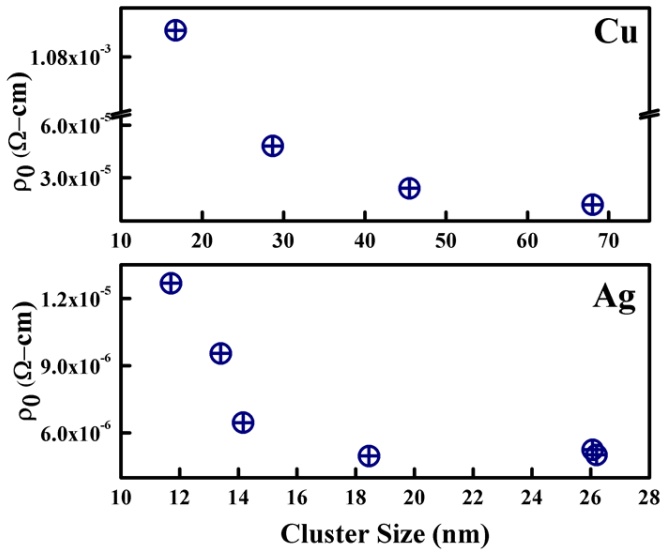

Fig. 4.26. ρ_0 scales with cluster size for NCA Cu and Ag films

For Cu films ρ_0 is around 5 orders higher than the bulk residual resistivity whereas for Ag it is around 4 orders greater than the corresponding bulk value. The preparation method used for these samples, keeps the impurity content to a minimum. Thus the cluster boundaries are the reason behind the high values of residual resistivity. Also ρ_0 is expected to scale with the cluster size. As the cluster size decreases the cluster boundary regions inside the nanomaterial increases. Therefore the number of boundaries increases, which results in an increased scattering of electrons and hence the increase in intrinsic resistivity. Thus the residual resistivity increases with a decrease in the cluster size.

4.7.4.2 Variation of fitting parameter A with cluster size

The coefficient 'A' that appears in the Bloch Gruneisen equation is a constant of the material. This term is given by the equation [36]

$$A = \frac{3\pi\hbar Q^6 \zeta^2(0)}{16e^2 mNK_B\Theta_D R^4 v_F^2} \qquad (13)$$

Where Q is the Debye Radius, $\zeta(0)$ is the electron phonon interaction energy, m is the electron mass, N is the number of unit cells per unit volume, K_B is the Boltzmann's constant, Θ_D is the Debye temperature, R is the Fermi radius and υ_F the Fermi velocity.

The magnitude of A for the nanosystem is two orders more than the corresponding bulk system and it is found to change to lower values with an increase in cluster size for both Cu and Ag films as shown in Fig. 4.27.

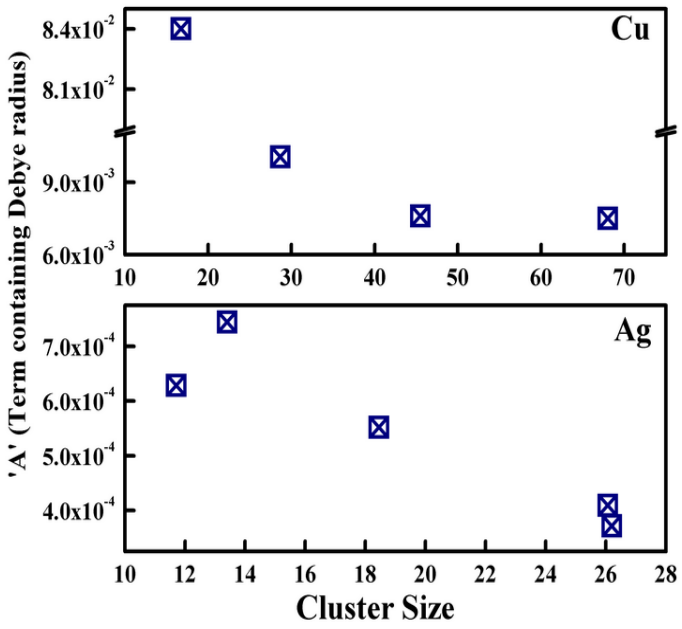

Fig. 4.27. The variation in the term 'A' with cluster size for NCA Cu and Ag films.

4.7.4.3 Variation of the temperature coefficient of resistance (TCR) with cluster size

The temperature coefficient of resistance (TCR) decreases with a reduction in the cluster size. This reduction is depicted in Fig. 4.28. The TCR values observed were lower than the bulk values. With an increase in the cluster size, the TCR slowly approaches the bulk value [23]. In the case of Cu NCA films the TCR was found to be 0.00058 K^{-1}, for a cluster size of 16.8 ± 0.2, which is around one order less than the bulk value. The TCR for Ag clusters of 11.7± 0.2 nm is 0.00063 K^{-1} which is also found to be one order less than the corresponding bulk value.

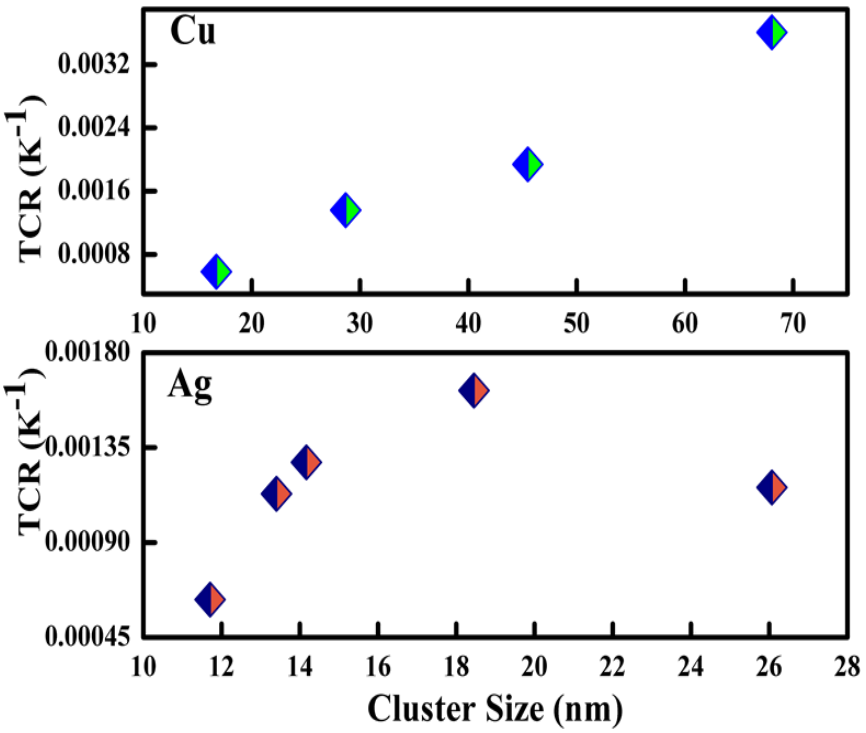

Fig. 4.28. The variation of TCR with increase in cluster size for NCA Cu and Ag films.

4.8 Conclusion

Nanocluster films of Cu, Ag and Au were synthesized using a nanocluster deposition system. The Cu clusters were found to form agglomerates because of the presence of a surface oxide layer whereas Ag and Au films did not show any incidence of oxide and were formed as separate clusters on the films. This oxide layer in Cu films could be removed by a heat treatment at ~⅓ of the melting temperature for 5 minutes. The removal of the oxide layer resulted in the disintegration of cluster agglomerates to individual clusters. The resistivity is found to be two to three orders of magnitude higher than that of the bulk due to an increase in the electron scattering from the cluster boundaries. These boundaries have a high degree of disorder and the volume fraction of atoms in the boundary regions is also large in nanosystems.

The temperature dependence of resistivity could be fitted to a simple model employing the Bloch Grüneisen function with the introduction of a lower limit θ_0 in the Debye integral. The upper limit of the integral was kept as the Debye temperature θ_D of the bulk metal. The values of θ_0 obtained for these systems is found to increase with a decrease in cluster size. This is understood as due to the expulsion of phonon states with smaller wave vectors. These results were compared with other experimental as well as theoretical data available for nanomaterials.

References

[1] Klaus Sattler, "Handbook of Thin Films Materials", ed. H. S. Nalwa, Vol. 5, Acdemic Press (2002).

[2] T. Vystavel, G. Palasantzas, S.A. Koch and J. Th. M. De Hosson,Appl. Phy. Lett., Vol. 82, 197 (2003).

[3] A. N. Goldstein, C. M. Echer, and A. P. Alivisatos. Science, Vol. 256, 1425 (1992).

[4] K. Koga, T. Ikeshoji and K. Sugawara,Phys. Rev. Lett, Vol. 92, 115507 (2004).

[5] I.D. Morokhov, V. I. Petinov, L. Trusov and V. F. Pertunin. UspekhiFiz. Nauk, Vol. 133. 653-692 (1981).

[6] I.D. Morokhov, L. Trusov and V. N. Lapovok. Energoatomizdat Moscow, 224 (1984).

[7] Yu. I. Petrov. Nauka. Moscow, 360 (1982).

[8] Yu. I. Petrov. Nauka. Moscow, 368 (1986).

[9] E.L. Nagaev. UspekhiFiz. Nauk, Vol. 162, 49-124 (1992).

[10] P. A. Montano, G. K. Shenoy, E. E. Alp and W. Schulze, J. Urban. Phys. Rev. Lett. Vol. 56, 2076-2079 (1986).

[11] H. J. Wasserman and J. S. Vermaak, Surface. Sci. Vol. 22, 164-172 (1970).

[12] H. Hovel and I. Barke, Progr. Surf. Sci. Vol. 81, 53 (2003).

[13] M. Blackman and J. R. Sambles, Nature, Vol. 226, 938-939 (1970).

[14] C. R. M. Wronski, Brit. J. Appl. Phys. Vol. 18, 1731-1737 (1967).

[15] J. R. Sambles. Proc. Roy. Soc. London. A Vol. 324. 339-351 (1971).

[16] C. G. Granqvist, and R. A. Buhrman, J. Appl. Phys., Vol. 47, 2200 (1976).

[17] Carl C. Koch. "Nanostructured materials: processing, properties, and applications". William Andrew Publishing. Norwich, NY, U.S.A

[18] A. Seeger, and G. Schottky, Acta. Metal., Vol. 7, 495 (1959).

[19] P.V. Andrews, W. B. West, and C. R. Robenson, Philos. Mag., Vol. 19, 887 (1969).

[20] M.B.Kasen, Philos. Mag. Vol. 21, 599 (1970).

[21] A. Gangulee, J. Appl. Phys. Vol. 43, 867 (1972).

[22] I. Nakamichi, J. Sci. Hiroshima Univ. Vol. 54, A49 (1990).

[23] C. Suryanarayana, Internat. Mater. Rev. Vol. 40, 41 (1995).

[24] H. Gleiter,Prog. Mater. Sci. Vol. 33, 223 (1989).

[25] T. Mütschele and R. Kirchheim, Scripta Metall. Vol. 21, 1101 (1987).

[26] I. Bakonyi, E. Toth-Kadar, T. Tarnoczi, L. Varga, A. Cziraki, I.Gerocs and B. Fogarassy, Nano. Struct. Mater. Vol. 3, 155–161 (1993).

[27] BattistionGiovanniA, RosalbaGerbasi and A. Agustin Rodriguez, Chem. Vap. Depos. Vol. 11, 130–135, (2005).

[28] M.C. Salvodori, A.R. Vaz, R.J.C. Farias and M. Cattani, Surf. Rev. and Lett. Vol. 11, 223–227 (2004).

[29] K. Lu, Mater. Sci. Eng: R: Reports, Vol. 16, 161–221 (1996).

[30] K. Yokota, K. Nakamura, T. Kasuya, K. Mukai and M. Ohnishi, J. Phys. D: Appl. Phys., Vol. 37, 1095 (2004).

[31] B.Z. Ding, Z.Q. Hu, K. Lu and Y.Z. Wang, Physica B, Vol. 192, 345–350 (1993).

[32] Y.Z. Wang, G.W. Qiao, X.D. Liu, B.Z. Ding and Z.Q. Hu, Mater. Lett. Vol. 17, 152–154 (1993).

[33] I. Nakamichi, J. Sci. Hiroshima Univ., Vol. 54A, 49 (1990).

[34] A. F. Mayadas and M ShatzkesPhys. Rev. B, Vol. 1, 1382 (1970).

[35] R.A. Matula, J. Phy. Chem. Ref. Data, Vol. 8, 1147 (1979).

[36] J.M. Ziman, "Electrons and Phonons-The theory of transport phenomena in solids" Oxford, Clarendon press (1960).

[37] Gruneisen E Ann. Phys. Lpz. Vol. 16, 530 (1933)

[38] Michael S. Fuhrer, Physics, Vol. 3, 106 (2010).

[39] F. Bloch, Zeitschriftfür Physik, Vol. 59, 208 (1930).

[40] Tania Claudio, Gabi Schierning, Ralf Theissmann, HartmutWiggers, Helmut Schober, Michael Marek Koza and Raphael P. Hermann.J. Mater. Sci. Vol. 48, 2836–2845 (2013).

[41] M. R. Hoare and P Pal. Adv. Phys. Vol. 20, 161-196 (1971).

[42] M. R. Hoare and P Pal. Adv. Phys. Vol. 24, 645-678 (1975).

[43] T. Fujita, K. Ohshima and T. Kuroishi. J. Phys. Soc. Japan. Vol. 40, 90-92 (1976).

[44] K. Ohshima, T. Fujita and T. Kuroishi. J. de Physique-Colloque C2 38, Suppl. No: 7, C2-163-C2-165 (1977).

[45] P. Buffat, Solid state Commun. Vol. 23, 547-550 (1977).

[46] M.P.A Viegers and J. M. Trooster, Phys. Rev. B, Vol.15, 72-83 (1977).

[47] G. Von Eynatten and H. E. Bommel, Appl. Phys. Vol. 14, 415-421 (1977).

[48] Sung-Jei Hong, Min-GiKwak and Jeong-In Han, J. Korean. Phys. Soc. Vol. 45, 721 (2004).

[49] Young-Hwan Kim and Woon-Jo Cho, J. Korean Phys. Soc. Vol. 46, 926 (2005).

[50] H.-S. Yang, S. P. Feofilov, D. K. William, J. C. Milora, B. M. Tissue, R. S. Meltzer and W. M. Dennis, Physica B, Vol. 476, 263-264 (1999).

[51] A. I. Gusev and A. A. Rampel,"Nanocrystalline Materials" Cambridge Int Science Publishing (2004).

[52] K. Suzuki and K. Sumiyama, Mater. Trans. JIM. Vol. 36, 188 (1995).

[53] B. Fultz, L. Anthony, L. J. Nagel, R. M. Nicklow, and S. Spooner, Phys. Rev. B, Vol. 52, 3315 (1995).

[54] J. Trampenau, K. Bauszuz, W. Petry, and U. Herr, Nanostruct.Mater. Vol. 6, 551 (1995).

[55] B. Fultz, J. L. Robertson, T. A. Stephens, L. J. Nagel and S. Spooner, J. Appl. Phys. Vol. 79, 8318 (1996).

[56] H. N. Frase, L. J. Nagel, J. L. Robertson and B. Fultz, Philos. Mag. B, Vol. 75, 335 (1997).

[57] B. Fultz, C. C. Ahn, E. E. Alp, W. Sturhahn and T. S. Toellner, Phys. Rev. Lett. Vol. 79, 937 (1997).

[58] H. Frase, B. Fultz and J. L. Robertson, Phys. Rev. B, Vol. 57, 898 (1998).

[59] J. Trampenau et. al. Nanostruct. Mater. Vol. 6, 551 (1995).

[60] L. Pasquini et. al. Phys. Rev. B, Vol. 66, 073410 (2002).

[61] F. Yue et. al. Phys. Rev. Lett. Vol. 93, 205501 (2004).

[62] Abdelkader Kara and Talat S. Rahman, Phys. Rev. Lett. Vol. 81, 1453 (1998).

[63] H. Frase and B. Fultz, Phy. Rev. B, Vol. 57, 21 (1998).

[64] Ranber Singh, S. Prakash, R Meyer, and P. Entel. Pramana, Vol. 60, 547-56 (2003).

[65] U. Stuhr, H. Wipf, K. H. Andersen and H. Hahn, Phys. Rev. Lett. Vol. 81, 1449 (1998)

[66] R. Meyera, S. Prakash, and P. Entel, A Multinational Journal, Vol. 75, 1-2 (2002).

CHAPTER V

ELECTRON TRANSPORT IN SPATIALLY SEPARATED Au NANOCLUSTER ASSEMBLIES

5.1 Introduction

Isolated nanoclusters are zero dimensional entities where electrons are spatially confined in all the three dimensions. These artificially controlled systems are perfect tools for understanding quantum effects as they bring out the wealth of all size related properties. In these clusters size being in the nano-regime confines the electrons inside that ushers in large energy level spacings. These discrete electronic energy levels originating from the reduced size, determine the fundamental properties of the system. Characterizing such systems of reduced dimensions is a real challenge. Compared to atomic size particles individual nanoclusters conduct effectively between electrodes. Thus they help in obtaining a glimpse of the properties exhibited by nano dimensions.

This chapter deals with isolated nanoclusters and the electron transport in an assembly of these small metallic entities. The mechanisms valid in such systems are governed by more or less the same physics that controls the quantum dots. Electron transport in the cluster assemblage occurs by the intra-grain diffusive electron motion and the electron tunneling between clusters which results in their sequential charging [1]. Therefore the interplay of the coupling between the clusters and the electron-electron Coulomb interaction that originates from the charging of the clusters control the transport properties of this system [2]. The discreteness of the electronic

levels in these nanoclusters also plays an important role, especially at low temperatures. The studies on electron transport and the localization effects in these artificially controlled systems are described in this chapter.

The system prepared for investigation consists of Au nanoclusters of a few nanometers with a small distribution in cluster sizes, which are spatially separated from each other and are deposited across inter-digital fingers of silver electrodes as sown in Fig. 5.1 (a) and (b).The mean energy level spacing δ in a single cluster is inversely proportional to the volume of the cluster. Then for smaller clusters of a few nanometers δ will be larger and the condition for the observation of quantum effects $k_BT \ll \delta$ will be satisfied.

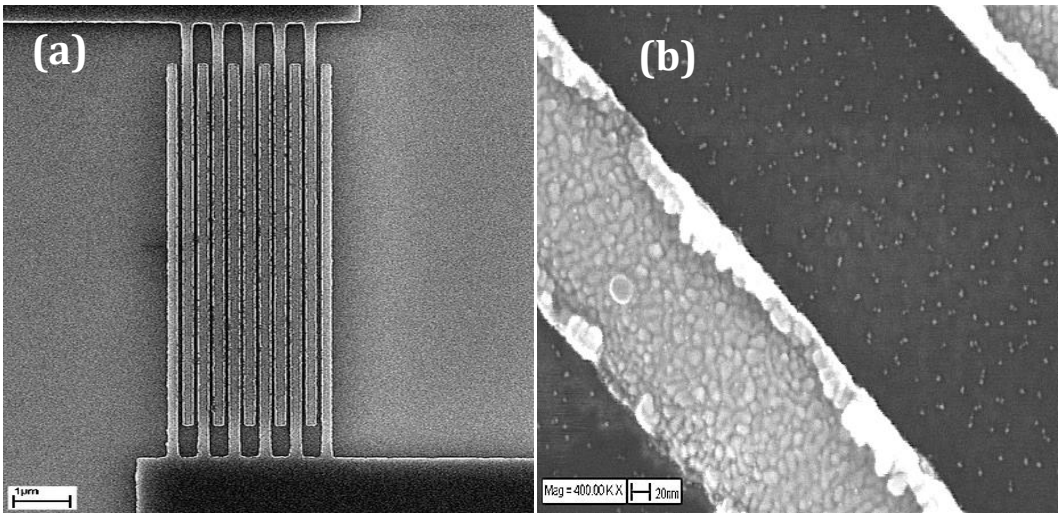

Fig. 5.1. SEM pictures of the electrodes across which, the isolated Au nanoclusters are deposited. (a) Image showing the inter-digital fingers of silver electrodes. (b) The individual electrodes in higher resolution revealing small atomic clusters between the electrodes.

The dispersion in the cluster sizes introduces disorder in this system and the nano size regime brings in the Coulomb blockade effects. This makes it ideal for the study of correlated electronic diffusion in the presence of both

disorder and strong Coulomb interactions [3, 4]. Physical properties of materials at nano-scale may not remain constant, but scale with the size of the particles. In systems like this both the electron interaction strength and the degree of disorder can be tuned by varying the inter cluster spacing as well as the size of the clusters. Understanding these may ultimately lead to the realization of designer materials, meeting unique needs in technology and application.

5.2 Preparation of Isolated Au nanoclusters

Isolated Au nanocluster assembly was prepared by the nanocluster deposition system. The deposition was done at room temperature without any bias. The duration of deposition was restricted to 3 min, which resulted in a distribution of isolated clusters of Au. The preparation conditions are shown in Table 5.1.

Table 5.1. Preparation conditions of Au clusters

Sample	**Isolated Au Clusters**
Argon gas flow	60 sccm
Aggregation Distance	140 mm
Base Pressure	8×10^{-7} mbar
Working pressure	2×10^{-5} mbar
Power	124.92 watts
Duration of Deposition	3 min

The silver fingers shown in Fig. 5.1 (a) were 11 μm long and 200 nm broad with an average spacing around 86 nm between them. Thin gold wires, wire-bonded to Ag electrodes, provided the system with electrical contacts.

This cluster assemblage provides an ideal system to study the electron transport in isolated metals particles.

5.3 Scanning Electron Microscopy

Fig. 5.2 shows the SEM images of as-deposited Au nanoclusters. The clusters were isolated from each other, not by any insulating matrix but by the spatial separation between them. This SEM Image with a magnification of 500 KX revealed clusters with a size ranging from 1 to 10 nm.

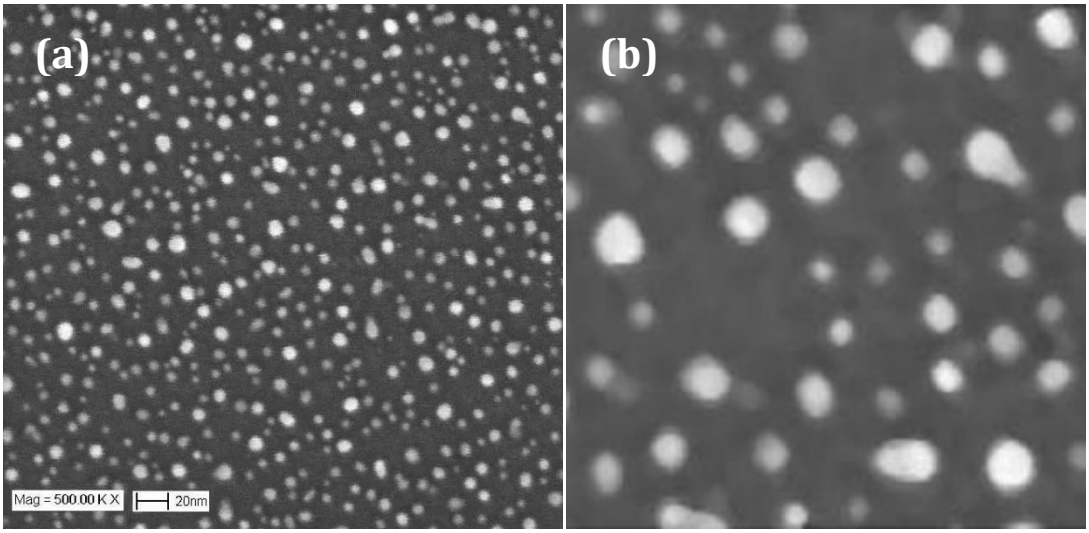

Fig. 5.2. SEM pictures of the isolated Au nanoclusters deposited between electrodes (a) Image showing the distribution of the nanoclusters (b) A magnified image of the same nanoclusters.

At this magnification they appear like small groups of 3-6 atomic clusters isolated from each other, but following a trail. In other words position of the clusters on the substrate was not completely random but it appeared to show a tendency to line up one after the other over a few nanometers. This kind of a behavior was also observed in the case of isolated Co nanoclusters [5]. The distribution of cluster size could be described by the

lognormal function, with a slight asymmetry towards larger cluster sizes, as shown in Fig. 5.3. The mean cluster size obtained from the curve fit is around 4.8 ± 0.2 nm.

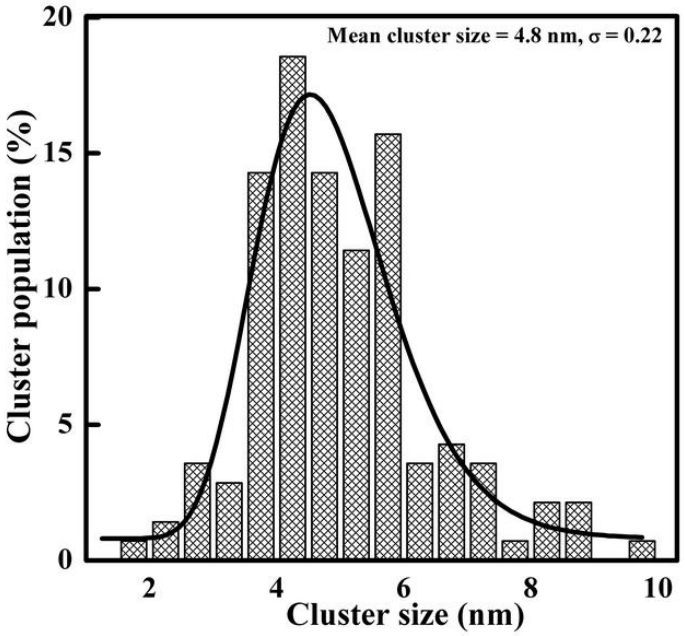

Fig. 5.3. Histogram showing the size distribution of isolated Au clusters. A lognormal curve fits the size distribution. σ is the standard deviation of the distribution of logarithm of size.

Thus it is clear from the SEM images that there is a distribution of the cluster radius varying between 0.5 to 5 nm. These are metallic clusters and if we assume they are spherical in shape, the capacitance of each cluster is given by $C = 4\pi\varepsilon_0 r$ where r is the radius. The variation in the cluster radius gives rise to a range of capacitances in our sample. Also there is a distribution in the inter-cluster distance in this assemblage as shown in Fig. 5.4. Individual nanoclusters are spatially isolated from each other over distances ranging

from 4 nm to 22 nm. This distribution could be fitted to a Gaussian curve obtaining a mean distance of 12.3 ± 0.6 nm

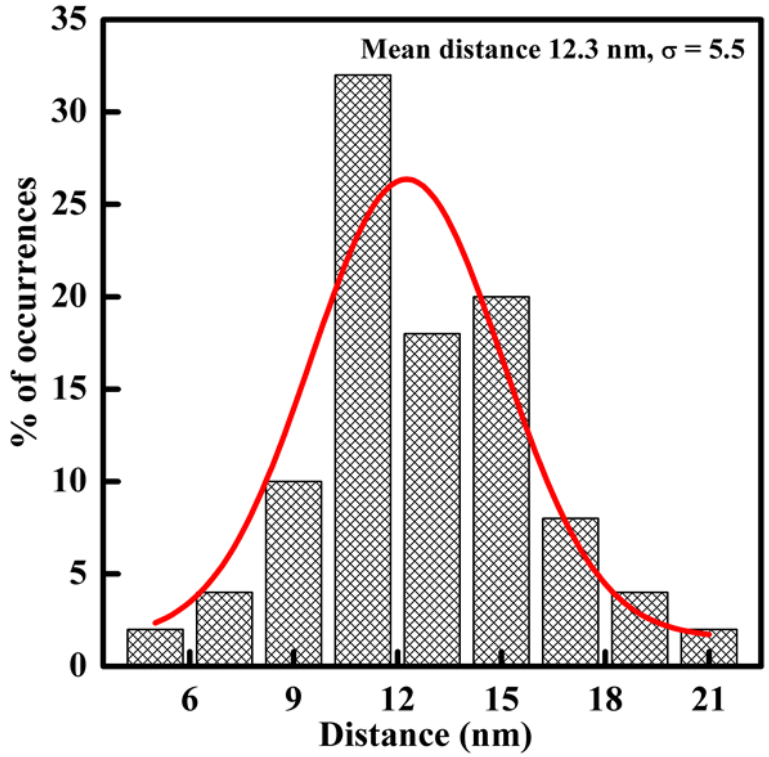

Fig. 5.4. Histogram showing the distribution of inter-cluster spacing in Au assemblage. σ is the standard deviation of the size.

5.4 Transport Measurements on Isolated Au Nanocluster Assembly.

The electronic resistance of this isolated cluster assembly was measured using a two-probe configuration and a closed cycle refrigerator. Care was taken to maintain the electric current low enough to avoid any signs of sample over-heating. The resistance for the temperature ranging from 205 K to 350 K was recorded (see Fig. 5.9). The measurements could not be done below 205 K, since the resistance became very high as compared to the

internal resistance of the nanovoltmeter that was used to measure the voltage. The resistance curve shows a rapid increase in the value of resistance with a decrease in temperature. This is an activated type behavior and not a metallic type behavior although the cluster assemblage consists of metallic nanoclusters.

The studies on metallic nanocluster assembled films, in chapter 3 where the clusters are not spatially separated but bound in insulating oxide layer, revealed a transport mechanism where electrons hop through localized states. In the present system we do not have an oxide layer on the naoclusters but they are spatially separated with a large inter-cluster average separation of 12.3 ± 0.6 nm. This will also lead to electron confinement and localization in the clusters and the current transport will be via electron hopping. So the resistance curve of isolated Au cluster assembly was also analyzed for the electron hopping behavior. Assuming that the resistance data follows the general hopping law:

$$R(T) = BT^{-m} \exp(T_0/T)^{x} \quad (1)$$

where R is the resistance, T_0 is a characteristic temperature and B and m are material dependent constants. As before, the analysis was carried out using Zabrodskii and Zinov'eva (Z-Z) method [7]:

$$\ln R(T) = \ln B - m \ln T + (T_0/T)^{x} \quad (2)$$

$$(\partial \ln R/\partial \ln T) = -m - x(T_0/T)^{x} \quad (3)$$

Defining $W(T) = -(\partial \ln R/\partial \ln T)$ we get:

$$W(T) = m + x(T_0/T)^{x} \quad (4)$$

In a system with exponential hopping dependence of resistance R, the parameter 'm' can be neglected since m ‹‹ $x(T_0/T)^x$.

This yields

$$W(T) = x\,(T_0/T)^{x} \quad (5)$$

$$\ln W(T) = \ln(xT_0^{x}) - x \ln T \quad (6)$$

The slope of the straight line obtained by plotting ln W and ln T will yield the value of the exponent *x*. The plot between ln W and ln T as displayed in Fig. 5.5 revealed

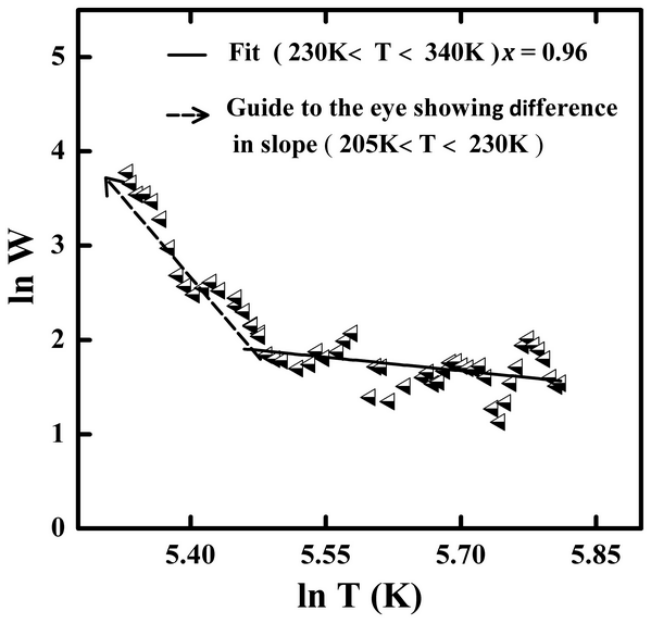

Fig. 5.5. Graph showing the plot between ln W and ln T, with the Z-Z method of analysis. The solid line is the least square fit to the data. The slope of the solid line yields the hopping exponent *x*, and the intercept is related to the characteristic hopping temperature T_0.

two regions with different slopes exhibiting a crossover of two different resistance behaviors. The slope for the data between 230 K and 340 K was determined to be 0.96 ± 0.31. The lower temperature part from 205 K to 229 K displayed a higher value of slope, which is explained later. The crossover takes place at a temperature of about 241 K.

The value of the exponent x obtained from the fit for the high temperature part shows that the electron transport in this region is due to electron hopping between localized states. The value of x, being 0.96± 0.31 closer to 1 confirms the exp (T_0/T) temperature dependence of resistance which characterizes the nearest neighbor hopping mechanism. As explained in chapter 3 this form of conduction is normally predominant in systems with strong localization resulting from the presence of disorder. In addition to this, the present system has a spatial separation of clusters and the electrons have to tunnel through high resistance insulating bridges between the clusters. This also gives rise to exponential temperature dependence at small vales of g_0 where g_0 is the tunneling conductance [8].

In the presence of strong localization, only the distance between the clusters limits the hopping of the electrons. Then the electron normally jumps to the state nearest in space because the wave function containing the electron transfer integral on each cluster falls off rapidly with distance. This kind of hopping is expected when $\gamma r_0 >> 1$, where γ denotes the electron transfer integral and r_0 is the average distance to a nearest neighbor [9]. This mechanism gives rise to an activated behavior for resistance:

$$R(T) = R_0 \exp(T_0/T) \qquad (7)$$

Activated conductance is a usual transport mechanism observed in several other disordered systems. It has been reported in granular metals [10] and in gold nanocrystalline arrays at temperatures above100 K [11, 12]. The values of the exponent *x* and the characteristic temperature T_0 obtained from the fit (Fig. 5.6) are presented in Table 5.2.

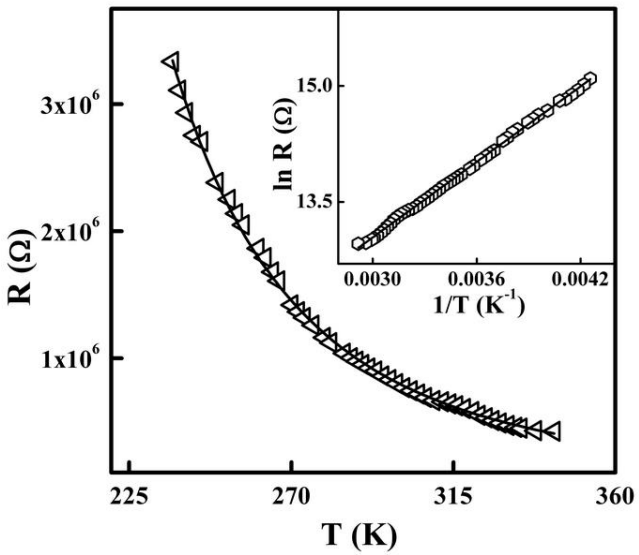

Fig. 5.6. The resistance vs. temperature data along with the fit to the equation R (T) = R_0 exp (T_0/T). Inset shows the linearity of the resistance data when plotted with 1/T.

Table 5.2. Fitting parameters obtained from Z-Z method (Fig. 5.5). Also parameters obtained from the fit using electron hopping law R (T) =R_0 exp (T_0/T) as shown in Fig. 5.6.

Method	***x***	**T_0 (K)**
Z-Z method	0.96 ± 0.31	1762 ± 10
Fit to R (T) =R_0 exp (T_0/T)	0.98 ± 0.11	1516 ± 10

The activation energy T_0 for metallic clusters has been shown to coincide with the Coulomb blockade energy in the limit of vanishing tunneling conductance $g \rightarrow 0$ [13]. As mentioned earlier a cluster of radius 'r' will have a capacitance given by $C = 4\pi\varepsilon_0 r$. For the electron to hop from one cluster to another cluster of capacitance C, it requires charging energy by an amount $e^2/2C$. The process of electrons hopping from cluster to cluster is accompanied by charging of the clusters involved. At low temperatures and at small-applied voltages, further electron transfer is suppressed because of this charging energy [14]. This is called the Coulomb blockade. Therefore the electron transfer between clusters of small enough capacitance, at low enough temperatures, such that $K_BT < e^2/2C$, is strongly suppressed coulombically. At low temperatures the electrons will not gain the activation energy needed for the hop and thus this requirement acts as a barrier.

The activation temperature T at which the electron overcomes the Coulomb blockade can be calculated by equating $e^2/2C$ to K_BT. The metallic clusters in our system fall in a range of sizes with differing radii, which results in varying charging energies. The average cluster size for this system was 4.8± 0.2 nm. The temperature corresponding to the average charging energy was then estimated to be 1738 K. This agrees reasonably well with the value of T_0 = 1762 K, that was obtained from the fits to the resistance data. This shows that Coulomb blockade effect [15] plays a major role in determining the properties of the system.

The value of the exponent for the data in between 205 K to 230 K obtained from the slope of the curve shown in Fig. 5.5 was around 11.18 ± 0.68. This value is extremely high in the context of electron hopping mechanisms which usually lie between 0 and 1. So it was clear that the

hopping may not be the appropriate electron transport mechanism in this temperature region. Thus we need to look for other possible ways to account for this behavior at low temperatures. To find out the exact region where the transport behavior changed from electron hopping ln R is plotted with 1/T in the entire temperature range as shown in Fig. 5.7.

From Fig. 5.7 the temperature region in which the curve deviates from the linear behavior (which was explained by electron hopping mechanism) was identified to be from 205 K to 229 K. The conductance in this region was found to obey an unusual temperature dependence, similar to that observed in certain granular metals [16]. The behavior was identified as a logarithmic temperature dependence of conductance ($\sigma = 1/R$) given by $\sigma = a + b \ln T$, where 'a' and 'b' are material dependent constants.

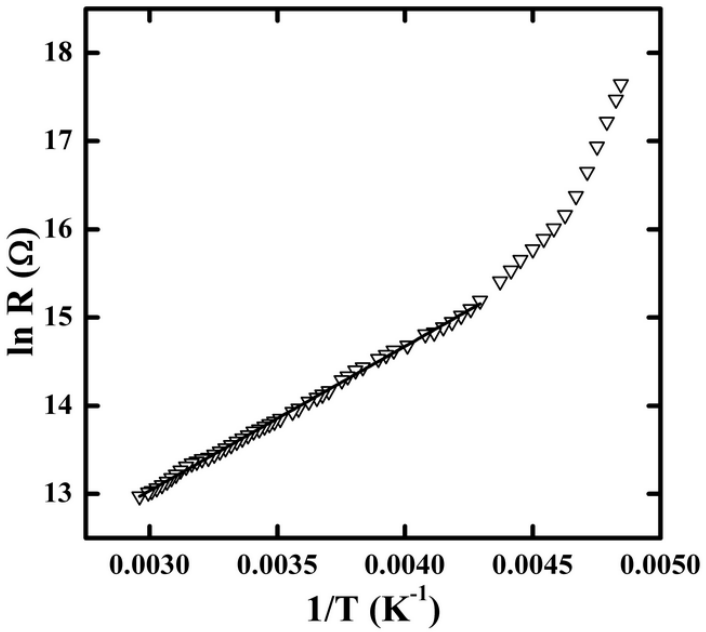

Fig. 5.7. Graph showing the plot between ln R and ln T. The linear fit shows the region, which has electron hopping transport mechanism. The deviation is observed at lower temperatures.

The exact origins of the logarithmic dependence of conductivity are still being debated and are a subject of current interest [17]. Different mechanisms in different types of systems such as the scattering of conduction electrons from isolated magnetic moments (Kondo effect) [18], quantum mechanical effects such as weak localization and electron-electron interactions in 2D systems have been shown to give rise to a logarithmic temperature dependence of conductivity at low temperatures [19]. With decreasing temperature, the localization effects considered with quantum corrections also give rise to a logarithmic temperature dependence of conductance [20] which may be the mechanism applicable to our system. Such corrections of the conductivity result from local quantum fluctuations of inter-cluster voltages between neighboring clusters. This effect was treated within the Ambegaokar-Eckern-Schoen (AES) model [21] and leads to logarithmic temperature dependence of the effective conductance. Efetov and Tschersich have shown that this logarithmic dependence $\sigma = a + b \ln T$ is valid in any dimensionality [8].

According to this model, important physical properties of such systems are described in terms of a parameter called the dimensionless tunneling conductance, $g_0 = G/(e^2/\hbar)$, where G is the average tunneling conductance between neighboring grains and $e^2/\hbar$ is the quantum of conductance. The logarithmic temperature dependence of conductivity is given as [4]

$$\sigma(T) = \sigma_0\left(1 - \frac{1}{\pi z g_0}\ln\left(\frac{g_0 E_C}{T}\right)\right) \qquad (8)$$

where E_C is the charging energy of an individual grain and z is the coordination number i.e. the number of neighbors for a single site on the

array. So the data in the temperature region 205 K - 229 K was fitted to the equation:

$$\sigma = a + b \ln T \qquad (9)$$

which is shown in Fig. 5.8. The value of the slope obtained from the data fit shown in the inset in Fig. 5.8 is b = 80.86. Comparing this value with the coefficient of ln T in (8) an estimate of the dimensionless tunneling conductance comes out to be $g_0 = 9.85\times10^{-4}$. This indicates that the tunneling conductance between clusters is small due to the large spatial separation. An average inter-cluster separation of about 12 nm is present in the system as shown earlier in Fig. 5.4.

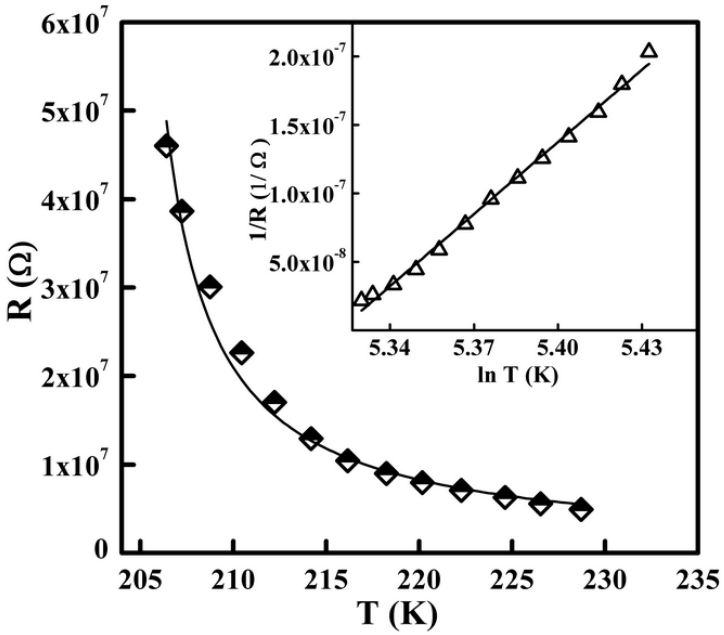

Fig. 5.8. The resistance vs. temperature data showing fit to the equation 1/R(T) = a + b ln T. Inset showing the linearity of the conductance data when plotted with ln T.

This is the first observation of logarithmic temperature dependence in a nanocluster assembled structure. Logarithmic temperature dependence was observed in many disordered systems as well as systems with reduced dimensions. These were systems exhibiting weak localization or electron-electron interaction effects [17]. There are reports on granular metals exhibiting this behavior by Simon et al. [17] and Gerber et al. [22]. The logarithmic dependence was observed in disconnected Pd films from 77 K to 0.05 K [23], in under doped $La_{2-x}Sr_xCuO_4$ crystals [24], granular niobium nitride films [17] and in some of the nanocrystalline samples earlier. This behavior has been observed in some cermet systems [25,26] also. In these systems it is observed that the logarithmic temperature dependence is very weak and occurs over a limited temperature range only [17].

Some of the experimental results [17,20,22] were showing the logarithmic temperature dependence of resistivity rather than conductivity whereas the theoretical models developed for understanding this mechanism show that the conductivity, not the resistivity should follow a logarithmic dependence (Please see the discussion on page no: 510 of the review paper by Beloborodov et. al. [4]). In Au nanocluster assemblage we have observed a logarithmic dependence of conductance which is according to the theoretical models.

The crossover of the conductivity from the activated behavior $\exp-(T_0/T)$ to the 'a + b lnT' behavior that is observed at about 241 K is depicted in the Fig. 5.9 below.

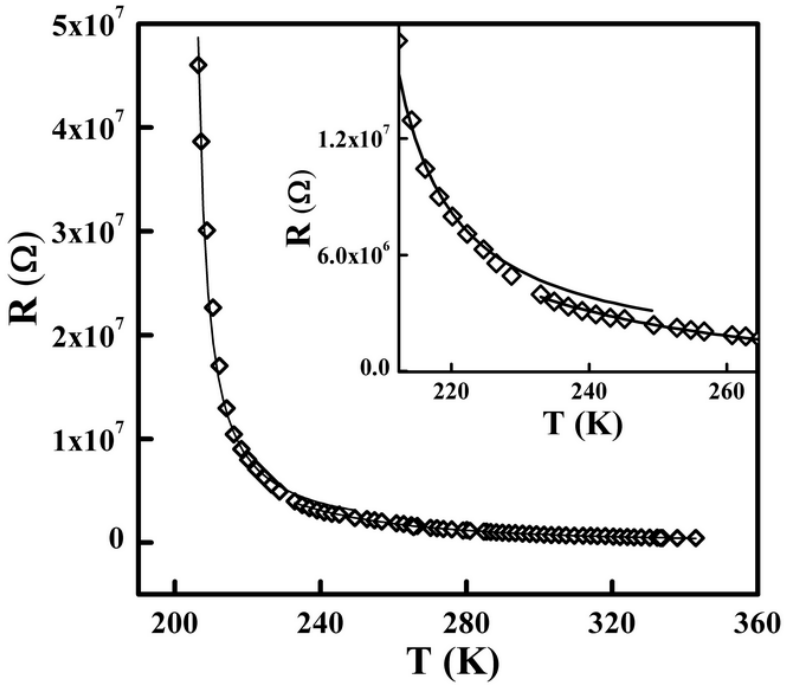

Fig. 5.9. The main figure shows the resistance of the nanocluster assemblage in the entire temperature range. The Inset shows the cross over from activated to logarithmic behavior.

5.5 I-V Characteristics

Nonlinear I-V characteristics as well as nonzero threshold voltages may emerge as a consequence of the Coulomb blockade in a system. The I-V responses of such systems may depend on the size, dimension, network connectivity etc. It may even depend on the screening length as well as the disorder in the system [27]. This is typically observed in nanocrystalline arrays in the regime of Coulomb blockade [4]. So I-V measurements were carried out on the gold nanocluster assembly.

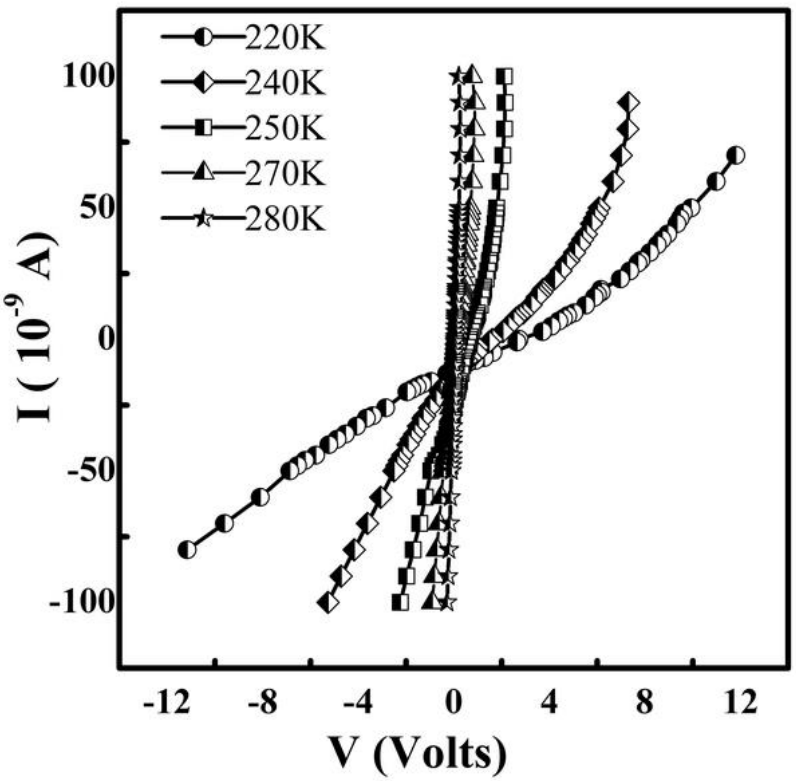

Fig. 5.10. The figure shows the I-V characteristic curve at different temperatures displaying the Coulomb blockade effect.

In I-V measurements recorded in Fig. 5.10, the non-linear increase of current with voltage is evident, showing the presence of Coulomb blockade in the system. The differential conductance (dI/dV) is obtained from the I-V characteristics and is found to reveal a dip in the conductance. This dip is found to increase with the decreasing temperature. Fig. 5.11 shows the (dI/dV) vs. V plot at 240 K revealing the dip at zero-bias. This dip is attributed to the presence of Coulomb blockade and the full width at half minimum of the conductance dip is given by [28]:

$$V_{1/2} = \left(\frac{5.439NK_BT}{e}\right) \qquad (10)$$

where N is the number of uniform junctions in series, in a symmetric linear array. The dip in conductance is fitted to a Gaussian curve and the value of full width at half minimum $V_{1/2}$ is found to be 5.2 V. The value of $V_{1/2}$ does not depend on any of the system parameter other than the number of junctions N [28]. Substituting the values for $V_{1/2}$ and T in (10) the number of junctions N in the system is estimated to be 46. The calculation presented in [28] is based on a uniform array of junctions whereas in our system we have a random two dimensional array of nanoclusters. So we apply a random walk model to estimate the number of junctions as follows:

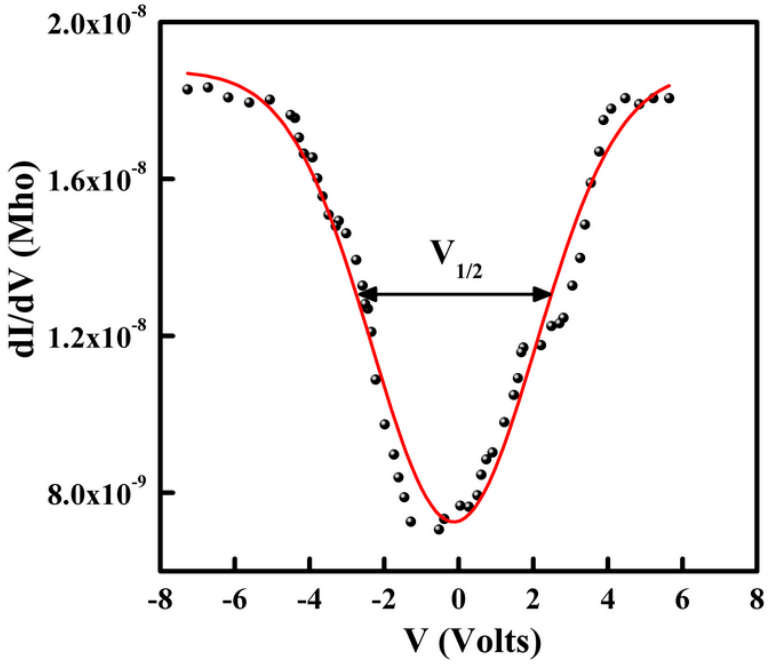

Fig. 5.11. The figure shows the differential conductance vs. Voltage for a temperature of 240 K.

The average distance 'D' between the interdigitated electrodes is 86 nm. Considering the electron makes a random walk from one electrode to the other with the step (l) being the average inter-cluster distance of 12.3 nm the number of junctions can be estimated using the equation:

$$D = l\sqrt{N} \qquad (11)$$

where D is the distance travelled, l is the step size and N is the number of steps. Substituting the value of D and l the number of steps in travelling from one electrode to the other comes out to be 49. Excluding the first and the last step the number of junctions in our system would be 47 which is in agreement with the estimate from $V_{1/2}$.

5.6.1 Conclusion

An assemblage of isolated Au nanocluster system was successfully prepared between inter-digitated electrodes using a nanocluster deposition system and various measurements were conducted. The prepared system consists of Au nanoclusters of average size of 4.8 ± 0.2 nm. Transport measurements revealed a conductivity of nearest neighbor hopping in the temperature range of 230 K to 340 K. Below 230 K, up to 205 K the conductivity behavior was identified as logarithmic temperature dependence given by $\sigma = a + b \ln T$. The presence of Coulomb blockade was also confirmed from the nonlinear I-V characteristics.

References

[1] I. S. Beloborodov, K. B. Efetov, A. V. Lopatin and V. M. Vinokur. Phy. Rev. B, Vol. 70, 205120 (2004).

[2] I. S. Beloborodov, K. B. Efetov, A. V. Lopatin and V. M. Vinokur. Phy. Rev. Lett. Vol. 91(24), 246801 (2003).

[3] T. B. Tran, I. S. Beloborodov, X. M. Lin, T. P. Bigioni, V. M. Vinokur and H. M. Jaeger, Phys. Rev. Lett. Vol. 95, 076806 (2005).

[4] I. S. Beloborodov, A. V. Lopatin, V. M. Vinokur and K. B. Efetov, Rev. Mod. Phys. Vol. 79, 469 (2007).

[5] S. A. Koch, T. Vystavel, G. Palasantzas and J. Th. M. De Hosson. Encyl. Nano Sc. and Nano Tech. Ed. H. S. Nalwa, Am. Sci. Vol. 14, 457-496 (2011).

[6] Jingshan Zhang and Boris I. Shklovskii Phys. Rev. B, Vol. 70, 115317(2004).

[7] Ralph Rosenbaum. Phys. Rev. B, Vol. 44, 3599 (1991).

[8] K. B. Efetov and A. Tschersich, Europhys. Lett. B Vol. 59, 114 (2002); Phys. Rev. B, Vol. 67, 174205 (2003).

[9] N.F. Mott and E. A. Davis, “Electronic Processes in Non-Crystalline Materials” Clarendon Press, Oxford, (1979).

[10] C. A. Neugebauer and M. B. Webb, J. of App. Phys. Vol. 33, 74 (1962).

[11] R. Parthasarathy, X. M. Lin, K. Elteto, T. F. Rosenbaum and H. M. Jaeger, Phys. Rev. Lett. Vol. 92, 076801 (2004).

[12] G. R. Wang, L. Wang, Q. Rendeng, J. Wang, J. Luo, and C.-J. Zhong, J. Mater. Chem. Vol. 17, 457 (2007).

[13] I. S. Beloborodov, A. V. Lopatin, V. M. Vinokur, and K. B. Efetov, Phy. Rev. B, Vol. 7, 125121 (2005).

[14] C.W. J. Beenakker, Phys. Rev. B, Vol. 44, No: 4, 1646-1656 (1991).

[15] "Single Electron Tunneling" Eds. H Grabert and M. H. Devoret, Plenum Press, New York and London (1992).

[16] A. R. Akhmerov and A. S. Ioselevich, JETP Lett. Vol. 83, 211–216 (2006).

[17] R. W. Simon et al. Phys. Rev. B, Vol. 36, 1962 (1987).

[18] Kondo J. Solid State Physics, Vol. 23, ed. F Seitz and D Tumbull (New York:Academic) 183-281 (1969).

[19] G. Bergmann, Phys. Rep. 107 (1984), P. A. Lee and R. V. Ramakrishnan, Rev. Mod. Phys. Vol. 57, 287 (1985).

[20] V. F. Gantmakher, D. A. Pushin, D. V. Shovkun, G. E. Tsydynzhapov, L. P. Kozeeva and A. N. Lavrovb, JETP Lett. Vol. 65, No: 11, 870-876 (1997).

[21] V. A. Ambegaokar, U. Eckern, and G. Schoen, Phys. Rev. Lett. Vol. 48, 1745 (1982); G. Schoen and A. D. Zaikin, Phys. Rep. Vol. 198, 237 (1990).

[22] A. Gerber et al. Phys. Rev. Lett. Vol. 78, 4277 (1997).

[23] A Gerber, J. Phys: Condens. Matt. Vol. 2, 8161 (1990).

[24] Y. Ando et al. Phys. Rev. Lett. Vol. 75, 4662 (1995).

[25] T. Chui, G. Deutscher, P. Lindenfeld and W. L. McLean, Phys. Rev. B, Vol. 23, 6172 (1981).

[26] J.Aftinito, N. Fortier and R. R. Parsons, J. Vac. Sci. Technol. A, Vol. 2, 316 (1984).

[27] J. E. Mooij and G. Schon, "Single Charge Tunneling", ed. H. Grabert and M. H. Devoret, Plenum, New York, 275–310 (1992).

[28] Frank Pobell , "Matter and Methods at low temperatures". Springer verlag, (1996).

CHAPTER VI

SUMMARY

This chapter discusses briefly the conclusions from the studies on the nanocluster assembled structures that are described in this thesis.

Nanocluster assembled structures consisting of cluster films of alloys such as FeAu, FePd and FePt, as well as metals such as Cu, Ag and Au, could be prepared using a nanocluster deposition system based on the inert gas phase condensation technique. The presence of a surface oxide layer around the clusters could be confirmed in all nanocluster systems except in the noble metals Ag and Au. The individual metal clusters were found to be spherical in shape and showed a strong tendency to agglomerate togetherin systems where the oxide layer was present.

The oxide was understood to form a shell around the clusters of FeAu, FePd and FePt which resulted in Anderson localization of electrons inside the metallic clusters. The as-deposited FeAu film showed resistivity values that were around 6 orders higher than the bulk resistivity values, whereas those for FePt and FePd films were only three orders higher than their bulk resistivity values. Analyzing the resistivity behavior of these Nano Cluster Assembled (NCA) films using Zabrodskii Zinov'eva method established the Variable Range Hopping (VRH) as the electron transport mechanism in these films. In the case of FeAu system a cross over from Efros-Shklovskii (ES) to Mott Variable Range Hopping (MVRH) was observed at 132 K where as for FePd and FePt the resistivity curve for the entire temperature range of 25 K to 350 K showed no cross over but remained to be ES-VRH. The oxide layer

around the FePd and FePt clusters could be reduced by carrying out a heat-treatment at 350^0C under Ar atmosphere, which was much lower than their bulk melting temperatures. This brought about a transition from the insulating state to a conducting state by the reduction of oxide layer in these systems. In the FeAu system a heat treatment at 350^0C did not result in an insulator to metal transition, rather it resulted in the disintegration of cluster agglomerates in to individual clusters. Heat treatments carried out on FeAu films at 350^0C for different durations (30 min, 1 hr and 2 hr) resulted in the variation of inter-cluster distances. With the reduction in the number of clusters in agglomerates as well as with variations in the distance separating the clusters the conduction mechanism was found to vary from ES-VRH to MVRH and then to Nearest Neighbor Hopping (NNH). Magnetic measurements were carried out on these alloy films. All the alloy clusters were below 10 nm and so each nanocluster acting as a single domain exhibited superparamagnetic behavior. From the blocking temperatures observed for these systems the estimates of anisotropy energies were obtained which showed an approximate agreement with their bulk values. Exchange bias was also present in these alloy films due to the presence of the oxide layer.

Agglomeration of clusters could be observed in Cu films. They also showed the presence of surface oxide which could be removed by a heat treatment at 1/3rd of its melting temperature. This resulted in the disintegration of cluster agglomerates to individual clusters. No oxide was present in Ag as well as Au films. The resistivity values of the Cu, Ag and Au NCA films showed a two to three order magnitude increase from the bulk resistivity. The oxide free Cu films as well as Ag and Au films showed a metallic temperature dependence of resistivity. The resistivity curves could be fitted to the modified Bloch Grüneisen function with the introduction of a

lower limit of integration Θ_0 for the phonon modes, while keeping the upper limit equal to Θ_D, the Debye temperature for the bulk metals. The values of Θ_0 observed from the fit is found to scale with the cluster size as the size of the clusters pose a limit on the phonon waves that can be sustained inside.

Isolated Au nanoclusters were deposited between interdigitated electrodes by carrying out cluster deposition for a very short time of 3 minutes. In this system the electron transport was found to be by NNH mechanism in the temperature range of 230K to 340K. Below 230K, the conductivity behavior was identified as a logarithmic temperature dependence given by $\sigma = a + b \ln T$. This was understood as being due to the inter-cluster voltage fluctuations that arise in Coulomb blockaded systems. The nonlinear I-V characteristics measured for this system also confirmed the presence of Coulomb blockade. From the full width at half minimum of the differential conductance data an estimate of the number of nanocluster junctions participating in electron conduction could be deduced which agreed with the microstructure observed from the SEM pictures.

In the present study, the variation in the inter-cluster distance is found to have an effect on the resistivity values as well as on the electron transport mechanism in a system. With an increase in the distance between the clusters, an increase in the localization effects are observed. Since there was the presence of oxide in these systems it was difficult to understand effects quantitatively in terms of inter-cluster distances. A systematic study on a metallic cluster assemblage preferably Ag or Au (as they are free from oxidation), with a variation in inter-cluster distances will be quite fascinating. This will hopefully bring about a transition in the resistance behavior from the separated nanoclusters in the insulating regime (as was observed in the case

of isolated Au nanocluster assemblage) to the well connected clusters in the metallic regime. Also it would be interesting to understand the transport mechanisms in these scenarios and to see how the transition from one mechanism to the other takes place. The electron transport in such systems is expected to follow hopping mechanisms like ES-VRH, MVRH and NNH in the insulating regime with variations in inter-cluster separations, whereas the metallic regime will be governed by the diffusive motion of electrons. With such a study as mentioned above we will be able to pinpoint the critical parameters that bring about transitions from one transport mechanism to the other. It would also be possible to tune the conductivity to the desired values over a wide range simply by changing the inter-cluster distance.

A major parameter determining the magnetic properties of a material is its magnetic anisotropy. Magnetic anisotropy affects a material's hysteresis loop and controls the coercivity and remnant magnetization [1]. For applications in magnetic data storage, a material should have high coercivity and remnant magnetization [2]. Superparamagnets usually exhibit small coercivity which is a limiting factor in their applications. A higher coercivity can be achieved by orienting the easy axis of all the particles in the same direction during deposition. In the case of nanoclusters deposited using a nanocluster deposition system this kind of a magnetic alignment was achieved [3] by applying a field near the substrate while the nanoclusters are being deposited. It would be interesting to persue the research in this direction depositing nanoclusters in a magnetic field and to understand the extent of increase in coercivity in the plane and perpendicular to the plane of the FePt cluster films.

References

[1] Julien Cucchiara, “Spin–transfer effects in nanopillars with perpendicular magnetization", Ph.D. Thesis, Nancy University, France,(2010).

[2] Günter Schmid Ed., “Nanoparticles: From Theory to Application”, John Willey and sons, (2006).

[3] D. LeRoy, R.Morel, A.Brenac, L.NotinJ. Magn. Magn. Mater. Vol.323, 127–129 (2011).

Publication List

Research Articles

1) Efros-Shklovskii variable range hopping in nanocluster metallic films, **Thejal Abraham**, Chandrahas Bansal, J. Thampi Thanka Kumaran and Ashok Chatterjee, Journal of Applied Physics 111, 104318 (2012) 1-4

2) Electronically tunable conductivity of a nanoporous Au-Fe alloy C.Bansal, S.Sarkar, A.K. Mishra, **Thejal Abraham**, C.Lemier and Hahn. Scripta Materialia 56 (2007) 705-708

3) Resistivity Measurements of Nanocluster assembled Cu Films **Thejal Abraham**, S.Sarkar and C. Bansal. Solid State Physics (India) 50 (2005) 433- 434

4) Transport properties of Nanocluster assembled Cu, Ag and Au films, **Thejal Abraham** and C.Bansal (Under Preparation)

5) Electron transport in isolated Au Nanocluster assemblage. **Thejal Abraham** and C.Bansal (Under Preparation)

6) Superparamagnetism and Exchange Bias in FeX (X=Au, Pt and Pd)/$Fe_{0.9}O$ Core/Shell Nanoclusters, **Thejal Abraham** and C.Bansal (Under Preparation)

7) Transport behavior in Nanocluster assembled PdNi films. **Thejal Abraham** and C.Bansal (Under Preparation)

Conferences Attended

1) Transport In Interacting Disordered Systems. Presented poster titled "Observation of Coulomb Gap in $Fe_{50}X_{50}$ (X=Pd, Pt, Au) Nanocluster films". **Thejal Abraham**, Chandrahas Bansal, J. Thampi Thanka Kumaran and Ashok Chatterjee. 2008 Rackeve, **Hungary.**

2) Department of Atomic Energy Symposium, Presented poster titled Resistivity Measurements of Nanocluster assembled Cu and Ag Films **Thejal Abraham**, S.Sarkar and C. Bansal. 2005, Mumbai, India.